MAGNETIC RESONANCE SPECTROSCOPIC IMAGING FOR IMPROVED TREATMENT PLANNING OF PROSTATE CANCER

by

Niranjan Venugopal

A Thesis submitted to the Faculty of Graduate Studies of

The University of Manitoba

in partial fulfilment of the requirements of the degree of

Doctor of Philosophy

Department of Physics and Astronomy

University of Manitoba

Winnipeg

Abstract

Prostate cancer is the most common malignancy afflicting Canadian men in 2011. Physicians use digital rectal exams (DRE), blood tests for prostate specific antigen (PSA) and transrectal ultrasound (TRUS)-guided biopsies for the initial diagnosis of prostate cancer. None of these tests detail the spatial extent of prostate cancer - information critical for using new therapies that can target cancerous prostate. With an MRI technique called proton magnetic resonance spectroscopic imaging (^{1}H-MRSI), biochemical analysis of the entire prostate can be done without the need for biopsy, providing detailed information beyond the non-specific changes in hardness felt by an experienced urologist in a DRE, the presence of PSA in blood, or the "blind-guidance" of TRUS-guided biopsy. A hindrance to acquiring high quality ^{1}H-MRSI data comes from signal originating from fatty tissue surrounding prostate that tends to mask or distort signal from within the prostate, thus reducing the overall clinical usefulness of ^{1}H-MRSI data. This thesis has three major areas of focus: 1)

The development of an optimized ^{1}H-MRSI technique, called conformal voxel magnetic resonance spectroscopy (CV-MRS), to deal the with removal of unwanted lipid contaminating artifacts at short and long echo times. 2) An in vivo human study to test the CV-MRS technique, including healthy volunteers and cancer patients scheduled for radical prostatectomy or radiation therapy. 3) A study to determine the efficacy of using the ^{1}H-MRSI data for optimized radiation treatment planning using modern delivery techniques like intensity modulated radiation treatment. Data collected from the study using the optimized CV-MRS method show significantly reduced lipid contamination resulting in high quality spectra throughout the prostate. Combining the CV-MRS technique with spectral-spatial excitation further reduced lipid contamination and opened up the possibility of detecting metabolites with short T_2 relaxation times. Results from the in vivo study were verified with post-histopathological data. Lastly, ^{1}H-MRSI data was incorporated into the radiation treatment planning software and used to asses tumour control by escalating the radiation to prostate lesions that were identified by ^{1}H-MRSI. In summary, this thesis demonstrates the clinical feasibility of using advanced spectroscopic imaging techniques for improved diagnosis and treatment of prostate cancer.

Key words: *Short TE, conformal voxel, magnetic resonance spectroscopic imaging, LCModel, prostate cancer, lipid contamination, lipid suppression, NTCP, TCP, histopathology, MRI*

Acknowledgements

This thesis could not have been possible without the mentorship, guidance and support of many special individuals. I sincerely and humbly wish to express my gratitude to those who have shaped my perception of the world and showed me that modern physics has its place in the advancement of medicine.

My first acknowledgment goes to the spiritual teachings of Bhagavan Sri Sathya Sai Baba, who once said, "The end of wisdom is freedom. The end of culture is perfection. The end of knowledge is love. The end of education is character." These words have always held deep philosophical and spiritual meaning for me. In the same breath, I would like to express my love and indebtedness to my mother and father, who sacrificed so much over the years so that I could enjoy the possibility of receiving a higher education and putting into practice what I have learned for the benefit of others. Because of them and their example, I learnt the value of social responsibility and humility.

Normally a graduate student would work under the supervision of a single thesis advisor. In my case, I was fortunate to receive the guidance of two well-respected and knowledgeable scientists, Dr. Lawrence Ryner an expert in Magnetic Resonance Imaging (MRI), and Dr. Boyd McCurdy an expert in Radiation Oncology Physics (ROP). Both were instrumental in specializing my knowledge of physics and together showed me that the fusion of two apparently separate branches of physics (MRI and ROP) can provide a benefit to prostate cancer sufferers through improved diagnosis and biologically guided radiation treatment. Their support and guidance throughout the years was undivided. They taught the importance of good scientific reasoning, and preparation. As well an appreciation to paying attention to

fine details while keeping an eye on the big picture. Their enjoyment and interest in the research kept me motivated even during challenging times. Out of all the things I learned from them, the most important lesson I will take away is that learning is a lifelong process and in a sense you are always a "student". Because of their training, I will always continue to challenge myself and never shy away from difficult problems. For taking me on as a student and for so much more, I sincerely thank you both.

Next I would like to thank Dr. Stephen Pistorius. Dr. Pistorius had an unique impact on my life, by giving me my first exposure to world of Medical Physics through a summer internship. Since then I've been hooked on Medical Physics research and have never looked back. As the head of the academic program, Dr. Pistorius graciously provided financial support which allowed me to attend several national and international meetings which helped shape my career as a young investigator.

I would also like to thank the members of my thesis advisory committee, Dr. Samar Safi-Harb, Dr. John Lewis, and Dr. Gabriel Thomas. Their feedback and encouragement was helpful in the development of this thesis. At the same time, I would like to extend my gratitude to the external examiner, Dr. Alex MacKay from the University of British Columbia. His critical review of the thesis helped me see the importance of our work and its broader application to the treatment of prostate cancer.

This research would not have been possible without the support from specialized staff including Urology (Dr. Darrel Drachenberg, Dr. Aziz Alamri, Dr. Gurdarshan Sandhu, Dr. Sri Sivalingam, Dr. Jeff Saranchuk, and Dr. Salem Al Mehairi), Radiation Oncology (Dr. Jinka Sathya, Dr. Amit Chowdhury, Dr. Shahida Ahmed and Gayle Nickol, R.N.) Pathology (Dr. Belinda Lategan and Dr. I. Aljada), and Medical Physics (Keith Nakonechny). Your technical and clinical expertise in each of your respective areas was invaluable and I deeply appreciate the time you spent helping complete this body of work, despite demanding clinical duties.

Over the years there were so many people with whom I shared many fond memories while working at both the NRC Institute for Biodiagnostics and CancerCare Manitoba. At CancerCare I would like to thank all the students and staff: Krista Chytyk, Troy Teo, Ganiyu Asuni, Tamar Chighvinadze, Heather Champion, Peter McCowan, Tim Van Beek, Jenna King, Mike Hebb, Huanjin Wu, Kyle Malkoske, Dr. Jeff Bews, Dr. Jorge Alpuche, Dr. Ryan Rivest, Dr. Muoi Tran, Dr. Anita Berndt, Dr. Daniel Rickey, Dr. Harry Ingleby, Dr. Idris Elbakri, Dr. Sankar Venkataraman, Dr. Daniel Flores-Tapia and Dr. Eric van Uytven. Similarly at NRC I would like to thank all the students and staff: Ernie Packulak, Sanaz Mohajeri, Mike Smith, Matt Sodomsky, Richard Young, Alex Demko, Dr. Jennifer Kornelson, Dr. Brandy Wicklow, Dr. Ian Smith, Dr. Roxanne Deslauriers, Dr. Omkar Ijare, Dr. Tedros Bezabeh, Dr. Jordan Hovdebo, Dr. Karl Edler, Dr. David Hoult, Dr. Scott King, Dr. Patricia Gervai, Dr. Jon McGavock, and Dr. Hacene Serrai. You all provided a great deal of support in a multitude of ways.

I would like to extend my love and gratitude to an extremely supportive group of family and friends who helped me through the years. Especially to my elder brother Srikanth-anna, sister-in-law Lynn, younger sister Shankari, brother-in-law Ounesh, younger brother Prasanna, Aunty Prema, Uncle Ranga, Uncle Kaiser, Aunty Hem, Uncle Mathur, Praveen, Nirusha, Michael, Reena, and Caroline. Each of you had such a special role in shaping my life. For that, I am forever grateful. If I was to list everyone who has supported me along the way, the list would be endless. Please excuse me if your name is not mentioned here.

Lastly, I am grateful to the following funding bodies for their financial support throughout my studies: CancerCare Manitoba, National Research Council of Canada-Institute for Biodiagnostics, Prostate Cancer Research Foundation of Canada, Manitoba Health Research Council, and the University of Manitoba.

To end my acknowledgements, I give my humble appreciation to all the saints, scientists, and great visionaries of our time whose words often inspire me day-to-day.

"...The modern physicist experiences the world through an extreme specialization of the rational mind; the mystic through an extreme specialization of the intuitive mind. The two approaches are entirely different and involve far more than a certain view of the physical world. However, they are complementary, as we have learned to say in physics...." - Fritjof Capra (Tao of physics, p.306, 2nd edition)

Dedication

To my parents who have worked tirelessly in service to others.

Table of Contents

Chapter 2

2. Technical Development

Chapter 3

3. Automatic Conformal prescription of very selective saturation bands for in vivo 1H-MRSI of the prostate

Chapter 4

4. Short echo time in vivo prostate 1H-MRSI

Chapter 5

5. Histopathological analysis of a novel in vivo MRSI technique

Chapter 6

6. IMRT planning of the prostate with boost to dominant intraprostatic lesion guided by 1H-MRSI

Chapter 7

Appendices

Bibliography

List of Tables

List of Figures

Abbreviations and acronyms

(by order of appearance)

DRE	Digital rectal exam
PSA	Prostate specific antigen
TRUS	Transrectal ultrasound
^{1}H-MRSI	Proton magnetic resonance spectroscopic imaging
CV-MRS	Conformal voxel magnetic resonance spectroscopy
VSS	Very selective saturation
PRESS	Point resolved spectroscopy
BPH	Benign prostatic hyperplasia
MRS	Magnetic resonance spectroscopy
NMR	Nuclear magnetic resonance
STEAM	Stimulated echo acquisition mode
CSI	Chemical shift imaging
CHESS	Chemical shift selective water suppression
OVS	Outer volume suppression
ROI	Region of interest
FOV	Field of view
FT	Fourier transform
RF	Radio frequency
PSF	Point spread function
LDR	Low dose rate

HDR	High dose rate
SLDR	Sublethal damage repair
3D CRT	Three dimensional conformal radiation therapy
MLC	Multi-leaf collimator
IMRT	Intensity modulated radiation therapy
PET	Positron emission tomography
CT	Computed tomography
LQ	Linear quadratic model
TCP	Tumour control probability
NTCP	Normal tissue complication probability
GUI	Graphical user interface
LCModel	Linear combination of model spectra
SAGE	Spectroscopy analysis by General Electric
CHSIMU	Chemical simulation function
SNR	Signal to noise ratio
FWHM	Full width half-maximum
BASING	Band selective inversion with gradient dephasing
CCF	Cross-correlation function
Cho	Choline
Cit	Citrate
Pa	Polyamines
Cr	Creatine
ACRIN	American College of Radiology Imaging Network

CSA	Chemical shift artifacts
SLR	Shinnar Le Roux
PFC	Perfluorocarbon
Glx	Glutamine/Glutamate
mI	Myo-inositol
sI	Scyllo-inositol
Ta	Taurine
HR-MAS	High resolution magic angle spinning
BTV	Biological target volume
CTV	Clinical target volume
PTV	Planning target volume
DIL	Dominant intraprostatic lesion
PROFIT	Prostate fractionated irradiation trial
AAA	Analytical anisotropic algorithm
OAR	Organ at risk
FID	Free induction decay

Preface

In this thesis the development and testing of a modified ^{1}H-MRSI technique for the diagnosis and treatment of prostate cancer is examined. The overall goals of this thesis are - a) the development of an optimized ^{1}H-MRSI technique, with b) an *in vivo* human study to test the CV-MRS technique (including healthy volunteers and cancer patients scheduled for radical prostatectomy or radiation therapy) and c) integration of these results into radiotherapy treatment planning, after correcting for spatial deformations, to assess the potential for improving treatment using targeted dose-escalation to cancerous areas. Together these three components have the potential to improve the diagnosis and treatment of prostate cancer.

The content of this thesis includes several chapters covering a range of topics. Chapters 2, 3 and 4 deal with the development and *in vivo* testing of the optimized ^{1}H-MRSI technique. Chapter 5 examines the histopathological results. Chapter 6 looks at the radiation treatment planning of the prostate cancer incorporating MRSI

of the prostate, and lastly chapter 7 provides a summary and some discussion of future work. In more detail:

- **Chapter 1** mainly looks at the scientific rationale behind this work. Specifically, this chapter addresses the main questions: What is prostate cancer? How is this cancer diagnosed in the clinical environment? How has magnetic resonance spectroscopy helped in the diagnosis of the disease? Furthermore, this chapter examines the basic underlying physics of nuclear magnetic resonance, in addition to outlining pertinent radiation biology, and radiation delivery techniques.
- **Chapter 2** presents the development of the CV-MRS technique on a 1.5T MR system with prostate-like phantoms. Specifically, the necessary pulse programming needed to modify the spectroscopic imaging sequence and the optimizations made to the sequence to help eliminate residual lipid signals due to T_1 re-growth is discussed. This involves implementing an optimal ordering of very selective saturation (VSS) pulses with modified flip angles. Additionally, a description of the phantom which ensured that the pulse sequence worked with a phase-array torso coil in combination with an endo-rectal coil, is presented. In the latter part of chapter 2, methods for automated analysis using a customized version of the spectra fitting software, LCModel, are discussed.
- **Chapter 3** looks at the results of our *in vivo* prostate study. The automatically placed spatial saturation bands, using the optimized CV-MRS technique, significantly reduce lipid contamination over the entire prostate volume. The reduction in lipids results in an improved baseline and robust peak fitting when using LCModel. The CV-MRS technique removes user variability in the placement of spatial saturation bands, and helps reduce the technical expertise needed to perform ^{1}H-MRSI. *(A portion of this chapter has been accepted for publication: Venugopal et al., Automatic conformal prescription of very selective saturation bands for in vivo 1H-MRSI of the prostate. NMR Biomedicine. 2011:In press.)*

- **Chapter 4** examines the use of the CV-MRS technique at short echo times. This chapter demonstrates a robust method to improve the quality of *in vivo* prostate MRSI data by utilizing the CV-MRS technique coupled with a spectral-spatial excitation PRESS pulse sequence for short echo time acquisitions. *In vivo* implementation of this optimized MRSI technique confirms the reduction in peripheral lipid contamination, and improved spectral quality throughout the prostate. This technique provides significant signal-to-noise improvement and the ability to reveal short TE metabolites to potentially improve prostate cancer detection. *(A portion of this chapter has been accepted for publication: Venugopal et al., Short echo time in vivo prostate 1H-MRSI. Journal of Magnetic Resonance Imaging. 2011:In press.)*
- **Chapter 5** investigates the detailed sectional histopathology of whole prostate organs obtained from radical prostatectomy and correlates histopathological diagnosis with diagnosis from classification of ^{1}H-MRSI spectra. Furthermore, to confirm the MRSI-determined spatial extent of cancer, the histopathological diagnosis for each sub-centimeter cubic volume throughout the prostate is compared to the corresponding spectrum in the MRSI dataset.
- **Chapter 6** deals with the integration of MRSI results into radiation treatment planning by comparing radiotherapy treatment plans with and without MRSI-targeted dose-escalation strategies. Organ deformation due to the endorectal coil is accounted for, and the MRSI data was used to map the metabolic activity of dominant intraprostatic lesions throughout the prostate. This data is used to calculate a modified tumour control probability (TCP – an estimate of the probability of controlling the local disease) for the entire prostate organ. The TCP was used to estimate the effect on patient outcome of incorporating the MRSI information into the treatment planning process.
- **Chapter 7** provides a summary of the entire thesis, including some discussion on how different elements of the thesis come together. The future direction this work could take is also examined.
- **Appendix A** was written to help cover the basic NMR concepts that could not be covered in the main body of the thesis. At certain points of the thesis the

reader is directed to these sections. This will hopefully assist the reader in understanding some the underlying physical principles used throughout this thesis.

Statement of thesis

Definition of the spatial extent of prostate cancer using an improved magnetic resonance spectroscopic imaging technique to identify the molecular markers of malignant prostate tissue may allow for improved treatment of prostate cancer through targeted radiation dose-escalation.

Chapter 1

Introduction

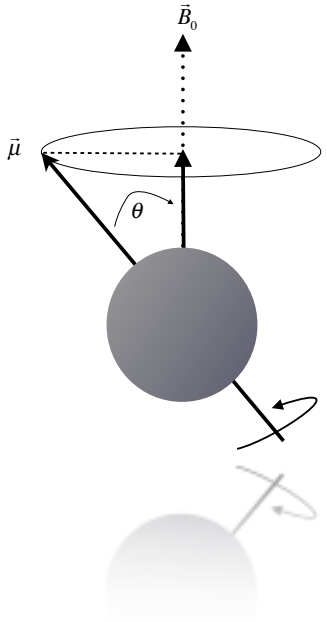

In this chapter we explore the basic principles that lay the foundation for this work, including relevant aspects of magnetic resonance imaging, radiation physics, and radiation biology.

1.Introduction

1.1. Prostate anatomy

The prostate gland is a critical part of the male reproductive system. A normal prostate is about the size of a walnut, and ranges in volume from 25-35 cc (1). Anatomically the prostate sits below the bladder. It surrounds the urethra, which is the tube through which urine flows out of the bladder as illustrated in Figure 1.1. The prostate gland's function is the production of seminal fluid, needed for the transport of sperm during ejaculation. The prostate's composition is approximately 70% glandular tissue and 30% non-glandular tissue. The zonal anatomy of the prostate divides the prostate into a peripheral, central gland, and transitional zones (2). As shown in the Figure 1B, the peripheral zone includes both the lateral and posterior aspects of the prostate and comprises most of the prostate volume (~70%). More importantly, for the context of this work, it is the zone in which 70% of prostate cancers arise (2). The central zone accounts for 5% to 10% of the glandular tissue of the prostate. Cellular proliferation in the transitional zone results in benign prostatic hyperplasia (BPH) - a benign condition in which the prostate gland enlarges. In addition, 20% of prostate cancers arise in the transitional zone.

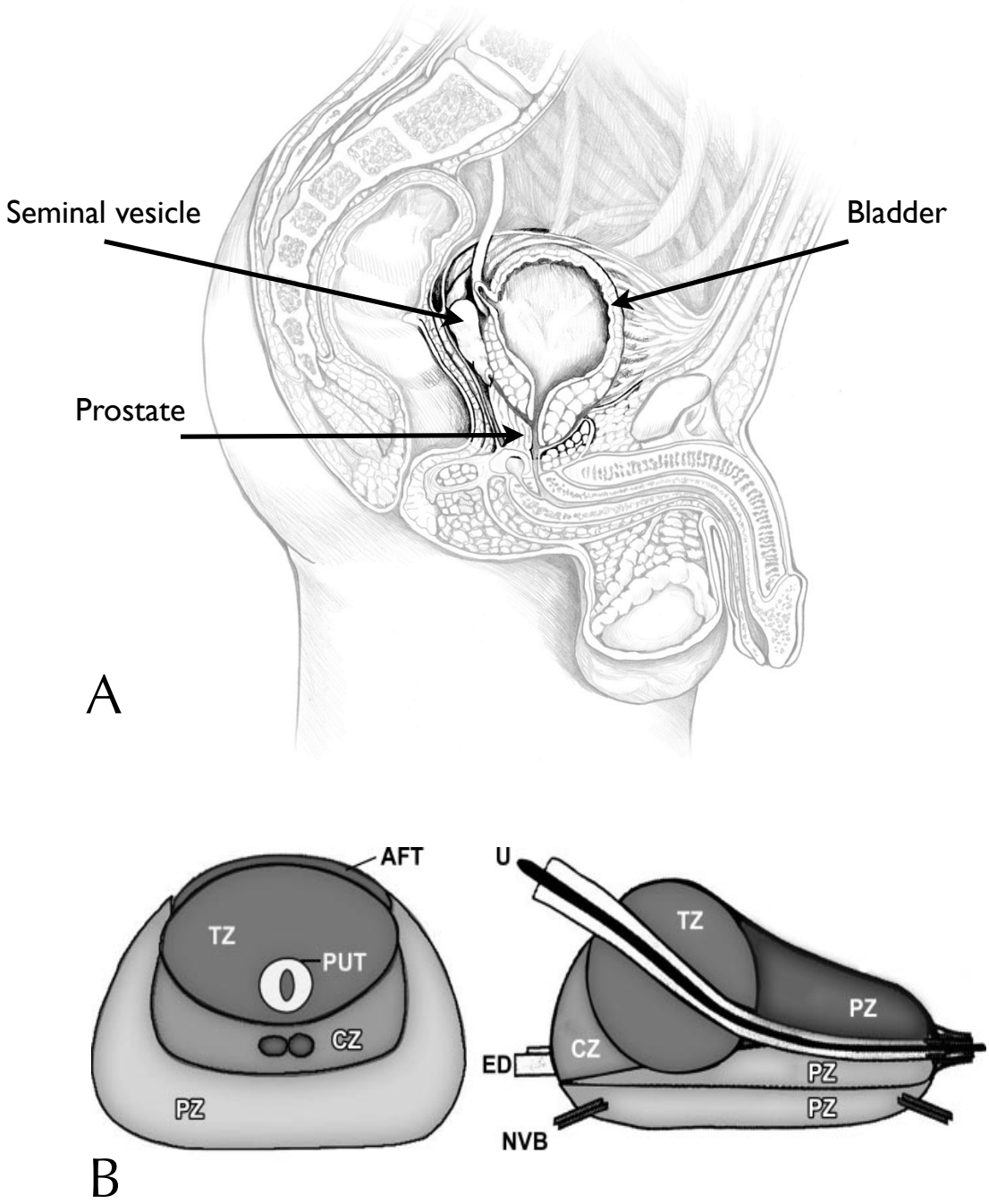

Figure 1.1 Prostate Anatomy

A - The anatomy of the male prostate. Pelvic anatomy(sagittal view). Note the location of the prostate behind the pubis between the bladder neck (superiorly) and the urogenital diaphragm (inferiorly) B- Schematics show the anatomy of the prostate in transverse and sagittal planes. AFT-anterior fibromuscular tissue,CZ-central zone, ED-ejaculatory duct, NVB-neurovascular bundle, PUT -periurethral tissue, PZ-peripheral zone, U-urethra, TZ-transitional zone. (© National Institute of Diabetes and Digestive and Kidney Diseases, National Institutes of Health. Used with permission - see Appendix C)

1.2. Current methods of diagnosing prostate cancer

Prostate cancer is the most common malignancy in Canadian men, with an estimated 25,500 new cases of prostate cancer diagnosed in Canada in 2011, and the third leading cause of death with an estimated 4,100 deaths in 2011 (3). Traditionally, the diagnosis of prostate cancer is made with the Digital Rectal Examination (DRE), in which the urologist manually identifies differences in the palpable characteristics of prostate tissue, and/or with measurements of prostate specific antigen (PSA) in the blood[1]. Transrectal ultrasound (TRUS) guided tissue biopsy is then used to confirm the presence of cancer through histopathological analysis. Histopathological samples are often reported by a "Gleason score", which is ascribed by the pathologist who has assessed the tissue under a microscope. The Gleason score is calculated by summing the grade of the two most common histological patterns observed by the core samples obtained from biopsy. The grading is scored on a scale ranging from 1-5. The TRUS guided biopsy and Gleason grade is displayed in Figure 1.2. According to this scale, aggressive cancers are associated with higher Gleason scores (poorly differentiated cell patterns), and less aggressive ones with lower scores (highly differentiated cell patterns). While histopathology remains highly accurate, there exists a high false-negative rate of about 30% due to inability to sample the entire prostate(4).

Despite their routine use, these tests are all relatively insensitive and are incapable of detecting small, well-differentiated cancers. These tests can detect

[1] The prostate specific antigen (PSA) is a protein produced by cells in the prostate gland. The PSA test measures the amount of the protein in a blood sample.

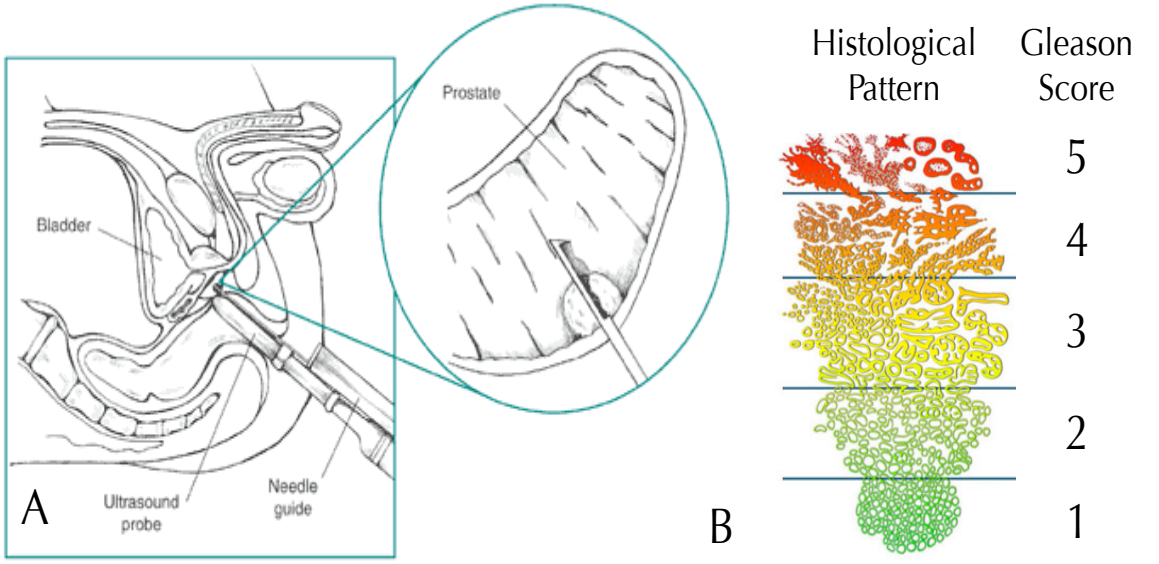

Figure 1.2 TRUS guided biopsy, and Gleason scoring system.
(A) TRUS guided biopsy is an invasive procedure that involves insertion of a biopsy needle into the prostate, and collection of prostate tissue samples. (B) Pathologists use histological patterns to determine Gleason score. Poorly differentiated glandular tissue has a more irregular pattern. (© National Institute of Diabetes and Digestive and Kidney Diseases, National Institutes of Health. Used with permission - see Appendix C)

only those tumours large enough to be palpable if located posteriorly for access with a DRE, visible on ultrasound, or capable of elevating the serum PSA level. The use of PSA, TRUS and DRE has resulted in earlier stage diagnosis and better long term survival, but improved diagnosis and treatment strategies are still needed.

The primary limitation of the PSA test, or any of its derivatives (PSA density, PSA velocity, age-specific PSA reference range and the ratio of free (unbound) PSA to total PSA), is that they do not provide information about the spatial location or extent of the cancer, information that is crucial for guiding confirmatory biopsy and/or targeted radiation treatment planning. Additionally, PSA is not specific to prostate cancer, therefore other prostate abnormalities such as BPH and prostatitis (prostatic inflammation) can also cause an elevation in the PSA value.

1.3. MRI in cancer diagnosis

Magnetic resonance imaging (MRI) can contribute to the clinical assessment of prostatic diseases by providing anatomical/morphological information which helps to identify prostate cancer. MRI is very useful in staging of the cancer (once the diagnosis has been established) since it offers several imaging advantages such as a multi-planar imaging capability, high contrast, and a small field of view (5-8). Prostate cancer generally appears as low-signal-intensity areas in the peripheral zone in T_2-weighted MR images, as seen in Figure 1.3A. However, there are a number of other medical situations that can generate low signal intensity, e.g., post-biopsy hemorrhage, prostatitis, and BPH (particularly stromal). Thus, a technique that improves the specificity of the diagnosis becomes essential. Magnetic resonance spectroscopy (MRS) has the potential to serve this purpose.

MRS provides biochemical and metabolic information associated with tumour growth and development, and is thus able to detect early, pre-morphological changes in tissue. Furthermore, it is conceivable that patient prognosis may be directly reflected in the MR-detectable biochemistry. The citric acid cycle, which occurs in all aerobic cells, is a series of chemical reactions which help oxidize citrate, and thus low-levels of citrate are typically found in normal cells throughout the body. However, cells within the prostate are different. Higher amounts of zinc prevent citrate from becoming fully oxidized, resulting in the accumulation of citrate in normal prostate cells. When a prostate cell becomes cancerous, the amount of zinc is reduced, and the citrate is oxidized causing a reduction in citrate. Furthermore, during the process of rapid cell division that

occurs in cancerous cells, the choline-containing proteins that are contained in the cell membrane are released into the local environment and accumulate in high concentrations (9). MRS is a useful *in vivo* method for identifying relative concentration of metabolites, and there have been several MRS studies reported on prostate tissue extracts and *ex vivo* studies (10). *In vivo* prostate MRS has confirmed the diagnostic utility of the metabolites choline, creatine, and citrate, in providing a specific marker for cancer within the peripheral zone, with 98% of cancers having a higher (choline+polyamines+creatine)/citrate ratio when compared to the normal ratio(11-13). While MRI has been used for staging of prostate cancer (once the diagnosis is established) for some time now, the clinical use of MRS in prostate cancer diagnosis is just starting to be adopted with good results (14-20). In Figure 1.3 B-E, spectroscopy data is displayed as a grid over the anatomical image.

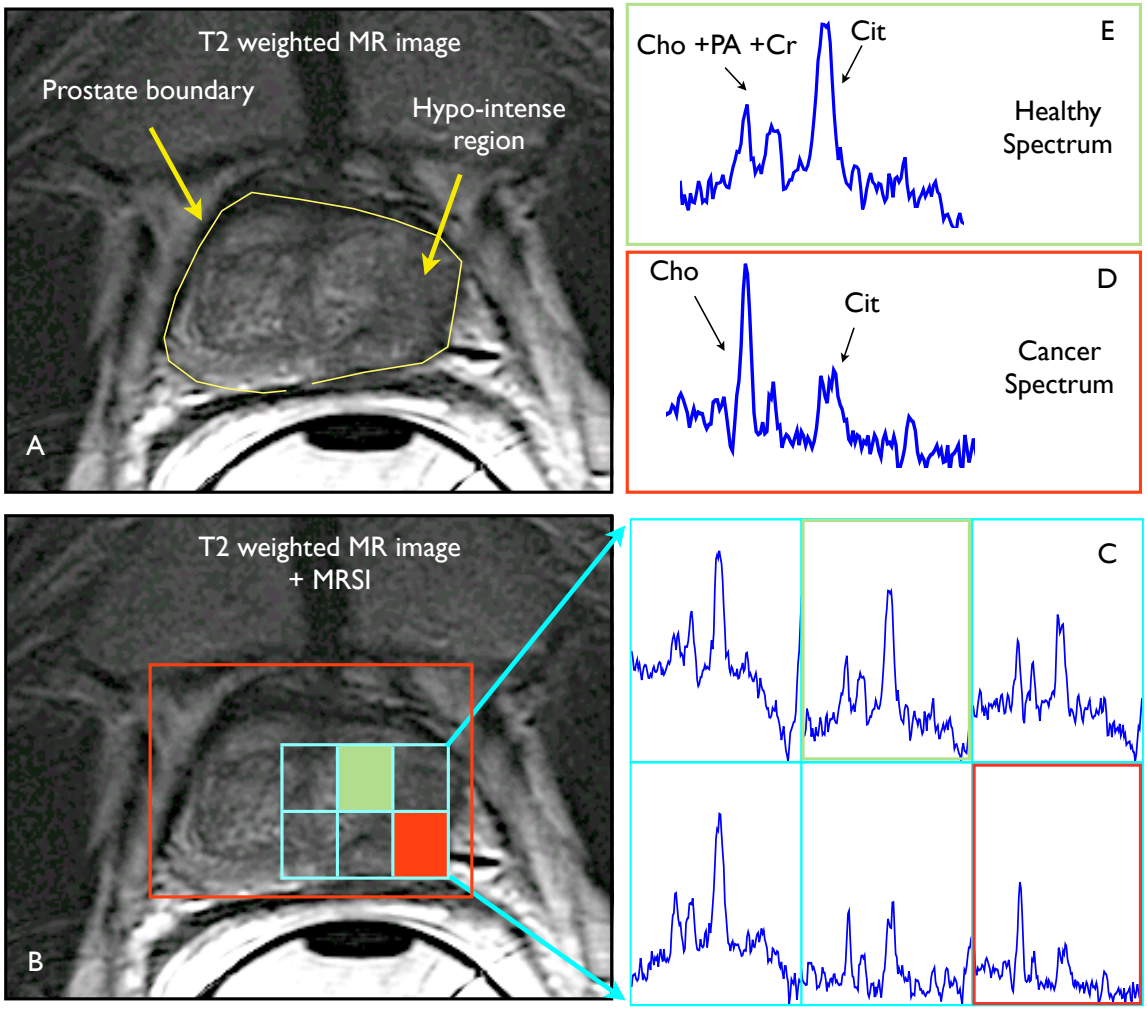

Figure 1.3 T_2 **weighted image of the prostate with corresponding spectroscopic imaging data**

In (A) a T_2*- weighted axial image showing the mid-gland of the prostate is presented demonstrating a region of hypo-intensity. In (B), the same prostate image is presented with a portion of the spectral grid overlaid on top. Zooming into the spectral grid (C), there are two highlighted regions, (D) in red, and (E) in green. In (D), there is an increased level of choline, and a decreased level of citrate, demonstrating a region of the prostate which is cancerous. This is compared to a healthy region, (E), which displays normal levels of citrate.*

1.4. Principles of Nuclear Magnetic Resonance (NMR)

1.4.1. Introduction

Magnetic resonance imaging (MRI) and magnetic resonance spectroscopic imaging (MRSI) are rapidly advancing imaging modalities. MRI has a well-established role in diagnostic radiology because of its ability to image soft tissues with excellent contrast. MRSI is beginning to establish itself as a critical radiology tool for examining the chemical composition of tissues *in vivo*. From previous sections, it is clear that the applications of MRI and MRSI have a significant role in the diagnosis of prostate cancer. The following sections will cover the fundamental theory used in these applications.

1.4.1.1. Classical description of Spin

Hydrogen is the simplest element, and also the most abundant element found in the human body, since it is found in water and fat (i.e. ~72% of human body mass is water). A hydrogen atom contains a single proton with an orbiting electron. A fundamental property of the proton is its intrinsic angular momentum or spin. The interaction of the proton with an external magnetic field $\vec{B}_0$ results in a precession of the proton's spin about the direction of $\vec{B}_0$, where the precession is defined as the circular motion of a spinning body about a secondary fixed axis. This precession is a result of the applied magnetic field creating a torque about the axis of $\vec{B}_0$. The applied external magnetic field on a proton with spin results in a

magnetic moment, $\vec{\mu}$, which is proportional to its spin. This is illustrated in Figure 1.4A.

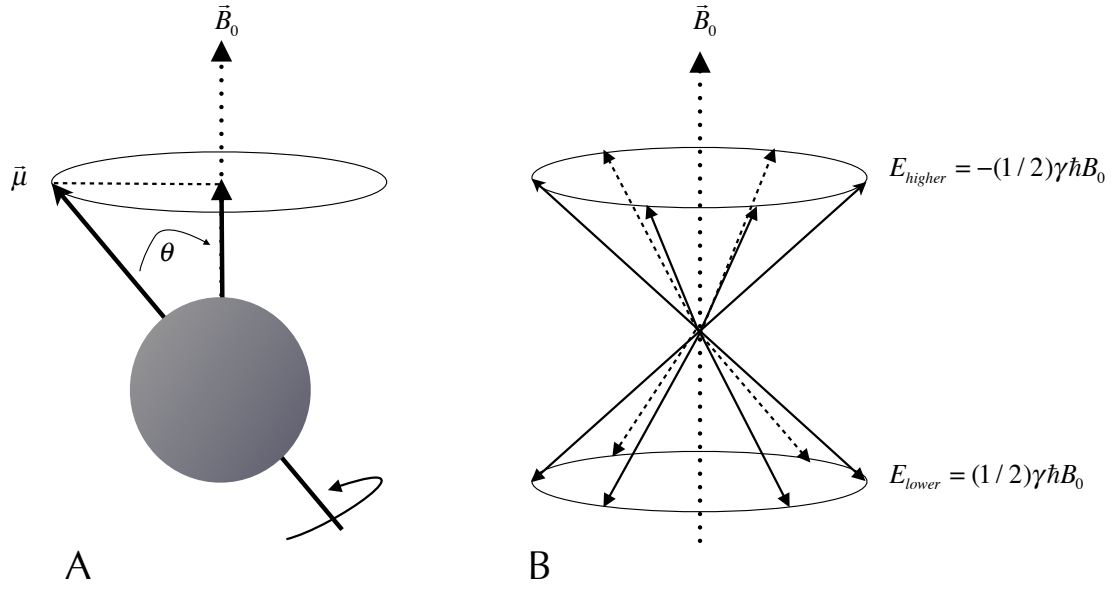

Figure 1.4 Vector representation of magnetic moment, and energy splitting.
In (A), much like a spinning top under gravity, the magnetic moment, $\vec{\mu}$, precesses in an external magnetic field, $\vec{B}_0$. In (B), according to the Boltzmann equation, a macroscopic sample of spins will distribute themselves to either a higher or lower energy state.

The magnetic moment of the proton occurs as a result of its spin properties. It is aligned to the axis of the proton, and it is mathematically expressed as:

$$\vec{\mu} = \gamma \vec{I} \tag{1.1}$$

where $\vec{I}$, is the angular momentum. Much like a spinning gyroscope, the proton will precess about the fixed axis, with an angular frequency given by the Larmor frequency. Classically, it can be shown that the Larmor frequency of precession, $\vec{\omega}_0$, is proportional to the strength of magnetic field $\vec{B}_0$,

$$\vec{\omega}_0 = -\gamma \vec{B}_0 \tag{1.2}$$

where γ is the gyromagnetic ratio. For hydrogen, the gyromagnetic ratio is ~2.68x10^8 rad/s/Tesla (or $\bar{\gamma} = \gamma / 2\pi$ is 42.6 MHz/Tesla). The gyromagnetic ratio is a property of the nucleus, and is proportional to its charge and mass. To further discuss the interaction of electromagnetic waves and nuclear spins, a quantum mechanical discussion is needed, as presented in the following section.

1.4.1.2. Quantum mechanical description of spin

Considering a quantum mechanical description, electromagnetic energy (i.e. X-rays, radio frequency waves, microwaves, etc.) can be described as a discrete energy packet. The relationship between the energy of the energy packet and its frequency is given by:

$$E = \hbar\omega_0 \tag{1.3}$$

where $\hbar$ is Planks constant ($\hbar$ = 1.0546x10^{-34} J s), and $\omega_0$is the Larmor frequency of precession.

In the process of emitting or absorbing an electromagnetic wave at the atomic level, an entire energy packet is either created or consumed. In order to conserve the total energy of the system, the nucleus at the same time must change to a different energy state. This is one the fundamental postulates of quantum mechanics. The angular momentum measured along a fixed axis may have only discrete values, equal to half-integer or integer multiples of $\hbar$. Angular momentum is defined as,

$$L = \sqrt{I(I+1)} \cdot \hbar \tag{1.4}$$

where I is the spin quantum number. The spin quantum number, I, can only be integer or half-integer numbers. Since $\vec{L}$ is a vector quantity, a second quantum number, m (called magnetic quantum number) is used to assign the direction of angular momentum. Along the z-direction, the angular momentum is defined by,

$$L_z = m \cdot \hbar \tag{1.5}$$

where m can have values ranging from m= I, I-1, I-2, ...,-I. For hydrogen, I=1/2, thus there are two discrete states, $L_z = \pm(1/2)\hbar$ and the difference in the z-component of the spin between the two states is $\Delta L_z = \hbar$.

The energy of the hydrogen nucleus depends on the orientation of its magnetic moment with respect to an external magnetic field, $\vec{B}_0$, which lies along the z-axis. Since the magnetic moment is parallel to its spin, the energy of the nucleus varies with spin direction such that:

$$E = -\gamma \vec{L} \bullet \vec{B}_0 \tag{1.6}$$

Further, the energy is proportional to the component of the spin along the z-direction.

$$E = -\gamma L_z B_0 \tag{1.7}$$

Equation 1.7 describes states with differing L_z values that have distinct energy states when subjected to an external magnetic field. Thus, the energy for spins in the higher energy state is given by $E_{higher} = -(1/2)\gamma\hbar B_0$, and the energy for spins in the lower energy state is given by $E_{lower} = (1/2)\gamma\hbar B_0$ (see Figure 1.4B).

Since, the angular momentum between states is given by $\Delta L_z = \hbar$, the corresponding energy separation between states is given by:

$$\Delta E = \hbar \gamma B_0 \tag{1.8}$$

Since γB_0 is the Larmor frequency, ω_0 , the energy difference can be re-written as $\Delta E = \hbar \omega_0$. Thus to excite the hydrogen nucleus to the next energy level requires the absorption of a electromagnetic wave that has an energy equal to this difference, such that $E_{photon} = \Delta E$. From this relation it can be derived that the frequency of the electromagnetic wave must precisely match the Larmor frequency of the hydrogen nucleus, $\omega_{photon} = \omega_0$.

From a quantum mechanical point of view, an incoming electromagnetic wave at a specific frequency excites the nucleus to a higher energy state. The now-excited nucleus may decay back to its initial state, while in the process releasing an electromagnetic wave of the same frequency. This constitutes the observed magnetic resonance signal. Quantum mechanics is the theory which provides the ultimate description and quantification of the NMR phenomena. In practice, classical principles are equally useful and still widely used to demonstrate the effects of radio-frequency pulses on macroscopic systems of spins.

1.4.1.3. Macroscopic magnetization

At a macroscopic level, the vector sum of all the microscopic magnetic moments will give rise to a total bulk magnetization, $\vec{M}$:

$$\vec{M} = \sum_{n=1}^{N_0} \vec{\mu}_n \tag{1.9}$$

where, $\vec{\mu}_n$ equals the magnetic moment of the "nth" nuclear spin, and N_0 is the total number of spins for a spin-1/2 system. Under the presence of an external magnetic field, $\vec{B}_0$, and using Boltzmann statistics the equilibrium magnetization can be calculated as :

$$M_0 = \frac{N_0 \mu \left(\frac{1}{2} e^{\frac{\mu B_0}{2\kappa T}} - \frac{1}{2} e^{-\frac{\mu B_0}{2\kappa T}} \right)}{\left(e^{\frac{\mu B_0}{2\kappa T}} + e^{-\frac{\mu B_0}{2\kappa T}} \right)} \tag{1.10}$$

where, κ is the Boltzmann constant (1.38x10^{-23}J/K), and T is the absolute temperature of the spin system.

However, when the ratio of $\mu B_0 / 2\kappa T$ is very small, and under Taylor expansion we can simplify the expression to:

$$\vec{M}_0 \simeq \frac{N_0 \gamma^2 \hbar^2 \vec{B}_0}{4\kappa T} \tag{1.11}$$

From equation (1.11), several important observations come to light concerning the sensitivity of an NMR experiment. For example, $\vec{M}_0$ has quadrature dependance on the gyromagnetic ratio which implies that nuclei that resonate at high frequencies also generate intense NMR signals. Further, the linear dependance of $\vec{M}_0$ on the magnetic field implies that higher field strengths also give rise to improved sensitivity. This relationship fuels the drive for higher field strengths for *in vivo* imaging. Lastly, the inverse dependence on temperature demonstrates that sensitivity could be enhanced at lower temperatures. For *in vivo* imaging, this last dependency is not realistic for day-to-day applications.

1.4.1.4. Chemical shift

Up until this point in our physics description, we have considered a simple system containing just one type of nuclear spin with a single resonance frequency given by the Larmor frequency. However, the resonance frequency itself does not only depend on the external magnetic field and the gyromagnetic ratio. It is also highly sensitive to the chemical environment that surrounds a particular nucleus. This effect is referred to as chemical shift, and is a direct result of the shielding of the nuclei from the external magnetic field by the surrounding orbital electrons. The precession frequency of a nucleus in a magnetic field is proportional to the field strength. The electron cloud created by the chemical bonds in the immediate vicinity of any given proton affects the magnetic field that is experienced by its'

nucleus. These local field changes are small, but form the basis of MR spectroscopy (MRS). An effective field at nucleus *j* can be expressed as,

$$\vec{B}_{eff} = \vec{B}_0(1-\sigma_j) \tag{1.12}$$

where σ_j is the chemical shielding constant for the nucleus *j*. The resulting precession frequency of nucleus *j* is then, $\omega_j = \gamma B_0(1-\sigma_j)$. For example, the resonance frequency of the water protons are different from the resonance frequency of fat protons. Other proton-containing metabolites are similarly affected. In common practice the chemical shift of a peak in a spectrum is given in terms of the relative difference in frequency from a reference peak. The chemical shift in parts per million (ppm) is also defined as:

$$\delta = \frac{\omega - \omega_{ref}}{\omega_{ref}} \times 10^6 ppm \tag{1.13}$$

where ω and ω_{ref} represent the resonance frequencies of the peak of interest and of the reference peak.

1.4.2. Scalar coupling

In performing NMR investigations of a sample with many metabolites, it is the known spectral pattern of an individual metabolite that allows the investigator to distinguish between the metabolites within the sample. An important observation in NMR spectra is the apparent splitting of spectral lines for a given compound, at specific resonance frequencies. This splitting of resonances is a phenomenon which

is governed by scalar coupling (also called spin-spin coupling or J coupling). This phenomenon exists because nuclei with magnetic moments can influence each other in two ways: 1) dipolar coupling-interactions through space or 2) scalar coupling-interactions through the chemical bonds. Though dipolar interactions are the main cause for relaxation in a liquid, the net total effect on chemical shift is zero since rapid tumbling effects between nuclei average out to zero. But this is different in the case of the scalar coupling caused by spin-spin interactions which are mediated by Fermi contact, and spin states that follow the Pauli's exclusion principle. The scalar coupling caused by chemical bonds result in interactions that do not average to zero and thus give rise to this phenomena.

1.4.2.1. One spin, and two spin systems

From quantum mechanics it is well-established that an intrinsic property of a nucleus is "spin". As described in section 1.4.1, spin is characterized by the quantum number $\vec{I}$. For the discussion in this section, let us consider nuclei that are "spin-half", such that $\vec{I}$ can only give rise to two energy levels. $\vec{I}$ is further characterized by the quantum mechanical number, m, which for a spin-half nuclei can only be values of -1/2 and +1/2. For energy levels with "spin-up" (i.e. m= +1/2), the traditional denotation is α and for energy levels with "spin-down"(i.e. m=-1/2) the traditional denotation is β. In the following discussions α is the lower energy state.

Consider a molecule with one spin. Quantum mechanics tells us that we are restricted to discrete energy states, either α or β. Following from discussions in section 1.4.1, the energy state for this single state system is:

$$E_\alpha = +\frac{1}{2}\omega\hbar \text{ and } E_\beta = -\frac{1}{2}\omega\hbar \tag{1.14}$$

where ω is the Larmor frequency of the spin. Because energy is discretized, systems of spins follow very specific selection rules that are related by specific quantum numbers and allowable energy states. This section will only briefly discuss the selection rules, and will not go in great detail about all quantum numbers and their significance.

For NMR the allowable transition is determined by the quantum number, *m*. It is possible to determine the frequency of the allowed transition in a single state system by simply subtracting the transitional energies from "initial state" and "final state" such that, $\nu_{\alpha\beta} = E_\beta - E_\alpha$, where $\nu_{\alpha\beta}$ (or $\nu_{\alpha\beta} = \omega_{\alpha\beta} / 2\pi$) is the Larmor frequency centered at a single peak as shown in Figure 1.5. In this simple case, a single spin system would give rise to a single spectrum, and a well-defined energy transition. However, this does not occur when dealing with systems of many spins that are coupled together.

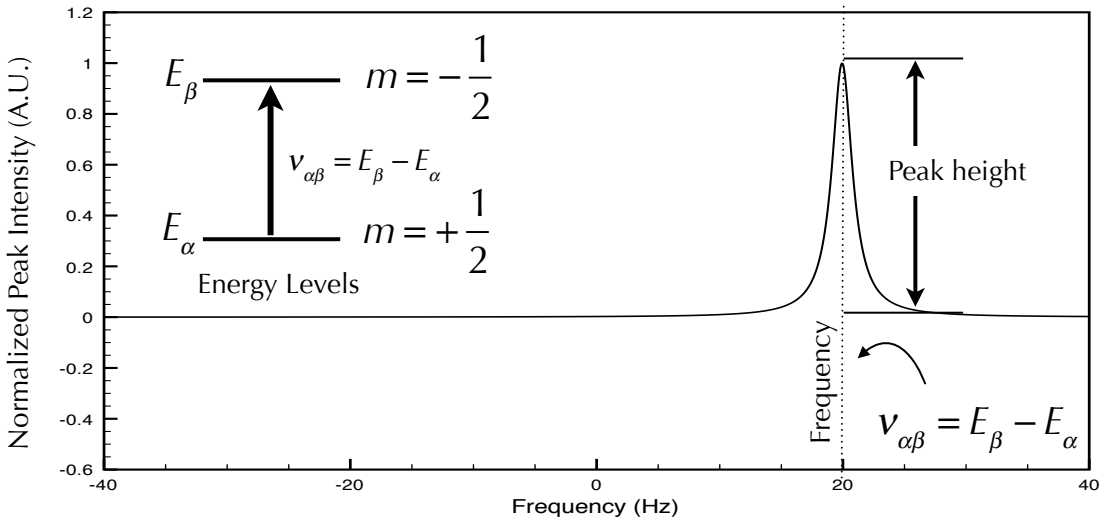

Figure 1.5 The transition between the two energy levels
The transition between the two energy levels of single spin-half system, resulting in a single peak at the Larmor frequency of the spin.

Consider now an extension of this simplest case, where we have a system of two coupled spins A and B. This is also referred to in the literature as a spin AB system. If the magnetic field of A interacts with the magnetic field of B, the resulting Larmor frequencies will be different and will result in a small shift in energy levels. In the uncoupled case, a spectrum of the spin AB system will contain two singlets centered at the same frequency (See Figure 1.6) . While in the case that the spins are coupled, the spectrum contains two doublets, each split by the same amount. The splitting between the two doublets is characterized by the scalar coupling constant, J, in units of Hertz.

The AB spins system has two spins which results in four possible energy levels. These are, $\alpha_1\alpha_2$, $\alpha_1\beta_2$, $\beta_1\alpha_2$, and $\beta_1\beta_2$. The characteristic energy levels are outlined in Table 1.1.

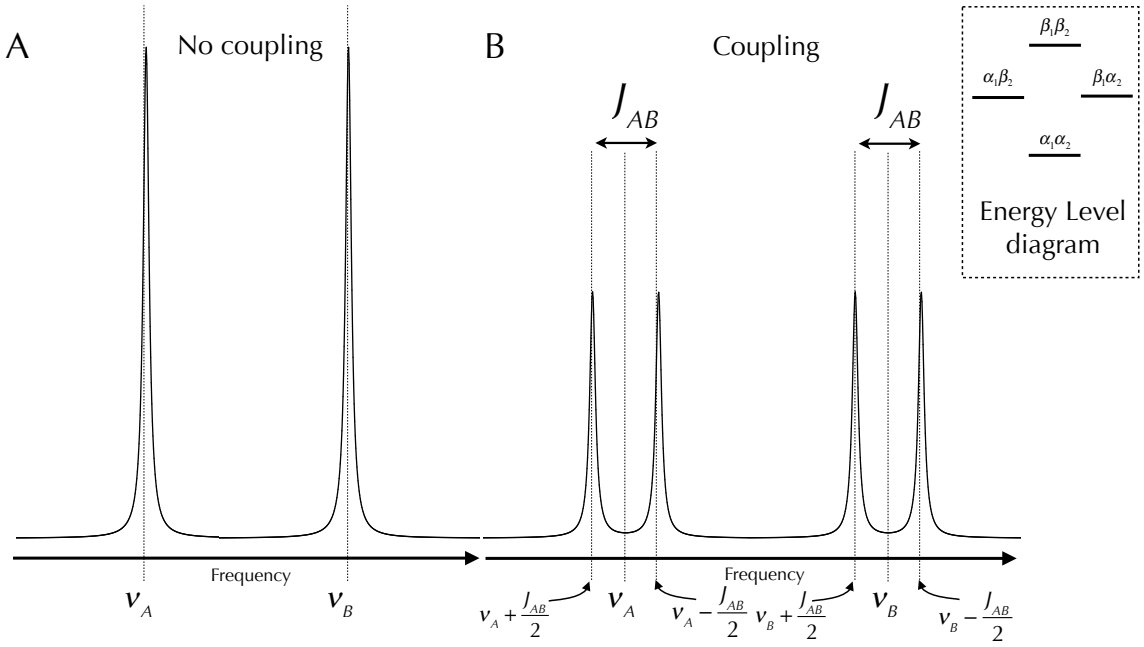

Figure 1.6 Spectra with and without J-coupling
In (A), the spectrum demonstrates no coupling. While in the case that the spins are coupled, the spectrum (B) contains two doublets, each split by the same amount.

Table 1.1 AB spin system energies

Energy levels	Spin state	Energy
1	$\alpha_1\alpha_2$	$+\frac{1}{2}h\nu_A + \frac{1}{2}h\nu_B + \frac{1}{4}hJ_{AB}$
2	$\alpha_1\beta_2$	$+\frac{1}{2}h\sqrt{(\nu_A - \nu_B)^2 + J_{AB}^2} - \frac{1}{4}hJ_{AB}$
3	$\beta_1\alpha_2$	$-\frac{1}{2}h\sqrt{(\nu_A - \nu_B)^2 + J_{AB}^2} - \frac{1}{4}hJ_{AB}$
4	$\beta_1\beta_2$	$-\frac{1}{2}h\nu_A - \frac{1}{2}h\nu_B + \frac{1}{4}hJ_{AB}$

These energies correspond to the energy level diagram shown in Figure 1.6. In this diagram, the uncoupled system allows for two transitions in which the frequencies for spin A and B are equal. Furthermore, in the coupled case the spectrum is split into doublets. Introducing more coupled spins, would further split the spectrum (i.e. coupled networks that take the form of triplets, quartets, etc.). While the scalar coupling plays an important role for line splitting, it also causes phase modulations in the spectrum. This is illustrated in Figure 1.7, where for varying echo times the two peaks of the doublet become out-of-phase with each other. This effect is dependent on the echo time, the J-coupling constant, and the particular pulse sequence being used. At an echo time (TE) of TE=1/J, the two outer peaks appear as an inverted doublet, while at a TE=2/J, the two outer peaks appear as a positive in-phase doublet, when using an ideal spin-echo sequence.

In summary, there are several properties of *J*-coupling that determine the final appearance of the spectra: 1) The coupling strength decreases with increasing number of bonds connecting coupled spins, 2) the coupling constant, *J,* is independent of the main field strength, 3) scalar coupling between magnetically equivalent nuclei do not give rise to observable splitting patterns, 4) the number of spectral lines can be calculated by $N_i + 1$, where N_i is the number of magnetically equivalent nuclei with spin *I*, 5) the coupling to different spin groups is additive, 6) for weakly coupled resonances, the line intensity patterns are distributed in a binomial pattern, and lastly, 7) strong coupling effects cause the appearance of more complicated spectra.

In the limit, where $|\nu_A - \nu_B| \gg J_{AB}$, the spins system is referred to as "weakly coupled", and is often referred to as a first order coupling. In the case where $|\nu_A - \nu_B| \approx J_{AB}$, the system is referred to as strongly coupled. In strongly coupled systems, the spin states $\alpha_1\beta_2$, and $\beta_1\alpha_2$ become mixed, and give rise to a more complicated spectrum, as illustrated in Figure 1.7. The strong coupling effect becomes important in the context of this work, and is discussed in detail in the next section.

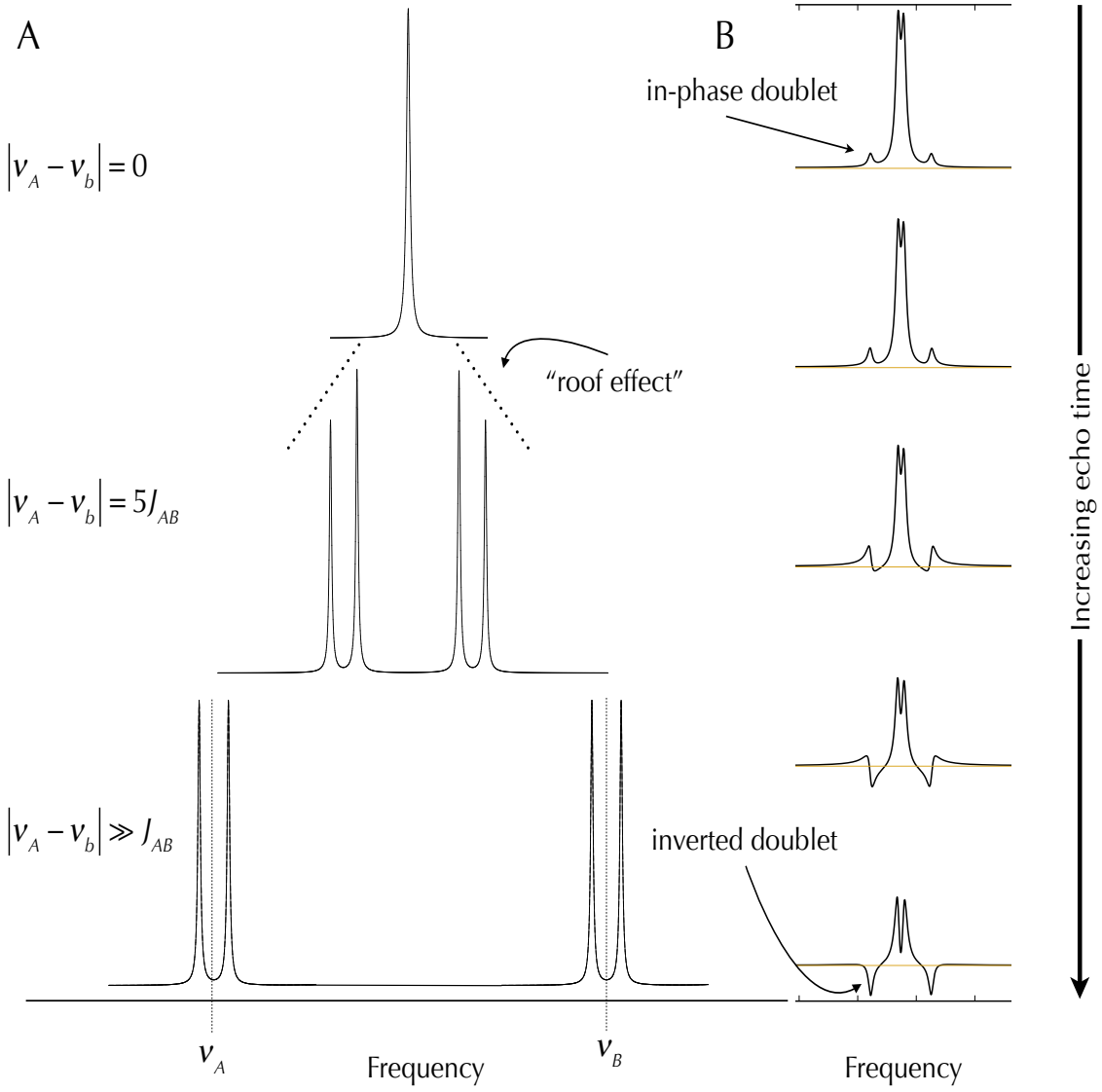

Figure 1.7 Quantum mechanical simulation of J-coupled spectrum
In (A) a series of spectra of a spin AB system is presented, where the Larmor frequency of spin A is held constant while the Larmor frequency of spin B is moved closer to spin 1. The spectra become more strongly coupled showing a pronounced "roof effect" until the two Larmor frequencies are equal and only one line is observed. In (B), the Larmor frequency of spin A and B are kept constant, and the spin AB system is excited by spin-echo excitation sequence. Varying the echo time in the PRESS sequence demonstrates the modulation of the phase of the outer-peak.

1.4.2.2. Citrate: A strongly coupled system

As discussed in the previous section, different spin systems give rise to very specific spectral patterns according to some fundamental rules outlined by quantum mechanics. In the context of this work, *in vivo* MR spectroscopy of the prostate is mainly concerned with the detection and identification of a system of metabolites, namely choline, polyamines, creatine, and citrate. Citrate is the central metabolite for the assessment of cancer and is often the metabolite of key interest when designing and manipulating pulse sequences (12, 13, 15, 21-24). The spectrum of citrate is of the strongly coupled AB type with the chemical shift difference equal to $(\nu_A - \nu_B)$ of the two unequal protons, as seen in Figure 1.8A. Since the chemical shift is small compared with the magnitude of the coupling constant J at the current field strength, the shape of the observed spectra will depend strongly on the external field strength. Wilman and Allen have extensively discussed the signal response of the citrate AB system to various localization sequences (i.e. point resolved spectroscopy-PRESS, and stimulated echo acquisition mode -STEAM) (26). In their work, they showed that for liquid MR spectroscopy, one must perform the quantum mechanical simulations to determine the appropriate signal response for a given pulse sequence. To begin discussing the quantum mechanical simulation, one begins by describing the total energy of the system. In quantum mechanics the total energy describing the spin system is given

by the Hamiltonian[2]. In this case of a spin AB system, the Hamiltonian consists of two parts, a dipole coupling term[3], H_d and scalar coupling term, H_J such that:

$$\begin{aligned} H &= H_d + H_J \\ &= \sum_{k=1}^{N} \omega_{0k} I_{kd} + \sum_{k=1, l<k}^{N} \vec{I}_k J_{kl} \vec{I}_l \end{aligned} \tag{1.15}$$

where $\vec{I}_k$ is the spin-angular momentum operator, ω_{0k} is the Larmor frequency of the spin k, and $\vec{J}_{kl}$ is the coupling constant between the spins.

Following methodologies that were established by Kay and McClung (25), the AB Hamiltonian can be split into two commuting parts, H_0 and H_1 which are:

$$H_0 = \bar{\omega}(A_d + B_d) + 2\pi J A_d B_d \tag{1.16}$$

and

$$H_1 = \delta\omega(A_d - B_d) - 2\pi J(A_+ A_- - A_- B_+) \tag{1.17}$$

where $A_\pm$ and $B_\pm$ are the spin-angular momentum operators, $\delta\omega$ is the chemical-shift difference between spins A and B, $\bar{\omega}$ is the average chemical shift, and Λ is the strong-coupling frequency, such that:

$$\delta\omega = \frac{(\omega_A - \omega_B)}{2}, \bar{\omega} = \frac{(\omega_A + \omega_B)}{2} \tag{1.18}$$

---

[2] In quantum mechanics, the Hamiltonian refers to the total energy of the system, and the spectrum of all the possible energy transitions results in making a measurement of the system. The classical analogy defines the Hamiltonian, H, as the sum of kinetic (T) and potential energies(V). (i.e. H=T+V)

[3]The dipole coupling term is sometimes also referred to as the Zeeman splitting term

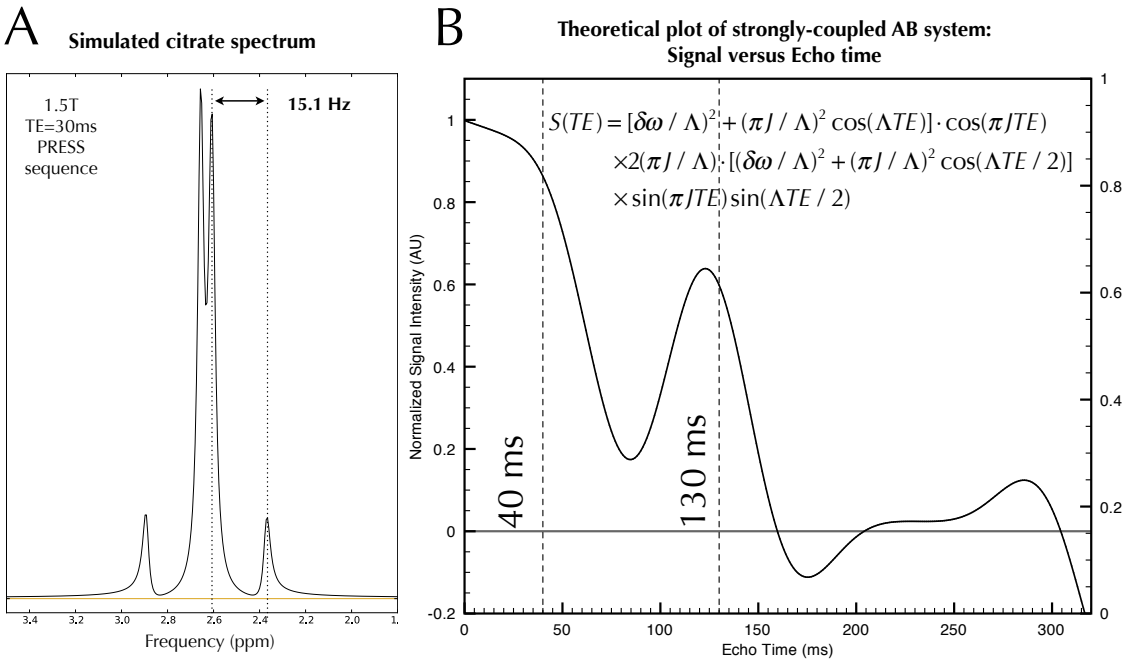

Figure 1.8 Simulated citrate spectrum and theoretical plot of the citrate signal using a PRESS sequence

The citrate molecule behaves as a strongly coupled AB system. The spectrum of citrate is presented in (A). For the PRESS sequence, the signal of the citrate-AB system decays exponentially with a sinusoidal variation (B).

and,

$$\Lambda = \left[\delta\omega^2 + (\pi J)^2 \right]^{1/2}. \qquad (1.19)$$

Without going into explicit quantum-mechanical derivations, *Wilman* and *Allen* pointed out that each component of the above Hamiltonian has time-dependent coefficients that affect the time evolution of the phase of the magnetization. Further, they illustrated that while weakly coupled systems are like strongly coupled systems (such that under RF pulses the coherence orders do not change during spin evolution), strongly coupled systems do however allow for an interchange between in-phase magnetization of A with anti-phase magnetization of B, within the Hamiltonian component, H_1. In the case of the widely used PRESS pulse sequence (26-28), the total signal is calculated as the total transverse

magnetization that is present at the start of the PRESS acquisition and is directly proportional to the total area of the spectrum under Fourier transform.

The calculated total signal, S, is given as a function of TE (with constants $\delta\omega$, $\bar{\omega}$, Λ, and J):

$$\begin{aligned} S(TE) = & [\delta\omega / \Lambda)^2 + (\pi J / \Lambda)^2 \cos(\Lambda TE)] \cdot \cos(\pi JTE) \\ & \times 2(\pi J / \Lambda) \cdot [(\delta\omega / \Lambda)^2 + (\pi J / \Lambda)^2 \cos(\Lambda TE / 2)] \\ & \times \sin(\pi JTE) \sin(\Lambda TE / 2) \end{aligned} \qquad (1.20)$$

Note that under weak-coupling limits (i.e. $\delta\omega \gg \pi J$) equation 1.20 reduces to $\cos(\pi JTE)$. This equation is an important result, as it gives us a direct indication of the total signal with dependence on echo time for a specific pulse sequence. The plot of the signal intensity versus echo time is displayed in Figure 1.8B, for equation 1.20. As the signal decreases with increasing echo times, it is observed that the signal decays exponentially with a sinusoidal variation. From this plot, the value of reducing echo times can be seen: as one chooses shorter echo times, more signal is retained. Improved signal intensity may result in better signal-to-noise, faster acquisitions, and detection of short TE metabolites. This result has been used by a number of *in vivo* experiments to calculate the best timing of RF excitation pulses for optimal citrate detection (26, 29-31).

1.4.3. Magnetic Resonance Spectroscopic Imaging

Up until now the discussion has been mainly about the fundamental physics of NMR related to basic spectroscopy. To make the transition from spectroscopy to spectroscopic imaging requires more detail about magnetic resonance imaging, in particular how the NMR signal is localized. Since localization techniques in NMR are well established their discussion has been placed in Appendix A. When more detail is needed, footnotes will be used to guide the reader to appropriate sections in the appendix.

The main difference between magnetic resonance imaging and magnetic resonance spectroscopic imaging, is the exclusion of chemical shift in the derivation of localization techniques[4]. Including the chemical shift effect extends the basic imaging technique to what is commonly known as "chemical shift imaging" (CSI) or "magnetic resonance spectroscopic imaging" (MRSI). In many clinical situations, it has been increasingly important to obtain biochemical information about the tissue of interest (32-38). This is especially true for the assessment of cancer in the prostate.

In section 1.4.1.4, it was described that the electronic shielding surrounding a nucleus gives rise to the *chemical shift effect*. In a solution with many chemical species, it is possible to separate each species by their unique frequency shift relative to the Larmor frequency of precession. In basic ^{1}H imaging, a gradient is used to frequency encode the FID during the read-out process[5]. In the simplest

[4] See Appendix A 8.4

[5] See Appendix A 8.4.4

case, the signal from a single voxel can be isolated by using three slice selective gradients. If one was to remove the read-out gradient in the pulse sequence, the resultant signal becomes a function of the time. The basic imaging equations for one, two, and three-dimensional magnetic resonance imaging[6] can be modified to include chemical shift dependence as follows,

$$\begin{aligned}
&\text{One dimension} \Rightarrow S(t') \propto \int \rho(\sigma) e^{i\sigma\omega_0 t'} d\sigma \\
&\text{Two dimensions} \Rightarrow S(k_x, k_y, t') \propto \iint \rho(x, y, \sigma) e^{-ik_x x} e^{-ik_y y} e^{i\sigma\omega_0 t'} dx dy d\sigma \\
&\text{Three dimensions} \Rightarrow S(k_x, k_y, k_z, t') \propto \iint \rho(x, y, z, \sigma) e^{-ik_x x} e^{-ik_y y} e^{-ik_z z} e^{i\sigma\omega_0 t'} dx dy dz d\sigma
\end{aligned} \tag{1.20}$$

where σ is the chemical shift, and ω_0 is the Larmor frequency of precession. The resultant NMR signal can be taken from the time domain into the frequency domain by using a three dimensional Fourier transform.

1.4.3.1. Point resolved Spectroscopy (PRESS)

One of the most common pulse sequences used in clinical spectroscopic imaging is the double-spin echo or point resolved spectroscopy (PRESS) method. The base PRESS pulse sequence that typically is supplied by the manufacturer has three main components: 1) Chemical Shift Selective Saturation (CHESS), 2) Outer Volume Suppression (OVS), and 3) PRESS Excitation, as seen in Figure 1.9.

[6] See Appendix A 8.4.4, equations A8.35-A8.37

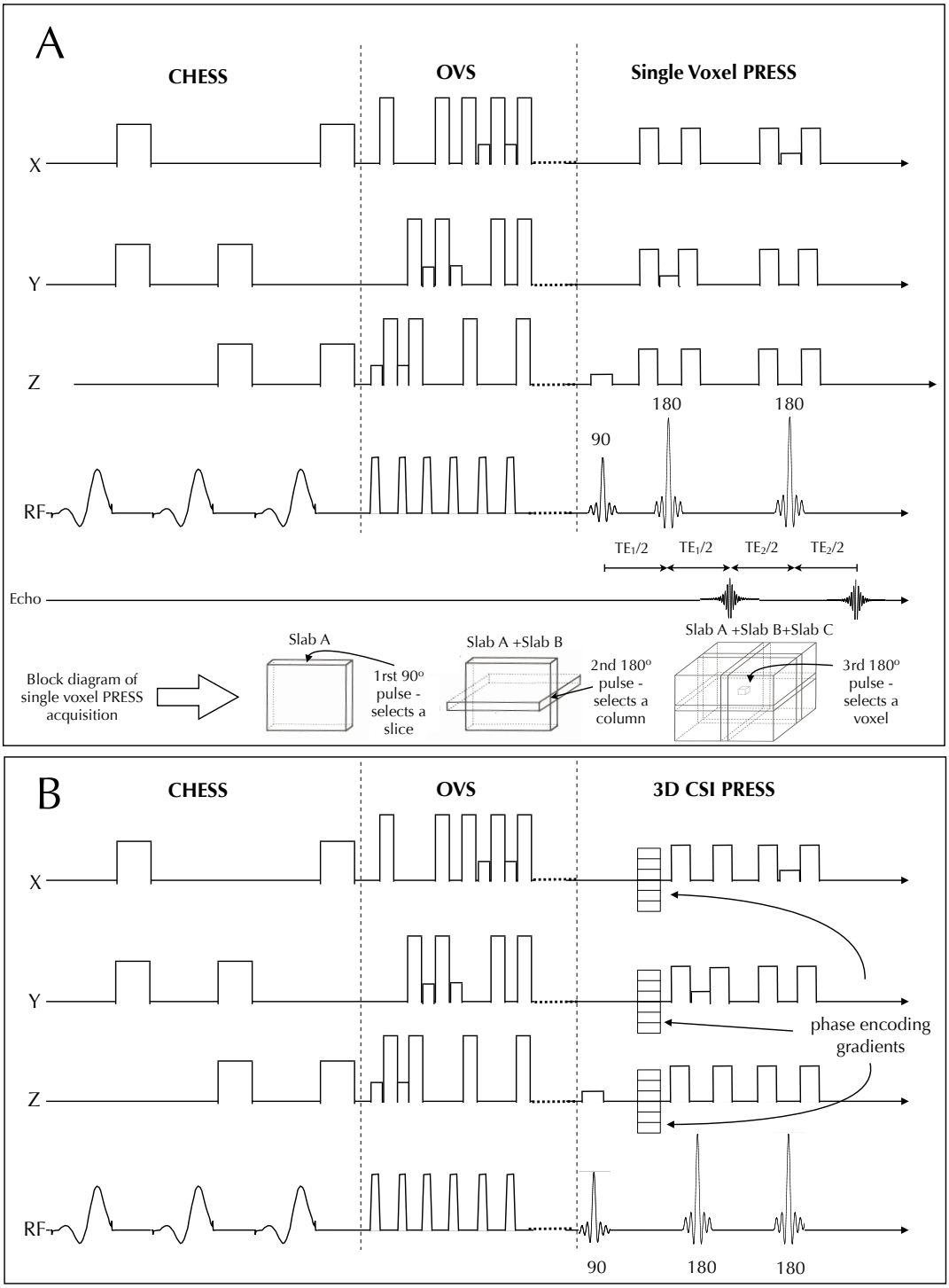

Figure 1.9 Both single voxel and 3D CSI PRESS pulse sequences
In (A), the single voxel PRESS sequence is shown. The addition of phase-encoding gradients in (B) changes the single voxel sequence into a full 3D CSI sequence. In both variations of the pulse sequence, the CHESS (water suppression), and OVS (lipid suppression) methods are used prior to execution of the PRESS sequence. (Note that the pulses are not to scale)

1.4.3.1.1. Water suppression

In MRS, sensitivity is extremely important for detecting signals from small concentrations of metabolites, while maximizing resolution and minimizing acquisition time. *In vivo* MRS is challenging, since there is a large water signal which is 10,000 to 100,000 times stronger than the concentration of metabolites. This is why CHESS is used to suppress the water signal. Chemical Shift Selective (CHESS) water suppression is a frequency selective technique which works to excite the water in the sample and bring the net magnetization into the transverse plane. The signal is then completely dephased by applying gradients along the main magnetic field, B_0. The main advantage of using CHESS is that it can precede any sequence without interfering with nearby metabolite resonances. As well, CHESS pulses can be repeated to obtain maximum water suppression. However, one of the disadvantages of CHESS is that it relies heavily on the homogeneity of the B_0 and B_1 fields. Typically, the CHESS sequence contains three frequency selective 90 degree pulses, each followed by a dephasing gradient pulse as shown in Figure 1.9.

1.4.3.1.2. Lipid Suppression

The two main signals in *in vivo* spectroscopy that require adequate suppression are water and fat. The preceding section discussed a method to reduce the large water signal. In a similar way, a typical spectroscopy experiment also tries to reduce fat signals from tissues containing lipids surrounding the region of interest (ROI). In MRSI of the prostate, the main lipid peaks appear between 0-1.5ppm. This

signal may correspond to lipids within the voxel of interest or from adjacent tissue. Spectral contamination from neighboring volumes is an unwanted effect of the point spread function, which will be discussed in following sections. In the case of the prostate this is a very real problem. Surrounding the prostate is a large amount of periprostatic fatty tissue which is well documented in the literature as an inhibitor to acquiring robust spectra (39-41). A technique which spatially saturates the signal from regions inside and outside the excitation volume has been traditionally used to help combat this problem. In general, methods which attempt to saturate signals from adjacent tissues are labeled as outer volume suppression (OVS) techniques. One of the most common OVS methods used in MRSI of the prostate is the use of the very selective suppression (VSS) pulses (42). First demonstrated by Tran *et al.,* these VSS pulses use a spatially selective 90 degree RF pulse to bring the net magnetization of the suppression region into the transverse plane (see OVS section Figure 1.9A-B). The VSS pulse is then followed by a gradient crusher pulse, that causes the maximum dephasing within a relatively short time interval (~5ms in total). Spatial prescription of the VSS pulses is done via a graphical user interface on the MRI scanner console. Typically, the user will have the anatomical image displayed, and then graphically places hash-marked slabs over the region that needs to be saturated. Each vendor console uses a different number of saturation bands, and different methods of prescription. Manual placement of saturation bands is inherently subjective and challenging with limited views that don't allow the user to fully inspect oblique placements. Currently, prescription of 8-10 of these saturations bands is done manually by an expert user.

VSS pulses have been shown to be clinically very useful in reducing lipid contaminating artifacts (42-46). However, methods which automate the placement of multiple saturation pulses have great potential to dramatically reduce lipid contaminating artifacts.

1.4.3.1.3. Single and multi-voxel acquisitions

Following Figure 1.9A, the next step in the MRS experiment is the excitation of the ROI using the PRESS localization sequence. To illustrate the volume localization of the PRESS sequence, a block diagram is placed below the PRESS excitation portion of Figure 1.9A. From this, it can be observed that the sequence starts with a slice selective 90 degree RF pulse[7], along the gradient G_z which excites a volume -Slab A. Next, a slice-selective 180 degree RF pulse refocuses the spins from another volume slab (Slab B) along the G_y gradient direction. Spins from the intersecting column of Slab A + Slab B begin to rephase resulting in the formation of an echo at a time TE_1 from the initial 90 degree RF pulse. This echo is not recorded. Lastly, a third volume slab (Slab C) is selected along the G_x direction by a second slice selective 180 degree refocussing RF pulse. The action of all three RF pulses along three gradient directions (i.e. combination of Slab A + Slab B + Slab C) results in the selection of a single voxel. Only spins that are in the intersected volume of voxel C are excited by all three pulses. The net magnetization of all three pulses produces the final echo which occurs at a time $TE_2/2$ from the second 180 degree RF pulse. The use of the refocussing pulse enables one hundred percent of the refocused signal to be retained, and is one of the main advantages of

[7] See Appendix A, equation A8.1 for definition of flip angle

using PRESS for single and multi-voxel localization. At this stage, the description has been about single voxel acquisitions. To extend the sequence for multi-voxel acquisitions, as used in magnetic resonance spectroscopic imaging (MRSI), a second set of linear gradients are introduced (see Figure 1.9B). Three phase-encoding gradients, one in each spatial direction, are used to create spatially dependent phase shifts to the precessional motion of the spins. Spatial localization is achieved by phase encoding in one (1D CSI), two (2D CSI), or three dimensions (3D CSI)[8]. A Fourier transform of the data collected in the time domain is performed to give us localized spectra in the frequency domain. The resulting spectral data can be examined in a number of different ways. One common method is to view the data as a spectral map as seen in Figure 1.10. Spectral maps are often overlaid on conventional anatomical MR images. In prostate MRSI, an endorectal coil is used to improve the signal to noise ratio. Increasing the overall signal allows one to collect data from voxel sizes as small as ~0.3cc (14, 17, 47).

1.4.3.2. Tradeoffs in MRSI of the prostate

Apart from the specific localization sequence used to acquire MRSI data, a clinically useful MRSI localization technique will demonstrate several important characteristics including: 1) an appropriate region of interest (ROI) that is defined by an anatomical image, 2) the spectra obtained from metabolites within the ROI should have minimal contribution from contaminating signals that lie outside the defined ROI, and 3) the resulting spectra should be of good quality (i.e. high signal-

[8] See Appendix A8.4.5

to-noise, flat-baseline and narrow peaks) and acquired in a reasonable amount of time. Trying to minimize all three of these constraints results in making certain trade-offs.

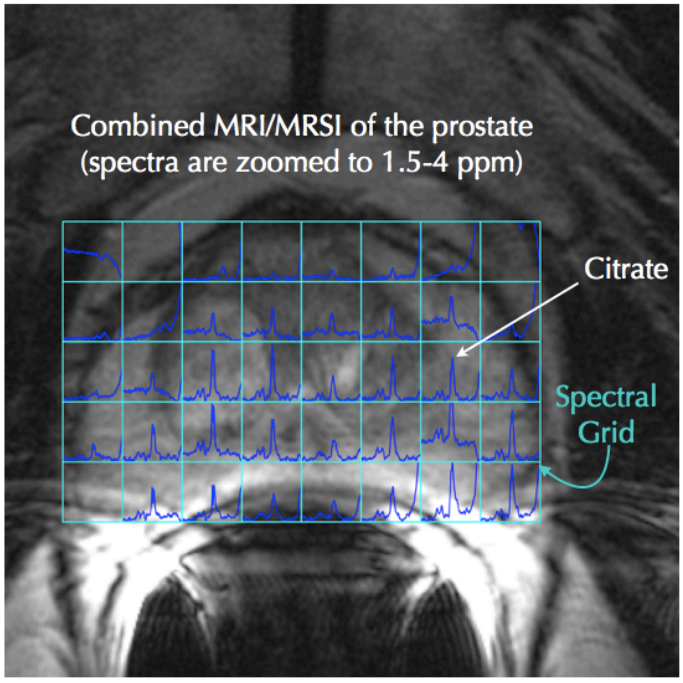

Figure 1.10 Final presentation of MRSI data as a spectral map overlay on an MR image of the prostate

In Figure 1.11A, a MRSI of the prostate was recorded with the following scan parameters, 16x8x8 phase encoding steps (Nx=16, Ny=8, Nz=8), TE=130ms, TR=1100 ms, field of view (FOV) of 120 mm by 60 mm by 60 mm , with a nominal voxel size of ~0.42 cm^3. In this example, choosing an appropriate region to determine the excitation ROI for the PRESS sequence can be challenging. In Figure 1.11A, the red dashed line represents the excitation ROI placed around the prostate. If one chose an excitation ROI well within the prostate, the spectra would result in less contaminating artifacts, but would exclude a large portion of the

prostate tissue. Choosing an ROI that encompasses the entire prostate improves the spatial coverage of the MRSI grid over the prostate, but includes some regions outside the prostate resulting in increased lipid contamination.

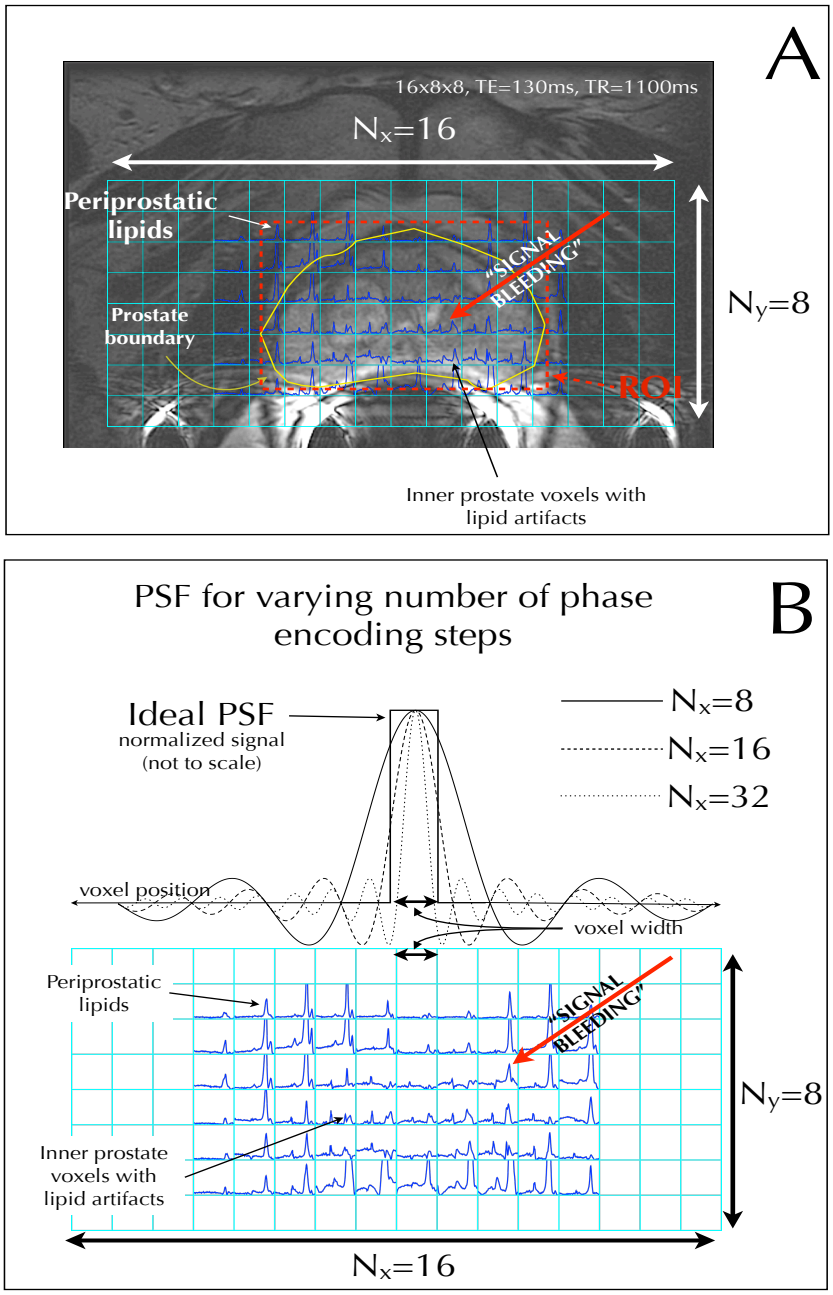

Figure 1.11 MRSI of the prostate and the point spread function
In (A) MRSI data was recorded with 16x8x8 phase encode sequence. The PSF function heavily influences the contamination effect or "signal bleeding" effect, as seen in (B).

The apparent contaminating effect or "signal bleeding" is intrinsically linked to the number of phase encoding steps used in the MRSI acquisition and the spatial resolution. In previous discussions, which outlined the signal equations for an MRSI experiment (equation 1.20), it was assumed that the spin density functions [9] were continuously sampled in k-space [10] over a long time period. In a clinical MRSI experiment, the signal is acquired over a finite time interval at discrete positions in k-space. Incremental changes in the amplitude of the phase encode gradients help navigate k-space, and sampling is performed in the time domain such that the Nyquist sampling criterion is fulfilled (48). Using similar equations as developed for imaging[11], the spatial resolution over the FOV is,

$$FOV = \frac{2\pi}{\gamma \Delta G t} = \frac{1}{\Delta k} \tag{1.21}$$

where Δk is the spatial frequency separation between two phase encoding gradients with units m^{-1}. By dividing the FOV by the number of phase encodes in any particular spatial direction, the nominal voxel size along each spatial direction is obtained:

$$\Delta v_x = \frac{FOV_x}{N_x}, \Delta v_y = \frac{FOV_y}{N_y}, \Delta v_z = \frac{FOV_z}{N_z} \tag{1.22}$$

As previously mentioned, sampling the time-domain signal, $S(k_x)$, for a long time would result in a well-defined signal upon Fourier transform. Due to practical and

[9] For a discussion of the spin density functions see Appendix A 8.4.5

[10] For a discussion on k-space see Appendix A 8.4.5

[11] For a discussion about spatial resolution in MR imaging see Appendix A 8.4.5, equation A8.38

clinical limitations, the time for an MRSI experiment is constrained. To limit the acquisition, a sampling function $F_s(K_Z)$ is used to obtain discretely sampled data. The Fourier transform of the sampling function results in what is commonly referred to as the *point spread function (PSF)*. The PSF is defined by the following equation,

$$\text{Point spread function } \Rightarrow FT[F_s(k_z)] \propto \frac{\sin(\pi N_x \Delta k_x x)}{\pi N_x x} \qquad (1.23)$$

which has the form of a sinc function, and is defined by the number of phase encoding steps, N_x. The fact that the resulting PSF has the form of a sinc function, has interesting implications for MRSI.

In Figure 1.11B, the PSF function corresponding to the sampling of a single value in k-space (i.e. a single voxel from the MRSI grid) is presented. The ideal PSF, has a square profile with zero signal spread to adjacent voxels. But because the MRSI is sampled over a finite time interval, the resulting PSF has the shape of a sinc function. In this figure, the PSF functions for three different phase-encoded steps are simulated. In all three cases, the signal response of the sinc function results in positive and negative side lobes which extend over the entire FOV and contribute signal to adjacent voxels. This is a key result and the answer to why high intensity lipid signals from surrounding voxels contaminate inner voxels. By increasing the number of phase encoding steps from 8 to 32 (while keeping the FOV constant), the PSF functions starts to approach the ideal PSF, with very minimal contribution of positive and negative side lobes to adjacent voxels. The natural conclusion from this discussion is that to help reduce contaminating effects due to the PSF one must increase the number of phase encoding steps.

Simply increasing the number of phase encodes does not fully solve the problem of signal bleeding and in fact, it introduces two further tradeoffs. By increasing the number of phase encoding steps the voxel size is dramatically reduced. Reducing the voxel size decreases the signal-to-noise, resulting in noisy spectra. This can be offset by increasing the number of excitations, but increasing the number of excitations and phase encoding steps can greatly increase the total time for an MRSI study.

MRSI requires a large number of acquisitions to adequately sample the tissue of interest. This has been one of the major drawbacks of the technique, and a deterrent to its routine clinical use. The total time for an MRSI experiment, T_{total}, is calculated by the following equation,

$$T_{total} = N_x \times N_y \times N_z \times N_{excitations} \times T_r \tag{1.24}$$

where $(N_x \times N_y \times N_z)$ are the number of phase encoding steps along each spatial direction, $N_{excitations}$ is the number of excitations, and T_r is the repetition time. Following the example from Figure 1.11A, if $N_{excitations}$=1, N_x=16, N_y=8, and N_z=8, and a T_r=1s, the acquisition time required is approximately 17 minutes. Consider just increasing the parameters slightly to $N_{excitations}$=2, N_x=16, N_y=12, and N_z=12, and a T_r=1s. The total time is increased to approximately 77 minutes. It is easy to see that scan times for higher resolution scans can get unreasonably long. In a clinical setting, acquiring scans quickly reduces the chances for motion artifacts to

occur (i.e. the patient is required to stay still for a shorter period of time), and can also increase patient throughput. In the field of prostate MRSI, there have been advancements in acquiring faster MRSI scans, with scans time now below 10-12 minutes (49, 50). This trend will continue as spectroscopy techniques advance, and when specialized sequences become incorporated into clinical imaging systems.

In MRSI experiments, another important aspect to keep in mind when using slice selective RF pulses in conjunction with linear magnetic field gradients, is that the spatial position of the localized volume will be affected by the chemical shift of the compound being excited at the Larmor frequency. Using information about the gradient, spatial position, and Larmor frequency the spatial position of a slice along the z direction can be calculated using the following formula, $\omega(z) = \omega_0 + \gamma G_z \Delta z$[12], relating frequency to spatial position. From this equation the spatial displacement (or chemical shift displacement) can be directly calculated by,

$$\Delta z = \frac{\Delta\omega}{\gamma G_z} \tag{1.25}$$

where $\Delta\omega$ is the frequency difference. Consider the following example, suppose a sample has a mixture of both water and fat. When a frequency selective RF pulse and accompanying linear magnetic field gradient is applied to the sample, the fat signal will appear shifted. At 1.5T the Larmor frequency difference between water and fat is approximately, 220 Hz. For a gradient with a nominal slew rate of 15mT/m, a spatial shift Δz, of approximately 0.35mm would result. To minimize this

[12] See appendix A8.4.4, equation A8.32

unwanted effect, one could increase the gradient strength which would result in a reduced chemical shift displacement effect. But increasing the gradient strength will in turn increase the signal bandwidth, and thus also reduce the signal-to-noise. To mitigate this tradeoff, optimal fat and water suppression techniques are used.

1.4.4. Summary of NMR principles

In summary, the preceding sections 1.4.1 to 1.4.3 have presented the basic underlying physics of NMR used in this thesis. From section 1.4.1 an examination of the origin of the NMR signal lead to section 1.4.2 which looked at the coupling phenomenon which gives rise to spectral patterns of the chemical species in NMR spectroscopy. Lastly, in section 1.4.3 methods in which one could spatially encode the NMR signal to give a spectroscopic image was discussed. One of the main messages from this section is that the acquisition of the MRSI data is a multi-step process and the acquisition of good quality data depends on many factors. These include the definition of an appropriate region of interest (including voxel size), optimal water and lipid suppression, PSF effects, and chemical shift displacement effects. While keeping these in mind, one can obtain high quality spectra with reasonable acquisition times.

1.5. Radiation treatment of the prostate

Radiation therapy is an important tool in the fight against cancer and is used in the treatment of approximately 50% of all cancer patients. In 2011, among Canadians, there will be an estimated 177,800 new cases of cancer and 75,000 deaths from cancer. The most common cancers in Canada continue to be breast cancer for women, and prostate cancer for men (3). Treatment options are typically determined by a multidisciplinary team of oncologists. The specific treatment approach for a particular patient is customized to the location, type, and stage of the disease, as well as the medical condition of the patient. A physician may choose to treat the cancer with drugs (i.e. chemotherapy), radiation (i.e. radiation therapy), or opt for surgery. Often a combination of these treatments are used to obtain the best treatment outcome. Radiation therapy is particularly useful in cases where surgical removal of the cancer is not possible or after surgery where the risk for recurrence is high.

Radiation therapy may be used to treat localized solid tumours, such as cancers of the skin, head and neck, brain, breast, prostate and cervix. As well, it may be used to treat microscopic disease which is present but not detectable via clinical exams or diagnostic imaging. Today, external beam radiation therapy is usually delivered by means of a linear accelerator. Linear accelerators use microwaves and waveguides to accelerate electrons to high energies. These high energy electrons can be used to form an electron beam, or a photon beam. A photon beam is produced by directing the electron beam at a high atomic number target material, which converts some of the electrons to photons via the

bremsstrahlung process. External beam radiation therapy typically uses X-rays, or photons, to treat tumours at depth, while electrons may be used to treat shallower targets. The higher the energy of the X-ray beam, the deeper the X-rays penetrate into the target tissue. Linear accelerators produce X-rays at various energies. Commercially available linear accelerators are able to rotate the radiation beam, allowing delivery of radiation from all angles. Multiple angles allow the maximum amount of radiation to be delivered to the tumour while minimizing the amount of radiation to the surrounding healthy tissue.

Radiation therapy may also be delivered by placing a small amount of radioactive material directly into the tumour (brachytherapy), either permanently (low dose rate - LDR), or temporarily (high dose rate - HDR). Some patients may receive both types of radiation treatment (external and brachytherapy). Independent of the method of delivery, the main goal of radiation therapy is to induce cell death in as many tumour cells as possible by providing a high lethal dose to tumours cells and simultaneously minimizing dose to normal tissues. The limiting factor in radiation therapy is constraining the dose to the known tolerance of surrounding tissues. For example in the prostate, the rectal wall, bladder, neurovascular bundles and femoral bones are sensitive tissues (51).

1.5.1. Radiation physics

The field of radiation therapy employs a variety of elements including radiation physics, radiobiology, and practical aspects of treatment delivery. Use of radiation has found an important place in modern treatment. Underlying treatments with radiation are the physical interactions of particles with matter that allow a radiation oncologist to deliver a specific cell-killing radiation dose to a specific target.

Radiation itself is the emission and propagation of electromagnetic energy. As radiation propagates through a medium (i.e. air, water, human tissue), it can interact with the atoms of the medium to deposit energy. Radiation can be classified as ionizing or non-ionizing. If the radiation has enough energy to eject an orbital electron, it is said to be ionizing. Ionizing radiation can be categorized into two basic groups by the nature of the physical interaction. Radiation can transfer energy to the medium either directly or indirectly. Indirect energy transfer occurs in two steps: the first step involving transfer of energy from a neutral particle (e.g. photon, neutron) to a charged particle, and the second step being the transfer of energy of the generated charged particle to the surrounding medium via Coulomb interactions. Direct energy transfer occurs when the incident radiation is composed of charged particles and energy is transferred directly to the medium via Coulomb interactions.

Dose is the quantity used to describe the energy deposited within a media, including tissues. Specifically, the absorbed dose is the amount of radiation energy

absorbed per unit mass and is given in SI units of the Gray (Gy). One Gray is equal to 1 Joule per kilogram.

X-ray radiation interacts with patients primarily through three physical interactions. The three dominant interactions are: a) the photo-electric effect, b) Compton scattering, and c) pair production. During the photo-electric process, an incident photon transfers its energy to an inner orbital shell electron. For the interaction to occur, the energy of the photon needs to be larger than the binding energy of the orbital electron. If this occurs then the orbital electron is ejected with energy equal to the difference between the incident photon and the electron's binding energy. In Compton scattering, the incident photon interacts with an orbital electron, transferring some energy to it and retaining the remaining energy itself as a scattered photon. The orbital electron is ejected and deposits its energy to the medium while the scattered photon moves off at its reduced energy and at an angle to the incident photon. The scattered photon may interact again in the medium via any of the interaction mechanisms. Lastly in pair production, an incident photon interacts with a nucleus, and the energy of the incident photon is converted into mass and causes the creation of an electron (e-) and positron (e+) pair. The electron deposits its energy in the medium via Coulomb interactions. The positron also interacts via Coulomb interactions, but eventually the positron encounters an electron with which it annihilates, producing two 'annihilation' photons. Considering that most therapeutic treatments involve radiation of energies in the range of 4-18 MeV, and human tissue has an average atomic number of about 7, the dominating photon interaction is Compton scattering (52).

1.5.2. Radiobiological principles

So far the mechanisms in which energy is imparted to tissue have been briefly discussed. However, this does not explain the rationale for using radiation for the treatment of cancer. This warrants a short discussion about the radiobiology of cancer. The main identifying feature of cancerous cells is that they divide and replicate uncontrollably. In the treatment of cancer, radiation is used to cause damage to the DNA structure within the cell, thus causing a disruption in the cell division of cancerous cells. There are two mechanisms by which the death of a cancer cell occurs via the energetic electrons produced by ionizing radiation. The first mechanism is 'direct action' and occurs in approximately 30% of interactions. In this situation, the electron directly disturbs the chemical bonds between the base pairs of the cells' DNA structure and causes cell death. The second method, occurring in roughly 70% of interactions, occurs when the incident radiation ejects an electron from a water molecule creating a free hydroxyl radical that can then damage the structure of the DNA (52). When the DNA is damaged, mitotic cell death occurs with the cell dying during the process of the cell division.

To maximize tumour cell death while minimizing death in normal tissues, a fractionated radiation delivery is used. Fractionation is the separation of a large dose into a number of smaller fractions, separated in time. This method employs the traditional philosophy of the four "R"s of radiation biology, which are Repair, Reassortment, Repopulation, and Reoxygenation and are briefly described here:

- Repair - Cells that are damaged from radiation may undergo repair. One such mechanism is through sublethal damage repair (SLDR). This occurs during the

interval between fractions. This gives a chance for normal cells to repopulate. Repair is dependent on the type of cancer and its response to irradiation. Therefore, it is essential to use the minimum useful fraction size to allow for SDLR to occur. This strengthens the need for a healthy time interval between fractions. Repair plays a crucial role, and depends on tissue types, but is more important in the context of late responding tissues, than in early responding tissues.

- Reassortment - While delivering a large dose to a cell population, there are more cells that die in the sensitive phases of the cell cycle, as compared to the resistant phases of the cell cycle. Because of this, the surviving population becomes partly synchronized and would then be located in the more resistant phases of the cell cycle. Therefore it is necessary to wait before administering the next dose (allowing these group of cells to cycle to sensitive phases).
- Repopulation - Waiting a longer time between fractions will allow for normal cell to regenerate. Furthermore, if the interval between applied dose fractions is longer than the length of the cell cycle, there will be an increase in overall cell survival. This is due to cell division and repopulation of new cells.
- Reoxygenation - This is a largely tumour specific process. It is also very dependent on the time (and fraction interval). The rate and extent at which reoxygenenation takes place varies widely from tumour to tumour. In general there is a region of tumour cells that are hypoxic (deprived of oxygen). After delivering a dose of radiation, cells that are more oxygenated will be eliminated faster than hypoxic cells. This is because radio-sensitivity of

oxygenated cells is higher compared to hypoxic cells. As a result, the remaining hypoxic cells are given access to available oxygen, and become reoxygenated and therefore more susceptible to radiation damage.

Using the four R's, fractionated radiotherapy becomes more useful from a treatment perspective and is subsequently used in almost all radiation treatment deliveries.

1.5.3. Advanced techniques in radiation treatment delivery

1.5.3.1. Intensity modulated radiation therapy (IMRT)

As previously mentioned, prostate cancer is the most predominant cancer among men in North America. Today patients have a variety of non-surgical therapeutic treatment options. Radiotherapy represents one of the principal methods of treatment, and has similar survival outcomes as surgery, in the early stages of cancer development (53). Over the last 50 years, megavoltage irradiation techniques (i.e. delivered by linear accelerators) have witnessed significant technological innovation. For example, in the 1990's the development of the multi-leaf collimator, an automated shielding device described in the next section, to replace manually-made lead shielding. Medical imaging has also witnessed significant advancements in the last several decades, many of which are incorporated into the management of cancer. For example the adaptation of computerized tomography (CT) imaging as a tool for radiotherapy in the 1980's and 1990's improved the accuracy in the placement of radiation beams and targeting cancerous tissues, and has subsequently reduced toxicity to critical structures or

organs-at-risk. Traditional external beam radiation therapy techniques for the prostate primarily used simple anterior-to-posterior pelvic radiation beams together with lateral oblique radiation beams to deliver a total dose of approximately 65 Gy to the prostate (54). In cases where the prostate cancer is advanced (i.e. Gleason score greater than 6 for high-grade tumours) an additional dose of 45 Gy is typically administered to the pelvic nodes. During the 1990's and 2000's, 3D conformal radiation (3D CRT) therapy came to maturity and is still widely used today (55). This technique is based on CT-simulation, conformal beams-eyes-view based methods of choosing radiation beams, accurate 3D dose calculations, combined together to allow virtual-planning and individual customization of the patient's radiation treatment. With 3D conformal radiation therapy, substantially better radiation plans are achievable, allowing for dose escalation strategies (up to 76 Gy) to help improve tumour control without significantly increasing rectal or bladder toxicities (56). Another step forward in the delivery of radiation therapy was the development of algorithms to allow for the computerized optimization of delivered radiation fluences by the MLC. This "intensity modulated radiation therapy" (IMRT) allows for non-convex dose patterns and even higher gradients than those achievable with 3DCRT, enabling the safe delivery of higher doses to the prostate (>80Gy) without increasing acute and late radiation toxicity (57). Over the last several years, a growing trend has been the incorporation of biological imaging techniques (i.e. MRSI, positron emission tomography (PET), etc.) into IMRT treatment planning. This is an ongoing development and the clinical benefits continue to be evaluated (58-63).

1.5.3.1.1. Intensity modulated radiation treatment of the prostate

IMRT is a radiation delivery technique that employs a very high level of precision, and has evolved from 3DCRT as the next generation of radiation treatment. Specifically, it is known for its ability to closely conform the radiation to the shape of target, even complex, non-convex targets. The is achieved by modulating the intensity of the radiation beam through explicit use of the MLC. An MLC is made up of multiple thick "leaves" of dense metal (typically tungsten) whose movements are independently controlled via dedicated electric motors and computer software. Not only can the MLC be shaped so that the radiation beam conforms to the tumour shape, but they can also be used to modulate the radiation in complex patterns. This is commonly achieved by sweeping the leaves of the MLC across the radiation beam. The velocity profile of the leaves is controlled to deliver an optimal radiation pattern, itself obtained via inverse, computer optimization methods. This is the mechanism that allows the creation of sharp dose gradients and non-convex dose patterns. This ability permits the reduction of the dose to surrounding critical structures (i.e. bladder, rectum, and femoral heads in prostate cancer treatments) (54).

In the last several years, IMRT has demonstrated improved clinical outcomes and the reduction of the normal tissue toxicities while using higher doses of radiation in the treatment of prostate cancer. Initial studies by Zelefsky *et al.*(64), showed the benefits of IMRT for prostate cancer treatment. In that study, which looked at 132 nonrandomized patients, the total dose was escalated to 81 Gy using either 3D CRT (n=61) or IMRT (n=171). This study showed significantly reduced

gastrointestinal and genitourinary toxicities in patients treated with IMRT. While being able to reduce normal tissue toxicity, there is relatively new data showing that dose escalation strategies can be administered using IMRT and achieve improvements in biochemical-free survival rate. Vora *et al*. (65), showed in their study of 272 patients treated with 3D-CRT (to 68.4 Gy) in comparison to 145 patients treated with IMRT (to 75.6 Gy), that the use of the higher dose in IMRT resulted in a 14% improvement in biochemical-free survival rate with very little change in toxicity to normal tissue. More recent studies by Zelefsky *et al*. have shown similar results using IMRT for the treatment of prostate cancer (66, 67). While IMRT has shown its strength to conform dose very well in current clinical practice, many feel treatment outcomes can be further improved. Currently, leveraging IMRT's ability to conform dose to small targets, several research sites are investigating the incorporation of advanced functional imaging techniques (i.e. PET, combined MRI/MRSI, etc.), which provide biochemical snapshots of the cancer within the prostate, to perform targeted intra-prostatic radiation dose escalation (16, 58, 68-74).

1.5.3.2. Magnetic resonance imaging applications for intensity modulated radiation treatment

While the methods of radiation treatment have evolved over the last 50 years, so have the imaging techniques used to identify the cancers within human tissue. In terms of 3D imaging, CT has been the main companion of radiation therapy for many years, as it provides the electron density information necessary to perform dose calculations. Furthermore, CT imaging data is also used for contouring of the diseased tissues (i.e. cancer) and the critical structures (i.e. surrounding organs that need their function preserved). However, CT imaging has poorer soft-tissue contrast when compared to MRI, a difference readily apparent for pelvic and brain anatomy. Over the last two decades MRI has been utilized in radiation therapy to take advantage of this improved tissue contrast, since it allows more accurate delineation of cancerous tissues. Clearly more accurate identification of these target tissues is of significant benefit to the patient. Figure 1.12 shows the soft-tissue contrast between a pelvic CT image and a pelvic MR image. In the MRI image the prostate boundaries are clearly visible, while on the CT they are not clear, especially in the posterior regions. To utilize the benefits of the MRI, the MR image data set first must be registered to the CT image data set (65). This is accomplished with image registration software which allows the MR data to be imported and registered to the CT data through a manual or automatic process. While there are a few academic centers looking at performing MRI-simulation without CT (66-69), the need for image registration techniques to incorporate MRI data is still common (61, 69).

Since MRI is also capable of providing functional imaging information (i.e. MRSI), it holds further potential for use in radiation therapy. In earlier sections, it was shown that MRSI of the prostate could establish regions in the prostate where there was increased metabolic activity, as determined by the [choline+polyamine +creatine]/[citrate] ratio. This information can then be imported into the radiation treatment planning software and used to target dominant intraprostatic lesions (DIL).

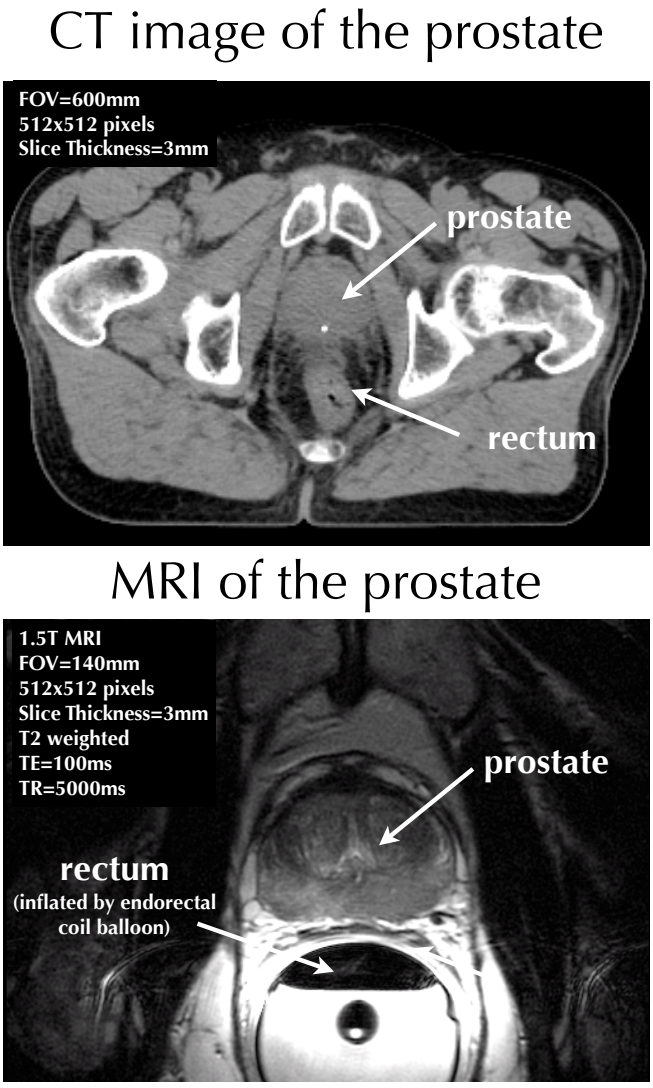

Figure 1.12 Soft tissue contrast comparison between CT and endorectal coil MRI

Specifically for radiation treatment of prostate cancer, IMRT has seen widespread adoption by many clinics to boost the dose to prostate and achieve better local control of the disease (53, 70, 71). Recent studies have shown that no differences were noted among low-risk patients for the various dose groups, but significant improvements were observed with higher doses for patients with intermediate- and high-risk prostate cancers (72). Since then there have been a number of studies which have looked at different dose fractionation schemes with the goal of achieving better disease control (62, 73, 74). Concurrently, researchers are also investigating the incorporation of radiobiological modeling as part of the treatment planning process with the similar goal of achieving improved disease control (75). Image guided therapy (i.e. MRI-guided treatment, combined PET-CT imaging) has allowed for better delineation of the target volume, and advanced imaging techniques such as MRSI can be used to target regions within the prostate to receive a dose boost for increased tumour control (61). Combining advanced methods in imaging to better delineate the target (i.e. MRI/MRSI), and the improved techniques of radiation delivery (i.e. IMRT) to increase the dose to the target may help in the overall goal of improving radiation treatment for prostate cancer (76, 77).

1.5.4. Radiobiological estimations for treatment outcome

1.5.4.1. The linear quadratic (LQ) model

Assessing and predicting the response of a tumour after irradiation is an important step in the radiation treatment planning process. Considering that there may be many different fractionation schemes it becomes clinically practical to have a numerical way to compare different treatment strategies. One of the most commonly used models for investigating the cell survival response to irradiation is the linear quadratic (LQ) model (52, 78). This model includes effects from both irreparable cellular damage and repairable cellular damage (that may cause mis-repair and may result in cell death). Currently there are several variations of the LQ model, depending on which of the"4 R's" of radiobiology are incorporated (75, 78-81) (i.e. Repair, Reassortment, Repopulation, and Reoxygenation). The basic form of the LQ model was derived from biological considerations, and its derivation has been examined by many authors (52, 78, 82, 83). The equation for the LQ model is stated as,

$$S(D) = e^{-\alpha D - \beta D^2} \tag{1.26}$$

where $S(D)$ is the fraction of clonogenic cells surviving a dose D, α is the number of logs of cell kill per Gray (from linear portion of survival curve), and β is the number of logs of cell kill per $(Gray)^2$ (from quadratic portion of survival curve). Typically treatments are delivered in multiple fractions such that the fractional dose is given by $d=D/n$, where D is total dose, and n is the number of fractions. Substituting this into equation 1.26, we arrive at,

$$S(D) = e^{(-nd)(\alpha+\beta d)} = e^{(-\alpha nd)(1+\frac{d}{\alpha/\beta})} \quad (1.27)$$

which is convenient formalism describing *S(d)* as the product of *nd* (total dose), and *(1+d/(α/β))* (relative effectiveness). In the LQ model, the α/β ratio is an inverse measurement of the tissue sensitivity to fractionation and to the size of the fraction given during each treatment. Typically values for α/β range from 3-10 Gy (84). In the case of prostate cancer, where the cancer slowly proliferates (i.e. a late responding tissue) the α/β has been proposed to be as low as 1 Gy (85). In contrast, very aggressive head and neck tumours may have an α/β greater than 10Gy (i.e. early responding tissue with increased cellular proliferation) (84). Early responding tissues have a fast cellular turnover and because of this normal tissue repair may occur over many days or weeks. In comparison, late responding tissues have much lower cellular proliferation and the effects of treatments may take many months or years to become effective. In recent years, there has been growing interest in incorporating radiobiological effects into radiation treatment planning (86-92).

1.5.4.2. TCP and NTCP

Radiobiological models are used to relate the radiation dose delivered to treatment outcome, and can be a useful tool in the prediction of treatment outcomes particularly when comparing competing treatment methods. The two main radiobiological objectives are (1) to maximize local tumour control

probability (TCP) while (2) simultaneously minimizing normal tissue complication probabilities (NTCP).

A common model for predicting NTCPs is the Lyman–Kutcher–Burman (LKB) NTCP model described by the following three equations (75):

$$NTCP = \frac{1}{\sqrt{2\pi}} \int_{-\infty}^{t} e^{\frac{-x^2}{2}} dx, \quad t = \frac{D_{eff} - TD_{50}}{mTD_{50}}, \quad D_{eff} = \left(\sum_i v_i D_i^{1/n} \right)^n \tag{1.28}$$

Where D_{eff} is the uniform dose to the volume (i.e. equivalent uniform dose, EUD). TD_{50} is the uniform dose given to the entire organ volume that results in a 50% risk of complications, m is a measure of the slope of the sigmoid curve represented by the integral of the normal distribution, n is a parameter that describes the magnitude of the volume effect, and D_i and v_i are the dose and fractional volume, respectively, of each bin used to tabulate the differential dose volume histogram.

One of the commonly used TCP models is based on the Poisson distribution. Using the Poisson model, the probability of tumour cells reaching cell death is given by (75):

$$TCP = \prod_{i=1}^{N} TCP_i = \exp\left[-\sum_{i=1}^{N} v_i \rho_i S(D_i) e^{\gamma_i (T - T_{lag})} \right] \tag{1.29}$$

Where, p_i denotes the number of tumour clonogens per cm^3 in the i^{th} tissue region, v_i is the volume of the i^{th} tissue region, $S(D_i)$ is the fraction of the tumour cells in the i^{th} tissue region that survive total treatment dose D_i, and T is the overall time to complete the treatment, and T_{lag} is the time interval in which accelerated repopulation will occur (75). To include the effects of subclinical disease in the tumour control probability, the clonogen density, ρ, can be decreased in regions

outside the gross tumour volume. In the case where the tissue region does not contain any tumour cells, the number of clonogens can be null, such that $\rho = 0$. In this case the TCP is unity, regardless of the administered dose. It is possible to modify the value for this parameter based on the metabolic activity information obtained by functional imaging, for example, magnetic resonance spectroscopy imaging.

For fractionated treatment courses, there is a time interval between delivered fractions. During this time interval (T_{lag}) there is an acceleration of tumour cell population which is characterized by, γ_i . The rate at which tumour cells are repopulating is given by $\gamma_i = \ln(2)/T_d$, where T_d is the effective tumour doubling time[13] (52).

In our use of these radiobiological models, we examine how to adapt the TCP formalism to incorporate the MRSI data, since it reflects tumour aggressiveness (i.e. Gleason score) (93). By incorporating this information into the treatment planning calculation we may better estimate the dose needed to achieve better control, while minimizing dose to critical structures. This will be focus of discussion in Chapter 6.

[13] The tumour doubling time, T_d is derived by the cell loss factor Φ, and potential tumour doubling time, T_{pot} such that $T_d = (1-\Phi)/T_{pot}$. Please see pages 369-70 of Eric Halls book, Radiobiology for the Radiologist, for an in-depth definition (56).

1.6. Summary

1.6.1. Utilizing several branches of physics for improved diagnosis and treatment

The introduction portion of this thesis has described two important areas of physics used in the diagnosis and treatment of prostate cancer. From the earlier sections of the introduction, the basic physics of NMR was presented to explain the formation of a spectroscopic image. It was shown that MRSI has an important role in the diagnosis of cancer. Combined MRI/MRSI allows for very detailed sub-centimeter metabolic analysis of the complete prostate volume. While the MRSI technique has room to improve (i.e. removal of lipid artifacts at short TE), it can provide a valuable biological map of the prostate. This information can be used to estimate the aggressiveness of prostate cancer. As important as the need to accurately define where the disease is, it is equally necessary to implement a radiation treatment technique that can deliver radiation to a specified target with a high degree of accuracy. Many years of clinical research studies have validated IMRT as a high precision delivery method. IMRT has the ability to target small regions of tissue with high doses of radiation, while keeping normal tissue toxicities within acceptable levels. Furthermore, metrics such as TCP and NTCP allow for useful estimations of the treatment outcome.

However, the question arises: how does one combine methods in MRI/MRS and radiation therapy to achieve a better treatment for the patient? The goal of this thesis work is to bring together these branches of physics to help answer this question. To bring the two areas together, an improved MRI/MRSI technique is

developed to more robustly identify the cancerous region within the prostate volume (Chapter's 2,3, and 4). The spectroscopy data, validated by histopathology (Chapter 5), is used to determine the aggressiveness and rate of tumour proliferation of the prostate cancer. Lastly, standard radiobiological models are implemented to estimate the impact of incorporating the improved MRSI technique into the treatment process (Chapter 6). Thus, this thesis defines the spatial extent of prostate cancer using an improved magnetic resonance spectroscopic imaging technique to identify the molecular markers of malignant prostate tissue that may improve treatment of prostate cancer through targeted radiation dose-escalation.

Chapter 2

Technical Development

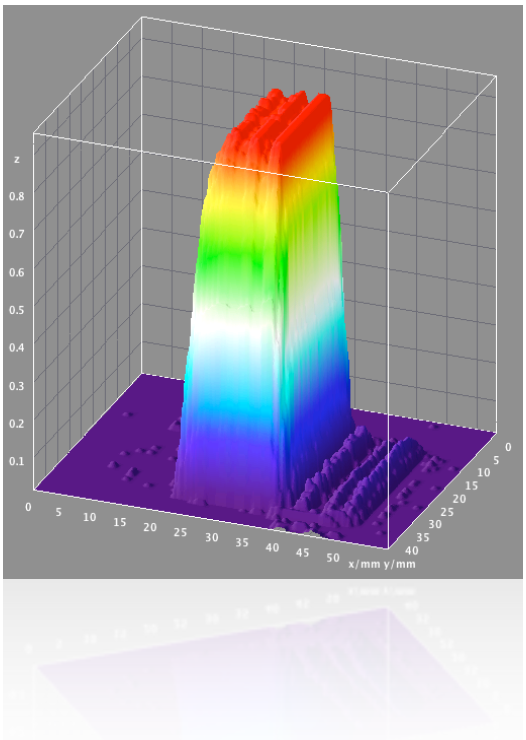

In this chapter we present the development of the conformal voxel magnetic resonance imaging technique on a 1.5T MR system with prostate-like phantoms. We provide a discussion of the pulse programming needed to modify the spectroscopic imaging sequence and the optimizations made to the sequence to help eliminate residual lipid signals due to T1 re-growth. In the latter parts of this chapter, methods for automated analysis using a customized version of LCModel are discussed.

A portion of this chapter has been published as conference proceedings in:
Venugopal et al., Improved Prostate MR Spectroscopic Imaging. AAPM 48th Annual Scientific Meeting; Orlando, Florida: Medical Physics; 2006. p. 2183.
Venugopal, et al., TH-C-L100J-05: In Vivo Prostate MRSI Using An Improved Outer Volume Suppression Technique. Medical Physics. 2007;34(6):2622.
Venugopal et al., Improved prostate MRSI employing a conformal voxel technique. Proceedings of the 16th Annual Meeting ISMRM. 2008 May 3-9:2767.

2. Technical Development

2.1. Pulse sequence design

As pointed out in section 1.4.3, one of the challenges faced in spectroscopic imaging of the prostate is signal contaminating artifacts from periprostatic fat surrounding the prostate. In a recent article by Casciani *et al.*, the authors explain the tradeoff and difficulty in choosing an appropriate ROI for the PRESS excitation volume and the placement of spatial saturation bands over an irregularly shaped object (20, 40) for the acquisition of high quality spectra. In their work, they cite the need to include the geometrical shape of the prostate in the optimization of the ROI and spatial saturation band placement.

To meet this challenge, Ryner *et al*. developed a technique which automates the spatial positioning of VSS pulses around a user-defined region of interest, called conformal voxel magnetic resonance spectroscopy (CV-MRS) (94, 95). This method, in conjunction with the PRESS localization sequence, automatically determines the spatial positions of the VSS pulses to shape a cuboid excitation volume to conform to a given convex volume. While this technique was initially tested on small cohort of brain tumour subjects (n=6) using single voxel acquisitions (95), the technique was not tested on other anatomical sites (i.e. prostate), nor using multi-voxel acquisition methods. Furthermore, given the significant problems with periprostatic lipids, methods to further optimize the CV-MRS technique were yet to be investigated.

In this chapter, we describe the pulse sequence development and optimization of the CV-MRS technique for use in prostate MRSI through phantom testing. In addition, methods to assist in performing fast and robust analysis of spectroscopic data were explored. Specifically this chapter examines:

1) Modifications to the OVS scheme to include a user-defined number of VSS pulses
2) Modifications to the VSS pulse flip angles to account for T_1 regrowth
3) Optimal ordering of the VSS pulses to overcome effects of multiple overlapping VSS pulses.
4) Inclusion of the spectral-spatial RF excitation pulse
5) Robust analysis of prostate spectra using LCModel
6) Storage and retrieval of MRSI data.

2.1.1. Basic Pulse Sequence (PRESS)

An MRI pulse sequence is a complex set of instructions (i.e. computer code) that specifies the duration, shape, and amplitude of RF pulses and linear gradients. In our study, we used a GE 1.5T Signal MRI scanner and EPIC pulse programming environment (General Electric, Milwaukee, USA). Each vendor (i.e. Siemens, Toshiba, and Philips) has their own unique pulse programming environment and set of tools to build pulse sequence programs. GE's EPIC pulse programming environment gave us access to the full source-code of the PRESS localization sequence.

The base pulse sequence of interest was the PRESS localization sequence. GE's implementation of the pulse sequence, illustrated in Figure 2.1, has three parts: 1) water suppression (via CHESS), 2) outer volume suppression (OVS), and 3) the PRESS sequence (characterized by the 90-180-180 RF pulse scheme). In the CHESS part of the sequence, there are three frequency selective water suppression pulses each followed by gradient crusher pulses. The flip angle of each water suppression pulse can be automatically calculated by the system or manually set by the user to achieve maximum suppression of the water peak. The OVS implementation on the GE platform includes the explicit use of VSS pulses. The VSS pulses used in this sequence have the following RF pulse characteristics: pulse duration = 3 ms, B_1 = 0.24 G for a nominal 90° pulse, pass bandwidth = 6 kHz, pass-band ripple = 1%, outer-band ripple = 1%, and transition band = 350 Hz (see Figure 2.2D). The main feature of the VSS pulse is its sharp profile (see Figure 2.2B-C). The sharp profile and narrow transition width of the VSS pulses allow them to be placed very precisely along the boundary of a ROI with minimal contribution of signal from the periphery to signal acquired within the ROI. After water suppression and OVS, the PRESS localization is executed. The PRESS localization contains three slice selective RF pulses - a 90 degree RF pulse, followed by two 180 degree RF refocussing pulses. The first slice selective 90 degree RF tips the net magnetization into the XY plane. Dephasing gradients are used to remove coherent signals from all three gradient directions (x, y, and z). Following this, a slice selective 180 RF refocussing pulse is excited along the y-gradient direction. This process of dephasing and refocussing is repeated for the second slice selective 180 RF

refocussing pulse, but along the x-gradient direction. The temporal ordering of gradient axes is entirely adjustable by the user.

Each aspect (i.e. RF pulse, gradient, VSS pulse) of the pulse sequence is created by specific source code available in the EPIC pulse sequence development environment. This code can be changed and manipulated to fit the needs of the pulse sequence designer (see Figure 2.1). All changes to the code are subject to two simple rules: a) RF pulses or gradients on the same channel shouldn't overlap and b) the total amplitude or duration of the RF pulses should not rise above the maximum specific absorption rate (SAR) for the anatomical site.

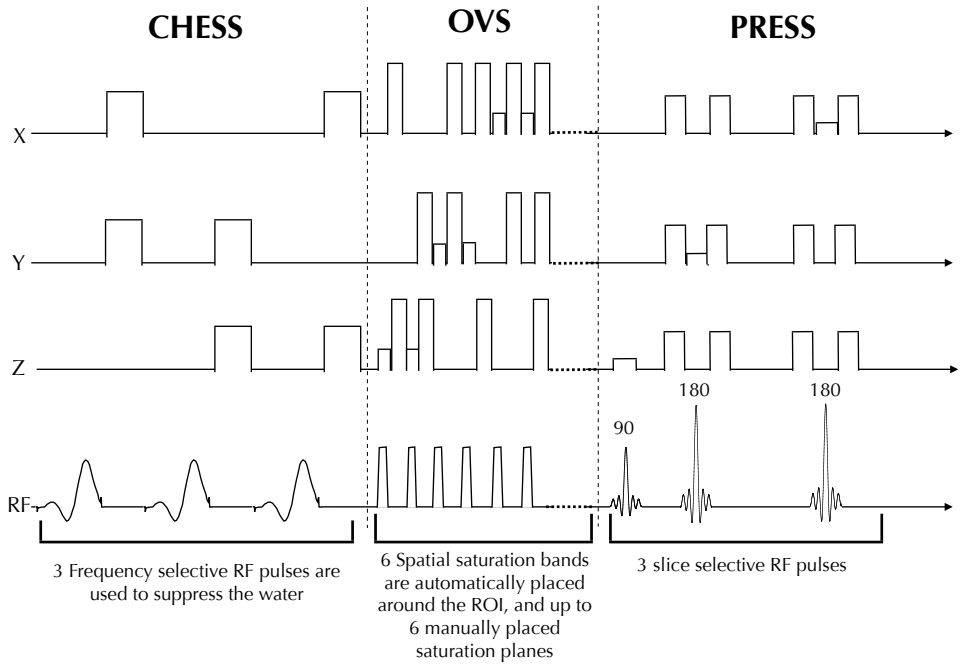

Figure 2.1 GE product PRESS localization pulse sequence
The GE product PRESS localization pulse sequence is shown with three distinct phases: 1) CHESS (water suppression, 2) OVS (lipid suppression), followed by PRESS localization. (Pulse sequence diagram is not to scale)

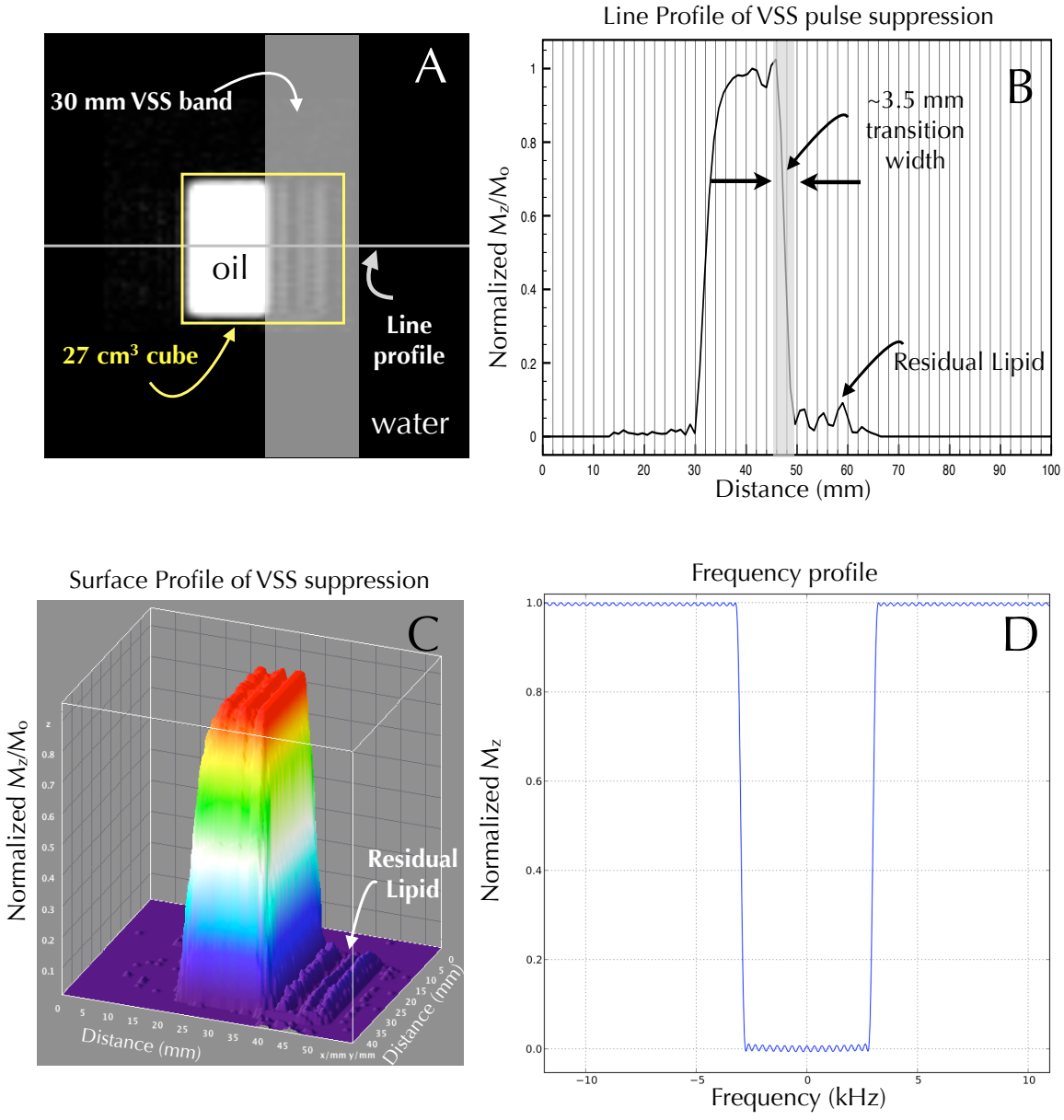

Figure 2.2 Spatial and frequency characteristics of a VSS pulse
An image (A) of single voxel PRESS localization using a homogenous oil (lipid) phantom was acquired (TE/TR=50ms/1000ms, 30mm x30mm x30mm). Prior to PRESS localization, a single VSS pulse was prescribed over ~50% of the volume (See A). The width of the spatial saturation band was 30 mm. In (B) and (C) both line and surface profiles are shown to demonstrate the narrow transition width (~3.5mm) and the effective suppression of lipids. In (D), the frequency profile of the VSS pulse showing the 6 kHz pass band, and 1% pass-band and outer-band ripple.

2.1.2. Modifications to OVS scheme

The first customization to the PRESS localization pulse sequence was the insertion of computer code to allow for an extended number of available VSS saturation pulses. This is shown in Figure 2.3A. Following every VSS pulse, there are a set number of gradient dephasing pulses (also called crusher gradients) applied to help provide additional phase dispersion of the saturated signal. The combined action of the spatial saturation pulse and the dephasing gradient pulse results in reduced signal from the volume being suppressed. These dephasing gradient pulses are used along all three spatial directions and are cycled so that residual signal along any particular direction is minimized. The cycling scheme that is used in GE's outer volume suppression technique follows an XZ, XY, and YZ pattern. In the train of VSS pulses, there are two distinct groupings of pulses as illustrated in Figure 2.3B. The first grouping of VSS pulses is called the ROI group. These VSS pulses are characteristically no different from any other VSS pulses, except in the way they are used. The first six VSS pulses are automatically aligned to the surface edges of the PRESS excitation box, which are usually defined by the user. The second group of VSS pulses is called the prescription group. This group of VSS pulses is available to the user to manually place around the object to provide oblique coverage over regions not saturated by the ROI group. On the 1.5T GE Signa scanner (version 9.1) used for this study, the user was limited to only 6 prescription VSS pulses. The pulse sequence code was modified to include a user defined number of VSS pulses (see Figure 2.3B). To facilitate the offline calculation of optimal saturation band

placement, the pulse sequence was designed to read in a text file containing the spatial positions for each spatial saturation band (i.e. rotation angles and offsets).

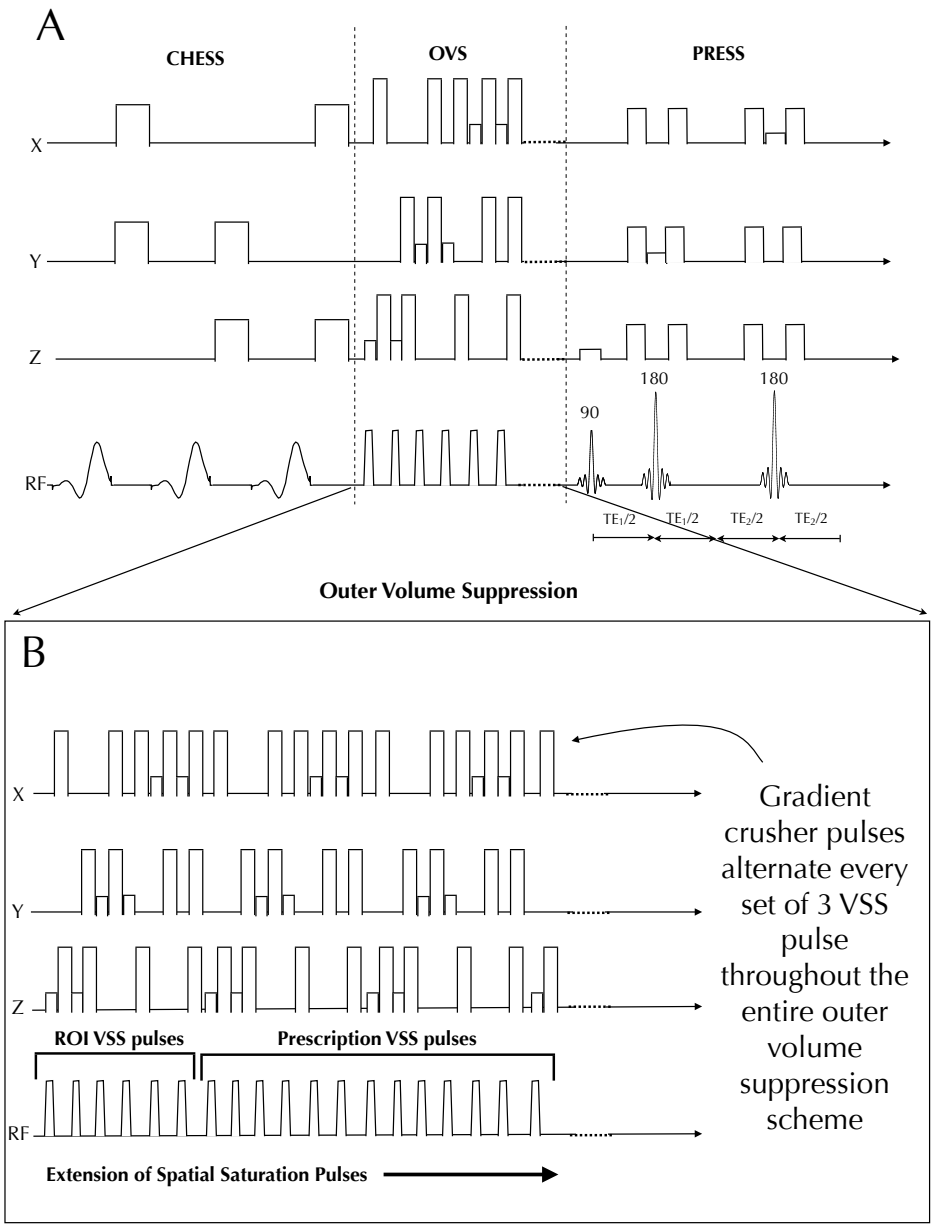

Figure 2.3 Extension of the OVS scheme
In (A), the base pulse sequence has an OVS scheme that includes 6 ROI VSS pulses, and up to 6 manually placed VSS pulses. In (B), the pulse sequence code was modified to include a variable number of VSS pulses (up to a maximum of 20 in the current implementation).

2.1.3. Optimal placement of VSS pulses using an improved CV-MRS technique

The modified pulse sequence, as discussed in the previous section, now has a user defined number of VSS pulses. The next step is to determine the optimal placement of the saturation planes as defined by a set of angular rotations and radial off-sets. The original software developed by Ryner *et al.*(94, 95) needed a number of enhancements in order for it to become more clinically usable. Some of the drawbacks of the initial implementation were: 1) the number of VSS pulses was fixed, 2) the plane calculation times were long (up to 2-3 minutes depending on the complexity of the object), and 3) the graphical user interface (GUI) was limited and did not allow the user to interact with the conformal voxel in three dimensions.

Following the same ideology put forth in the patent by Ryner *et al.*(94), the CV-MRS technique was modified by Sharma *et al.* and Hovdebo *et al.* (96, 97) to include these additional features. The current implementation of the CV-MRS software was written in IDL (ITT Visual Information Solutions, Boulder, CO, USA) and is platform independent (See Figure 2.4). At the heart of the CV-MRS tool is a robust algorithm which calculates the locations of the saturation planes in less than 1 second. The current technique operates by optimizing the saturation plane locations directly from the shape/surface of the segmented ROI. This is illustrated in Figure 2.5. From a set of acquired MR images (see Figure 2.5A), the object of interest is segmented either automatically or manually. Based on the segmentation of the object, the PRESS excitation box is automatically calculated using the maximum and minimum spatial extents of the object. Next, using a surface

simplification (or mesh decimation) algorithm (98), all adjacent vertices of the surfaces are examined to find pairs which can be combined while causing the least modification of the surface's shape. This simplification of the surface continues until the user-defined number of faces remain (see Figure 2.5B). The final "conformal-voxel" is a multifaceted object (in this example the object has 20 sides), that matches the original ROI as closely as geometrically possible (see Figure 2.5C). The plane locations for surfaces of the multifaceted object are then written to a text file, with the following format:

α	β	Z
0	0	-75.80488
0	1.5708	-42.30183
0	3.14159	-36.69512
0	4.71239	-26.13567
1.5708	0	-38.4375
4.71239	0	-32.8125
5.46544	0.71723	-34.86671
0.05318	2.63954	-37.17016
.	.	.
.	.	.
.	.	.

Where α is the azimuthal angle, β is the inclination angle, Z is the radial distance from the isocenter of the MR scanner. The first six plane locations are specified for the ROI group (highlighted in gray), and the number of remaining plane locations are specified for the prescription group. These follow the right-handed coordinate

(RAS)[14] system used by the scanner. As seen in Figure's 2.4A-C and 2.5C, the current version of the CV-MRS software has a user friendly GUI, which allows for better three-dimensional visualization of the plane locations. The additional voxel tool provides the user with the ability to adjust individual saturation plane locations.

The redesigned CV-MRS tool now includes many new features that assist in making it more robust and clinically usable. The main strengths of the new technique are the improvement in plane optimization time, and the automatic calculation of the PRESS excitation box. Previous versions of the plane optimization algorithm took many minutes, while the new version takes less than one second. Also, the old algorithm would occasionally result in odd placement of saturation planes (i.e. directly through the tissue of interest). In addition, the new software makes direct use of the MR image database and is platform independent.

[14] The RAS notation stands for, R-right, A-anterior, and S-superior.

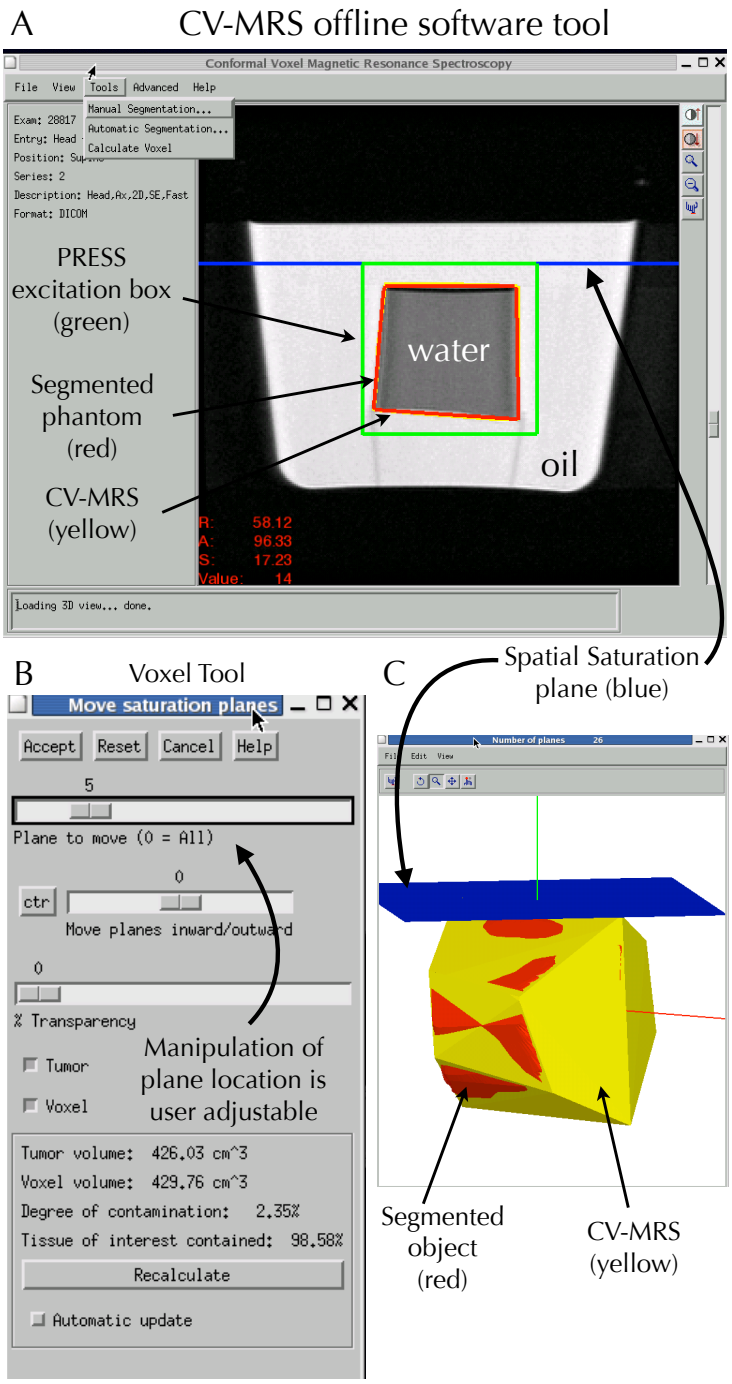

Figure 2.4 CV-MRS offline tool

The offline tool, written in IDL allows the user to upload data via DICOM or directly from the image database located on the console (see A). The offline tool displays the imaging data, calculates the locations of the saturation bands, and overlays the segmented regions with the conformal voxel. A supplementary tool (B) was created to allow the user to manipulate the plane locations (if minor adjustments are needed). As well, one can now visually assess the three dimensional location and orientation of each plane (C).

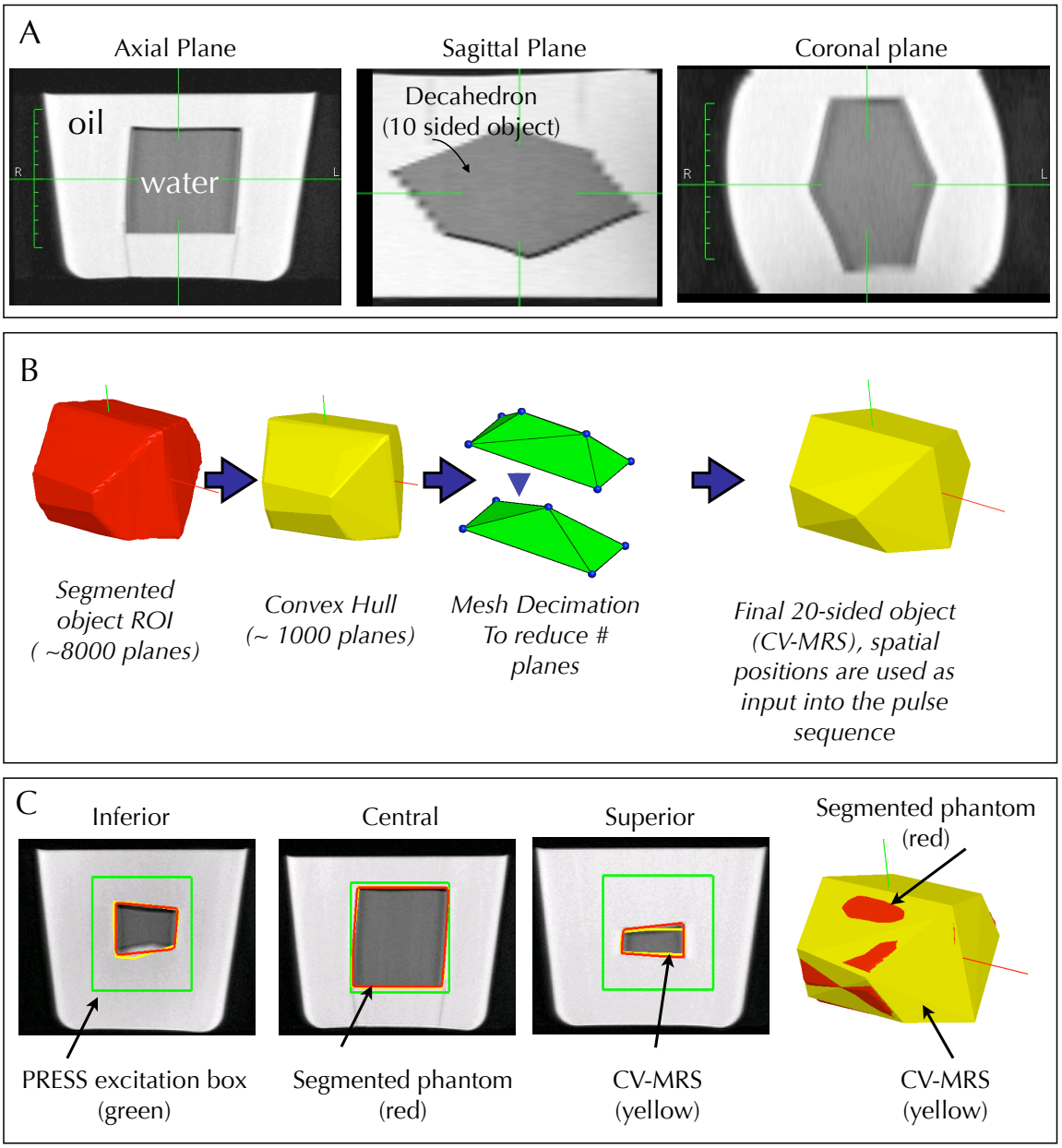

Figure 2.5 The CV-MRS algorithm

A set of MR images were collected from a water phantom with 10 sides submerged in an oil bath (A). Using built-in region-growing algorithms, the 10 sided object was segmented. In (B), from left-to-right, a step-by-step illustration of the surface simplification algorithm is shown. The plane locations of the final 20 sided object is shown. For all inferior, central, and superior slices, the CV-MRS algorithm conforms very tightly to the ROI of the segmented object.

2.1.4. OVS Optimizations

There are two primary challenges when using a long train of VSS pulses - signal regrowth and overlapping planes. Firstly, between the start and end of the VSS pulse train, there can be more than a 100 ms time difference during which the signal from the volume saturated by the first VSS pulse will have started to regrow due to T_1 relaxation effects. In the prostate, T_1 regrowth of the periprostatic lipid signal following saturation will be significant after a long train of spatial saturation pulses (T_1 =260ms). Ideally to solve this problem, the flip angle is increased (causing a slight inversion of the lipid signals' net magnetization, resulting in zero net residual magnetization at the time the PRESS localization sequence is executed). The second challenge is closely tied to the first. Modifying the flip angle to null residual lipid only works if none of the spatial saturation planes overlap. But clearly in our modifications to the OVS scheme, using a large number of VSS pulses will undoubtedly result in significant overlap of VSS pulses, depending on the three-dimensional orientation and spatial positioning of the individual pulses. Overlapping saturation pulses may lead to significant remagnetization of previously saturated volumes causing poor optimization of the entire OVS scheme.

To help solve these challenges and further optimize the OVS scheme, a computer simulation of the train of VSS pulses was performed to assess: 1) The effect of modifying the VSS pulse flip angle and, 2) How changing the ordering of VSS pulses may help reduce effects due to flip angle modification. This will be the focus of discussion in the following sections.

2.1.4.1. Optimizing the VSS pulses for T_1 relaxation

From equation A8.13, we know the longitudinal magnetization M_z is given by,

$$M_z = M_0(1-(1-\cos(\alpha))\cdot e^{\frac{-t}{T_1}}) \quad (2.1)$$

where α is the flip angle of the RF pulse, T_1 is the characteristic time constant, and t is the time over which the recovery occurs. For lipids, the T_1 time constant is approximately 260ms.

Consider the scenario where a single VSS pulse is used 100 ms before PRESS excitation. Using a flip angle of 90 degrees, the resulting net magnetization due to regrowth would be approximately 33% (See Figure 2.6A). Using equation 2.1, the optimal flip angle resulting in zero net magnetization would be 117 degrees (See Figure 2.6A). Using this methodology alone, we could incrementally modify the flip angle of each of the twenty VSS pulses to receive a slightly larger flip ranging between 90 to 117 degrees. Assuming there is no overlap, this would ideally null any T_1 regrowth effects and result in zero signal from any of the spatial saturation planes.

Let's now consider an example where there are two overlapping VSS pulses with modified flip angles in the train of 20 VSS pulses. The first pulse receives a flip angle of 117 degrees. As an example, consider another pulse 20ms later, VSS pulse number five (with flip angle = 111 degrees) that overlaps with VSS pulse number one. Assuming that there are no further overlapping pulses, the resulting net magnetization from the intersecting volume of these two saturation planes is increased by approximately 45%. The negative effect of modifying the flip angles can been seen in Figure 2.6B. This effect can be minimized by reordering the VSS

pulses such that the overlapping pulse is located further away in time in the train of pulses (for example, at the position of VSS pulse number 16). In this example, smart reordering of the VSS pulses minimizes the residual net magnetization (see Figure 2.6C).

To further examine the effect of overlapping VSS pulses, a three-dimensional computer simulation of the OVS scheme with multiple VSS pulses was performed. Using MR images from an oil/water phantom, the CV-MRS software tool generated the VSS plane locations that would be used by the pulse sequence. The simulation software works by loading the MR images of the phantom, and then mimicking the placement of the VSS bands at the spatial locations specified by the CV-MRS algorithm by overlaying a graphical representation on the imaging data. Each band is represented as a graphic object containing pixels of value 1, and pixel values from all used bands are accumulated to give a representation of all overlapping regions. Therefore volumes of bands that have no overlap with other bands have a pixel value =1, two overlapping bands result in a pixel value =2, three overlapping bands result in a pixel value = 3, etc. The T_1 regrowth and number of overlapping VSS bands are tracked for each pixel in the MR image (See figure 2.7A). The simulation provided several interesting observations. One, as each additional VSS band is added, there is a significant increase in the number of overlapping regions over the duration of the OVS sequence (see Figure 2.7B). In this example, 68% of the saturated volume experienced multiple overlapping volumes (see Figure 2.7C). Looking further into the overlapping effects of multiple VSS pulses, we also observed that volumes experiencing an even number of overlapping VSS pulses

early in the train of VSS pulses resulted in an increase in net residual magnetization (up to 3 times for 4 overlapping VSS pulses) (see Figure 2.7D).

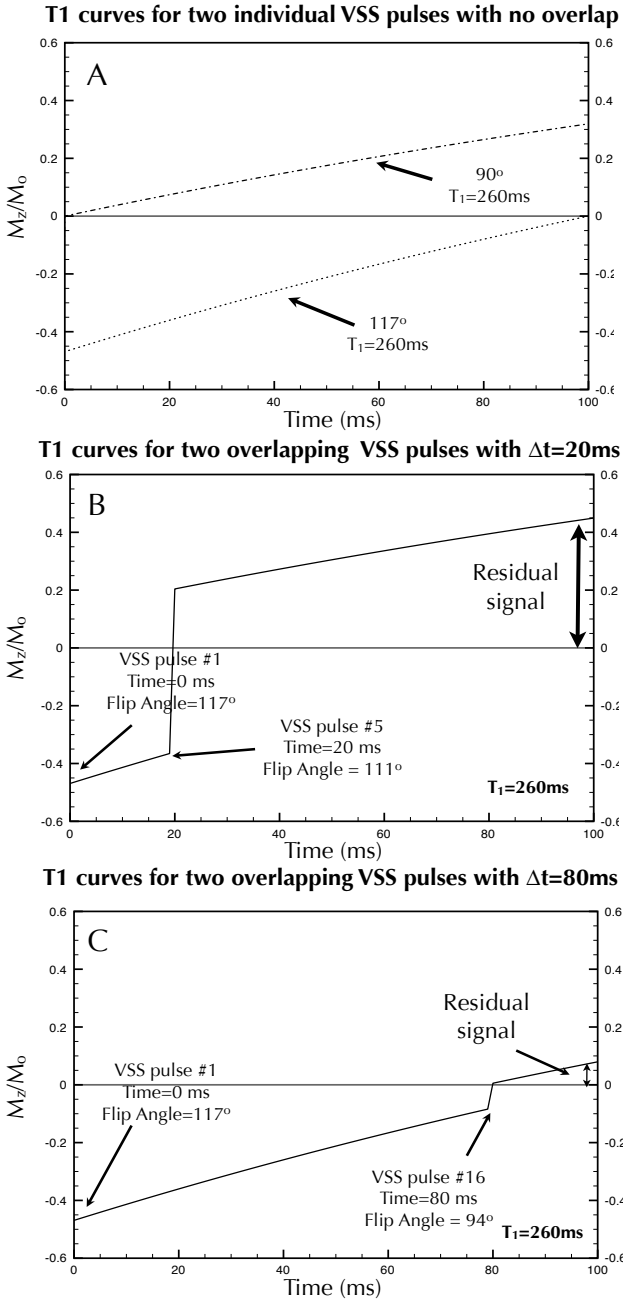

Figure 2.6 Playing with flip angles

(A) The T_1 *regrowth curves for two individual VSS pulses starting at the t = 0 ms. (B) The* T_1 *regrowth curve for two overlapping pulses with different flip angles and* Δt*=20ms. (C) The* T_1 *regrowth curve for two overlapping pulse with different flip angles and* Δt*=80ms.*

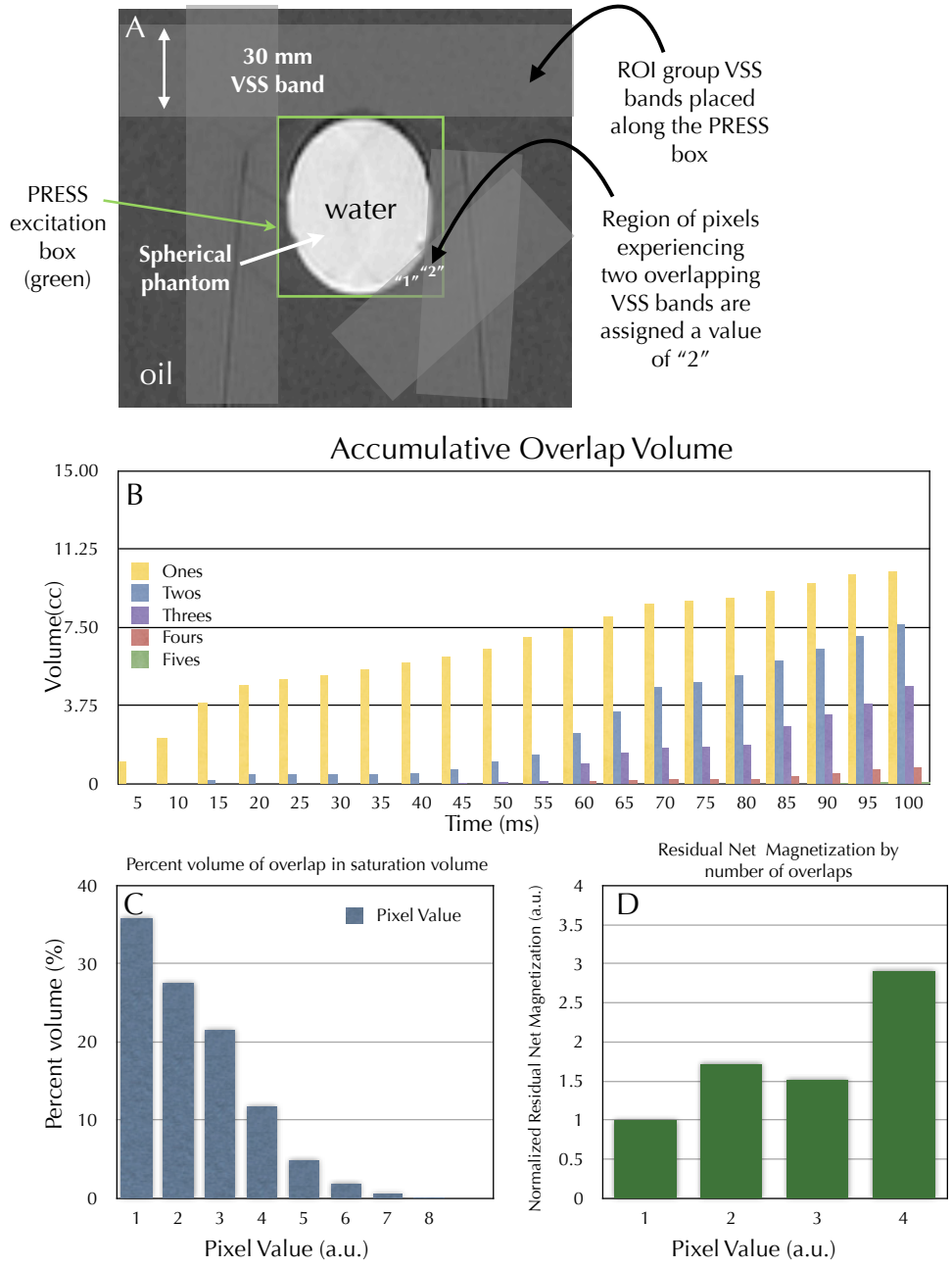

Figure 2.7 OVS simulation

(A) Using a 3D model to simulate the overlapping of the VSS pulses, each VSS pulse is given a pixel value of 1. Adding all VSS pulses to our model produces an effective pixel mapping of overlapping volumes. VSS pulse volumes that have no overlap have a pixel value =1, volumes with two overlaps have a pixel value =2, volumes with three overlaps have a pixel value =3, etc. . (B) The accumulative overlap volumes are calculated, demonstrating that the number of overlapping volumes significantly increases over time. (C) We calculated that 68% of the saturated volume experiences multiple overlapping pulses. (D) Even number of VSS pulses early in the VSS pulse train may result in a high net residual magnetization.

2.1.4.2. Optimal ordering of VSS pulses

While modifying the flip angle of VSS pulses to offset the negative effects of T_1 regrowth may reduce net residual lipid magnetization, in the previous section it was demonstrated that this simple approach only works when saturation planes do not overlap. Given that a large fraction of the saturated volume experiences multiple overlapping volumes, we sought to optimize the sequence further by examining the effect of temporally ordering VSS pulses based on individual VSS pulse contributions to the overlapping volumes.

In the simulation, we calculated the contribution of individual VSS bands to the number of overlapping bands (i.e. one's, two's, three's, etc.) within the saturation volume over time (see figure 2.8). This plot demonstrates the individual contribution of each saturation pulse with respect to the ordering specified by the CV-MRS software tool. The saturation planes specified by the CV-MRS software are randomly ordered and thus give rise to a unique pattern of overlapping saturation pulses over time. We learnt from the previous section that temporal separation of VSS pulses, such that overlapping pulses occur further apart in time, resulting in reduced residual net magnetization. As well, we know that an even number of overlapping pulses can contribute up to 3 times as much residual net magnetization as an odd number of overlapping pulses. Additionally, from figure 2.8A we observe that near the end of the VSS pulse train, almost the entire volume being saturated is experiencing multiple overlapping pulses. This information can be used to help further optimize the sequence.

A subroutine to optimally order the VSS pulses was written, such that the volumes from individual VSS pulses that give rise to an even number of overlapping volumes were ranked from largest to smallest. The VSS pulses contributing to the largest of the even overlapping volumes were moved further back in OVS sequence to achieve minimal residual net magnetization. At the same time, individual VSS pulses contributing to zero overlap volumes (i.e. labelled "one") were moved to the beginning of the OVS sequence (see figure 2.8B). By reordering the VSS pulses in the OVS sequence we further reduce the net residual magnetization prior to PRESS excitation.

Modifying the flip angle and reordering the VSS pulses results in an optimized OVS sequence. The optimized sequence was tested on phantoms and is presented in the results section (section 2.4) of this chapter.

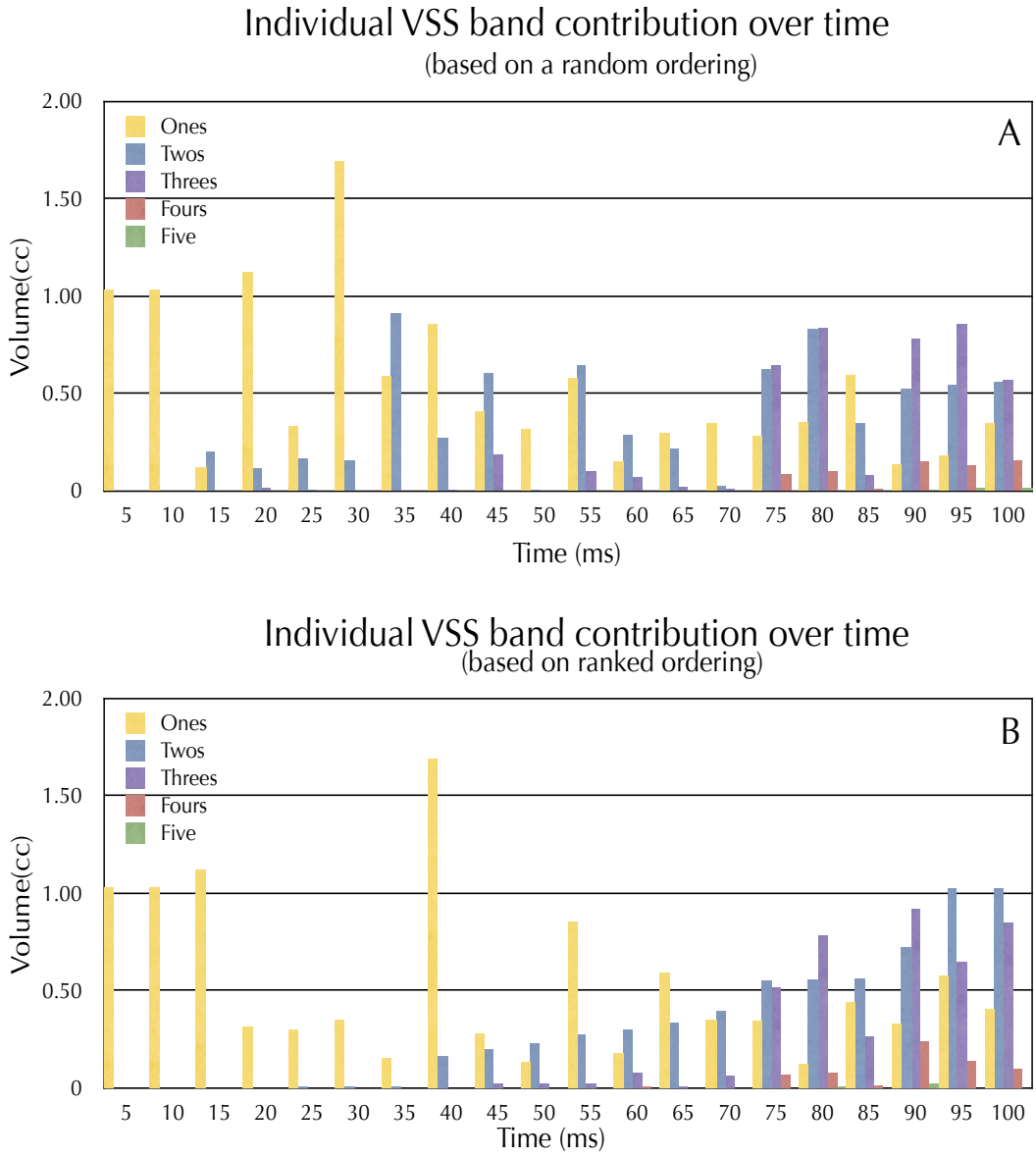

Figure 2.8 Optimal ordering of VSS pulse

(A) Based on the direct output of the CV-MRS software, the initial ordering of the VSS bands are randomly ordered resulting in distribution of overlapping volumes developing over the duration of the train of VSS pulses. (B) Using a ranking system based on the individual contribution from each VSS pulse, the largest volumes of even overlapping volumes were moved further back in the OVS sequence, while VSS pulses contributing to no overlap were moved to the back.

2.1.5. Specialized RF pulses

The last modification made to the pulse sequence was the addition of a spectral-spatial RF pulse. A spectral-spatial RF pulse forms a group of RF pulses that excite magnetization having both a specific slice location and spectral content. This is advantageous as it allows one to selectively excite the magnetization from one chemical species (i.e. water), while at the same time not affecting the magnetization of another (i.e. lipids). Spectral-spatial RF pulses have a number of advantages:

- Better tolerance to B_1 inhomogeneities when compared to lipid saturation RF pulses
- Fairly short pulse durations
- Very limited excitation of magnetizations from non-selected chemical species
- Can provide additional reduction of lipids when used with other techniques (i.e. OVS)

Within the context of spectroscopic imaging of the prostate, spectral-spatial RF pulses have had an extensive history of use (99, 100). Current clinical implementations use spectral-spatial 180 degree refocussing RF pulses with long pulse durations (on the order of 25-30 ms) (28, 101). Thus putting strict restrictions on the minimum achievable echo time.

For our use we chose a spectral-spatial 90 degree RF excitation pulse instead of a refocussing pulse (102). The spectral-spatial 90 degree RF pulse consists of multiple RF sub-pulses that are played under a broad RF envelope as seen in Figure 2.9. The shape of the RF envelope determines the spectral region of interest, and

bipolar slice-selection gradients are used to specify the spatial content. The characteristics of the spectral-spatial RF pulse used in our implementation were as follows: true nulling (in contrast to opposed nulling), a frequency offset of -120 Hz (with water at 0 Hz), a nulling frequency of 110 Hz (placing nulling points at 0 Hz-water, and 220 Hz-lipids), a spectral bandwidth of 90 Hz, a spatial bandwidth of 1750 Hz, with 4 trapezoidal gradient cycles leading to a total pulse width of 18.2 ms.

The spectral-spatial 90 degree excitation RF pulse presented here has a number of advantages. The relative short duration of the pulse allows for a minimum echo time of 40 ms. Secondly, the design of the modified pulse sequence enables us to use the spectral-spatial RF pulse on-the-fly, such that it can be exchanged with the standard 90 degree excitation at any time. This allows flexibility for future experiments. Additionally, we expect that in combination with the optimized CV-MRS technique, the spectral-spatial 90 degree RF pulse will help further reduce lipid contamination at short echo times during spectroscopic imaging of the prostate.

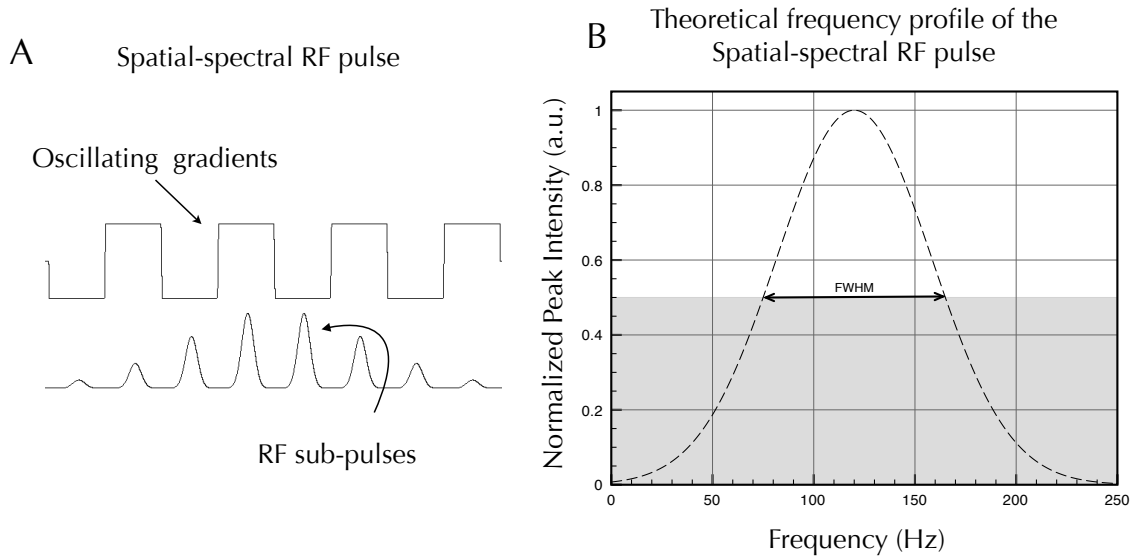

Figure 2.9 Spectral-spatial RF characteristics
(A) Both the oscillating gradient waveform, and the RF sub-pulses are shown. (B) The theoretical frequency profile of the spectral-spatial RF excitation pulse.

2.2. Scans required for phantom testing

To test the optimized pulse sequence a series of phantom experiments were performed to measure the efficacy of the modifications prior to our *in vivo* prostate study.

2.2.1. Phantom design

All MR scans were performed on a General Electric 1.5T Signa MR scanner outfitted with Echospeed gradients using a standard head coil or combined torso array coil with single channel endorectal coil. To perform in-house phantom tests of the modified pulse sequence, two phantoms were built to simulate the prostate and surrounding lipid signal. One phantom was spherical (22.4 cm^3) and the second was multifaceted (10 sides, with volume ~ 400 cm^3). The spherical phantom contained a 70 mM citrate solution (NaCl and $CuS0_4$ were proportionally added to adjust for conductivity and T_1 relaxation). The multifaceted object was filled with deionized water. Both objects were placed inside an oil bath to simulate periprostatic lipid.

2.2.2. MR imaging

All images were acquired using a T_2 weighted fast spin echo (TR/ TE=1000/180ms) sequence along the axial direction. Images were collected over the entire volume of each object. We generally obtained 20-30 slices with a resolution of 256 x 256 pixels, a slice thickness of 5 mm, 1.5 mm spacing and 24 cm field of view. The collected images were used as input into the CV-MRS software tool. The CV-MRS tool generates the plane locations for the excitation

voxel and all the spatial saturation planes, and outputs a text file which is read directly by the pulse sequence.

2.2.3. Profile measurement of-spectral-spatial 90 degree RF pulse

Using the spherical phantom, and employing the modified pulse sequence (CV-MRS with optimizations and PRESS with spectral-spatial excitation with TE/TR =130/1100 ms), 13 consecutive single voxel spectra were collected using an eight channel head coil. For each scan the CHESS sequence was disabled allowing full magnetization of the water peak. Next, for each consecutive scan the center frequency of the water signal was incrementally shifted by 20 Hz, thus allowing the water peak to pass through the full spectral range of the spectral-spatial 90 degree RF pulse.

2.2.4. ^{1}H-MRS single voxel measurements using different methods

For these single voxel experiments the spherical phantom was used. In total, we collected five single voxel spectra using the head coil. To facilitate a relative comparison of the optimizations (i.e. flip angle modifications and temporal ordering) made to the pulse sequence, spectra were collected with the following acquisition settings:

1) Manually placed spatial saturation bands and PRESS with TE/TR =130/1100 ms; An expert user manually placed saturation planes around the object. A total of 10 VSS pulses were used (a limit imposed by the GE software version running on our scanner)
2) CV-MRS without optimizations and PRESS with TE/TR =130/1100 ms.

3) CV-MRS with optimizations and PRESS with TE/TR =130/1100 ms.

4) CV-MRS with optimizations and PRESS with spectral-spatial excitation with TE/TR =130/1100 ms.

5) CV-MRS with optimizations and PRESS with spectral-spatial excitation with TE/TR =40/1100 ms.

A total of 20 VSS pulses were used for all CV-MRS acquisitions. In this experiment, we used a voxel size of 40x40x40mm^3, spectral width=1000Hz (with 512 pts), 128 scans, and 2 averages. For each single voxel acquisition, 8 unsuppressed water scans were collected for internal water referencing. To help reduce chemical shift artifacts, the PRESS excitation volume is over-prescribed (over-PRESS) by a factor of 1.3 in all three directions (x, y, and z). At 1.5T, the CSA artifacts are small, since high bandwidth Shinnar Le Roux optimized pulses (~10 kHz) were used. For all scans the thickness of the spatial saturation bands was 30 mm.

2.2.5. ^{1}H-MRSI measurements using three methods with head coil

In a similar set of experiments, spectra were acquired using multi-voxel acquisitions (^{1}H-MRSI) with the multifaceted object using an eight channel head coil. Again, to make a relative comparison, three scans were performed:

1) Manually placed spatial saturation bands and PRESS with TE/TR =130/1100 ms; An expert user manually placed saturation planes around the prostate. A total of 10 VSS pulses were used.

2) CV-MRS with optimizations and PRESS with TE/TR =130/1100 ms.

3) CV-MRS with optimizations and PRESS with spectral-spatial excitation with TE/TR =40/1100 ms. The properties of the spectral-spatial pulse were the same as specified in section 2.1.5.

Similar to single voxel measurements, to help reduce chemical shift artifacts the PRESS excitation volume is over-prescribed (over-PRESS) by a factor of 1.3 in all three directions (x, y, and z). Each 3D MRSI acquisition used a 16x8x8 phase encode matrix, with a nominal voxel size of 1.25 cm^3, a spectral bandwidth of 1000Hz (with 512 points) and an acquisition time of 29 minutes. For all spectroscopic imaging scans the width of the spatial saturation bands was 30 mm. For post-processing frequency corrections the water suppression for each scan was adjusted to retain a small amount of residual water.

2.2.6. ^{1}H-MRSI measurements using three methods with endorectal coil

For *in vivo* measurements we used a single channel disposable endorectal coil (Medrad Inc., Warrendale, USA) in combination with a torso phased-array coil. To ensure that the optimized sequence works with the endorectal coil configuration the same experiments from the previous section (2.2.5) were repeated. Each 3D MRSI acquisition used a 16x8x8 phase encode matrix, with a nominal voxel size of 0.42 cm^3, a spectral bandwidth of 1000Hz (with 512 points) and an acquisition time of 29 minutes. For all spectroscopic imaging scans the width of the spatial saturation bands was 30 mm. For post-processing frequency corrections the water suppression for each scan was adjusted to retain a small amount of residual water.

2.2.7. SNR profile of the endorectal coil

Lastly, a set of axial T_2 weighted FSE imaging scans were acquired without any phantom to facilitate an SNR calculation over the entire sensitive region (a matrix of 256 x 256, TE/TR = 112/5500 ms, slice thickness = 2 mm, spacing = 2 mm, ETL = 16, and FOV = 30 cm).

2.3. Analysis Methods

2.3.1. LCModel for prostate spectra

Post-processing of data collected using single voxel and multi-voxel acquisition techniques was performed using the SAGE[15] software platform and LCModel[16]. Post-processing of the acquired data consisted of several steps which will be discussed in this section.

The raw time domain data was loaded into the SAGE environment. The SAGE software platform was used primarily to visualize the data and perform minor spatial and spectral apodizations. In the time domain, a 1.25Hz Gaussian spectral-apodization filter was used. This was followed by a Fourier transform into the spatial and frequency domain. Next, a spatial apodization filter (Fermi diameter =100%, Fermi transition width=50%) was applied to help reduce signal bleeding effects.

---

[15] SAGE ver2007.1, Spectroscopy Analysis by General Electric, © 1998 General Electric

[16] LCModel Version 6.2, Dr. Stephen Provencher,

The data was then ported into a modified version of LCModel. The LCModel fitting package has an extensive history in the robust fitting of spectra (103-114) . The LCModel fitting algorithm works by analyzing an *in vivo* spectrum and comparing it to a known *in vitro* spectrum (115). The *in vitro* spectrum consists of a linear combination of model spectra forming a basis set from which estimations about the *in vivo* metabolite concentrations are made. The LCModel algorithm uses a nearly model-free constrained regularization method, and is completely automated, making it attractive for multi-voxel analysis (115). LCModel can handle strong baseline and lineshape variations without any interactive input from the user. The built-in routine to handle baseline variations is able to automatically account for large distortions due to residual lipids or water. Additionally, variations in lineshape due to eddy-currents or imperfect shimming can be accounted for by the software. One of the main strengths of the LCModel software is the final display showing the raw data with the LCModel fits and the tabular output of the estimated metabolite concentrations reporting their uncertainties (reported as Cramer-Rao lower bounds or %SD).

While LCModel has traditionally used *in vitro* data to form a basis set for comparison to *in vivo* data, it is also possible to use LCModel's built-in commands to generate a simulated basis set based on known spectral linewidths and patterns[17]. Within the framework of LCModel, we used the chemical simulation function (CHSIMU) to simulate prostate metabolites and lipid macromolecules. To demonstrate the use of the CHSIMU function let's consider one of the key

[17] Personal communication from Dr. Provencher led to development of a simulated basis set for prostate spectra

metabolites in prostate spectroscopy, citrate. At an echo time of 130 ms, the phase of the two dominant inner peaks are positive and are centered at 2.6 ppm. To simulate a metabolite within LCModel the CHSIMU function would be called using the following notation (116):

chsimu(1)='metabo @ ppm1 +- sdppm FWHM= fwmin1 < fwex +- sdfw AMP= amp1'

where *chsimu()* is the system variable, *metabo* is the assigned name of the metabolite (as displayed in the output table), *ppm1* is the chemical shift value of the metabolite, *+-sdppm* is the expected standard deviation of the chemical shift in the simulated spectrum, *fwmin1* is the minimum full-width-half-maximum of the peak, *fwex* is the expectation value of the peak, *+-sdf* is the standard deviation of the expected value of the peak, and *AMP* is the effective number of protons contributing to peak. Using citrate as an example, the two peaks would be fit using two separate function calls:

chsimu(1)= 'Cit1a @ 2.67 +- .03 FWHM=.10 < .12 +- .01 AMP=1.'

chsimu(2)= 'Cit2b @ 2.61 +- .03 FWHM=.10 < .12 +- .01 AMP=1.'

Similarly any metabolite in the spectrum can be simulated, and the relative resonance area for each peak is reported with an estimation of the goodness-of-the-fit quantified by the Cramer-Rao Lower Bound (CRLB) (quoted by percent standard deviation -%SD). Additional LCModel control parameters were used to help improve the analysis, these include specifying the simulation type (sptype='prostate'), and modifying to include both the residual water and citrate peaks in the calculation of the cross-correlation function (CCF) (i.e. nrefpk(1)=1,

nrefpk(2)=2, ppmref(1,1)=4.7 for water, and ppmref(1,2)=2.6 for citrate). The modifications resulted in good fits of the metabolites at short and long echo times. Metabolites that fell within the spectral range of 0.6-3.85 ppm were fitted using this modified LCModel package.

In the current version of LCModel, the algorithm operates by analyzing voxels in series, which on a single processor may take up to 30-45 minutes to process for an entire data set. To speed up the analysis a UNIX shell script was written such that each spectroscopy slice (specified by a unique LCModel control file) was sent to a different processor-core on a multi-processor system. The computer system used housed two quad-core 64 bit enabled Xeon processors with 32GB of RAM. Using this method the time for analysis for each data set was significantly reduced. The current analysis time for approximately 200 voxels is less than 5 minutes.

2.3.2. Rejection criteria

To eliminate poorly fitted peaks from the analysis, a set of rejection criteria were imposed to prevent further analysis of poorly fitted peaks. The first criterion was that all spectra must pass LCModel's built-in mechanism to reject voxels containing spectra with very poor baselines. LCModel baseline routine can handle a large range of complicated situations (i.e. lipid artifacts, signal not present in the basis set, signal with very short T_2 times, and incomplete water suppression). Poor baselines are typically characterized by very large dips present in the spectrum. These voxels are automatically rejected since they may report inaccurate

concentrations. The second criterion is based on signal-to-noise ratio (SNR). LCModel calculates the SNR of each voxel as the ratio of the maximum peak in the spectrum-minus-baseline over the analysis window to twice the RMS residuals. Spectra with a SNR of less than or equal to 2 can return misleading fits and are rejected. The third criterion is based on the goodness-of-fit. We used a CRLB of 20% as a threshold or cut-off, as recommended by the LCModel user manual.

2.3.3. Lipid reduction

To determine the effectiveness of the optimized CV-MRS technique in reducing peripheral lipid contamination, we calculate the *percent relative lipid reduction* between the consecutive acquisitions for all voxels within the object (having at least 75% of the ROI). This is calculated by the following formula:

$$\%\,relative\,lipid\,reduction = \left[1 - \frac{Lipids_{acqusition\#2}}{Lipids_{acqusition\#1}}\right] \times 100\% \qquad (2.2)$$

Where $Lipids_{acquisition\#1}$, and $Lipids_{acquisition\#2}$ are the fitted areas determined by LCModel.

2.3.4. SNR image analysis

The SNR of the imaging data was calculated by first selecting a signal-free region of interest. The standard deviation of the pixel values in this region were calculated, $\sigma_{signal\ free\ region}$. To determine the SNR map over the entire image, each pixel value is divided by $\sigma_{signal\ free\ region}$. A line profile extending from the posterior to

anterior portion of the coils' sensitive region was obtained to demonstrate the SNR as a function of depth. In practice, this would give us a relative comparison of the SNR that we would expect to observe for *in vivo* measurement (i.e. posterior region representing the peripheral zone and the anterior part the central zone).

2.3.5. Data storage

Interpreting and displaying a multitude of spectra can be difficult without adequate software and storage. Concurrently in our lab a comprehensive database software package was developed for the purpose of handling all the output files generated by LCModel (117). The software package was written in Python, and uses the open-source PostgresSQL[18] software to store and retrieve data. The integrated analysis platform has a user-friendly GUI which allows the user to visualize and display spectra in combination with the anatomical reference images. All data processed with LCModel were uploaded to the database and PostgreSQL queries were written to extract data for analysis.

2.4. Results

Results from the different acquisition strategies are presented. The acquisition number is presented for each spectrum, and relates back to the specific scanner settings for each measurement given in section 2.2.

[18] PostgreSQL is an open source object-relational database system, http://www.postgresql.org/

2.4.1. Profile measurements of spectral-spatial 90 degree RF pulse

The measured profile of the spectral-spatial 90 degree RF excitation pulse is displayed alongside the theoretical profile in Figure 2.10B. Both the measured and theoretical profile are in good agreement with each other, with similar FWHM (~90Hz), and nulling points at 0 Hz (water) and 220 Hz (lipids).

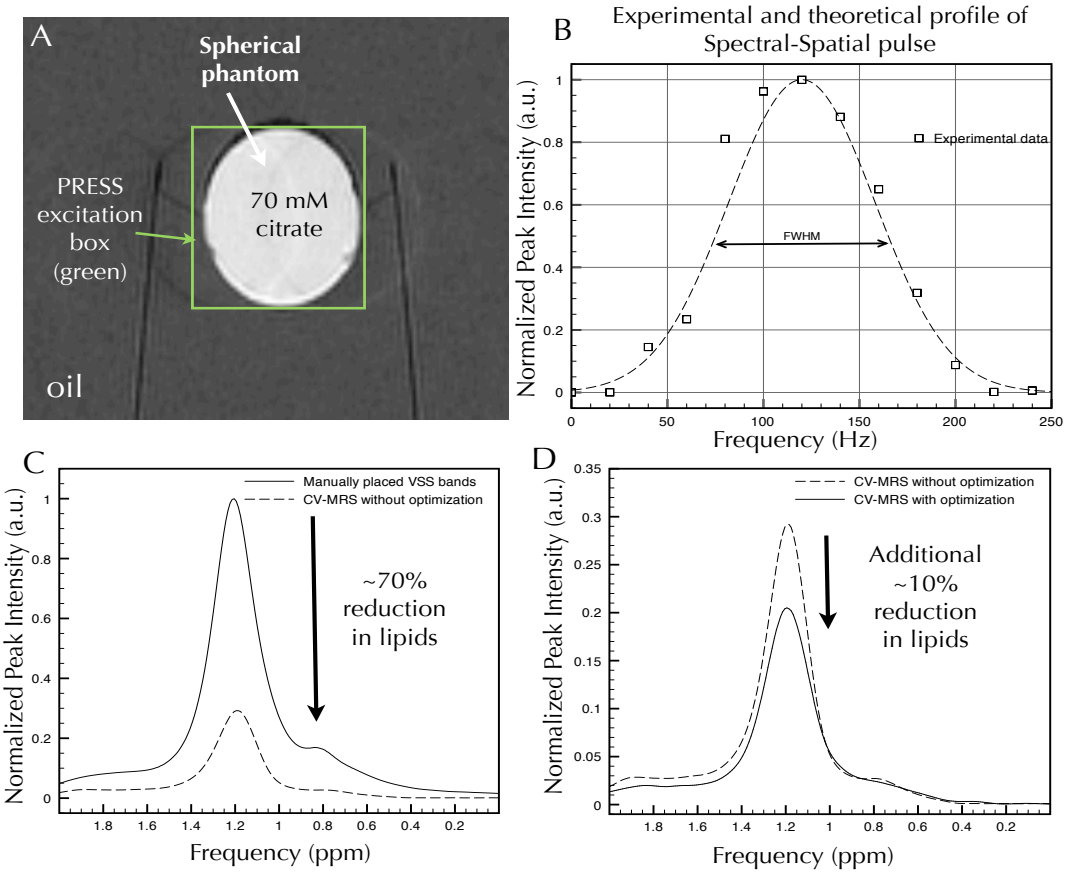

Figure 2.10 Measured spectral-spatial profile and SVS demonstrating lipid reduction

(A) Spherical phantom containing 70mM citrate solution. The PRESS excitation box was chosen to encompass the entire object. (B) Both the measured and theoretical frequency profile of the spectral-spatial RF excitation pulse demonstrate good agreement and sharp signal fall-off at 0 and 250 Hz. (C) Normalized spectra showing ~70% reduction in residual lipids going from the manually placed technique to using CV-MRS. (D) Normalized spectra showing the effect of the OVS optimizations which account for T_1 *regrowth and reordering of VSS pulses.*

2.4.2. ^{1}H-MRS single voxel measurements

Single voxel spectra from five different measurements were obtained and are displayed in Figures 2.10 and 2.11 displaying lipids and citrate respectively. Focussing on the measurements of residual lipids, in Figure 2.10C we observe an approximately 70% percent reduction in residual lipid signal when comparing spectra obtained using the manually placed VSS pulses to those placed automatically using the CV-MRS technique (acquisitions 1 and 2). In Figure 2.10D, we demonstrate that an additional 10% reduction in lipids can be achieved when using the T_1-flip angle and reordering optimizations (acquisition 3). In total we observed an approximate 80% reduction in residual lipids when using the optimized CV-MRS techniques. Furthermore, the spectrum of citrate displayed in Figure 2.11A demonstrated a very good (%SD=2%) LCModel fit using simulated basis sets (acquisition 3). In Figure 2.11B, spectra overlays of single voxel measurements obtained with and without the spectral-spatial excitation show no variation in peak intensity, or line shape (acquisitions 3 and 4). Lastly, spectra using the optimized CV-MRS technique at TE=40ms demonstrate the expected spectral pattern of citrate and good LCModel fitting of citrate (acquisition 5).

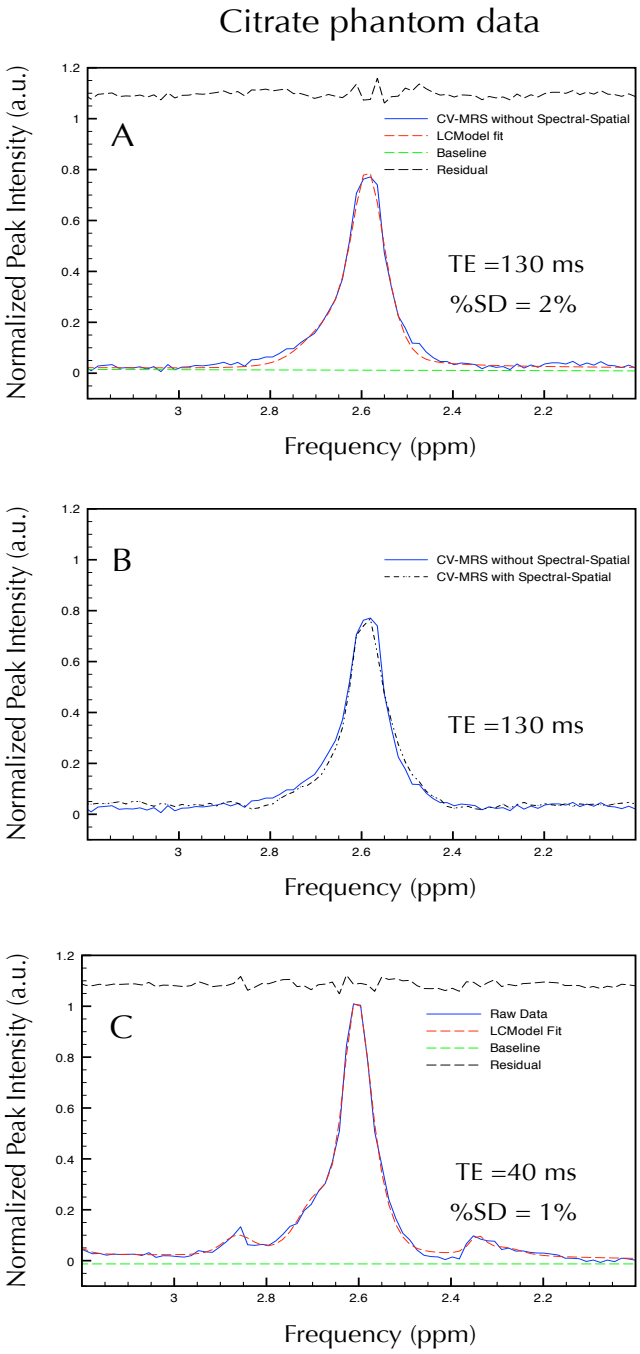

Figure 2.11 LCModel fits of spectra at long and short echo times
(A) A single voxel spectrum of citrate was acquired at TE=130ms, using the optimized CV-MRS without spectral-spatial excitation, and fitted using LCModel with simulated basis sets. (B) A single voxel collected with the same settings as in (A), but with the spectral-spatial 90 degree excitation pulse turned on. The overlay of the two spectra demonstrates no spectral change. (C) Lastly, a single voxel spectrum of citrate acquired at TE=40ms, demonstrating the positive phase of the outer peaks of the strongly coupled spin AB system. In general, we have demonstrated robust fitting of spectra using simulated basis sets with LCModel.

2.4.3. ^{1}H-MRSI measurements with a head coil

In a similar set of experiments but for multi-voxel acquisition, three consecutive 3D ^{1}H-MRSI measurements were made demonstrating the efficacy of the optimized CV-MRS technique. In Figure 2.12 A to C, progressive improvements in reducing the lipid contamination effect were observed. Using the manual placement technique (Figure 2.12A), residual lipids show strong contaminating effects within voxels at the periphery and in voxels near the centre of the object (acquisition 1). Using the optimized CV-MRS technique (acquisition 2) we observed a dramatic reduction in contaminating lipids (see Figure 2.12B). Lastly, the optimized CV-MRS with spectral-spatial excitation (acquisition 3) nearly nulls all contaminating lipid signals throughout all voxels (Figure 2.12C).

2.4.4. ^{1}H-MRSI measurements with a endorectal coil

Following the exact same set of scans described in the previous set of measurements, three consecutive 3D ^{1}H-MRSI measurements were acquired using a combined endorectal coil and torso-phased array coil. In Figure 2.13 A to C, we observe a similar progressive improvement in reducing lipid contaminating signals. Likewise, using the manual placement technique (Figure 2.13A), we observe strong signal contamination from lipids within voxels at the periphery and voxels near the core of the object (acquisition 1). The optimized CV-MRS technique (acquisition 2) dramatically reduced contaminating lipids (see Figure 2.13B). In the last 3D ^{1}H-MRSI (acquisition 3), the optimized CV-MRS with spectral-spatial excitation, nearly nulled all lipid contaminating signals throughout all voxels (Figure 2.12C).

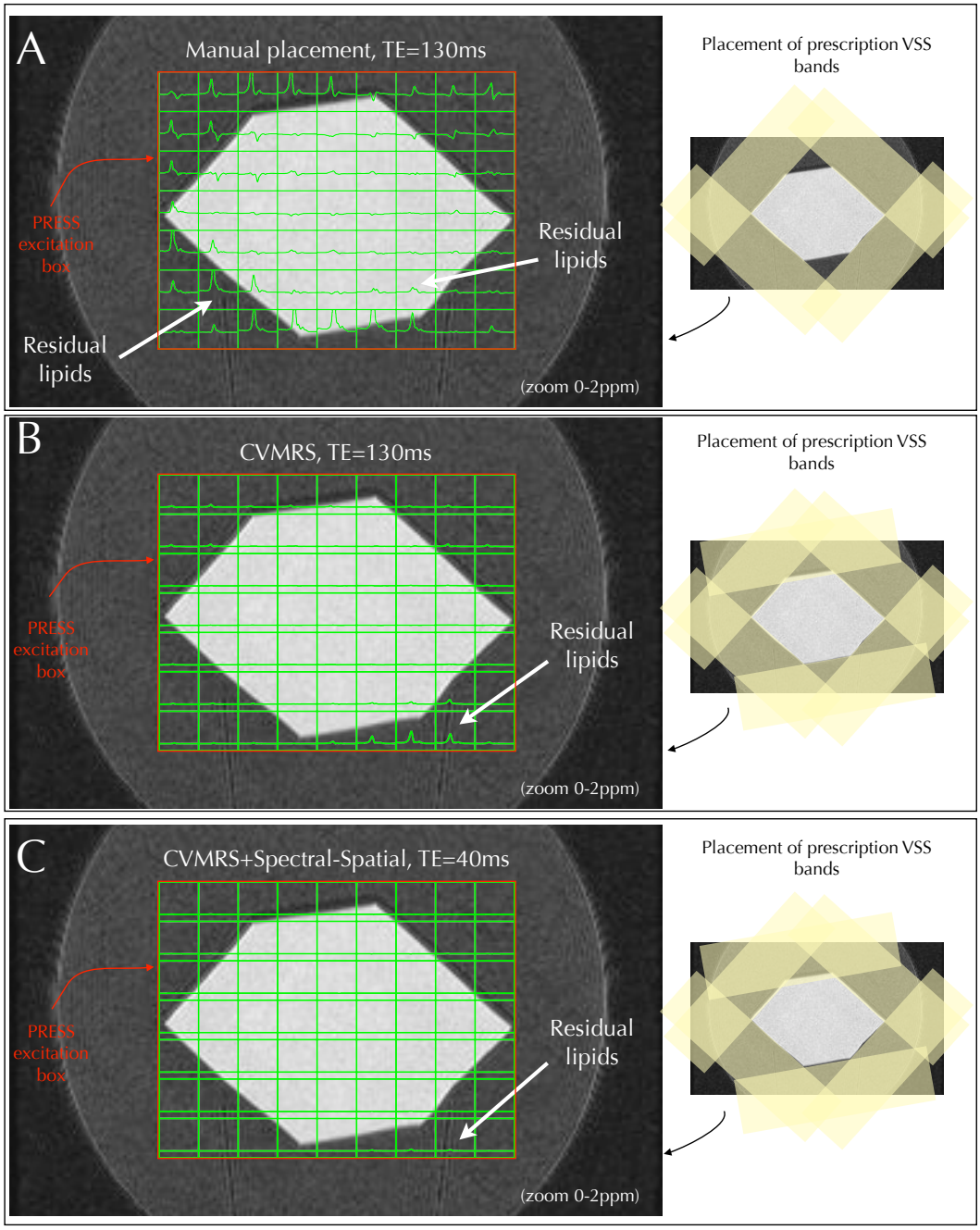

Figure 2.12 3D ^{1}H-MRSI phantom data using a head coil

3D ^{1}H-MRSI data were collected from an irregularly shaped object. T_2 weighted images of the phantom are presented with the spectral grid overlay. Each grid point has been zoomed into the region 2.0 ppm to 0.0 ppm, to focus on the lipid peak which resonates at 1.2 ppm. In (A), the 10 manually placed spatial saturation bands are used (TE = 130 ms). In (B) the optimized CV-MRS employing 20 spatial saturation bands was used (TE = 130 ms), and lastly in (C) the optimized CV-MRS in combination with spectral-spatial excitations was used (TE = 40 ms). In (A) it is clear that within the object significant lipid contamination is present. Using the improved techniques in (B) and (C), lipid contamination due to peripheral lipid is nearly completely suppressed.

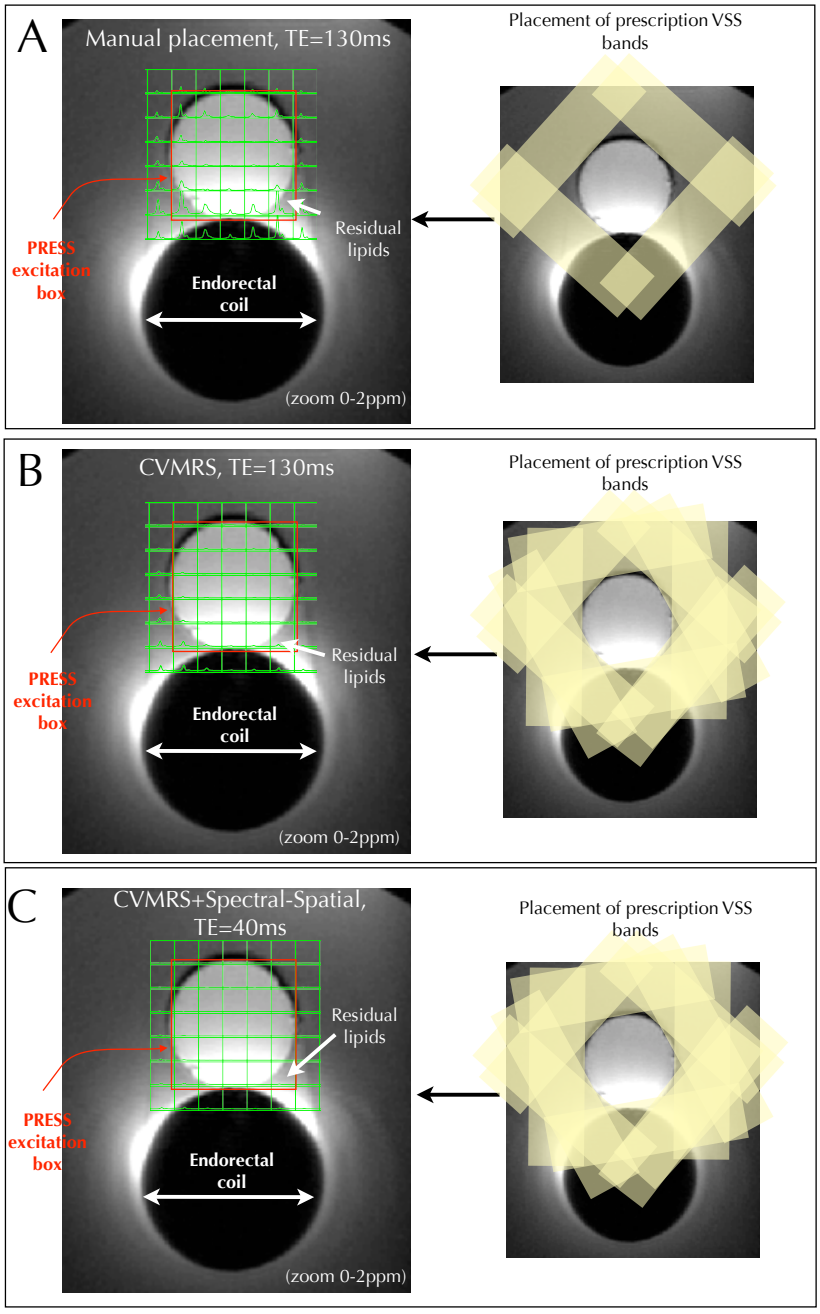

Figure 2.13 3D ^{1}H-MRSI phantom data using an endorectal coil

3D ^{1}H-MRSI data were collected from a spherical prostate-like phantom using a combined single channel endorectal coil with a torso-phased array coil. T_2 weighted images of the phantom are presented with the spectral grid overlay. Each grid point has been zoomed into the region 2.0ppm to 0.0ppm, to focus on the lipid peak which resonates at 1.2ppm. Similar to data acquired with the head coil, we observed significant lipid contamination within the object when using manually placed VSS bands (see A). Using the improved techniques at short and long echo times, we observed reduced lipid contamination due to peripheral lipid (See B and C).

2.4.5. SNR profile of the endorectal coil

Lastly, the SNR map over the axial region of the endorectal coil was calculated (see Figure 2.14). A line profile of the SNR map is shown in Figure 2.14B. Examining the normalized SNR profile as a function of depth, we observe that the signal significantly drops as we move from the posterior to anterior region (~70%). To compare this result to what we would expect to see in the prostate, we superimposed the typical region size and locations of the peripheral and central zones (see Figure 2.14B). In this comparison we observed that over the "peripheral zone" (5- 10 mm) there is a fall-off in signal ranging from 90-65 percent. Further, we observe that the signal continues to fall over the "central zone" (10-35 mm) from 65-20 percent. This resulted in a significant SNR fall-off over the region of the prostate demonstrating the expected SNR of spectra collected at those spatial positions.

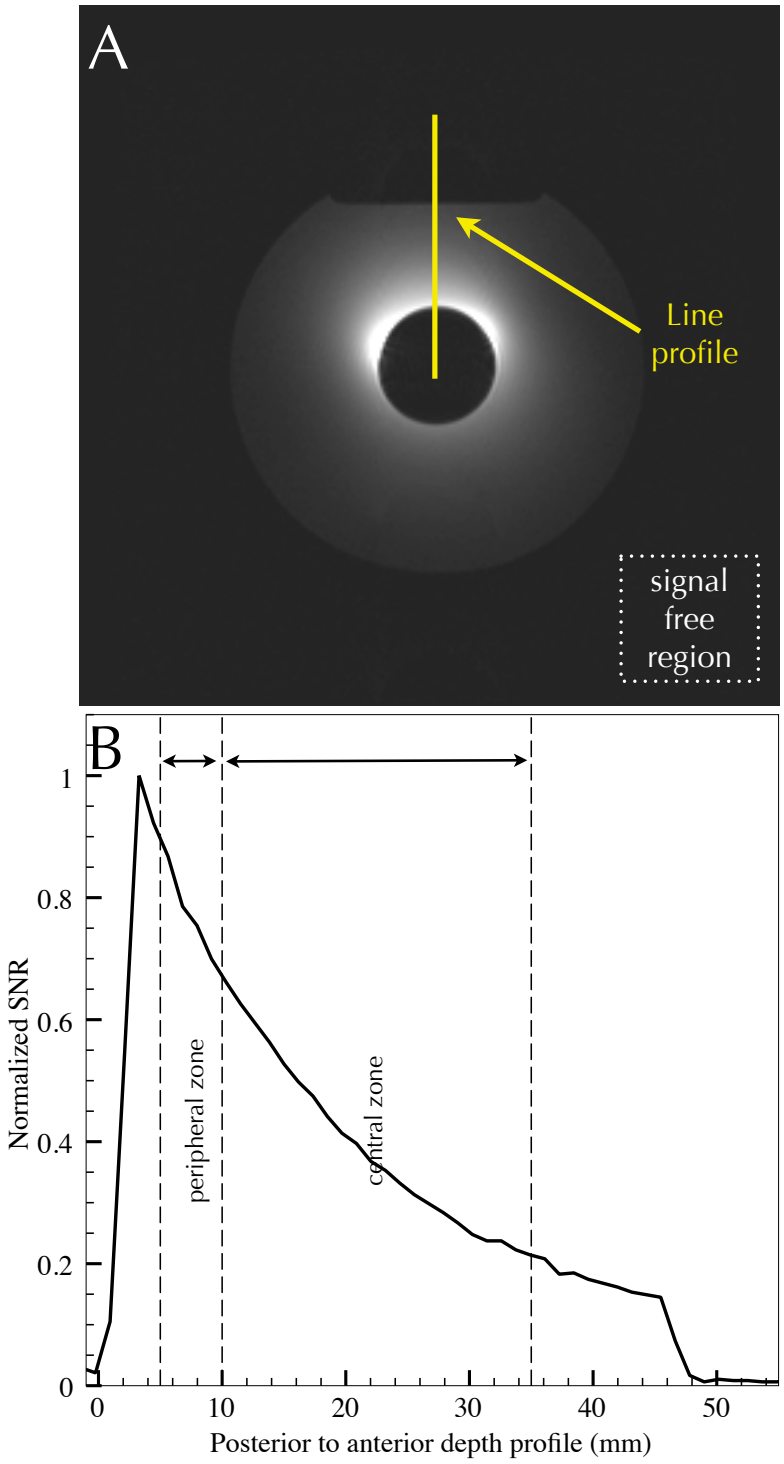

Figure 2.14 SNR line profile of the endorectal coil

A line profile of the SNR map was taken from posterior region extending to the anterior region (A) of the coil sensitive region and is shown in (B). Over the region of the prostate there is a ~70% drop in signal from the edge of the peripheral zone to the outer edge of the central zone.

2.5. Summary of results

In this chapter a number of useful results were presented. First, a modified PRESS sequence was developed which now includes a revised and much improved version of the CV-MRS algorithm. The current algorithm, which uses modern computer graphics techniques (i.e. surface simplification), takes less than one second to optimize the spatial orientation of VSS bands around an object of interest. The new software tool not only allows for a much improved user experience, it provides a great deal of flexibility for both viewing, and manipulating individual VSS bands. To match the software, modifications to the GE PRESS localization sequence were made to include a varying number of VSS pulses within the OVS scheme. Next, we optimized the flip angles of all VSS pulses to account for the negative effects of the T_1 regrowth. To counter balance the effects of modified flip angles and overlapping saturation pulses, an optimal ordering routine was introduced to minimize residual lipid magnetization (based on a full 3D computer simulation). Lastly, the pulse sequence was modified to incorporate a spectral-spatial RF excitation pulse for further reduction of lipids at short echo times.

Several phantom measurements were performed using the optimized techniques demonstrating significantly reduced contaminating effects from lipids. In general we observed an approximately 80% reduction in residual lipids for both single voxel and multi-voxel acquisitions when employing the CV-MRS technique. (118-121). From Figure 2.12 and 2.13, 3D ^{1}H-MRSI data demonstrated the progressive improvement in reducing lipid contaminating effects at both long and

short echo times (TE=130ms and TE=40ms respectively). Similar results were obtained using either a head coil or endorectal coil.As well, we observed no deteriorating effects on the spectral appearance of metabolites when using the CV-MRS technique in conjunction with spectral-spatial excitation. Analysis with LCModel (using simulated basis sets) demonstrated robust fitting of metabolites for both single voxel and multi-voxel acquisitions. Additionally, optimized UNIX shell scripts now allow for very fast LCModel analysis of spectral data.

Calculating the SNR over the effective prostate region demonstrated a large signal fall-off (~70%) when using the endorectal coil alone. While the fall-off is significant, using no coil would result in greatly reduced SNR over the prostate region at 1.5T. Furthermore, since most cancers are found in the peripheral zone, where we only observed a 25% change in the SNR, the drop in signal may only have a marginal effect when calculating the relative ratios of the metabolites in the prostate.

One of the main concerns when using multiple RF pulses is the possibility of stimulated or spurious echoes. Spurious echoes can appear as a ringing artifact in the raw FID. In our work, we examined the raw FID from multiple acquisitions and did not observe any ringing artifacts. Secondly, we also examined the possibility of stimulated echoes being produced by the gradient crusher refocusing pulses in the OVS scheme. While choosing different cycling schemes we examined our data for any spectral changes, and did not observe any noticeable differences. Lastly, the sequence's SAR values were checked against the scanner's built-in safety

mechanism and were found to be well below tolerances, making it safe for use in human studies.

In summary, phantom measurements using single voxel ^{1}H-MRS and 3D ^{1}H-MRSI techniques were acquired using an improved OVS technique. Results from phantom measurements demonstrated significantly improved control over lipid contaminating effects at both long and short echo times. With these results we proceeded to test this technique for the acquisition of *in vivo* human data.

Chapter 3

Automatic Conformal prescription of very selective saturation bands for *in vivo* ^{1}H-MRSI of the prostate

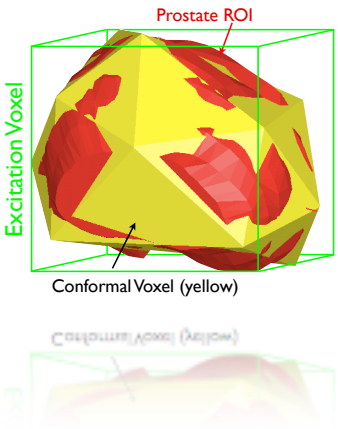

Automatically placed spatial saturation bands, using the optimized conformal voxel magnetic resonance spectroscopy technique (CV-MRS), reduced lipid contamination on average by 50±17% over the entire prostate volume. The reduction in lipids resulted in an improved baseline, and robust peak fitting when using LCModel. In summary, the CV-MRS technique removes user variability in the placement of spatial saturation bands, and helps reduce the technical expertise while performing ^{1}H-MRSI.

A portion of this chapter has been accepted for publication:
Venugopal et al., Automatic conformal prescription of very selective saturation bands for in vivo ^{1}H-MRSI of the prostate. NMR Biomedicine. 2011:In press.

3. Automatic Conformal prescription of very selective saturation bands for *in vivo* ^{1}H-MRSI of the prostate

3.1. Introduction

Proton magnetic resonance spectroscopic imaging (^{1}H-MRSI) has become a valuable technique for non-invasively determining the concentration of biomarkers associated with benign and malignant prostate tissue. Much of the initial research and development in this field was performed by Kurhanewicz *et al*. (122) and Heerschap *et al*. (123). Since then, a number of centers around the world have implemented ^{1}H-MRSI routinely for the diagnosis and management of prostate conditions (at both 1.5 and 3 Tesla) (6, 19, 49, 124-127) ranging from benign prostate hyperplasia (BPH) to prostate carcinoma (PCa). Spectroscopic imaging can distinguish biochemical differences between normal tissue, BPH and PCa(128, 129). ^{1}H-MRSI provides biochemical and metabolic information associated with tumour growth and development, and is thus in a position to detect early, premorphological changes (130, 131) in tissue as well as estimate cancer aggressiveness and proliferation (132). Over the last several years there has been increased commercial availability and clinical use of ^{1}H-MRSI packages for evaluating prostate cancer (6). *In vivo* prostate ^{1}H-MRSI has confirmed the diagnostic utility of the metabolites choline, polyamines, creatine and citrate, in providing a specific marker for cancer within the peripheral zone, with 98% of cancers having a (choline + creatine)/citrate ratio of greater than 3 standard

deviations above the normal ratio (133-135). In 10 studies examining low-risk prostate cancer populations, ^{1}H-MRSI had a mean specificity of 85% (95% confidence interval, 78-90%), and sensitivity of 68% (95% confidence interval, 56-78%) (134). In addition, *in vivo* prostate ^{1}H-MRSI data is being used to identify areas of increased metabolic activity within the prostate volume (11, 128, 129). The diagnostic value of combined magnetic resonance imaging and spectroscopic techniques has encouraged radiologists and oncologists to include it increasingly for clinical use (125, 136-140).

The acquisition of ^{1}H-MRSI data is a multi-step process. Each step is important to acquire ^{1}H-MRSI data that are artifact-free and have optimal signal-to-noise-ratio (SNR). A large amount of research has led to the development of routines to achieve excellent image quality, shimming of the main B_0 field, and combined water and lipid suppression pulse sequence designs to reduce spectral artifacts and decrease acquisition time. Crucial steps, such as placement of the endorectal coil, and graphical placement of the ROI and spatial saturation pulses are still done manually, and are therefore prone to human error. In recent review articles, Casciani *et al*. (20, 41, 141) discuss an important limitation that hinders the acquisition of good quality ^{1}H-MRSI data. They specifically address problems associated with inadequate coverage of the prostate. Furthermore they highlight the significant tradeoff between choosing an appropriate region-of-interest (ROI), and spectral quality (41), specifically illustrating that choosing a large spectroscopic excitation box results in increased periprostatic lipid contamination. Better quality spectra can be obtained by choosing a smaller spectroscopic excitation box,

however, this results in portions of prostate tissue being completely excluded. This situation is illustrated in Figure 3.1(a), which shows that when the ROI includes more of the peripheral tissue, the high intensity signal from peripheral lipids significantly contaminates neighboring voxels of interest. This effect was demonstrated earlier by Kurhanewicz *et al*. who showed that severe spectral degradation can occur in the presence of contaminating lipids (142), and could be reduced by manually placing spatial saturation bands around the prostate (42). Spatial saturation bands are an effective method to null peripheral lipid signals, but the manual placement is a subjective process and can lead to errors in graphical placement. Furthermore there is a critical need to maximize the volume of prostate tissue within the ROI while minimizing lipid contamination and obtain consistently good quality spectra throughout the prostate.

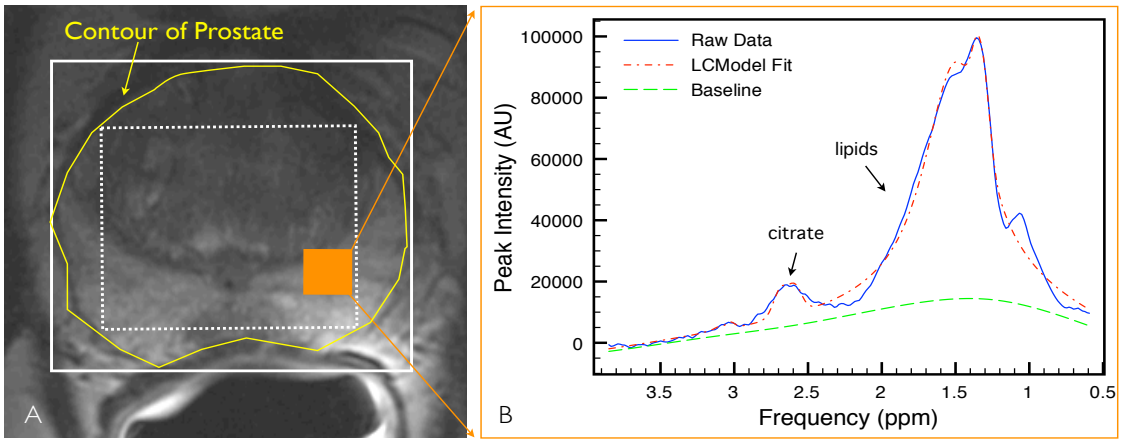

Figure 3.1 Choosing an appropriate excitation volume
In (A), if the spectroscopic excitation volume box or ROI is taken over the entire prostate (solid white line) including some peripheral tissue, the resulting spectrum from the shaded sub-volume will contain unwanted contaminating lipid, as seen in (B). To avoid contamination, the ROI could be placed within the prostate (dashed white line), but a considerable amount of peripheral prostate tissue would be excluded.

3.1.1. Application of conformal voxel MRS (CV-MRS) for *in vivo* Prostate ^{1}H-MRSI

A number of techniques have been reported to reduce the negative effects of periprostatic lipid, including outer volume suppression (OVS), band selective inversion with gradient dephasing (BASING), and spectral-spatial radiofrequency (RF) pulses (27, 42, 143, 144). These techniques operate at different stages of the pulse sequence. OVS methods have had long history of development for use in MRI (42, 145-147). In OVS, a limited number of spatial saturation bands are manually placed over regions surrounding the prostate, to eliminate as much peripheral lipid signal as possible. The spatial saturation band uses a spatially selective 90^{o} pulse to flip the longitudinal magnetization into the transverse plane. Each spatial saturation pulse is followed by a set of dephasing gradient pulses that are placed on different gradient axes to provide additional phase dispersion. The combined action of the spatial saturation pulse and the dephasing gradient pulse results in reduced signal from the volume being suppressed. While the placement of spatial saturation bands does reduce signal from surrounding tissue, the manual graphical placement of these spatial saturation bands is limiting especially for fine positioning and angling of double-oblique saturation bands. In addition, since the number of available spatial saturation bands is limited (up to 10 on a typical MRI scanner), there is inadequate coverage around the prostate (20, 41). As well, graphical prescription of additional spatial saturation bands would be a time consuming process.

Spectral-spatial RF pulses are used to limit excitation to a defined spectral region that excludes lipids within a defined slice. Current techniques utilize spectral-spatial pulses that are implemented by using two 180° spectral-spatial refocusing pulses of the spectroscopic pulse sequence (143). While this technique has proven its clinical usefulness, its implementation lengthens the minimum echo time (TE). This results in a physical time constraint and inability to measure the concentration of metabolites with short T_2 relaxation times. In light of these shortcomings present in both the OVS technique and RF excitation scheme, there is a need for: (a) improving the OVS technique by introducing a computerized algorithm to calculate the optimal positioning and orientation of the spatial saturation bands with respect to the volume of interest, and (b) a different RF excitation scheme allowing for a shorter TE.

In this study, the application of *conformal voxel magnetic resonance spectroscopy* (CV-MRS) is utilized for the acquisition of prostate ^{1}H-MRSI data (36) (94). The technique uses a variable number of spatial saturation bands that are optimally placed around the volume of interest, via a computer algorithm, to closely match the shape of the object of interest. Employing this optimized *in vivo* prostate ^{1}H-MRSI technique results in improved identification of metabolites using robust spectral fitting routines .

3.2. Materials and methods

3.2.1. Volunteers

This study received ethics approval from the local research ethics board. Subjects were recruited to the study as part of an ongoing study being performed at the Winnipeg Health Sciences Centre, in conjunction with the National Research Council Institute for Biodiagnostics (NRC-IBD), and CancerCare Manitoba. Informed consent was obtained from 16 healthy volunteers who participated in this study. Each volunteer was screened to meet the inclusion criteria of the study. All volunteers were healthy, showed no abnormalities upon digital rectum examination (DRE), and had no prior history of genitourinary disease. Four subject data sets were corrupted due to subject motion, resulting in data acquisition errors. Subsequently, the data were removed from the study resulting in 12 useable data sets. The ages of the subjects ranged from 25 to 78 years of age, with a mean age of ~52 years. The distribution of age, prostate volume, and number of voxels falling within the prostate can be seen in Table 3.1.

3.2.2. MR Imaging

All MRI/MRSI examinations were performed on a General Electric 1.5T Signa MR scanner (General Electric, Milwaukee, USA) equipped with Echospeed gradients. For optimal signal reception a standard disposable endorectal coil (Medrad Inc., Warrendale, USA) in combination with a torso phased-array coil was used. To ensure that the coil was positioned tightly against the prostate, the

endorectal probe was inflated with approximately 75ml of FC-77 FLUO- RINERT, a perfluorocarbon (PFC) compound (3M, St. Paul, MN, USA). The use of the PFC compound as substitute for air significantly reduced magnetic susceptibility artifacts and improved B_0 homogeneity throughout the prostate volume (148). Initial scout scans in all three orthogonal planes were acquired to ensure that the coil was placed directly beneath the prostate, with maximum surface covering the posterior surface of the prostate. Once the coil was appropriately placed, axial T_2 weighted images of the entire prostate gland were acquired using a fast spin-echo imaging sequence (TE/TR=102/5000ms; matrix size =256x256; field of view= 140mm; slice thickness=3mm; no gap).

3.2.3. *In vivo* conformal voxel magnetic resonance spectroscopic imaging

Novel spectroscopic techniques have been developed for acquiring robust non-cuboidal ^{1}H-MRSI data (94, 96). Extensive testing in phantoms was performed and demonstrated good potential for *in vivo* studies (118). The proposed prostate MRS acquisition uses a modified point resolved spectroscopy pulse sequence. The modified pulse sequence, shown in figure 3.2, utilizes the chemical shift selective (CHESS) method for water suppression (99), and VSS pulses (42) for OVS (with up to 20 additional pulse in the current application) and PRESS excitation. To optimize the position, flip angles, and order of the VSS pulses an offline user-friendly application was built in IDL (ITT Visual Information Solutions, Boulder, CO, USA).

This stand-alone application can run on many platforms using a freely available virtual machine.

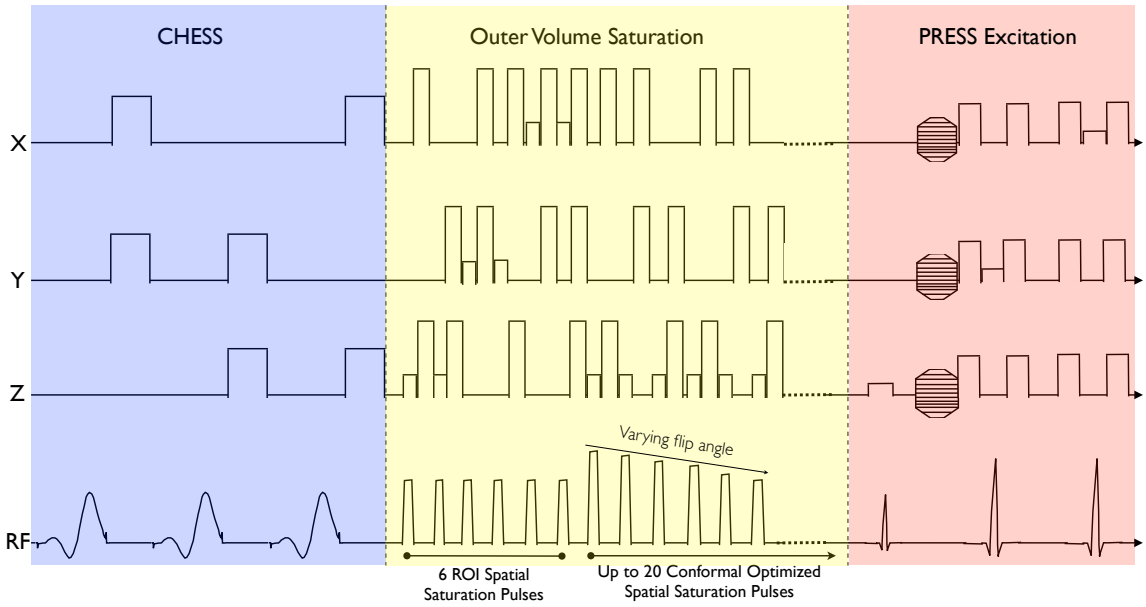

Figure 3.2 CV-MRS optimized pulse sequence
The product PRESS pulse sequence was modified to include an extended number of VSS pulses (up to 20). This elongates the Outer Volume Suppression portion of the sequence by ~100ms. To account for T_1 *lipid re-growth and overlapping pulses, the VSS pulse were optimally ordered with varying flip angles. The optimization algorithm works to maximize the lipid suppression while minimize overlapping effects. In this diagram, the vertical and horizontal axis are not to scale.*

3.2.4. The conformal voxel technique

The CV-MRS technique conforms the acquisition to the ROI by automatically placing a series of spatial saturation bands that remove unwanted signal from tissues surrounding the ROI. To implement the CV-MRS technique clinically, a platform-independent software package was developed to function directly on the scanner console (38). The CV-MRS algorithm operates in near real-time (~less than 1 second). The application is very intuitive to navigate, and utilizes the user-defined prostate ROI to determine the three-dimensional location of the spatial

saturation planes. A step-by-step summary of the use of the CV-MRS software tool is illustrated in Figure 3.3.

In the first step, as seen in Figure 3.3A, the acquired T_2 weighted prostate images are loaded into the application directly from the GE image database or through DICOM import. Secondly, the prostate images are manually segmented using a point-by-point spline-based method. This generates a set of ROIs, as seen in red in Figure 3.3B, defining the boundary of the prostate. The bounding surface of the prostate is used to calculate the optimal excitation volume. Furthermore, the set of ROIs are used as input into the conformal voxel algorithm. In the third and fourth step, the orientation and location of the optimally placed planes are calculated and used to modify the pulse sequence.

The set of ROIs are used to define a three-dimensional triangulated surface (~7500 planes). Next, a convex hull routine (98) is used to reduce the number of surface planes (~1300 planes). Following this, a surface simplification algorithm is implemented (98), whereby all adjacent vertices of the surface are examined to find pairs that can be combined while causing the least modification of the surface's shape. This simplification of the surface continues until the user-defined number of faces remains (20 planes in the current implementation). The position and location of each triangle defines the inner face of a spatial saturation slice. The CV-MRS software tool has a voxel modification tool, displayed in Figure 3.3F, which allows the user to manually modify the plane locations if desired. Built into the software is a reporting mechanism, which calculates the volumes of the prostate ROI and the conformal voxel, and the coincidence between the two volumes. Plane locations

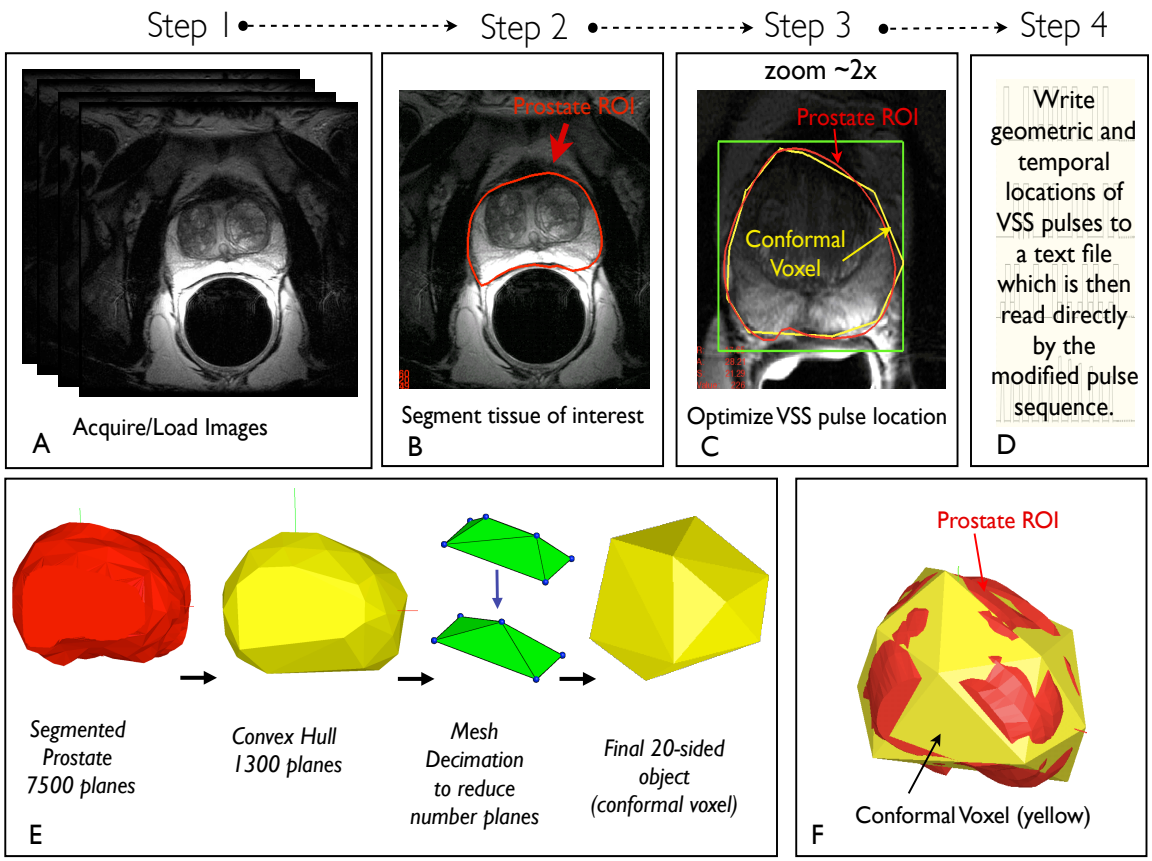

Figure 3.3 Using the CV-MRS tool

The VSS pulse plane locations are optimized using an offline software tool. In the first step, the acquired prostate images are loaded into the application (A). Secondly, the prostate images are segmented to isolate the prostate ROI (B). In the third step, (C) the conformal voxel algorithm calculates the size and location of the cuboidal excitation voxel (green), as well as optimal plane locations and temporal ordering. Lastly (D), this information is written to a text file, which is read by the modified pulse sequence. In (E), the decimation of the prostate ROI, using a combination convex hull is presented. The application has a three-dimensional voxel tool built into it, which allows the user to manually adjust the plane locations as needed. As shown in (F), the prostate ROI (red), is tightly surrounded by VSS pulses (yellow). In (G) the tool to manually shift planes is shown, along with the statistics box showing the volume of the contoured ROI and the conformal voxel as well as the percentage of outer ROI signal included in the conformal voxel and percentage of the tissue of interest (TOI) retained. The total time to implement the technique in a clinical situation is less than ~5 minutes.

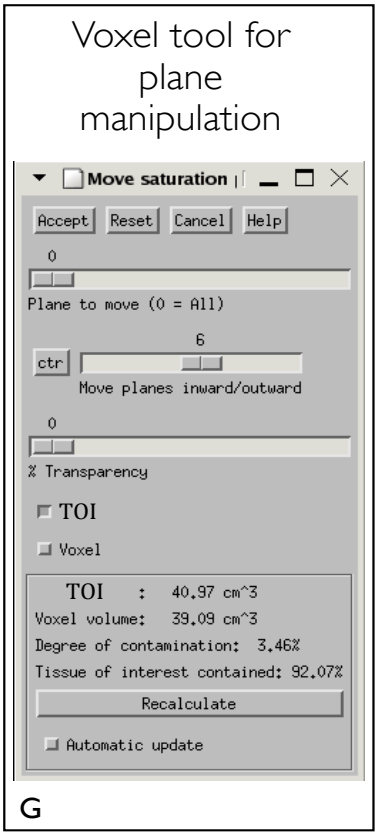

in this study were not modified manually. In this example, the conformal voxel (39.1 cm^3) almost completely coincides with the prostate volume (41.0 cm^3), with approximately 3.46% contamination of peripheral tissue. In this study, the average prostate volume was 41.4±18.9 cm^3, with a minimum volume of 18.1 cm^3 and maximum volume of 89.0 cm^3 (Table 3.1).

Table 3.1

Percent relative lipid reduction for voxels located in the inner, outer, and entire prostate volume

				Percent Relative Lipid Reduction		
Data Set	Age	Number of Voxels	Prostate Volume (cm^3)	Prostate	Outer	Inner
1	67	89	42.7	49	60	40
2	49	94	46.1	64	58	67
3	55	51	27.4	67	65	69
4	78	47	25.5	68	73	62
5	40	58	33.1	64	68	56
6	43	28	16.6	42	42	43
7	25	43	28.0	54	58	47
8	68	60	40.4	61	43	64
9	61	117	61.0	56	55	58
10	49	168	85.5	12	7	17
11	52	45	26.3	38	54	2
12	37	50	28.6	27	42	5
Average	52±15	71±40	38.4±18.9	50±17	52±17	44±24
Minimum	25	28	16.6	12	7	2
Maximum	78	168	85.5	68	73	69

Implementing a long chain of repeated VSS pulses presents an added challenge. The time between the first VSS pulse and the start of the excitation pulse in the PRESS sequence is ~100ms. Lipid (or adipose) tissue that surrounds the prostate has a T_1 relaxation constant close to ~260ms (149).During the time (Δt) between the first VSS pulse and the PRESS sequence, there is an approximate 26% re-growth of signal from the lipid volume suppressed by the first VSS pulse. To

reduce re-growth of lipid signal the pulse sequence was modified to allow each VSS pulse to have an independently varying flip angle. The appropriate flip angle of the VSS pulse was recalculated such that the first VSS pulse received a slightly larger flip angle than the last, and that the re-growth of lipid signal will be close to zero at the time the PRESS sequence commences. This optimization works when saturation planes do not overlap. Overlapping planes can cause unwanted over-rotation of the net magnetization, which can cause incomplete saturation. To minimize the effect of multiple overlapping pulses, temporal ordering of the VSS pulses was re-calculated to temporally increase the time between RF pulses of overlapping planes.

In summary, the current conformal voxel program takes into account the spatial position, orientation, flip angle, and temporal ordering of the saturation bands for maximum lipid reduction. Additionally, the excitation voxel is automatically calculated based on the prostate ROI. This information is written to a text file. Finally in the last step, the plane locations and temporal ordering contained in the text file are read directly by the modified pulse sequence directly on the scanner console. The pulse sequence is executed, with the appropriate TE and TR.

3.2.5. Scans acquired for *in vivo* testing

To facilitate a comparison between manual placement techniques and the proposed optimized technique, two separate consecutive 3D ^{1}H-MRSI acquisitions were obtained for all 12 subject studies. The first acquisition was obtained utilizing

manual placement of the VSS pulses followed by the standard PRESS excitation with TE/TR =130/1100ms. To help reduce chemical shift artifacts, the PRESS excitation volume is over -prescribed (over-PRESS) by a factor of 1.3 in all three directions (x, y, and z). At 1.5T, the CSA artifacts are small, since high bandwidth pulses (~10 kHz) were used optimized using the Shinnar Le Roux (SLR) algorithm. Without these optimizations the CSA effect would be considerably larger at higher field strengths (i.e. 3T). An expert user manually placed saturation planes around the prostate. A total of 10 VSS pulses were used in the manual placement, a limit imposed by the GE software version running on our scanner. The second acquisition employed the optimized CV-MRS technique with 20 VSS pulses followed by the standard PRESS excitation with TE/TR =130/1100 ms. Each 3D ^{1}H-MRSI acquisition used a 16x8x8 phase encode matrix, a nominal voxel size of 0.42 cm^3, a spectral bandwidth of 1000Hz, and 512 points. The total acquisition time for each scan was ~19 minutes. For all scans the thickness of the spatial saturation bands was 30 mm. Lastly, for each scan the water suppression was adjusted to pass a minimal amount of residual water, which was used as an internal reference for chemical-shift correction.

3.2.6. Post-processing

Postprocessing of the ^{1}H-MRSI data sets was performed using the SAGE (SAGE ver2007.1, Spectroscopy Analysis by General Electric, © 1998 General Electric) software platform with extensive use of the LCModel fitting package (LCModel Version 6.2, Dr. Stephen Provencher). Post-processing consisted of

several steps. Using LCModel automated routines, only minor phase correction was necessary. Further post-processing consisted of the application of a Gaussian spectral apodization filter (1.25Hz line broadening), and application of a spatial apodization filter (Fermi diameter=100%, Fermi transition width=50%), followed by a Fourier transformation to spatial and frequency dimensions. To fit signals in the frequency domain a modified LCModel package was employed for robust fitting of key metabolite signals in the prostate. The steps included specifying control parameters for special spectra, chemical simulation of the citrate multiplet (i.e. sptype='prostate'), and use of LCModel's robust lipid fitting routines. Further the automated referencing method was modified to include both the residual water and citrate peaks in the calculation of the cross-correlation function (CCF). The modifications resulted in good fits, and ratios of creatine, polyamines, choline with respect to citrate were calculated and presented in a table as part of the output file. Metabolites that fell within the spectral range of 0.6-3.85 ppm were fitted and for each fitted metabolite peak, the relative resonance area was calculated with an estimation of the goodness-of-the-fit quantified by the Cramer-Rao Lower Bound (CRLB) and quoted as a percent standard deviation (%SD). LCModel rejects spectra with poor baselines caused by contaminating artifacts or very poor water suppression. LCModel operates by analyzing voxels in series, which on a single processor may take up to 30 minutes to process for an entire prostate data set. Currently LCModel is running on a multiprocessor system, which has reduced our analysis time to less than 5 minutes per prostate. Lastly, only voxels within the ROI that contain at least 75% prostatic tissue were used for analysis.

3.2.7. Rejection Criteria

For all voxels analyzed, a set of rejection criteria were imposed to prevent further analysis of poorly fitted peaks. The first criterion was that all spectra must pass LCModel's built-in mechanism to reject voxels containing spectra with very poor baselines. These voxels are automatically rejected. The second criterion is based on signal-to-noise ratio (SNR). LCModel calculates the SNR of each voxel as the ratio of the maximum peak in the spectrum-minus-baseline over the analysis window to twice the RMS residuals. Spectra with a SNR of less than or equal to 2, as seen in Figure 3.4C, can return misleading fits and are rejected. Voxels where the SNR was between 2 and 10, see Figure 3.4B, returned reasonable fits. Voxels with an SNR greater than 10, presented excellent spectra, as seen in Figure 3.4A. The third criterion is based on the goodness-of-fit. The LCModel user manual suggests using a CRLB of 20% as a threshold or cut-off, based on work mainly performed in *in vivo* brain studies. As a point of investigation the spectra were analyzed over a range of CRLB's to determine a CRLB cut-off appropriate for prostate spectra, understanding that the quality of spectra from both prostate and brain differ significantly. Figure 3.5 presents an example of varying the CRLB over a range of values. For each technique, the total number of peaks meeting the rejection (i.e. choline, polyamines, creatine, citrate, lipids) are counted and compared.

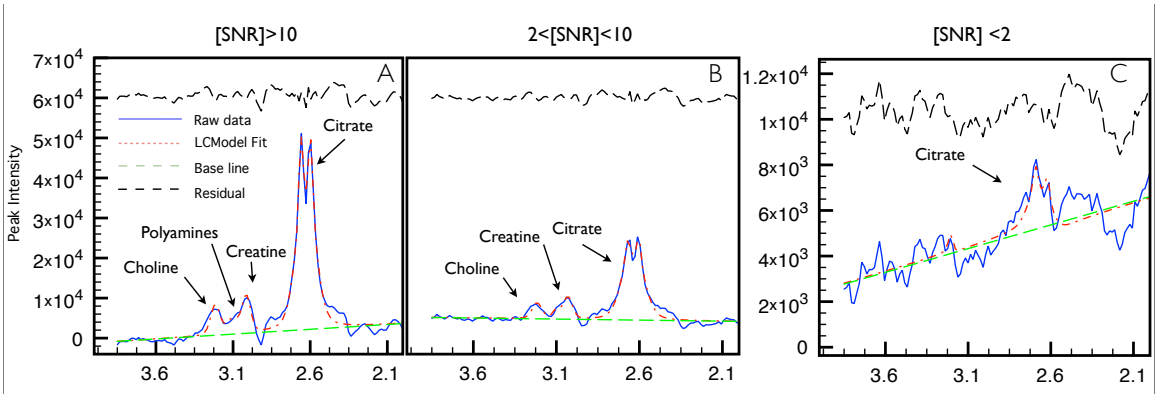

Figure 3.4 SNR and quality of spectra

In (A) typical prostate spectra with a SNR greater than 10 is shown. Even with a slight increase in noise, as seen in (B), the spectra are still well fitted. In comparison, to (C) where the SNR is less than 2, LCModel attempts to fit the noise, but the low SNR allows us to remove voxels containing spectra of this type.

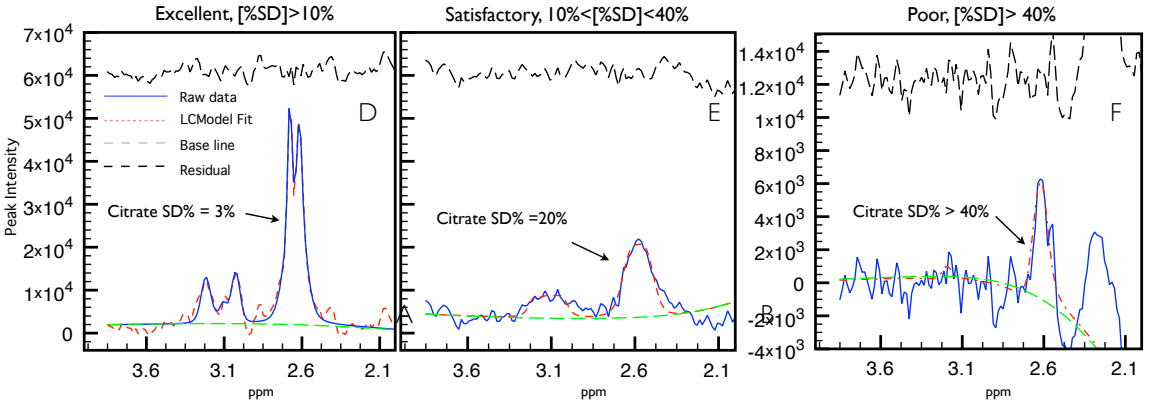

Figure 3.5 %SD and quality of spectra

Throughout the prostate, the quality of spectra obtained from an individual voxel may vary depending on the quality of the B_0-shim and contaminating artifacts .In (A), the presented spectra (zoomed to 2.0-3.85ppm) has a %SD less than 10%, indicating a very good fit to the simulated peak shapes, and is considered excellent. If the field homogeneity is slightly decreased one may still obtain spectra that are satisfactory. Spectra observed, as seen in (B), ranging between 10% and 40% are of satisfactory quality. Conversely, voxels that have been either partially excited, suffer from poor B_0.

3.2.8. Lipid Reduction

To determine the effectiveness of the CV-MRS technique in reducing peripheral lipid contamination, we calculate the *percent relative lipid reduction* between the CV-MRS and manual placement technique for both "inner" (prostate interior) and "outer" (prostate edge) voxels. This is calculated by the following formula:

$$\%\ \text{relative lipid reduction} = \left[1 - \frac{CVMRS_{lipids}}{Manual_{lipids}}\right] \times 100\% \qquad (3.2)$$

Where $CV\text{-}MRS_{lipids}$, and $Manual_{lipids}$ are the fitted areas determined by LCModel. An "inner" voxel is defined as a voxel containing 100% prostate tissue, while an "outer" voxel is defined as a voxel containing 75-99% prostate tissue. Voxels with less than 75% prostate tissue were excluded from analysis, for the purposes of this study.

3.3. Results

A large global reduction of peripheral lipid contamination was observed *in vivo* using the CV-MRS technique as compared to the manual technique. On average, the percent relative lipid reduction was 50±17%, when compared to the manual technique. The full range of percent relative lipid reductions are presented in Table 3.1. Over the entire prostate a range of reductions from 12% to 68% was observed. This is consistent with our phantom tests, which achieved a global lipid reduction of ~80% using the optimized CV-MRS technique when compared to the

standard technique. In both the outer and inner voxels, similar ranges of lipid reductions were observed. Comparing the lipid reduction observed in the whole prostate, the outer voxels, and the inner voxels, there was a consistent improvement. Comparing both inner and outer voxels, on average and within standard deviation comparable lipid reduction in the inner and outer voxels at 52±17% and 44±25%, was observed respectively. Among inner voxels, there is greater variation in the lipid reductions, ranging from 2% to 69% averaged over each prostate. Along the outer voxels we measured a range of reduction from 7% to 73%. In some individual voxels there were reductions greater than 95% along the periphery. This is illustrated in Figure 3.6, where the limitations of manual saturation plane positioning are illustrated. Inferior and superior slices (Figure 3.6E-H), typically show large lipid contamination when using the manual placement technique. These effects are effectively nulled using the CV-MRS technique, as seen in Figure 3.6I-L. The rolling baseline caused by large lipid signals, can distort metabolites severely and interfere with automated baseline correction, auto-phase adjustments, and eddy-current corrections used in robust fitting algorithms. To illustrate this effect and the usefulness of the CV-MRS technique, *in vivo* prostate data are presented in Figure 3.7. Use of the optimized CV-MRS technique resulted in reduced contaminating artifacts, and improved the quality of peaks of key metabolic markers as described below.

After implementing the rejection criterion outlined in the previous section, the number of high quality peaks obtained over the entire prostate was counted for both techniques. Table 3.2 presents the distribution of peaks that passed the

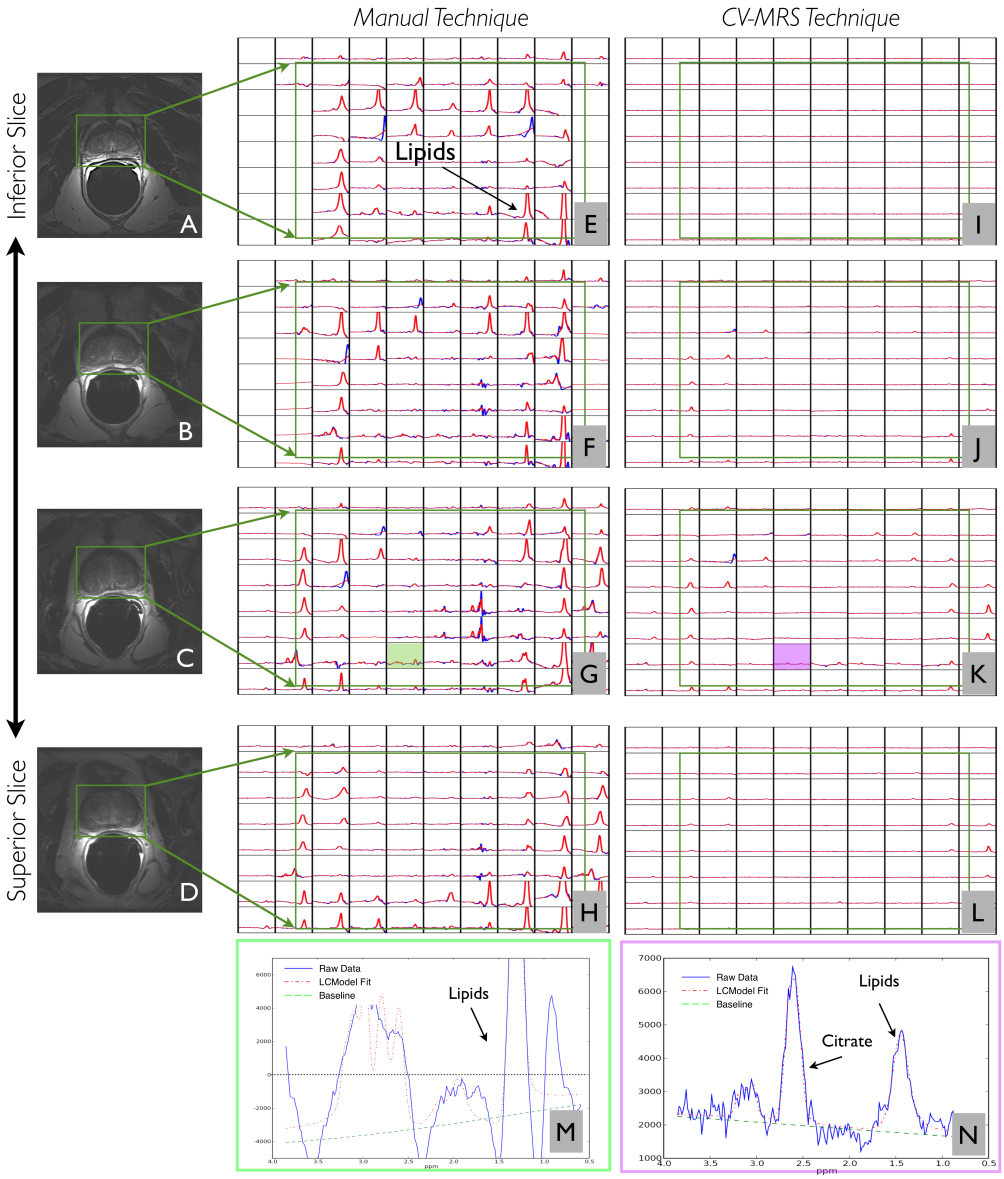

Figure 3.6 *In vivo* prostate spectra showing lipid reductions

In vivo data was collected for healthy volunteers. In A-D, the excitation region of interest (ROI) is outlined in cyan, which extends as a cube in three dimensions. Typically the excitation region is prescribed along the central slice, which makes two-dimensional graphical prescription of the ROI, and manual placement of spatial saturation planes very challenging. The resulting spectra acquired using manual placement of spatial saturation planes, shown in E-H, zoomed to 0-4ppm, reveal intense lipid contamination. The resulting spectra in I-L, zoomed into 0-4 ppm, demonstrate the massive global reduction of peripheral lipid signals for this subject. This clearly demonstrates the advantages of using the CV-MRS technique. Zooming into spectra directly along the periphery, as seen in (M) and (N), a greater than 95% reduction in lipid when using the CV-MRS technique is observed, and citrate that previously was undetectable is now observed.

rejection criteria test and the relative improvement for two cut-off values (%SD=20, and %SD=40) for all voxels within the prostate. The total number of peaks is calculated by summing the number of peaks for choline (Cho) at 3.22ppm, polyamines (Pa) at 3.11ppm, creatine(Cr) at 3.0ppm, and citrate (Cit) at 2.60ppm that satisfy the peak rejection criteria. To determine improvement based on spatial position, the number of acceptable peaks was examined in both the outer and inner voxel locations. At the CRLB of 40%, the improvement in the number of peaks increases by 66% and 61% for outer and inner voxels. On average the reduction in lipid at the periphery gave rise to an overall improvement in the quality of peaks throughout the prostate volume.

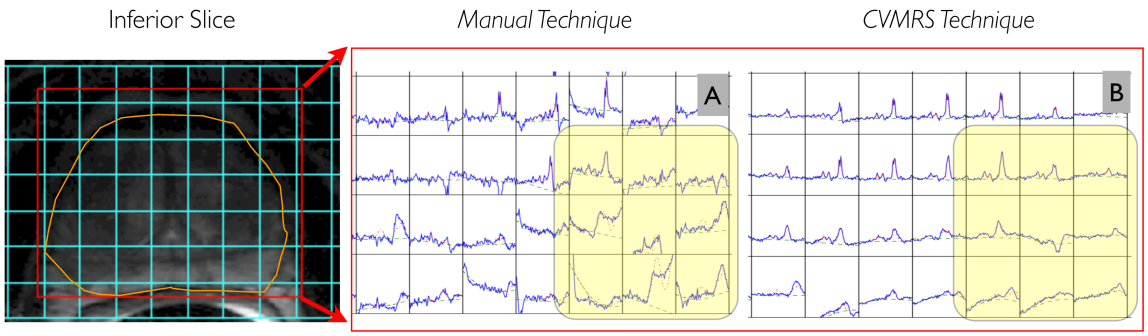

Figure 3.7 Improvement of baseline using CV-MRS
To illustrate the difficulty in acquiring spectra over the irregular shape of the prostate, spectra are presented from an inferior portion of the prostate close to the apex. The excitation region, when trying to cover the entire prostate, includes a significant amount of peripheral tissue. Using the manual placement technique, the region of spectra highlighted in yellow (A), zoomed to 4-0ppm, is highly contaminated and has caused major baseline distortions, incorrect phasing, and the fitting of metabolites. By reducing the lipids, as seen in (B), the quality of spectra has significantly improved.

Table 3.2

Distribution of the number of peaks that meet the rejection criteria using the Manual and CV-MRS technique for two different cut-off values

		Number of Peaks							
		SD <20%				SD < 40%			
		Outer		Inner		Outer		Inner	
Data Set	# of Voxels	Manual	CV-MRS	Manual	CV-MRS	Manual	CV-MRS	Manual	CV-MRS
1	89	6	11	23	29	14	20	39	50
2	94	12	10	21	19	23	24	62	55
3	51	1	1	0	2	6	6	8	10
4	47	14	25	8	18	32	44	16	33
5	58	3	22	8	41	7	37	15	74
6	28	5	8	6	9	7	11	14	16
7	43	6	11	3	14	14	26	8	24
8	60	3	6	11	22	8	12	29	43
9	117	13	22	47	78	22	44	86	147
10	168	9	13	42	86	25	31	90	142
11	45	12	25	9	24	18	42	21	38
12	50	7	12	20	32	15	21	36	51
Total	850	91	166	198	374	191	318	424	683
% Relative Improvement (out and inner)		82%		89%		66%		61%	
% Relative Improvement (total prostate)			87%				63%		

3.4. Discussion

Results from this study have demonstrated the clinical utility and robustness of using the CV-MRS technique for *in vivo* prostate ^{1}H-MRSI. Periprostatic lipids completely surround the prostate, making an optimal OVS scheme highly beneficial. In this work, the lipid contamination was reduced over the entire prostate by on average 50±17%. By reducing the lipid contamination, the baseline of the spectra was dramatically improved. As seen in Figure 7E-H, peripheral voxels can potentially be distorted when lipid contamination is present. In 3D ^{1}H-MRSI, this is a challenging problem since contaminating signal is coming from all

directions. Thus, it is reasonable to expect a stronger contaminating effect at the outer prostate regions, decreasing toward the center of the prostate. In this regard, a range of lipid reductions was observed from the peripheral regions towards the center, from 73% to 7%. By reducing the contamination along the peripheral region of the prostate, an average reduction of 52±17% reduction of lipid in the inner core region of prostate was achieved, with a range of 2% to 69%. Voxels as far in as 15mm can be affected by severe signal bleed-through, due to the point-spread function (PSF) effect. Application of the CV-MRS technique reduced lipid contamination from all three directions, decreased the baseline distortions and significantly improved fitting of the peaks in the spectrum. This is demonstrated in figure 7I-L, where it was observed there was an overall reduction in lipid contamination.

By removing the baseline distortions introduced from signal bleeding effects, it is reasonable to expect that the fitting of metabolites should improve as well. LCModel has been implemented for the robust fitting of prostate metabolites (i.e. citrate, creatine, polyamines, and choline), and as a standardized benchmarking tool to determine statistically significant differences between two techniques. When comparing the fraction of acceptable peaks that are found in the outer versus inner voxels, its observed that ~70% of acceptable peaks were found in the outer voxels. In Table 3.2, the distribution of peaks is presented for %SD at 20% and 40%. In each case, the number of acceptable peaks greatly improves when using the CV-MRS technique. At %SD less than 20%, the number of peaks improved by 82%

and 89% for both outer and inner voxels, and at %SD less than 40% the number of peaks improved by 66% and 61% in the outer and inner region.

The choice of an appropriate cut-off remains user-dependent, and is at the discretion of the expert user to make an interpretation of the data. Using a strict criteria, as used in this study, may not useful in all studies. The LCModel user manual recommends that a %SD equal to 20 be used as a threshold to eliminate poorly fitted peaks. Such a cut-off results in a reduction, as high as 50%, in the number of acceptable peaks. In many reports on prostate spectroscopic imaging, a wide range of methods have been used to determine whether or not a spectrum from a given voxel is useful. This can range from an expert review, using a combination of visual inspection on the basis of SNR data, line-width, and the presence of water- and lipid-induced baseline distortions (150), to the use of sophisticated fitting routines such as LCModel (151). We found that when the initial setup and configurations were met, LCModel can perform robust, rapid analysis of prostate spectra and allow the user to easily determine the quality of the spectra without time consuming visual inspection, an important feature when analyzing multi-voxel 3D ^{1}H-MRSI data sets. In this work we found that a %SD cut-off of 40% was reasonable in achieving good fits. Upon visual inspection, the quality of fits diminishes quickly for peaks with %SD greater than 40%.

The prostate gland was a useful clinical site to investigate the CV-MRS technique because of the large amount of periprostatic fat and the non-cuboidal shape of the prostate, which makes prescribing spatial saturations bands difficult. The conformal voxel technique presented here brings a different paradigm for

performing *in vivo* ^{1}H-MRSI in a clinical setting, based directly on the shape of the tissue of interest. On most clinical scanners, the ROI is prescribed by a box that surrounds the tissue of interest. Many anatomical structures are irregularly shaped. Thus, the utility of a technique that directly uses the shape of the tissue of interest becomes clinically relevant. The proposed technique removes user subjectivity in choosing the appropriate positions of saturation planes and the appropriate excitation box. In a recent review, Mountford *et al*. discusses the need for manufacturers to automate/optimize the many steps needed to perform a successful spectroscopic imaging exam (7, 152). Furthermore, Mountford *et al*. described the high level of technical expertise needed to perform spectroscopic exams and concluded that this was one of the pitfalls of the recently published American College of Radiology Imaging Network (ACRIN) prostate trial investigating the role of spectroscopic imaging for prostate treatment (153). Similar techniques are concurrently being investigated for studies of the whole brain (154, 155). These techniques use an algorithm with a longer computational time, and limited number of saturation pulses. In the implementation proposed here, the user can specify any number of saturation pulses. The introduction of the CV-MRS technique for 3D prostate ^{1}H-MRSI has dramatically reduced contaminating signals from peripheral tissue, while reducing the variability inherent in the manual placement of saturation bands.

A major challenge for ^{1}H-MRSI is that it requires a high degree of user expertise for execution of a successful scan and interpretation of the data. Manufacturers have commercially available packages that have seen success in

obtaining clinically useful data (14, 22, 23, 47, 156, 157). To our knowledge these packages do not yet have an automated method for saturation plane placement. These packages use a combination of spectral-spatial, BASING, or MEGA-pulses which are used for the suppression of lipids detected from the voxel. However these techniques are restricted to longer echo times. In contrast, the OVS style of lipid suppression permits prostate spectroscopy at short echo times, with good preliminary results (158).

A limitation of this work was the comparison to a standard PRESS acquisition with manually placed spatial saturation bands, as opposed to a prostate-specific acquisition utilizing BASING or MEGA-pulses. Despite this challenge, the CV-MRS demonstrates good promise as an automated technique for prescription of the excitation voxel and placement of spatial saturation bands in spectroscopic images. Recent work by Henning *et al*. (159, 160), showed that further optimizations to the flip-angles of the spatial saturation pulse could additionally reduce unwanted peripheral lipid signal without interfering with metabolite signals. These optimization schemes are being considered in future development of this technique.

3.5. Conclusion

In summary, the application of the conformal voxel magnetic resonance spectroscopy (CV-MRS) technique to obtain *in vivo* ^{1}H-MRSI data for the prostate has been presented. The method employs a user-defined number of automatically positioned VSS pulses (20 in the current work) that null signal from periprostatic lipids while closely conforming the shape of the excitation voxel to the shape of the prostate. In this technique, the ROI of the prostate is directly used to determine the spatial position and orientation of the VSS pulses. Results of this implementation demonstrate a dramatic decrease in lipid contamination in voxels throughout the prostate. To determine the efficacy of the technique, the number of fitted peaks was compared using a modified version of LCModel. Using a Cramer-Rao Lower Bound of 40%, we observed a 63% improvement in the number of fitted peaks over all 850 voxels analyzed. The CV-MRS technique presents a different paradigm for prescribing an ROI for spectroscopic study with potential applications to many other anatomical sites.

Chapter 4

Short echo time *in vivo* prostate ^{1}H-MRSI

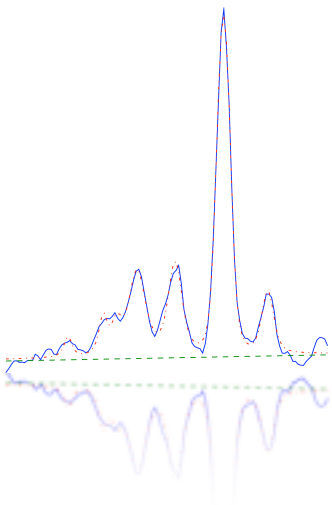

In this chapter a robust method to improve the quality of in vivo prostate MRSI data by utilizing an optimized conformal voxel technique coupled with a spectral-spatial excitation PRESS pulse sequence for short echo time acquisitions is presented. In vivo implementation of this optimized MRSI technique confirmed the reduction in peripheral lipid contamination, and improved spectral quality throughout the prostate. This technique provides significant signal-to-noise improvement and the ability to reveal short TE metabolites to potentially improve prostate cancer detection.

A portion of this chapter has been accepted for publication:
Venugopal et al., Short echo time in vivo prostate ^{1}H-MRSI. Journal of Magnetic Resonance Imaging. 2011:In press.

4. Short echo time *in vivo* prostate ^{1}H-MRSI

4.1. Introduction

Magnetic resonance imaging (MRI) of the prostate continues to grow as a clinically useful tool in the assessment of prostate cancer, with active research and development at many centers over the last decade (125, 130, 134, 161-166). The combination of an internal endorectal coil and an external phased-array coil has demonstrated increased signal intensity over the prostate volume with superb spatial resolution (167). This improvement in signal and spatial resolution has resulted in unsurpassed anatomical imaging of the prostate and surrounding soft tissues. In parallel, improvements in proton magnetic resonance spectroscopic imaging (^{1}H-MRSI) of the prostate have provided spatial maps of the biochemical variation within diseased prostate tissue (125, 162, 168-170). ^{1}H-MRSI can detect changes in tissue biochemistry that can be assessed by observing significant deviations in the relative concentrations of metabolic markers such as choline-containing metabolites (Cho), creatine (Cr), polyamines (Pa), and citrate (Cit). It is well established that prostate cancer is associated with reduced levels of citrate and increased levels of choline, which are both detectable *in vivo* with ^{1}H- MRSI (171).

On most current clinical MR systems (both 1.5T and 3T), highly specialized pulse sequences incorporating water suppression, lipid suppression, and outer-volume suppression are used for robust collection of multi-voxel spectroscopic

acquisitions. Most centers use a variation of the point resolved spectroscopy pulse sequence, or PRESS pulse sequence, which has the general form of 90 – τ_1 – 180 – τ_2 – 180 – (τ_2 -τ_1), where an appropriate echo time (TE) is chosen (i.e. TE = 2×τ_2 =130ms), such that the phase of the spin-coupled citrate-multiplet structure is optimized.

The timing of the PRESS pulse sequence, to achieve the optimal line shape of citrate, has been well examined in the literature (21, 23, 29, 31). The spectral shape of the four methylene protons in the citrate multiplet, at 1.5T and 3T, is described by a strongly coupled AB-type system where the spin-spin coupling constant J and the chemical shift difference δ, are of the same order of magnitude at these field strengths. Centered at 2.6ppm, the spectral-shape of the citrate multiplet strongly depends on the timing of the PRESS sequence. In general, timing parameters in the PRESS sequence (i.e. τ_2 and τ_1) are adjusted such that there is maximum signal of the inner multiplet peaks versus the outer peaks since the outer multiplet resonances overlap with other nearby resonances (i.e. creatine at 3.02 ppm). Quantum mechanical simulations have been used to calculate the appropriate timing of the PRESS sequence to determine the optimal spectral shape for citrate (21, 23, 29, 31). Wilman *et al*. specifically looked at the response of the strongly coupled citrate system to the PRESS localization sequence, and determined change in signal intensity with varying echo times and fixed τ_1. This theoretical prediction is presented in Figure 4.1A, where the normalized signal intensity is plotted with increasing echo time. Wilman *et al*. showed that the signal intensity of the strongly coupled citrate system decays as a damped sinusoidal function with increasing

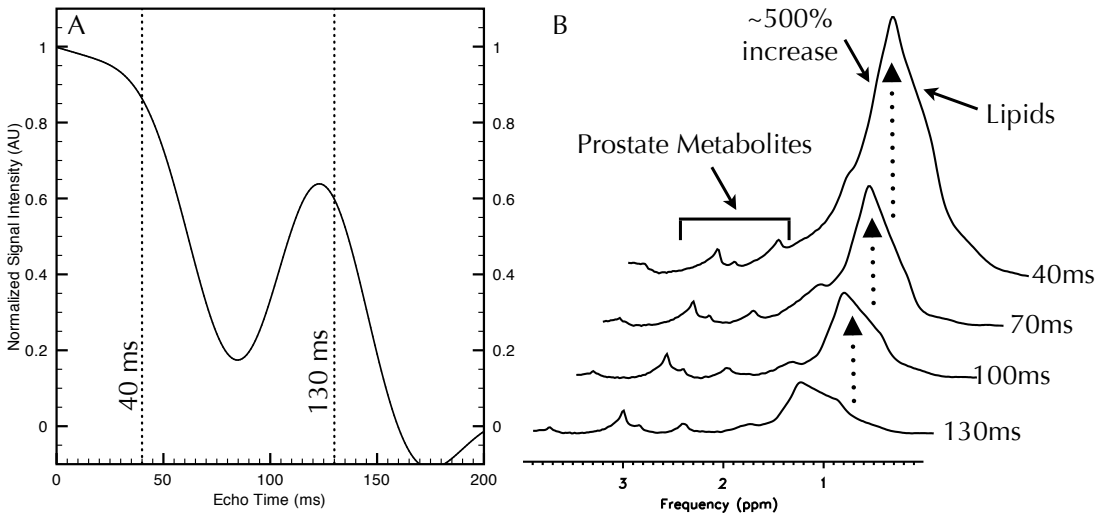

Figure 4.1 Echo time dependance for citrate and lipids
In Figure 4.1A, a quantum mechanical simulation of the normalized signal intensity of the strongly coupled citrate multiplet is shown. To minimize lipids, and to reach an optimal signal and phase of the spectrum, an echo time of 130ms is typically chosen in most ^{1}H-MRSI experiments. Reducing the echo time (i.e. less than 50ms) results in improved SNR but at the expense of increased lipid contamination signal, as seen in 4.1B. The signal intensity of the lipids can increase to as high as ~500%, causing massive baseline distortions resulting in poor fitting of metabolite peaks.

echo time. This variation in signal intensity makes it challenging to choose an appropriate echo time, especially when observing the dips in the signal intensity at TE's of 85 and 175 ms. In *in vivo* ^{1}H-MRSI, an echo time is chosen which gives optimal signal intensity and phase with respect to the nearby metabolites and contaminating artifacts caused by lipids (1.2 ppm). Ideally, a very short echo time would be chosen to detect metabolites with both short and long T_2 values, and to maximize signal intensity. However, by decreasing the echo time, the signal intensity from neighboring lipid resonances increases greatly. The increased lipid signal intensity has the potential to severely distort the spectral baseline and obscure detection of metabolites needed for spectral analysis. This is illustrated in Figure 4.1B, where it is observed that when decreasing the echo time from TE=130

ms to TE=40 ms, signal intensity from the lipids can be increased by as much as ~500%. Thus, it becomes a challenge to balance the echo time and timing parameters of the PRESS sequence to maximize signal intensity of citrate while minimizing the artifacts created by nearby lipid resonances.

The effective suppression of periprostatic lipid signals to reduce contaminating artifacts is vital for obtaining good spectroscopic data from *in vivo* prostate MRSI for long and short echo time acquisitions. To facilitate optimal coverage of the prostate, we previously presented an outer volume suppression technique, called conformal voxel MRS (CV-MRS) (97, 118), which automatically optimizes the placement of numerous spatial saturation planes to adapt the excitation volume to the shape of the prostate. Employing an offline program, the CV-MRS algorithm uses the acquired prostate MR images to calculate the slice positions and rotations of the spatial saturation planes, as well as the location and size of the PRESS excitation voxel. In addition, the program performs two further optimizations: (1) modification of the flip angle of each spatial saturation pulse to account for T_1 regrowth, and (2) temporal re-ordering of the spatial saturation planes to minimize the impact of overlapping planes. Together, these optimizations have resulted in reduced lipid contamination in prostate MRSI. Previous results showed very effective lipid suppression over all subjects(118, 172). By reducing the contaminating lipid, the overall baseline of the spectra improved, resulting in better fitting of key metabolites (i.e. citrate, choline, creatine, and polyamines) used in assessing normal and malignant prostate tissue. To assess the improvement of employing the CV-MRS technique we performed a voxel by voxel comparison

between the commercially available MRSI technique versus the CV-MRS approach which showed a large improvement in the number of fitted metabolite peaks over the whole prostate.

In this study, we report on the application of a modified PRESS sequence that utilizes the CV-MRS technique in combination with a spectral-spatial 90 degree RF excitation pulse. A combined endorectal-phased array coil was used to record data from the prostates of healthy volunteers using both single voxel ^{1}H-MRS and 3D ^{1}H-MRSI acquisitions. We demonstrate that high quality spectra can be obtained by reducing the echo time to 40ms, while maintaining optimal signal intensity of the citrate multiplet and detection of short TE metabolites (i.e. myo-inositol, scyllo-inositol, taurine, glutamine/glutamate), while also minimizing lipid artifacts. Additional acquisitions were obtained at an echo time of 130 ms using manual saturation band placement and compared to the CV-MRS method.

4.2. Materials and Methods

4.2.1. Volunteers

Subjects were recruited to this study as part of an ongoing study being performed at the Winnipeg Health Sciences Centre, in conjunction with the National Research Council Institute for Biodiagnostics (NRC-IBD), and CancerCare Manitoba, with full approval from the local research ethics boards. Informed consent was obtained from 10 healthy volunteers who participated in this study. Each volunteer was screened to meet the inclusion criteria of the study: healthy,

with no prior history of genitourinary disease, and no abnormalities under digital rectal examination. The ages of the subjects ranged from 25 to 69 years of age, with a mean age of ~50 years.

4.2.2. MR Imaging

MRI examinations were performed on a General Electric 1.5T Signa MR scanner outfitted with Echospeed gradients. For improved reception of signal, a standard disposable endorectal coil (Medrad, Pittsburg, PA) was used. The endorectal probe was inflated with approximately 75ml of FC-77 FLUORINERT, a perfluorocarbon compound (PFC) (3M, St. Paul, MN, USA). This ensured that the coil was firmly placed against the prostate. Using the PFC compound significantly reduced magnetic susceptibility artifacts and improved B_0 homogeneity throughout the prostate volume(148). Prior to clinical imaging of the prostate, a scout scan in three orthogonal planes was acquired to ensure that the coil was not rotated, and was placed directly beneath the prostate achieving maximum surface coverage of the prostate. Following this, axial T_2 weighted images of the entire prostate gland were acquired using a fast spin-echo imaging sequence (TE/TR=102/5000ms; matrix size =256x256; field of view= 140 mm; slice thickness=3 mm).

4.2.3. ^{1}H-MRS single voxel measurements with varying echo time

In a single subject we collected ten single voxel spectra at varying echo times using the CV-MRS method. In this experiment, we used a voxel size of 20x20x20 mm^3, TR=1100 ms, Spectral Width=1000Hz, 512 pts, 128 scans, and 2 averages. The voxel was placed in the central zone of the prostate to avoid unwanted lipid contamination. The data was collected at echo times of 40, 50, 65, 80, 95, 110, 130, 150 and 170 ms. To demonstrate the efficacy of the CV-MRS technique, one more single spectrum at 130 ms was collected without the CV-MRS technique (i.e. using manual placement of spatial saturation planes). For each single voxel acquisition, 8 unsuppressed water scans were collected for internal water referencing.

4.2.4. ^{1}H-MRSI measurements using three methods

The PRESS pulse sequence was modified to include the CV-MRS technique. The modified PRESS is presented in Figure 4.2. To perform a relative comparison, *in vivo* prostate spectra were obtained using three different acquisition methods: 1) manually placed spatial saturation bands and PRESS with TE/TR =130/1100 ms; 2) CV-MRS and PRESS with TE/TR =130/1100 ms; 3) CV-MRS and PRESS with spectral-spatial excitation with TE/TR =40ms/1100 ms. The properties of the spectral-spatial pulse were: true nulling (in contrast to opposed nulling), a frequency offset of -120 Hz (with water at 0 Hz), a nulling frequency of 110 Hz (placing nulling points at 0 Hz-Water, and 220 Hz-Lipids), a spectral bandwidth of

90 Hz, a spatial bandwidth of 1750 Hz, with 4 trapezoidal gradient cycles leading to a total pulse width of 18.2 ms. Each 3D MRSI acquisition used a 16x8x8 phase encode matrix, with a nominal voxel size of 0.42 cm^3, and an acquisition time of 19 minutes. For all spectroscopic imaging scans the width of the spatial saturation bands was 30 mm. For post-processing frequency corrections the water suppression for each scan was adjusted to retain a small amount of residual water.

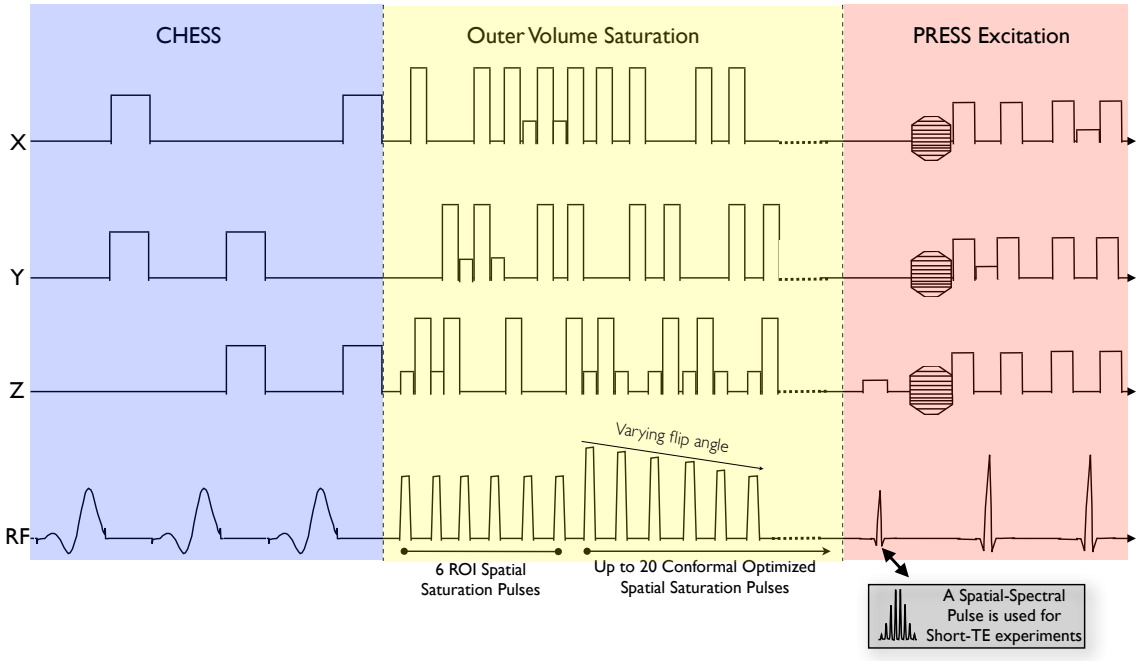

Figure 4.2 Modified pulse sequence with spectral-spatial pulse
The product PRESS pulse sequence was modified to include an extended number of automatically placed VSS pulses (up to 20). The current pulse sequence was designed to interchange RF pulses 'on–the-fly'. For short echo time acquisitions, a spectral-spatial 90 degree RF pulse was used. In this diagram the vertical and horizontal axis are not to scale.

4.2.5. Post-processing

4.2.5.1. Single and multivoxel analysis

Comprehensive and robust analysis of the spectra was achieved using LCModel (173), a dedicated spectral fitting software. LCModel was used to simulate the key prostate metabolites (i.e. citrate, choline, etc.) and for its sophisticated lipid fitting routine. This fitting package was modified specifically for analyzing *in vivo* prostate spectra at long and short TE's. The SAGE software platform (SAGE ver2007.1, Spectroscopy Analysis by General Electric, © 1998 General Electric) was used to display the data before inputting it into LCmodel. The automated referencing method was modified to include both the residual water, choline, creatine, and citrate peaks in the calculation of the cross-correlation function (CCF). After this procedure, usually only minor phase correction was necessary. Further post-processing consisted of the application of a Gaussian spectral apodization filter (1.25Hz line broadening), and application of a spatial apodization filter (Fermi diameter=100%, Fermi transition width=50%), followed by a Fourier transformation to spatial and frequency dimensions. Ratios of creatine (Cr), polyamines (PA), choline (Cho), myo-inositol (mI), scyllo-inositol (sI), taurine (Ta), and glutamine/glutamate (Glx) with respect to citrate were calculated and presented in a table as part of the output file. Only voxels that fell within the spatial excitation region corresponding to the prostate and containing at least 75% prostate tissue were analyzed. Metabolites that fell within the spectral range of 0.6-3.85ppm were fitted using LCModel. An estimate of the goodness-of-fit of each

metabolite quoted by the Cramer-Rao Lower Bound (CRLB) and quoted as a percent standard deviation (%SD) was recorded. Rejection criteria for the spectral fitting included LCModel's built-in poor baseline estimates (due to contaminating artifacts or very poor water suppression) as well as a percent standard deviation threshold of 40% in order to reject poorly fitted peaks. Additionally, spectra that had an SNR less than 2 were removed to help eliminate poor spectra from the analysis. LCmodel analysis was performed on a multi-processor system that accelerated analysis of each prostate data set. The average time of analysis for each prostate data set was less than 5 minutes. A total of 775 voxels were analyzed.

4.3. Results

Spectra were obtained using both single voxel and multi-voxel techniques to demonstrate the efficacy of obtaining high quality spectra at short echo times. The pulse sequences for both single ^{1}H-MRS and 3D ^{1}H-MRSI acquisitions were modified to include the CV-MRS method, and the spectral-spatial 90 degree RF excitation pulse.

4.3.1. ^{1}H-MRS single voxel measurements with varying echo time

Ten single voxel prostate spectra were obtained from a 43 year old healthy male. The voxel was placed in the central zone, as seen in Figure 4.3A. In Figure 4.3C, nine spectra acquired at echo times varying from TE=170ms to TE=40ms are

presented. The spectra demonstrate the expected variations of phase of the outer-lines in the citrate multiplet, due to the spin-spin coupling effect. More importantly, using the CV-MRS technique helped control the lipid contamination even at a relatively short echo time of 40ms. By decreasing the echo time, a 57% improvement in SNR between spectra acquired at TE=130ms and TE=40ms was measured. Additionally we clearly resolve other short TE metabolites demonstrated by Heerschap *et al*. in previous studies[24]. To illustrate that the CV-MRS technique does not negatively affect the spectral intensity or line-shapes of the metabolite peaks, a tenth spectrum was acquired without the CV-MRS technique. This spectrum was collected at TE=130ms and is shown in Figure 4.3B alongside a spectrum collected using the CV-MRS technique at the same echo time. Both spectra have comparable SNR and spectral resolution. The spectrum obtained using the CV-MRS technique has 90% less lipid contamination when compared to the spectrum acquired with manually positioned spatial saturation bands.

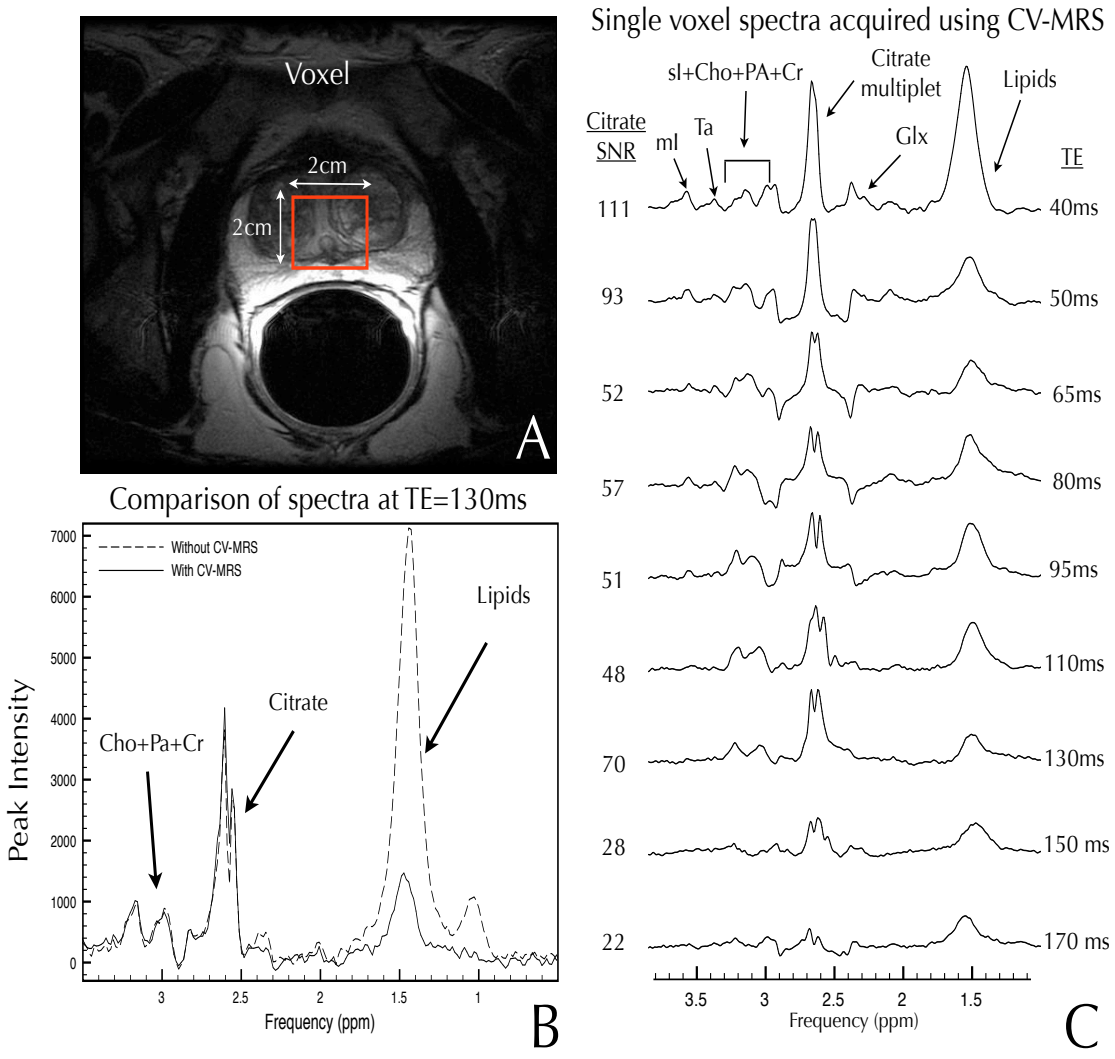

Figure 4.3 J-modulation of citrate with varying echo time

Single voxel spectra were obtained from a 43-year old male with a healthy prostate, and no prior prostate conditions. A 20x20x20mm^3 voxel was placed in the central zone of the prostate, see Figure 4.3A. Two spectra acquired with and without the CV-MRS technique are shown in Figure 3B demonstrating no change in key prostate metabolites. In 4.3C, nine in vivo spectra at varying TE demonstrate minimal baseline distortions, and well-resolved peaks. By decreasing the echo time to 40ms, and controlling the lipids the full citrate multiplet is observed, in addition to myo/scyllo-inositol, taurine, polyamines, and glutamine/glutamate. (citrate-Cit, creatine-Cr, polyamines-PA, choline-Cho, myo-Inositol-mI, scyllo-Inositol-sI, taurine-Ta, glutamine/glutamate-Glx).

4.3.2. ^{1}H-MRSI measurements using three methods

A comparison of the three ^{1}H-MRSI acquisitions – 1) manually placed spatial saturation bands and PRESS with TE=130ms; 2) CV-MRS and PRESS with TE=130ms; 3) CV-MRS and PRESS with spectral-spatial excitation with TE=40ms – is shown in Figure 4.4 demonstrating the progressive improvement in spectral quality. Figure 4.4 (A) illustrates spectra obtained using manually placed saturation planes at an echo time of 130ms. Many voxels throughout the inferior and superior portions of the prostate suffer from massive lipid contamination. In Figure 4.4 (B) the same voxels are presented but acquired using the CV-MRS technique at the same echo time. Lipid contamination artifacts were greatly reduced, confirming previous work [25]. Lastly in Figure 4.4 (C) spectra acquired at an echo time of 40ms utilizing the CV-MRS technique and spectral-spatial pulse to help further remove unwanted lipids clearly demonstrate the full citrate multiplet structure which correlated with quantum mechanical simulation, as well as significant improvements in SNR[19, 26]. In addition we detected several other short TE metabolites, such as myo-inositol, scyllo-inositol, taurine, and glutamine/glutamate (Figure 4.4C). Zooming into a single spectrum along the peripheral zone, a clear improvement in spectral quality is seen when comparing the three acquisitions (Figure 4.5 A-C) – a large reduction in lipid signal, an improvement in the spectral baseline, improved spectral resolution, high quality LCmodel fits (see Figure 4.5 D), and an overall improvement in SNR.

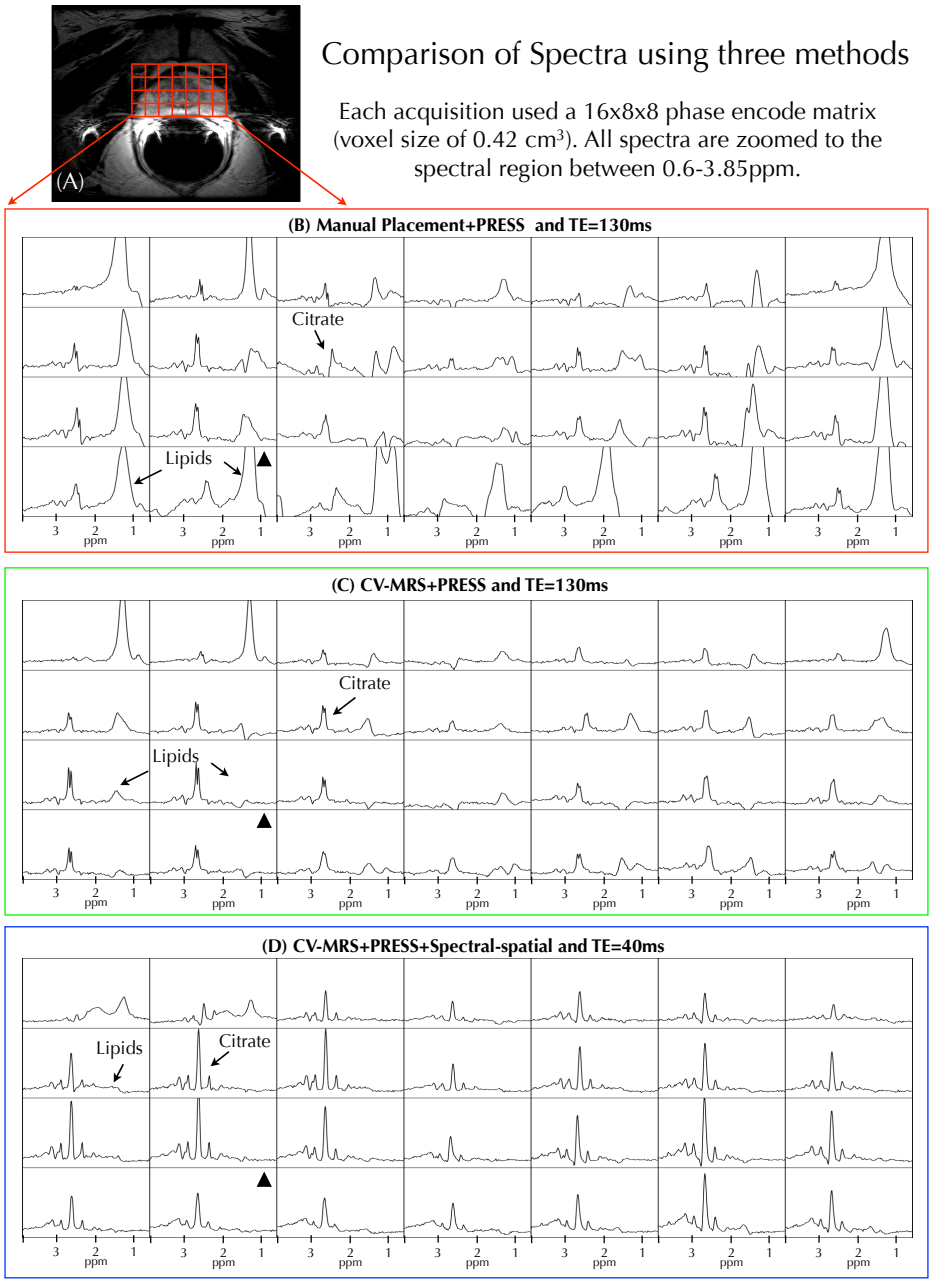

Figure 4.4 Improvement of ^{1}H-MRSI at short echo times

In vivo MRSI data (A) was collected from a 61 year old healthy volunteer close to the superior region of the prostate using all three MRSI techniques – (B) manually placed spatial saturation bands and PRESS with TE=130ms; (C) CV-MRS and PRESS with TE=130ms; (D) CV-MRS and PRESS with spectral-spatial excitation with TE=40ms. In (B) the spectra acquired by manually placing the spatial saturation planes over the entire prostate suffer from massive lipid contamination. In (C) spectra acquired using the CV-MRS technique show dramatically reduced lipid contamination. Employing the short TE acquisition technique (D) provides superior quality spectra, with minimal lipid artifacts and improved signal-to-noise.

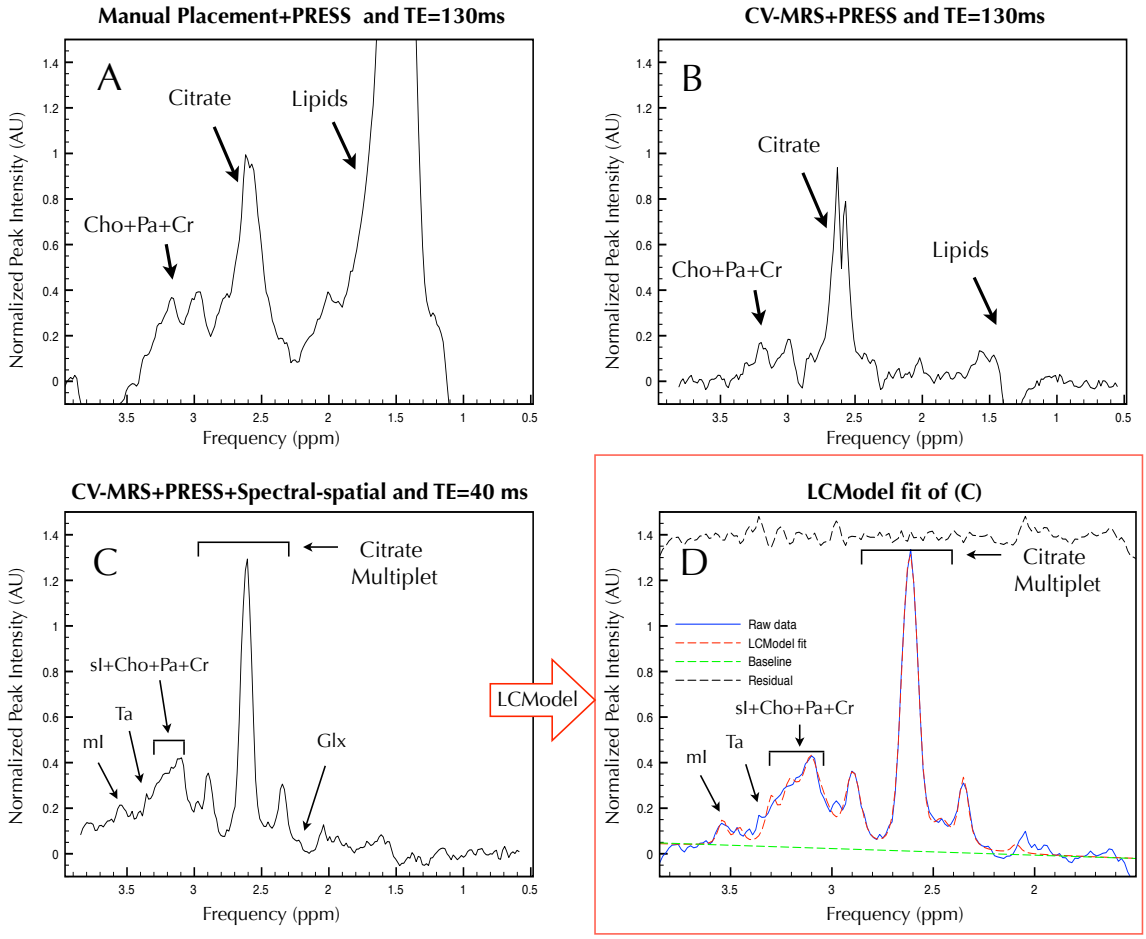

Figure 4.5 Improvement of ^{1}H-MRSI in the peripheral zone

Zooming into a single voxel along the peripheral zone (voxel marked "▲" from Figure 4) the progressive improvement of spectra quality using each technique is illustrated (A-C). In (C) the citrate multiplet is visualized with improved signal-to-noise as well as complete removal of contaminating lipids at 40ms. In addition, short TE metabolites are detected, including inositol, taurine, polyamines, and glutamine/glutamate. (citrate-Cit, creatine-Cr, choline-Cho, inositol-In, taurine-Ta, glutamine/glutamate-Glx). The spectrum from (C) is shown in (D) along with the LCModel fit and minimal residual signal. The citrate in spectrum (A) has been normalized to unity. Each other spectrum is normalized to (A).

In Table 4.1, the number of peaks that meet the rejection criteria using the CV-MRS technique alone at TE=130ms and the combined CV-MRS with spectral-spatial pulse at a TE=40ms are shown. Examining the number of acceptable peaks of the key metabolite groupings (i.e. Cit), we observe a 35% improvement in the number of peaks. Furthermore, in Table 4.1B we show our results from our data at short echo times. Our analysis, while using the same rejection criteria, revealed a large number of short TE metabolites that were previously undetectable at longer echo times. These include the myo-inositol, scyllo-inositol, taurine, and glutamine/ glutamate groups.

Overall, we have observed an improvement in the number of metabolite peaks when comparing the longer to shorter echo time acquisitions. This has also resulted in increased citrate detection. Taking into account the changes in citrate line-shape between long and short echo times, we calculated a relative improvement in the citrate spectral intensity between successive acquisitions. In Table 4.2, the normalized percent relative improvement of the detection of citrate within the prostate volume using both techniques is presented. On average we observe a 42±24% relative improvement in detection of citrate over the entire prostate volume, with a range of improvements from 16% to 100%.

Table 4.1

Number of fitted metabolite peaks using LCModel with %SD less than 40%

(A) Acquired using the CVMRS technique (TE=130ms)										
Data Set	Number of Voxels	Cit	PA+Cr	Cho+Cr	Cho+PA+Cr	mI	Ta	sI	Glx	sI+Cho+PA+Cr
1	42	13	7	15	17	-	-	-	-	-
2	62	42	37	36	44	-	-	-	-	-
3	83	57	40	38	51	-	-	-	-	-
4	61	39	6	15	20	-	-	-	-	-
5	138	117	75	77	92	-	-	-	-	-
6	196	135	59	89	109	-	-	-	-	-
7	57	35	31	24	42	-	-	-	-	-
8	64	48	23	27	30	-	-	-	-	-
9	72	34	31	31	40	-	-	-	-	-
Total	775	520	309	352	445					
(B) Acquired using the Short TE technique (TE=40ms)										
Data Set	Number of Voxels	Cit	PA+Cr	Cho+Cr	Cho+PA+Cr	mI	Ta	sI	Glx	sI+Cho+PA+Cr
1	42	17	10	7	12	5	5	7	9	15
2	62	58	38	23	42	17	18	30	27	44
3	83	75	47	41	57	39	31	49	25	64
4	61	60	26	35	45	31	19	36	30	49
5	138	136	95	78	110	39	36	83	68	104
6	196	170	91	92	131	76	71	114	67	148
7	57	53	39	33	47	12	17	25	29	40
8	64	64	42	21	49	20	17	29	26	48
9	72	68	36	29	44	24	19	34	42	49
Total	775	701	424	359	537	263	233	407	323	561

Table 4.2

Relative improvement in the number of voxels that contain detectable citrate

	% of total prostate volume with detectable Citrate (%)		
	Acquisition Method		
Data Set	CV-MRS (TE=130ms)	Short TE (TE=40ms)	Normalized Percent Relative Improvement (%)
1	33	43	31
2	63	87	38
3	60	78	32
4	67	103	54
5	81	94	16
6	67	84	26
7	56	85	51
8	74	98	33
9	50	100	100
Average	61±14	86±18	42±25

4.4. Discussion

The accurate and robust measurement of metabolites in prostate spectroscopy is key for biochemical assessment of normal versus malignant tissue. MRSI is a technique that is very technically demanding, and requires expert knowledge in clinical and physical aspects of data collection and analysis [27]. Several centers have successfully performed prostate MRSI and investigated its use for diagnosing prostate disease, but the quality and analysis of the results vary from center to center (31, 47, 125, 134, 157, 170, 174, 175). Thus, there is still a need to improve on the technical aspects of data collection and automated analysis.

Our initial *in vivo* work demonstrated improved lipid suppression and an average lipid reduction of 60±18% over the entire prostate volume when using the CV-MRS technique at long echo times (i.e. TE=130 ms) (118). This significant improvement led to an improved baseline and easily visualized spectra throughout the prostate. In this work we demonstrated that severe signal bleeding from peripheral voxels containing high amounts of periprostatic lipids can clearly be a problem, as illustrated in Figure 4.5 A. The effect of optimally suppressing peripheral lipid results in superior fitting and identification of metabolite peaks as seen in Figure 4.5B. By effectively nulling contaminating lipids, we demonstrated that short TE acquisitions are possible with good results. As seen in Figures 4.4C and 5C, the citrate multiplet structure can be clearly visualized with a significant improvement in SNR. As well, other short TE metabolite such as myo-inositol, scyllo-inositol, taurine, glutamate/glutamine, and polyamines are also detected. By comparing the number of fitted peaks (CRLB < 40%) we observed a 35%

improvement in number of peaks comparing long and short TE acquisitions. Furthermore, by utilizing a spectral-spatial 90 degree RF excitation pulse and reducing our TE to 40 ms, we have improved citrate detection, and detected short TE metabolites.

To date, there are very few investigations that have examined the feasibility of acquiring 3D-MRSI at reduced echo times to study short TE metabolite structures in the prostate. Most of the work that has been done was performed using two-dimensional J-resolved techniques (35, 176, 177), and using high field proton high resolution magic angle spinning (HR-MAS) techniques (178-181). This has been mainly due to limitations in timing parameters available in most commercial pulse sequences, the challenge of controlling lipid contaminating effects while reducing echo times, and limited access to large bore-high field systems to acquire high resolution spectra similar to that found using HR-MAS techniques. These techniques, despite having distinct spectral advantages, such as improved spectral separation of metabolites, and superior line-widths are not feasible for routine clinical use.

We demonstrated in Figure 4.1 that lipids can increase by up to ~500% when approaching shorter echo times. In this work we have overcome these challenges by utilizing the CV-MRS technique for optimized outer volume suppression, and using a PRESS sequence with a spectral-spatial 90 degree RF excitation pulse scheme. This scheme uses two traditional Shinnar Le Roux (SLR) optimized 180 degree pulses whose pulse duration and timing allow for shorter echo times (182). Our *in vivo* results presented in Figure 4.4C, have clearly

demonstrated the feasibility of acquiring high quality spectra at short echo times. Further, the additional benefit of using a modified LCmodel kernel for automated analysis has helped improve fast (less than 5 minutes per prostate on a multiprocessor system) and robust measurement of short TE metabolites such as myo-inositol, scyllo-inositol, taurine, and glutamine/glutamate. The reduction in lipids near 1.2 ppm may also help improve measurements of the polyamine groups located at 2.1 ppm.

The role of metabolites found in the prostate has been well studied (125, 126, 134, 180, 183, 184). It is well accepted that in the diagnosis of prostate cancer, citrate, choline, creatine and polyamines are the primary metabolites used to determine whether or not a portion of prostate tissue is suspected to be cancerous(6). In our study of healthy volunteers, we have shown that the proposed method has improved the overall detection of citrate by 42±24% over the entire prostate volume. This improvement ranged from 12-100% over all subjects. The large variation was dependent on the increased number of higher quality spectra, improved signal intensity, and the full citrate multiplet observed at short echo times. This significant enhancement has potential to help in the diagnosis of prostate conditions, especially in the inferior and superior regions, where spectroscopic imaging is challenging to perform. Additionally, previous high-resolution HR-MAS studies by Swanson *et al*. showed that the key metabolite scyllo-inositol was shown to increase in regions of cancerous tissue. The results presented in Table 4.1, have demonstrated that acquisition strategies employing the CV-MRS at short echo times can be used to make reliable measurement of the clinically significant short TE

metabolites, like scyllo-inositol, as well other metabolites. While this study has shown some initial promise, an extensive study examining a larger cohort of subjects, including prostate cancer patients, would be needed to examine the full potential of using a short TE acquisition strategy.

The use of the CV-MRS in combination with a spectral-spatial 90 degree RF excitation pulse at short echo times has improved the MRSI acquisition at 1.5T. Consequently by reducing the echo time we have also improved the SNR over all subjects. Using the short echo acquisition technique we improved the number of acceptable spectra in the superior and inferior portions of the prostate. The improvement in SNR corresponds to theoretical expectations described by Wilman *et al.*, in that voxels acquired at a short echo time demonstrated increased SNR compared to long echo time acquisitions(21). Lastly, using CV-MRS in combination with spectral-spatial excitation may provide an alternate method to explore short echo time acquisitions at higher fields.

4.5. Conclusion

In summary, we have developed a technique which utilizes the CV-MRS technique and spectral-spatial 90 degree RF excitation pulse for short echo time (TE=40ms) acquisition of 3D MRSI data in the prostate at 1.5T with the use of an endorectal coil. Using a modified version of LCModel we consistently measured short TE metabolites throughout the prostate (i.e. myo-inositol, scyllo-inositol, taurine, glutamine/glutamate). Furthermore, we significantly improved the number and quality of the spectra by 35% at a shorter echo time (TE=40ms) when

compared to longer echo times (TE=130ms). Furthermore, spectra throughout the prostate demonstrated better SNR and improved baseline. On average the detection of citrate throughout the prostate was improved by 42±24% using the modified technique, demonstrating the potential for clinical efficacy.

Chapter 5

Histopathological analysis of a novel *in vivo* MRSI technique

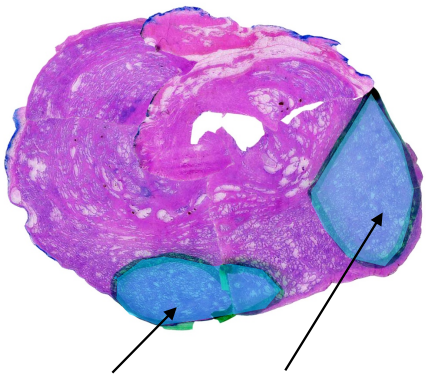

Cancerous region as defined by histopathology

In this chapter data obtained using a newly improved technique for MRSI of the prostate is compared with pre and post-surgical histopathology. Spectra from voxels that correspond to malignant and normal tissue were analyzed using a modified version of LCModel. The reduction of citrate in voxels corresponding to malignant tissue matched well with expected spectral patterns of cancerous tissue. In this chapter, we found that using the optimized CV-MRSI technique has improved the quality of spectra throughout the prostate, which has correlated well with initial histopathological findings.

5.Histopathological analysis of a novel *in vivo* MRSI technique

5.1. Introduction

Prostate cancer has been shown through histological analysis to be both multifocal and heterogeneous (16). Currently for the early diagnosis of prostate cancer, physicians use the prostate specific antigen (PSA) test as one of the main methods for screening. Typical PSA values suggesting atypical prostate conditions range between 4 to 10 ng/ml. The use of the PSA test has enabled physicians to detect cancer much earlier, and has also increased the rate of cancer detection in men (16). While of high clinical value, the PSA test lacks diagnostic accuracy since there is a broad range of prostate conditions that can also cause an increase in PSA besides prostate cancer. These include non-malignant abnormalities such as prostatitis and benign prostatic hyperplasia (BPH)(47, 185-187). Thus, PSA tests typically are combined with needle biopsy of the prostate to allow further characterization of the prostate cancer. Prostate needle biopsy is an invasive procedure that involves the insertion of a needle, under transrectal ultrasound-guidance (TRUS), through the rectal wall into the prostate where a sample of the prostate tissue is collected. Normally 12 to 16 prostate tissue samples are biopsied from different regions of the prostate volume. Even when sampling the prostate directly, TRUS-guided biopsy has been shown to have significant sampling errors and in some cases missing as many as 30% of prostate cancers. Furthermore,

TRUS-guided biopsy does not accurately define the full three-dimensional extent of cancer within the prostate (185, 188).

The wide spread use of the endorectal coil has enabled high resolution MR/MRS imaging with reasonable scan times (185). MRS imaging of the prostate allows for the detection of the key metabolic markers of disease. These are, citrate (Cit) at 2.6 ppm, choline (Cho) at 3.2 ppm, polyamines (PA) at 3.15 ppm, and creatine (Cr) at 3.0 ppm (18). In normal prostate tissue and glandular BPH there exist high levels of citrate relative to creatine and choline. In cancerous tissue where there is a high cell membrane turnover, choline-containing compounds are released into the local cellular environment causing a higher level of choline relative to polyamines, creatine and citrate. Thus the ratio of (Cho+Pa+Cr)/(Cit) becomes important in the assessment of prostate cancer. At 1.5T, the choline and polyamine resonances are sometimes indistinguishable.

The acquisition of prostate MRSI data has many technical challenges. Contamination from surrounding lipids has the potential to distort the spectral baseline and potentially alter the estimate of metabolites within a voxel. Recent work by Venugopal *et al*. has shown the feasibility of performing short echo time MRSI to assess the prostate while minimizing lipid contaminating artifacts and detecting short TE metabolites (i.e. myo-inositol, scyllo-inositol, taurine, glutamine/glutamate) (189). Studies using High-Resolution Magic-Angle Spectroscopy (HR-MAS) techniques at very high field strengths (>3T), have indicated that short T_2 metabolites like scyllo-inositol can be used as additional biomarkers to determine malignancy (130, 131, 190, 191). But prostate MRSI studies over the last two

decades recorded spectra at long echo times, and comparisons to histopathology have only been made with spectra collected at long echo times (178, 187, 190, 192). Another challenge lies in the spectral processing and use of various techniques to assess the spectra. Since many groups use different spectral-processing techniques, it becomes hard to compare results between studies (47, 150). Thus it is necessary to use a standardized method of spectral processing which enables ease of comparison of data collected at different sites.

This study has two objectives: The first objective is to compare and correlate post-radical prostatectomy histopathology data with MRSI data acquired using the CV-MRS+ PRESS technique at TE=130 ms. The second objective is to compare this result with short echo time MRSI data acquired using the CV-MRS+PRESS with spectral-spatial excitation at TE=40 ms. Therefore this study assesses the utility of the short echo time MRSI acquisition in combination with the CV-MRS technique, in the diagnosis of prostate cancer.

5.2. Materials and methods

5.2.1. Volunteers

Subjects were recruited to this study as part of an ongoing study being performed at the Winnipeg Health Sciences Centre, in conjunction with the National Research Council Institute for Biodiagnostics (NRC-IBD), and CancerCare Manitoba, with approval from the local research ethics boards. Our study included 8 subjects with biopsy-proven prostate cancer. Each subject underwent systematic biopsies at least 6 weeks prior to MRSI to minimize the effects of post-biopsy

hemorrhage and did not undergo any therapy before the MR examination. Radical prostatectomy was performed within a few weeks after MRSI. Following surgery, radical prostatectomy specimens were submitted for sectional pathologic evaluation.

In three subjects the study was stopped midway because the subjects could not withstand the pressure caused by the endorectal MR coil. In one of these three subjects, partial data was collected. Although this resulted in the loss of two and a half data sets, the actual scans had been completed and the data was still useable. In total, we were left with data from 6 subjects (median age, 55.5±8.7 years; range 44 – 66 years).

5.2.2. Histopathology

After surgery, the resected prostate was sent for sectioning. The prostate was cut using the local standard protocol. This included cutting the prostate into 3-4 mm slices from the base to the apex, trying to match the orientation of axial MR images as closely as possible. For each slice, the position along the inferior and superior was marked with its relative distance from the middle of the gland. Each slice was further cut into four quadrants. These pieces were fixed in 10% formalin. All pieces of the prostate were embedded in paraffin wax, and mounted. H&E staining was performed and a pathologist carefully examined each prostate piece under a microscope. Each prostate quadrant was checked for cancer, and the pathologist delineated the tumour regions, and assigned a Gleason score. The stained images were scanned and the four quadrants of each slice were photo-

stitched together. Lastly, using internal anatomical markers (i.e. nodules, shape and appearance of central and peripheral zones), the location of the histopathology slice was matched to the best corresponding combined MRI/MRSI image along the superior and inferior directions(176).

5.2.3. MRI/MRSI acquisitions

All MRI/MRSI examinations were performed on a General Electric 1.5T Signa MR scanner equipped with Echospeed gradients. For optimal signal reception, a standard disposable endorectal coil (Medrad Inc.) in combination with a torso phased-array coil was used. To ensure that the coil was positioned tightly against the prostate, the endorectal probe was inflated with approximately 75-80ml of FC-77 FLUORINERT, a perfluorocarbon (PFC) compound (3M, St. Paul, MN, USA). The use of the PFC compound as substitute for air significantly reduced magnetic susceptibility artifacts and improved B_0 homogeneity throughout the prostate volume (148). Initial scout scans in all three orthogonal planes were acquired to ensure that the coil was placed directly beneath the prostate, with maximum coil area covering the posterior surface of the prostate. Once the coil was appropriately placed, axial T_2 weighted images of the entire prostate gland were acquired using a fast spin-echo imaging sequence (TE/TR=102/5000ms; matrix size =256x256; field of view= 140mm; slice thickness=3mm; no gap).

Consecutive MRSI studies were performed back-to-back after acquiring the T_2-weighted images. To perform the comparison, *in vivo* prostate spectra were obtained using two different acquisition methods: 1) CV-MRS and PRESS with TE/TR

=130/1100 ms (long echo time); 2) CV-MRS and PRESS with spectral-spatial excitation with TE/TR =40ms/1100 ms (short echo time). The properties of the spectral-spatial pulse were: true nulling (in contrast to opposed nulling), a frequency offset of -120 Hz (with water at 0 Hz), a nulling frequency of 110 Hz (placing nulling points at 0 Hz-water, and 220 Hz-lipids), a spectral bandwidth of 90 Hz, a spatial bandwidth of 1750 Hz, with trapezoidal gradient cycles leading to a total pulse width of 18.2 ms. Each 3D MRSI acquisition used a 16x8x8 phase encode matrix, with a nominal voxel size of 0.42 cm^3, and an acquisition time of 19 minutes. For all spectroscopic imaging scans the width of the spatial saturation bands was 30 mm. For post-processing frequency corrections the water suppression for each scan was adjusted to retain a small amount of residual water.

5.2.4. Post-processing with LCModel

Post-processing of the spectra was achieved using LCModel which has a sophisticated lipid fitting routine (173). LCModel was used to simulate the key prostate metabolites (i.e. citrate, choline, creatine, etc.). This fitting package was modified specifically for analyzing *in vivo* prostate spectra at long and short TE's. The SAGE software platform (SAGE ver2007.1, Spectroscopy Analysis by General Electric, © 1998 General Electric) was used to display the data before inputting it into LCModel. The automated referencing method was modified to include both the residual water, choline, creatine, and citrate peaks in the calculation of the cross-correlation function (CCF). After this procedure, usually only minor phase correction was necessary. Further post-processing consisted of the application of a

Gaussian spectral apodization filter (1.25Hz line broadening), and application of a spatial apodization filter (Fermi diameter=100%, Fermi transition width=50%), followed by a Fourier transformation to spatial and frequency dimensions. Ratios of creatine (Cr), polyamines (PA), choline (Cho), myo-inositol (mI), scyllo-inositol (sI), taurine (Tau), and glutamine/glutamate (Glx) with respect to citrate were calculated and presented in a table as part of the output file. Only voxels that fell within the spatial excitation region corresponding to the prostate and containing at least 75% prostate tissue were analyzed. Metabolites that fell within the spectral range of 0.6-3.85 ppm were fitted using LCModel. Estimates were made of the goodness-of-fit of each metabolite quoted by the Cramer-Rao Lower Bound (CRLB) and as a percent standard deviation (%SD). Rejection criteria for the spectral fitting included LCModel's built-in poor baseline estimates (due to contaminating artifacts or very poor water suppression) as well as a percent standard deviation threshold of 40% in order to reject poorly fitted peaks. LCmodel analysis was performed on a multi-processor system that accelerated analysis of each prostate data set. The average time of analysis for each prostate data set was less than 5 minutes.

5.2.5. Image Registration

Once acquired, each data set was converted to a binary image mask outlining the known cancerous regions defined by histology. A nonlinear registration method was employed to account for the differences in tissue deformation of the histopathology slices and the combined MRI/MRSI data. The image registration method, previously developed by Venugopal *et al*. requires

manual control point selection between the histopathology slices and the combined MRI/MRSI data (193). These control points were used as input for the image registration algorithm and the resulting registration map was applied to the histopathology data set, the combined MRI/MRSI data set and the corresponding masks. Doing this helped remove the distorting effect of the inflated coil and aligned the two images together. The approach used in this study is illustrated in Figure 5.1. After the registration was complete, a voxel by voxel comparison of the overlapping histopathological data and MRSI data was performed to determine the mean ratio for all MRSI voxels containing at least 75% percent normal tissue or cancerous tissue (as identified by histopathology and registered to the MRSI data). The voxel by voxel comparison was done for each MRSI acquisition (i.e. CV-MRS and PRESS with TE=130 ms CVMRS+PRESS+spectral-spatial excitation with TE=40 ms). For the long echo time acquisitions a metabolite ratio of (Cho+PA+Cr)/Cit was used, and for short echo time acquisitions a metabolite ratio of (sI+Cho+PA+Cr)/Cit was used. The mean ratios for normal and cancerous tissue were calculated for individual subjects and over all subjects using both MRSI techniques.

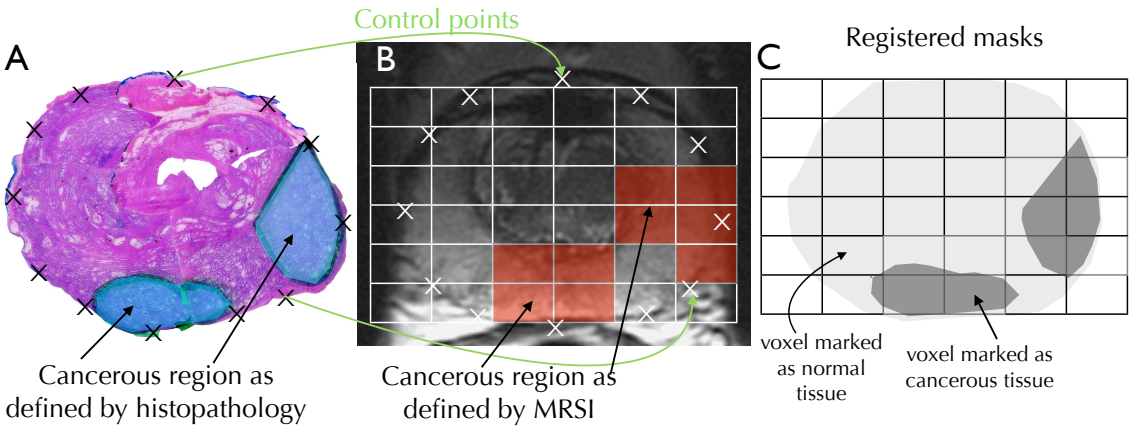

Figure 5.1 Image registration of histopathology image to combined MRI/MRSI image
The deformation of the prostate caused by the use of an endorectal coil can be accounted for by using a thin-plate spline warping image registration algorithm to 'correct' the image. In (A), a set of control points was selected along the periphery of the histopathological image. Along the periphery of the corresponding MRI/MRSI image congruent anatomical tie points were selected (see B). In (C), a binary mask was used to identify MRSI voxels that overlap with at least 75% of normal tissue or cancerous tissue.

5.3. Results

In this preliminary study, a small cohort of subjects was examined ranging in age from 44-66 years of age. The subjects recruited were all diagnosed with prostate cancer, with a pre-histopathological Gleason score ranging from 6 to 7, with five out of the six subjects having a pattern of 3+3 and one with a pattern of 3+4 (see Table 5.1).

Table 5.1 Summary of pre- and post- histopathology results

	Pre-Histopathological Assessment			Post- Histopathological Assessment			
Subject	Age	# of Positive Cores	Gleason Pattern	*Tumour Location	% of Gland involved	Gleason Pattern	Dominant nodule size (cm)
1	56	6/12	3+3	RP,LP, APEX	10	3+4	1.7
2	44	3/12	3+3	RA,RP, LP	10	3+3	1.3
3	66	5/12	3+3	All lobes	5	3+4	1.8
4	49	5/12	3+3	RP,LP	20	3+3	2.5
5	53	4/12	3+4	RA,RP, LA,LP	10	3+3	1.3
6	65	3/12	3+3	RA,RP, LA,LP, APEX	50	4+3	4.2

*RP-right posterior, LP-left posterior, RA-right anterior, LA-left anterior

The post-histopathological assessment correlated well with the pre-histopathological assessment with similar Gleason score, which was confirmed by microscopic examination of the prostate cancer tissue. Overall the cancers were multifocal, appearing in the right and left posterior lobes, right and left anterior lobes, and the apex. The percentage of the gland involved over all subjects ranged from 5-50% with the dominant cancerous nodule ranging in size from 1.3 to 4.2 cm. Using the CVMRS+PRESS technique with TE=130ms, spectra from regions overlapping normal tissue had a mean metabolite ratio of 0.31±0.20 while spectra from regions overlapping cancerous tissue had a mean metabolite ratio of 0.74±0.23. In a similar analysis, but using the CV-MRS+PRESS+spectral-spatial excitation technique with TE=40 ms, spectra from regions overlapping normal tissue had mean metabolite ratio of 0.29±0.12 while spectra from regions

overlapping cancerous tissue had a mean metabolite ratio of 0.78±0.16. Both techniques were able to distinguish between normal and cancerous tissue (see Figure 5.2).

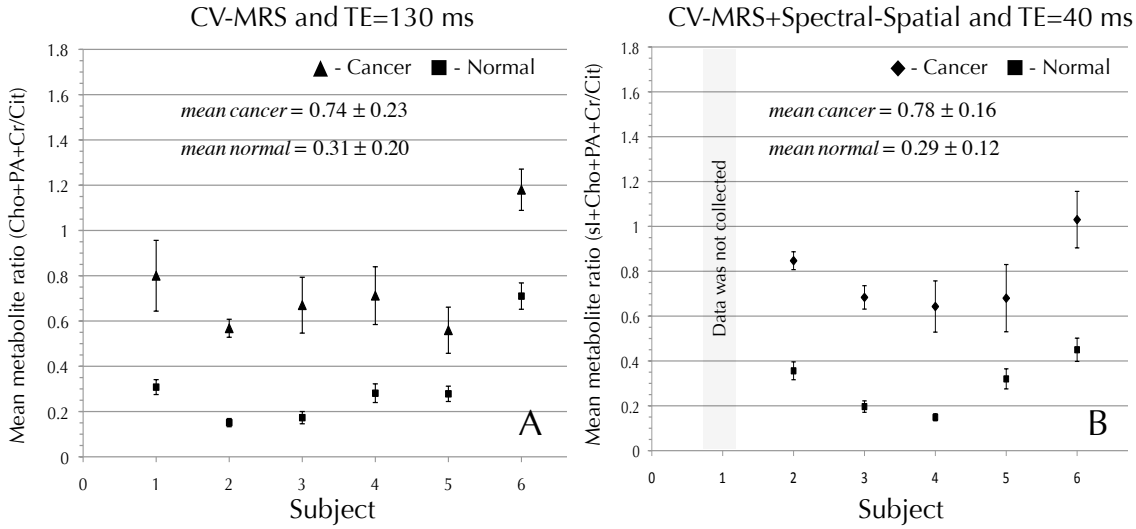

Figure 5.2 Metabolite Ratios
In (A), the metabolite ratio of Cho+PA+Cr/Cit for long echo time acquisitions is shown for both normal and cancerous spectra for each subject. Similarly, in (B) the metabolite ratio of sI+Cho+PA+Cr/Cit for short echo time acquisitions is shown for both normal and cancerous spectra for each subject. Spectra overlapping normal tissue demonstrated high levels of Cit in comparison to Cho+PA+Cr while spectra overlapping cancerous tissue demonstrated reduced levels of Cit in comparison to Cho+PA+Cr. This was also true for short echo time acquisitions where we have now added scyllo-inositol into the ratio.

Sample spectra from normal and cancerous voxels are shown in Figure 5.3. For long echo time acquisitions there was a wider range of metabolite ratios for both normal and cancerous tissue, 0.15-0.71 and 0.56-1.18. In particular, subject 6 demonstrated much higher ratios in comparison to the rest of the subjects for long echo time acquisitions. In Figure 5.4 spectra from subject 6 is shown. Zooming into a single voxel (see Figure 5.4) we observed for long echo time acquisition the spectrum overlapping normal tissue had a higher metabolite ratio, 0.94±0.09. In

comparison, a spectrum acquired from the same location at short echo time showed a reduced metabolite ratio of 0.29±0.03. At both long and short echo times, the spectra showed statistically good separation between mean metabolite ratio of cancer and normal tissues. In some cases, at both long and short echo time acquisitions, a reduction in citrate was observed in regions of histopathologically confirmed prostate cancer (see Figure 5.6) with no increase in choline.

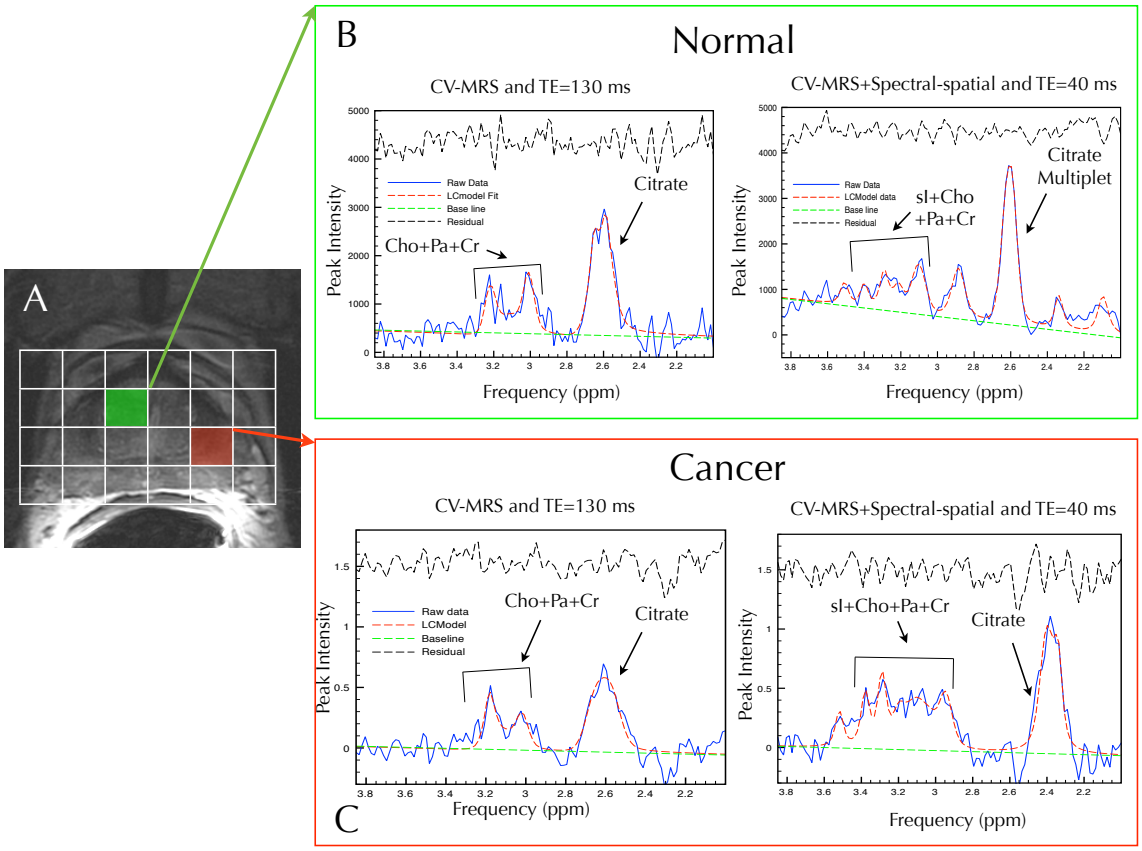

Figure 5.3 Normal and cancer spectral patterns

The spectral patterns for normal and cancerous spectra were taken from a 53year old prostate cancer patient demonstrating multifocal disease. In (A), voxels were selected from regions that were identified as normal (colored green), and cancerous (colored red). At both long and short echo times, spectra demonstrated higher levels of citrate. In (B), at short echo times, the spectrum presented shows a higher SNR, full citrate multiplet, and detection of sI. In comparison to normal spectra, in (C) spectra from cancerous voxels are presented demonstrating an increase in Cho relative to Cit at long echo times, and for short echo times an increase in sI+Cho+PA+Cr relative to Cit. At both long and short echo time acquisitions, Cit was dramatically reduced.

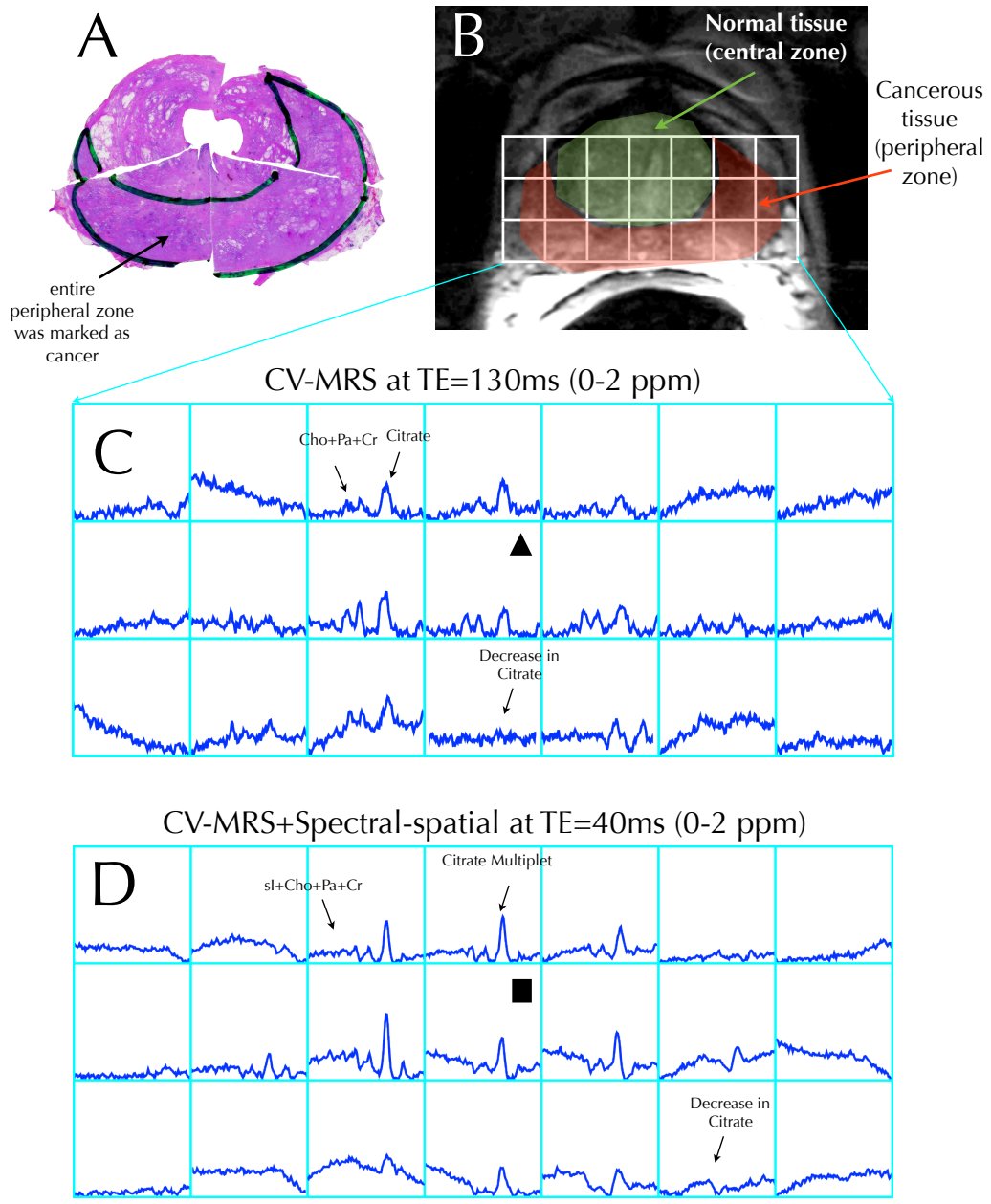

Figure 5.4 Peripheral zone prostate cancer
Spectroscopic imaging was performed on a 65 year old male with histopathologically confirmed prostate cancer, with Gleason score of 6. Regions of histopathologically identified prostate cancer (see A) demonstrate a dominant distribution of cancer throughout the peripheral zone, with a region of healthy normal tissue along the central zone (see B). In (C), spectra are presented using the CV-MRS technique at TE=130ms. In (B), spectra using the CV-MRS technique with spectral-spatial excitation at TE=40ms is shown. Along the peripheral zone a reduction of citrate is observed. Spectra along the central zone demonstrated increased citrate, indicating healthy prostate tissue.

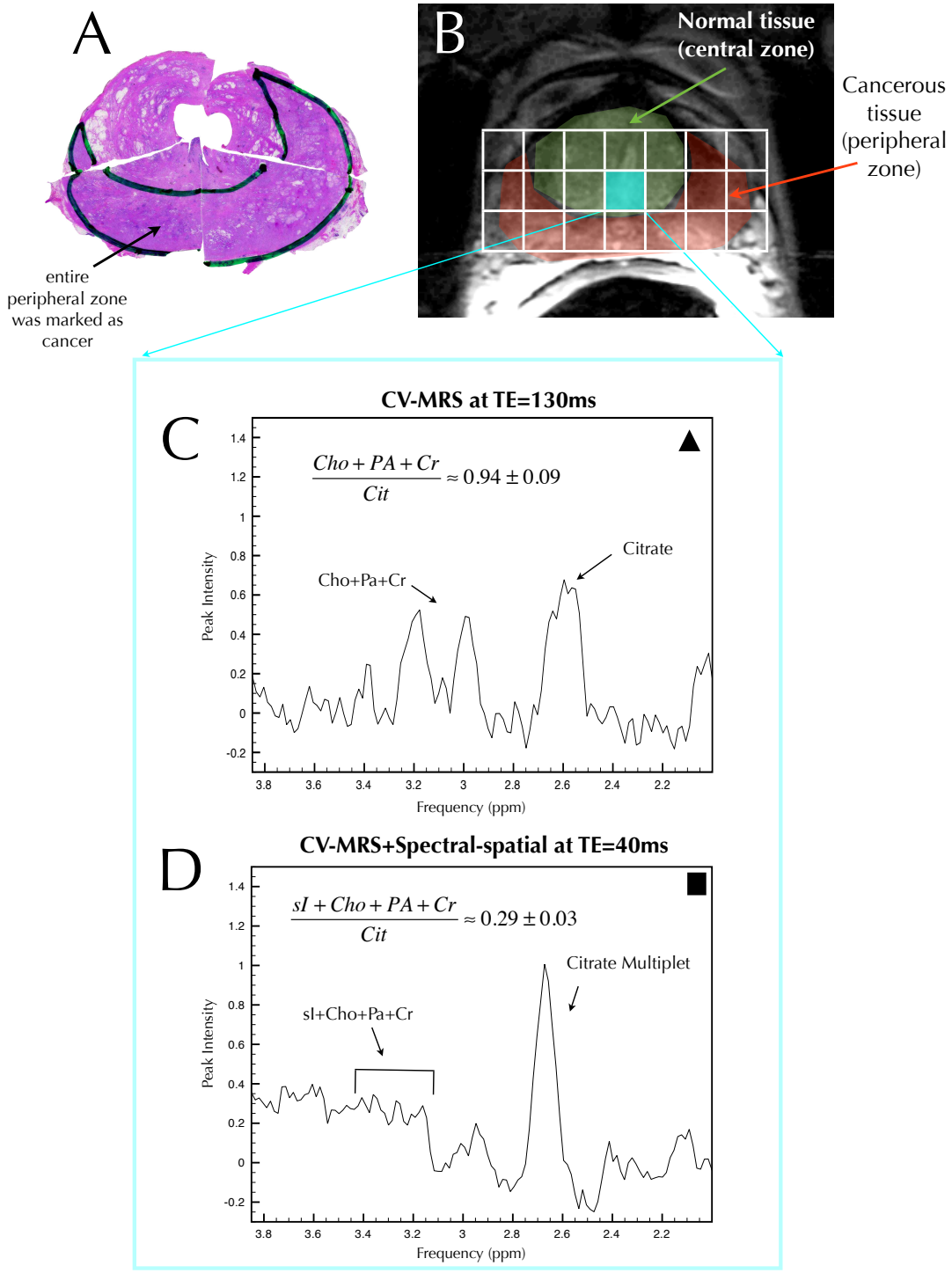

Figure 5.5 Short TE for differential analysis

The same images as in Figure 4, zooming in to spectra labeled "▲", and "■" showing two spectra acquired using both techniques which overlap normal prostate tissue as identified by histopathology. In (C), Cho+PA+Cr/Cit ratio is 0.94 ±0.09 while the ratio of sI+Cho+PA+Cr/Cit from the same voxel using the second method is 0.29±0.03.

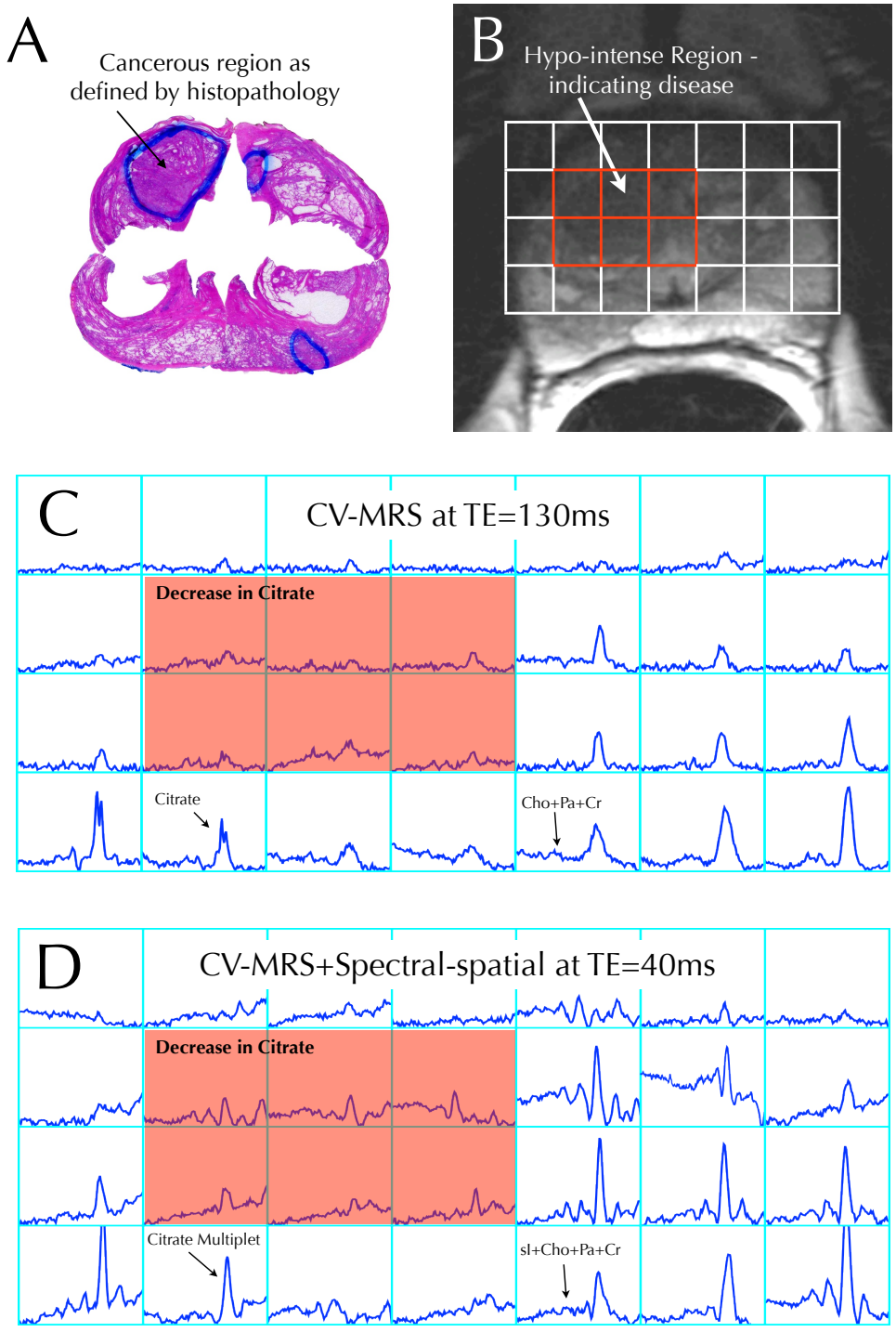

Figure 5.6 Reduction of citrate is an indicator of cancer
Spectroscopic imaging was performed on a 66 year old male with histopathologically confirmed prostate cancer, with Gleason score of 6 and 5% involvement. In regions of histopathologically identified prostate cancer (see A) a significant reduction in citrate was observed when compared to spectra overlapping normal tissue (B). This was observed at both long (C) and short (D) echo times.

5.4. Discussion

In current practice, the diagnosis of prostate cancer still relies heavily on the use of systematic sextant[19] TRUS-guided biopsy and remains the gold standard method among urologists. However, systematic sextant TRUS-biopsy has been shown to be associated with a high false negative rate ranging between 15-34% (194-197). As such, it was also reported that between many centers no single biopsy sampling scheme is generally accepted as a standard method (198). Furthermore, there isn't a current imaging modality used in practice that can reliably distinguish prostate cancer from normal or non-malignant prostate conditions. For this reason combined MR/MRSI is now slowly emerging as a method to target biopsy, and to assess the full three-dimensional extent of prostate cancer. In many centers, urologists and radiologists are actively using MRI to target biopsies, and utilizing this functional imaging information (i.e. MRI/MRSI, DCE-MRI, DWI, etc.) to help define the course of treatment for an individual (190, 195, 199-202). From this study we have demonstrated that the novel CV-MRS approach at both short and long echo times can be used to identify prostate cancer. In comparison of long and short TE times, our mean metabolite ratio obtained for normal spectra at both long (0.31±0.20) and short (0.29±0.12) echo time acquisitions correlated well to previously published values from several centers (99, 150, 203, 204). For example, Jung *et al*. reported a value of 0.25±0.12 over a

[19] Systematic sextant TRUS guided biopsy involves collecting samples from a pre-defined grid that is common for all prostate based on anatomical locations, and angulations of the biopsy needle

subject pool of 37. Similarly our mean metabolite ratio for cancerous spectra recorded at both long (0.74±0.23) and short (0.78±0.16) echo times compare well to previously published values, which range from 0.92-1.08 (151, 205). A positive outcome of this study is that the CV-MRS technique was able to detect differences in the (Cho+PA+Cr)/Cit ratios between normal and cancer spectra. Furthermore, short echo time acquisitions, which included scyllo-inositol, demonstrated that the (sI+Cho+PA+Cr)/Cit could also detect differences between normal and cancerous spectra. Short echo time acquisitions may be better suited to differentiate normal and cancerous tissue (see Figures 5.4 and 5.5).

In a case study of subject 6, we observe that at long echo times many voxels that overlapped with normal tissue (as defined by histopathology) demonstrated higher metabolite ratios (0.71±0.06), when compared to the rest of the subjects (range ~ 0.15 to 0.31). At short echo times, the spectral pattern changes due the appearance of the citrate multiplet and detection of short TE metabolites (i.e. scyllo-inositol). In this case, at short echo times we observed lower ratios of sI+Cho+PA+Cr/Cit over the entire region marked as normal by histopathology. This result demonstrated that at short echo times we may be able to provide better definition of normal tissue, and provide an alternate pathway for differential analysis of prostate cancer. While this conclusion is limited by the low number of subjects used in this study, a study with a larger patient cohort would help to strengthen these findings.

Another interesting observation of our study is the utility of LCModel fitting software to quickly process data collected using long and short echo time techniques. Historically, LCModel was mainly used for analysis in spectroscopy of

the brain, with many publications citing the robust analysis and ease-of-use for both qualitative and quantitative analysis [18, 36-40](103, 173, 206-208). Clearly, the use of a systematic processing package in prostate spectral analysis allows users to make robust comparisons that can be shared by users from other centers using LCModel. At present, LCModel is gaining more use in the prostate spectroscopy community (15, 157, 209).

From the data collected from subjects participating in this study, it was clear that in both long and short echo time acquisitions, the prostate cancer malignancy was not always associated with high levels of choline compared to citrate. We observed in a number of voxels (see Figure 5.6) that a reduction in citrate is also an indicator of malignancy. This effect has been well studied and is mainly attributed to the metabolic and structural changes of prostate tissue (12, 210, 211). In the progression of prostate cancer, cells initially become less differentiated, causing a breakdown in the glandular structure of the prostate tissue. Next, the glandular tissue is replaced by proliferating cells whose increased energy needs start to oxidize citrate, causing its apparent reduction (9). In this study, we have demonstrated that MRSI at both long and short echo times can detect the metabolite variations associated with malignancy (9).

While there were a number of positive outcomes in this study, there were also several limitations that should be addressed. Firstly, the voxel size used in this study was fairly large (~0.42 cm^3). A larger voxel size was needed to obtain adequate SNR for spectra, but resulted in an overestimation of the cancerous regions when compared to histopathology. In Figure 5.6, we observe that the total

cancerous area identified by MRSI was larger than the delineated cancer region identified by histopathology. As a result, a voxel-by-voxel comparison across subjects with a small percentage of glandular involvement (5-20%) may tend to overestimate cancerous regions. Approximations that were made in order to perform the image registration also contribute to uncertainty. These include approximating the superior-inferior direction of the histopathology through slice-by-slice visual inspection based on dimensions measured at the time the resected prostate was cut, and the process of photo-stitching the four prostate quadrants together. In-plane registration discrepancy may be a major source of uncertainty in this analysis. In combination with a large voxel size, the attempt to detect small, multifocal tumours in three-dimensions using MRSI data would be effected by uncertainty in the image registration. Furthermore, it would have been desirable to use whole-mount step section histopathology as used by other centers , but this capability was not available at our center (176, 209, 212, 213). For example, in the case where the prostate cancer occupied ~50% of the prostate gland, the registration matched well with the zonal anatomy of the prostate. While we have demonstrated the feasibility of using this registration as method of comparison, a larger study with more subjects would again help further validate these techniques.

As previously mentioned, prostate MRSI has been mainly performed at long echo times. In this study, we have shown the feasibility of using the CV-MRS+PRESS technique to reduce lipid contamination and obtain spectra at long echo times (TE=130ms) with mean metabolite ratios that can discriminate between normal and cancerous tissue. Furthermore, we have shown comparable results using the CV-

MRS+PRESS+spectral-spatial excitation at short echo times (TE=40ms) while also utilizing scyllo-inositol as part of the metabolite ratio calculation. Metabolites such as scyllo-inositol are present in cancerous spectra and are detectable at short echo times. Calculations using the ratio of (sI+Cho+PA+Cr)/Cit demonstrated good LCModel fits over the spectral range of 3.5 - 3.0 ppm with the inclusion of scyllo-inositol. While more studies need to be performed to determine the full efficacy of short echo time acquisition, this study shows that there is potential to use short echo times acquisitions to aid in accurately defining the spatial extent of the prostate cancer.

5.5. Conclusion

In summary, both long (CV-MRS and PRESS with TE=130 ms) and short (CV-MRS and PRESS with spectral-spatial excitation with TE =40 ms) echo time acquisitions were performed on six prostate cancer subjects and compared to histopathology results. The mean Gleason score was 6 (3+3), and tumours presented were multifocal, ranging from 5-50% glandular involvement. Both techniques had comparable performance outcomes. For long and short echo times the mean normal metabolite ratios were 0.31±0.20 and 0.29±0.12 respectively. In contrast, for the long and short echo times the mean cancer metabolite ratios were 0.74±0.23 and 0.78±0.16. For both acquisition techniques, our data corresponded well to reported values in the literature. In conclusion, this feasibility study provided an initial validation of the CV-MRS technique at long and short echo times, but a larger study with more subjects is needed to help demonstrate its full efficacy in a clinical environment.

Chapter 6

IMRT planning of the prostate with boost to dominant intraprostatic lesion guided by ^{1}H-MRSI

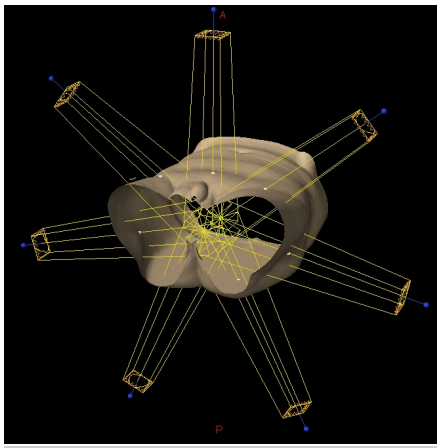

Chapter 6 attempts to bring together what we have learnt from Chapters 3 to 5. Using the CV-MRS method, spectroscopic maps of dominant intraprostatic lesions are identified. Spectroscopic imaging data is then used to modify radiobiological parameters, to better estimate tumour control. Radiobiological models and radiation treatment strategies, including dose escalation, are discussed.

6. IMRT planning of the prostate with boost to dominant intraprostatic lesion guided by ^{1}H-MRSI

6.1. Introduction

External beam radiation therapy is still one of the primary methods to treat cancer of the prostate. The main goal of radiation therapy of the prostate, as with other anatomical regions, is to deliver a high dose of radiation to the region of cancer, while keeping radiation doses to surrounding normal tissues as low as possible (i.e. bladder, rectum, lower bowels, femoral bones). Using this ideology, the goal of radiation treatment is to achieve the maximum killing of cancer cells within the treatment volume, while achieving minimal radiation damage to normal tissues. While this is the general goal for radiation treatment, the effective delivery of radiation to the prostate depends on the assessment of the tumour location, as well as the tumour aggressiveness. This information will help determine the appropriate dose to deliver in order to gain control over the cancer.

Advanced techniques in external beam treatment, such as intensity modulated radiation therapy (IMRT) now allow for very conformal treatment of the prostate. Over the last decade IMRT has matured into a robust radiation treatment modality. But it has only been in the recent few years that functional imaging modalities have started to find their way into concurrent use with traditional computed tomography (CT) used in treatment planning. These imaging modalities

include positron emission tomography (PET), advanced magnetic resonance imaging (MRI) techniques, and proton magnetic resonance spectroscopic imaging (^{1}H-MRSI) (72, 214-222). If these imaging techniques can accurately locate intraprostatic tumour volumes or dominant intraprostatic lesions (DIL), IMRT could facilitate a dose delivery strategy that would escalate the dose to these DILs with the advantage of maintaining low doses to the critical structures.

Early work by Ling *et al*., demonstrated the feasibility of defining biological target volumes (BTV), and showed the feasibility of performing "dose painting" to regions within the prostate (223). Furthermore, in a clinical study by Zelefsky *et al*. it was shown that delivering high doses to the prostate can achieve better tumour control with lower acute and late rectal toxicities (224). Additionally, IMRT can now deliver high doses (>85 Gy) of radiation to dominant intraprostatic lesions (DIL) or prostate sub-volumes of high cancer cell density, while minimizing tolerances to critical structures (72).

Over the last decade ^{1}H-MRSI has entered the clinical environment as a useful tool to identify and spatially map prostate cancer (14, 17, 18, 47, 225). In ^{1}H-MRSI of the prostate, the measurement of the metabolic markers such as choline, polyamines, creatine, and citrate are used to determine the malignancy of the tissue of the tissue throughout the prostate. *In vivo* prostate ^{1}H-MRSI confirmed the diagnostic utility of the metabolites choline, creatine, and citrate in providing a specific marker for cancer within the peripheral zone, with 98% of cancers having a higher (choline+creatine)/citrate ratio when compared to the normal ratio(6, 125, 130, 226). Pickett *et al*., first demonstrated the use of incorporating intraprostatic

volumes for a localized boost with prostate cancer (23)(226). They showed that using a standard, 7 field IMRT plan, one could treat a single lobe of the prostate to 90 Gy, while concurrently treating the entire prostate to greater than 70 Gy without increasing the dose to normal tissues. This was an important result as it lead the way for methods attempting to treat multi-focal lesions as sub-volumes within the prostate. The clinical value of utilizing spectroscopic information for the radiation treatment of the prostate has been demonstrated by both van Lin *et al*. and Kim *et al*. (72, 139). The work by Kim *et al*. showed that by using high dose rate (HDR) brachytherapy, the dose to the DIL can be escalated to 150% of the prescribed dose without significantly changing tolerances to critical structures (139). In their work, the DIL was identified using combined MRI/MRSI. In a similar study, but using IMRT, van Lin *et al*. showed the feasibility of the using combined dynamic-contrast enhanced (DCE) MRI/MRSI to identify DILs ranging in volume from 1.1-6.5 cc's. Furthermore, van Lin *et al*. showed, through radiobiological modeling, an improvement in the therapeutic ratio by decreasing the normal tissue complication probability (NTCP) while maintaining adequate tumour control probability (TCP). In their study they assumed a uniform α and β parameters ($\alpha = 0.26 \pm 0.06$ Gy^{-1}, $\alpha/\beta = 8.3$ Gy) for both the DIL and prostate volumes, but varied the number of clonogens over the DIL and prostate volume (107 and 105 cells/cc respectively), while assuming no proliferating effects (72).

The current goal of prostate radiation therapy treatment plans is to achieve a uniform dose over the entire target volume. This is done under the assumption that the cancer is uniformly spread throughout the entire prostate volume. This

assumption does not include biological variations that might exist in the treatment volume like, for example, regions of acute hypoxia and differences in the spatial distribution of cancer cell density or cancer cell aggressiveness. Several studies now suggest that there may be significant therapeutic benefits to biologically guided radiation therapy (83, 227-229). For the radiation treatment of the prostate, the studies by Pouliot *et al.*, van Lin *et al*. and Kim *et al*. demonstrate the feasibility of including biological information (i.e. ^{1}H-MRSI) (72, 139, 230).

Up until now, ^{1}H-MRSI data has been used to spatially identify and delineate DILs within the prostate volume. But ^{1}H-MRSI also provides metabolic information associated with tumour growth and development, and can also estimate cancer aggressiveness (130, 131). Tumour proliferation effects play a crucial role in the way a cancer develops. Furthermore, examining the biochemical nature of tumour cell proliferation may give insight into how a tumour responds to radiation treatment, and assist in determining follow-up treatment, although that is not the focus of this work. In recent studies, both Zakian *et al.* and Wang *et al.* compared the histopathological relationship between Gleason grade and metabolite ratio determined by ^{1}H-MRSI (132, 171). These results indicate that the metabolite ratio obtained from MRSI is correlated to the Gleason grade of the tumour, which itself is an indication of tumour cell aggressiveness. Currently, radiobiological assessments of IMRT treatment plans are not routinely done, but they can provide a powerful tool for comparing treatment plan effectiveness by estimating the dose needed to control disease with long-term disease free survival (67). When implemented they do not take into account spatial variations of the

cancer, and they typically assume that the underlying radiobiological parameters (i.e. α, β, and number of clonogens) are uniform throughout the structure.

To determine the dose needed to obtain adequate tumour control for localized prostate cancer we examine the utility of incorporating spectroscopic imaging data into the radiobiological modeling of prostate cancer. Current radiobiological models that are used to calculate TCP assume that the prostate cancer is homogeneous throughout the prostate volume. However, from histopathology analysis of biopsy and radical prostatectomy samples, as well as from spectroscopic imaging of the prostate we know that the cancer is not homogenous and can appear in well-defined regions of the prostate (i.e. DIL). To account for the spatial variation of the cancer, we propose to use the spectroscopic data to map regions of the prostate that demonstrate increased metabolic activity and then use the metabolic information (i.e. the ratio of Choline+Creatine/Citrate) to directly modify the TCP calculation (including its associated radiobiological parameters like α, α/β, number of clonogens) on a voxel-by-voxel basis throughout the prostate. To evaluate the effect of including spectroscopic imaging data we perform both theoretical and experimental calculations of TCP to determine if we can achieve better tumour control through targeted dose escalation.

In this study we perform a comparison of two IMRT plans, with and without the inclusion spectroscopic imaging data, to demonstrate that spatially varying radiobiological parameters with spectroscopic imaging data may be used to estimate tumour control probability and this in turn may be used to estimate increases in dose required for significant improvement in patient outcomes.

6.2. Materials and methods

6.2.1. Volunteers

Subjects were recruited to this study as part of an ongoing prostate fractionated irradiation trial (PROFIT, sponsored by the Ontario Clinical Oncology Group) being performed at CancerCare Manitoba, in conjunction with the National Research Council Institute for Biodiagnostics (NRC-IBD), and the Winnipeg Health Sciences Centre, with approval from the local research ethics boards. Our study included 8 subjects with biopsy-proven prostate cancer. The inclusion criteria for the study were: histopathologic diagnosis of carcinoma of the prostate within 6 months, without evidence of metastatic disease to the lymph nodes, bone or lung, and the prostate staged as intermediate risk[20] (i.e. T1-2a, Gleason score <6, PSA 10.1-20.0 ng/ml; T2b-c Gleason <6, PSA ≤ 20.0 ng/ml; T1-2, Gleason 7, PSA ≤ 20.0 ng/ml). Each subject underwent systematic biopsies at least 6 weeks prior to ^{1}H-MRSI to minimize the effects of post-biopsy hemorrhage and did not undergo any therapy before the MR examination.

One subject was removed since they were receiving concurrent hormonal treatment. In total, we were left with data from 7 subjects (median age, 68.1±8.1 years; range 57 – 83 years).

[20] The clinical definitions used in staging prostate cancer (i.e. TNM descriptions) are presented in Appendix B

6.2.2. CT Imaging

CT data was acquired using a Philips Brilliance scanner (Philips Healthcare, Andover, MA, USA). The clinical CT protocol used for radiation treatment simulation was performed for each subject. The acquisition parameters were: FOV of 60cm and slice thickness of 3mm to include the entire patient pelvis.

6.2.3. Combined MRI/MRSI of the prostate

All MRI/MRSI examinations were performed on a General Electric 1.5T Signa MR scanner equipped with Echospeed gradients. For optimal signal reception, a standard disposable endorectal coil (Medrad Inc.) in combination with a torso phased-array coil was used. To ensure that the coil was positioned tightly against the prostate, the endorectal probe was inflated with approximately 75-80ml of FC-77 FLUORINERT, a perfluorocarbon (PFC) compound (3M, St. Paul, MN, USA). The use of the PFC compound as substitute for air significantly reduced magnetic susceptibility artifacts and improved B0 homogeneity throughout the prostate volume (148, 231, 232). Initial scout scans in all three orthogonal planes were acquired to ensure that the coil was placed directly beneath the prostate, with maximum surface area covering the posterior surface of the prostate. Once the coil was appropriately placed, axial T_2 weighted images of the entire prostate gland were acquired using a fast spin-echo imaging sequence (TE/TR=102/5000 ms; matrix size =256x256; field of view= 140mm; slice thickness=3mm; no gap). Next, ^{1}H-MRSI studies were acquired using the optimized CV-MRS and PRESS technique

with TE/TR =130/1100 ms with a 16x8x8 phase encode matrix, with a nominal voxel size of 0.42 cm^3, and an acquisition time of 19 minutes. For all spectroscopic imaging scans the width of the spatial saturation bands was 30 mm. For post-processing frequency corrections the water suppression for each scan was adjusted to retain a small amount of residual water. At the end of the spectroscopic imaging scan, the endorectal coil was deflated and a second set of axial T_2 weighted images of the entire prostate gland were acquired using the same scan parameters.

6.2.4. Post-processing of ^{1}H-MRSI data

Post-processing of the spectroscopy was done using LCModel (173). LCModel was used to simulate the key prostate metabolites (i.e. citrate, choline, creatine, etc.) and for its sophisticated lipid fitting routine. The SAGE software platform (SAGE ver2007.1, Spectroscopy Analysis by General Electric, © 1998 General Electric) was used to display the data before inputting it into LCModel. The automated referencing method was modified to include the residual water, choline, creatine, and citrate peaks in the calculation of the cross-correlation function (CCF). After this procedure, usually only minor phase correction was necessary. Further post-processing consisted of the application of a Gaussian spectral apodization filter (1.25Hz line broadening), and application of a spatial apodization filter (Fermi diameter=100%, Fermi transition width=50%), followed by a Fourier transformation to spatial and frequency dimensions. The ratio of choline +creatine/citrate (Cho+Cr/Cit) was calculated and presented in a table as part of the

output file. Only voxels that fell within the spatial excitation region corresponding to the prostate and containing at least 75% prostate tissue were analyzed. Metabolites that fell within the spectral range of 0.6-3.85 ppm were fitted using LCModel. An estimate of the goodness-of-fit of each metabolite quoted by the Cramer-Rao Lower Bound (CRLB) and quoted as a percent standard deviation (%SD) was recorded. Rejection criteria for the spectral fitting included LCModel's built-in poor baseline estimates (due to contaminating artifacts or very poor water suppression) as well as a percent standard deviation threshold of 40% in order to reject poorly fitted peaks. LCModel analysis was performed on a multi-processor system that accelerated analysis of each prostate data set.

6.2.5. DIL delineation

The metabolite ratio of (Cho+Cr)/Cit greater than 0.74 was used as a cut off value to identify voxels as cancerous (151, 205). The identified spectroscopic voxels were assigned pixel values (corresponding to metabolite ratio), and then interpolated to generate a spatial map which was overlaid on a corresponding anatomical T_2 weighted MR image.

6.2.6. Image registration

The endorectal coil, although required for MRSI to improve signal-to-noise, poses a potential problem for the radiotherapy treatment planning of the prostate. The coil is filled with approximately 75-80ml of PFC which is required to expand

the coil and position it adjacent to the prostate. Consequently, the inflation of the coil deforms the prostate. As such, the combined MRI/MRSI data that is collected from the prostate is also deformed. Routine radiation treatment planning of the prostate relies on computed tomography (CT) images to provide patient density information needed to perform accurate dose calculations. These CT images of the prostate do not experience the same deformation as the MRSI data, since the endorectal coil is not present during the CT imaging. The deformation in the MRSI data will prevent accurate anatomical coincidence when registering the deformed MRSI information with the non-deformed CT image data using standard, rigid-body image registration methods. To overcome this problem, two sets of MR images were acquired, one with the endorectal coil inflated and one with it deflated. Using the freely available 3D Slicer software package (www.slicer.org), an automatic deformable b-spline algorithm was used to register the combined MR/MRSI "inflated" data set to the "deflated" MRI data set (233). The corrected MR/MRSI data set was then imported via DICOM import into the Eclipse radiation treatment planning system version 8.6.17 (Varian Medical Systems, Inc., Palo Alto, USA). Using rigid registration techniques available on the treatment planning system the combined MR/MRSI containing the interpolated DIL region was co-registered with the CT image and contoured as a separate treatment volume.

6.2.7. IMRT planning

To determine the efficacy of using spectroscopic imaging data to perform more accurate radiation dose delivery to the target volume, we performed a retrospective comparison of two IMRT treatment plans of the prostate with and without the inclusion of ^{1}H-MRSI data. The first IMRT plan, which did not use the ^{1}H-MRSI data, followed the protocol used in a clinical trial (PROFIT). This IMRT plan, termed "IMRT-PROFIT" for this discussion, was the standard radiation treatment plan used throughout this study. Using the combined MRI/MRSI, we then identified a localized region of the prostate with a region of dominant metabolic activity (DIL), based on the (Cho+Cr)/Cit ratio exceeding 0.74. Using a modified TCP formula, which incorporates the ^{1}H-MRSI data, we then determined what dose distribution would enable equivalent control of the prostate cancer by escalating the dose to the localized DIL. Once the appropriate dose was calculated, a retrospective IMRT plan or "IMRT-DIL" was created. The TCP and NTCP for both plans were calculated, and compared. The following sections describe the process of creating the IMRT-PROFIT and IMRT-DIL plans while also discussing radiobiological assumptions that make it possible to incorporate the ^{1}H-MRSI data into the TCP calculations.

6.2.7.1. Initial IMRT treatment plan (IMRT-PROFIT)

An IMRT plan following the PROFIT trial was created for each subject in the study. The prescribed dose was 7800 cGy in 39 fractions. Additional planning

constraints that were imposed were as follows: (1) Clinical Target Volume (CTV) was limited to the prostate only, except for patients at greater than 15% risk of seminal vesicle involvement (Gleason Score 7 & PSA 4-20 ng/ml), (2) The planning target volume (PTV) was the CTV plus 10 mm in all planes except towards the rectum, where it was only 7 mm, and (3) For patients with more than 15% risk of SV involvement, the CTV included the proximal seminal vesicles. As laid out in the PROFIT trial, at least 99% of the CTV must receive the prescription dose and at least 99% of the PTV must receive at least 95% of the prescribed dose. The maximum dose to 1 cc of the PTV must not exceed 105% of the prescribed dose. The treatment plans consisted of seven equi-spaced beams and used the dynamic MLC ("sliding window") delivery method. Plans were generated using the inverse planning optimization algorithm of Eclipse (DVO version 8.6.14, Varian Medical Systems, Inc. Palo Alto, CA, USA), with the final dose calculation performed using the Eclipse analytical anisotropic algorithm (AAA) dose algorithm at a 2.5 mm dose grid resolution. Optimization objectives for the CTV, PTV and organ at risk structures (bladder wall, rectal wall and femoral heads) were given an initial priority of 100 and set at the protocol target values. Only the target structure priorities were adjusted (increased) if required to satisfy the protocol doses, i.e., no attempt was made to further minimize the organ at risk doses, as this was not the goal of the study.

6.2.7.2. Retrospective IMRT treatment plan with ^{1}H-MRSI data (IMRT-DIL)

The delineated DIL was treated as a simultaneous integrated boost clinical target volume and as such was given an associated planning target volume (DIL_PTV), created using the same expansions from the DIL as the CTV (10 mm all around except 7 mm posterior). Revised prescription doses were determined by the *specTCP* calculations as described in detail in the next section. Dose uniformity to the DIL and DIL_PTV, as well as the original CTV and PTV, was a planning goal using the revised prescription doses together with the aforementioned PROFIT constraints for organs at risk (OAR). Since the DIL and DIL_PTV boosted volumes were inherently "nested" within the CTV and PTV, the PROFIT-defined upper constraints on the latter were not physically achievable and therefore were removed. Therefore attempts were made in inverse planning to keep the doses to the CTV and PTV as close as possible to the revised prescription dose without compromising coverage of the DIL and DIL_PTV. As with the treatment plans for the non-^{1}H-MRSI data, the organ at risk objectives were given fixed priorities of 100 and no attempt was made to minimize the doses. Priorities for the targets were adjusted if required for dose homogeneity.

6.2.7.3. Radiobiological assessment using TCP and NTCP

To facilitate a comparison between the IMRT-PROFIT plans and the IMRT-DIL plans, the TCP and NTCP values were calculated for each plan. The NTCP values for the initial IMRT plans were calculated using the Lyman–Kutcher–Burman

model (for rectum-TD_{50}=80 Gy, n=0.12, m=0.15, bladder-TD_{50}=80, n=0.5, m=0.15 and femoral head- TD_{50}=65, n=0.25, m=0.12) (75, 234). For TCP calculations, the Poisson-based model of Tome and Fowler was used (83). The model parameters were taken from Wang *et al.* (α= 0.15 ± 0.04 Gy^{-1}, α/β =3.1±0.5 Gy) (80) for non-aggressive prostate cancer and Nahum *et al.* (α= 0.26 ± 0.06 Gy^{-1}, α/β =8.3 Gy) (235) for aggressive prostate cancer. The values for the number of clonogens were scaled between 10^5 cells/cc for normal prostate tissue and up to 10^7 cells/cc for aggressive tumour tissue (6, 236-238). The scaling of the TCP parameters will be discussed in the following section.

6.2.7.4. Modified TCP calculation

Using biological models to guide radiation treatment is a practical method to determine the relative effectiveness of radiation treatment plans. In typical treatment situations, one would assume a single set of biological parameters (i.e. α/β , number of clonogens, etc.) to describe all of the cancer cells uniformly within the radiation treatment volume. However, in certain cases the prostate cancer is localized to a specific sub-volume of the prostate (i.e. DIL) and is not homogeneous throughout the prostate. As well, the metabolic activity of the cancerous region is not homogenous throughout the volume of the tumour itself. Thus, making the assumption that the prostate cancer is spread homogeneously throughout the treatment is not accurate. Therefore, using a single set of radiobiological parameters may not correctly describe what is happening within the treatment volume, since

the location and metabolic activity of the tumour (i.e. the estimation of its aggressiveness) is heterogeneous throughout the treatment volume. To take advantage of what we have learnt from spectroscopic imaging of the prostate, we incorporated the metabolic spectroscopic imaging information into the TCP calculations by scaling the appropriate radiobiological parameters (i.e. alpha/beta, clonogen density) according to the (Cho+Cr)/Cit ratio measured within the prostate voxels.

From our current understanding of radiobiology, we know that for less aggressive tumours the α/β ratio is low, between ~1-4 Gy, while more aggressive cancers may have an α/β value greater than 10 Gy. Research by Wang *et al.*, suggests that the radiosensitivity parameters for slowly proliferating prostate cancers are, $\alpha = 0.15 \pm 0.04$ Gy^{-1}, $\alpha/\beta = 3.1 \pm 0.5$ Gy (80), while Nahum *et al.*, suggest for highly proliferating prostate cancers the radiosensitivity parameters are, $\alpha = 0.26 \pm 0.06$ Gy^{-1}, $\alpha/\beta = 8.3$ Gy (235). Furthermore, early studies by Steel *et al*. estimated that the clonogen density of cancerous tissue fell in the range of 10^5-10^7 cells/cc (236-238). In a research article by Shukla *et al*. that examined the metabolite ratios of prostate cancer tissue, they demonstrated that the (Cho+Cr)/Cit ratios can range from 0.6 ± 0.0 to as high as 7.9 ± 0.8 for voxels identified as prostate cancer (239).

In order to study the effect of incorporating the metabolite ratio information into treatment planning, we implemented modified, non-uniform radiobiological parameters in the TCP formalism as follows:

a) The metabolite ratio is related to the aggressiveness of the prostate cancer, which in turn is related to the cellular proliferation. For low (Cho+Cr)/Cit

ratios of ~0.6, we considered the prostate cancer to be slowly proliferating, and its radiosensitivity parameters were be approximated by values reported by Wang *et al*. (i.e. $\alpha = 0.15 \pm 0.04$ Gy^{-1}, $\alpha/\beta = 3.1 \pm 0.5$ Gy), while for high (Cho+Cr)/Cit ratios of ~7.9, we consider the prostate cancer to be proliferating more quickly, and its radiosensitivity parameters were approximated by values reported by Nahum *et al*. (i.e. $\alpha = 0.26 \pm 0.06$ Gy^{-1}, $\alpha/\beta = 8.3$ Gy)(5, 44). Using the (Cho+Cr)/Cit values of 0.6 and 7.9 as low and high endpoints respectively, a linear mapping of the α and α/β can be used to determine the appropriate radiosensitivity values for each voxel throughout the prostate.

b) The number of clonogens per unit volume linearly increases from a value of 10^5 cells/cm^3 for low α/β to 10^7 cell/cm^3 for high α/β, based on the work of Van Lin *et al*. (5).

Using a simple linear mapping, the radiosensitivity parameters for each spectroscopy voxel can be calculated independently such that $f_\alpha = 0.02*Met\_ratio + 0.14$, $f_{\alpha/\beta} = 0.71*Met\_ratio + 2.7$, and the number of clonogens, $f_N = 1x10^6*Met\_ratio$. These relationships were derived performing a linear interpolation between endpoints. For example, to determine the function, $f_{\alpha/\beta}$, we calculate the line equation using a set of two points (x_1, y_1) and (x_2, y_2) where $x_1=0.6$, $x_2=7.9$, $y_1=3.1$ and $y_2=8.3$. Where the slope is the Met_ratio (Cho+Cr/Cit ratio) calculated by LCModel. It should be noted that a linear mapping was chosen arbitrarily, and the

true mapping may not be linear, although the results will not be strongly dependent on this relationship as long as a monotonically increasing function is used.

Using a common formulism of TCP, based on the Poisson distribution:

$$TCP = \prod_{i=1}^{N} TCP_i = \exp\left[-\sum_{i=1}^{N} v_i \rho_i (\alpha n_f d_i \left(1 + \frac{d_i}{\alpha / \beta} \right) e^{\gamma_i (T - T_{lag})} \right] \quad (6.1)$$

where p_i denotes the number of tumour clonogens per cm^3 in the i^{th} tissue region, v_i is the volume of the i^{th} tissue region, d_i is fractional dose in the i^{th} tissue region, α and α/β are the relative measures of tissue sensitivity to fractionation and to the size of the fraction given during each treatment, n_f is the number of fractions, N is the number of voxels in the target structure, γ_i is the rate constant which is related to the tumour doubling time (T_d) via $\gamma_i = ln(2)/T_d$, T is the overall time to complete the treatment, and T_{lag} is the time interval in which accelerated repopulation will occur. For all calculations, T_d=42 days, and T_{lag}=0, based on Wang *et al.* (80). It should be noted that ideally the T_d parameter would also be defined using the metabolite ratio data, but there is a lack of information in the literature about what this value should be for aggressive prostate cancer. Including the linear variability of the radiosensitive parameters, equation 6.1 now becomes:

$$specTCP = \exp\left[-\sum_{i=1}^{N} f_N v_i (f_\alpha n_f d_i \left(1 + \frac{d_i}{f_{\alpha/\beta}} \right) e^{\gamma_i (T - T_{lag})} \right] \quad (6.2)$$

where *specTCP* is the modified tumour control probability that incorporates the radiobiological parameters based on the spectroscopic imaging data in each voxel. All parameters are the same as in equation 6.1, with the addition of f_N, f_α and $f_{\alpha/\beta}$

which are the radiobiological parameters that incorporate the spatial mapping of spectroscopic imaging.

6.2.7.5. Dose Predictions based on TCP calculations

Incorporating spectroscopic data into the selection of radiobiological parameters, on a voxel-by-voxel basis, will alter the TCP when compared to the standard approach of using uniform radiobiological parameters across the entire prostate. We calculate how the TCP will change when incorporating non-uniform radiobiological parameters. We anticipate using a non-uniform TCP will decrease the TCP. To compensate for a change in TCP, we determine, through computer simulation, what additional dose would be needed to achieve the same TCP used in current treatments. To estimate the required therapeutic dose TCP and dose calculations were performed based on three scenarios:

1) Standard IMRT plan using PROFIT protocol with no DIL, delivering a perfectly uniform dose to the target (78Gy to CTV, and uniform number of clonogens throughout the CTV-10^5 cells/cm^3, $\alpha = 0.15 \pm 0.04$ Gy^{-1}, $\alpha/\beta = 3.1 \pm 0.5$ Gy). TCP is calculated with equation 6.1.

2) Standard IMRT plan using PROFIT protocol with DIL identified by combined MRI/MRSI data, delivering a perfectly uniform dose to the target (78Gy to CTV+DIL; Linearly varying radiosensitivity parameters). TCP is calculated with equation 6.2.

3) Modified IMRT plan using PROFIT protocol with DIL identified by combined MRI/MRSI data, delivering a particular uniform dose to the DIL and a

different uniform dose to the remainder of the target structure. The dose levels to the DIL and remainder of the target structure were set to maintain the TCP calculated with the conventional estimates in scenario 1 (above). An iterative sub-routine was written such that the dose to the entire prostate was initialized to a dose of 78Gy over the prostate. Next, the dose to DIL was incrementally increased until the TCP response from the DIL was effectively removed (i.e. change in TCP response was <0.1%). The dose to the remainder of the CTV structure was then incrementally modified to match (within 0.1%) the TCP calculated in scenario 1, and this dose value was identified as the required prescription dose for the prostate CTV (excluding DILs). In this manner, the required prescription dose to the DIL and the remainder of the structure were set to reproduce the TCP in scenario 1 (above). Note that linearly varying radiosensitivity parameters were used with the *specTCP* formalism in equation 6.2.

The theoretical dose increase needed to recover the standard TCP calculation was then used as the prescription dose for the seven patient IMRT-DIL treatment plans, and compared to the standard IMRT-PROFIT plans.

6.3. Results

In this study we examined the IMRT planning of 7 subjects who met the inclusion criteria of the PROFIT trial. The age, disease pathology, and treatment volumes are presented in Table 6.1. The average prostate volume was 45.5±14.2 cm^3 with a range in values from 25.8 to 69.3 cm^3. The contours for the prostate and DIL (both PTV and CTV) are displayed for all three axes in Figure 6.1. Each plan used a standard 7-beam approach, with beams angles of 0, 51, 102, 153, 204, 255, and 306 degrees as illustrated in Figure 6.2.

Table 6.1 Subject scheduled for IMRT PROFIT clinical trial

				Treatment Volumes					
				Targets		Organs at Risk			
Subject	Age (years)	PSA (g/ml)	Gleason Score	Prostate CTV (cm3)	DIL volume (cm3)	Bladder wall (cm3)	Rectal Wall (cm3)	Right Femoral Head (cm3)	Left Femoral Head (cm3)
1	83.0	11.3	7.0	35.7	7.1	29.9	25.8	87.9	86.3
2	71.0	14.0	7.0	45.8	10.2	23.0	17.2	100.0	93.9
3	65.0	13.0	7.0	55.8	2.8	28.4	25.8	53.1	55.3
4	65.0	9.7	6.0	47.2	4.1	27.0	23.6	79.4	67.5
5	57.0	15.4	7.0	38.9	2.3	10.9	24.4	62.2	61.2
6	65.0	7.7	6.0	69.3	4.4	27.5	29.3	73.3	70.1
7	71.0	9.9	7.0	25.8	2.9	8.1	23.4	74.6	71.9

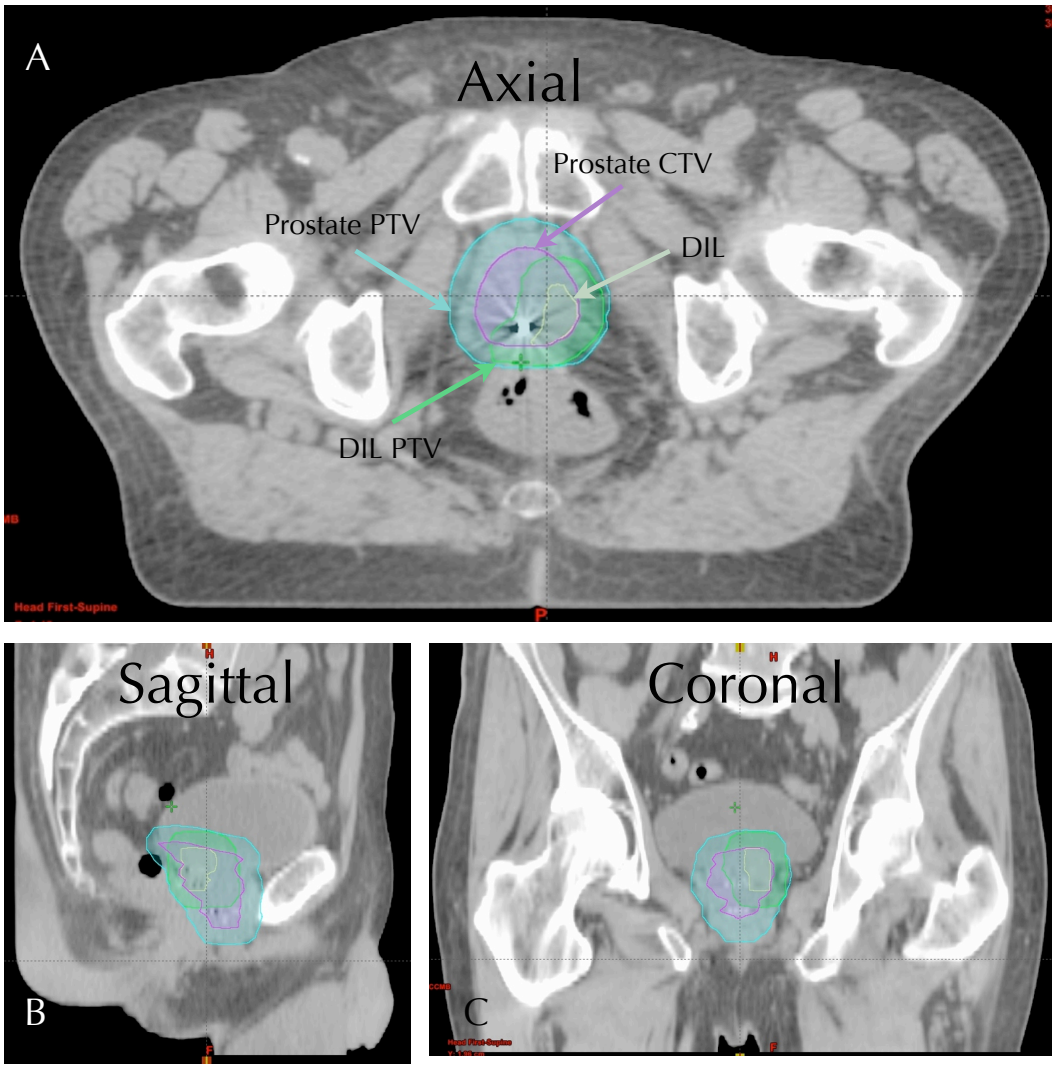

Figure 6.1 Contours of target structure showing CTVs and DILs
Contours of target structure from subject one, showing CTVs and DILs (A-axial, B-sagittal, and C-coronal). Expansions specified by the PROFIT trial were used for the DIL and CTV (10 mm all around except 7 mm posteriorly).

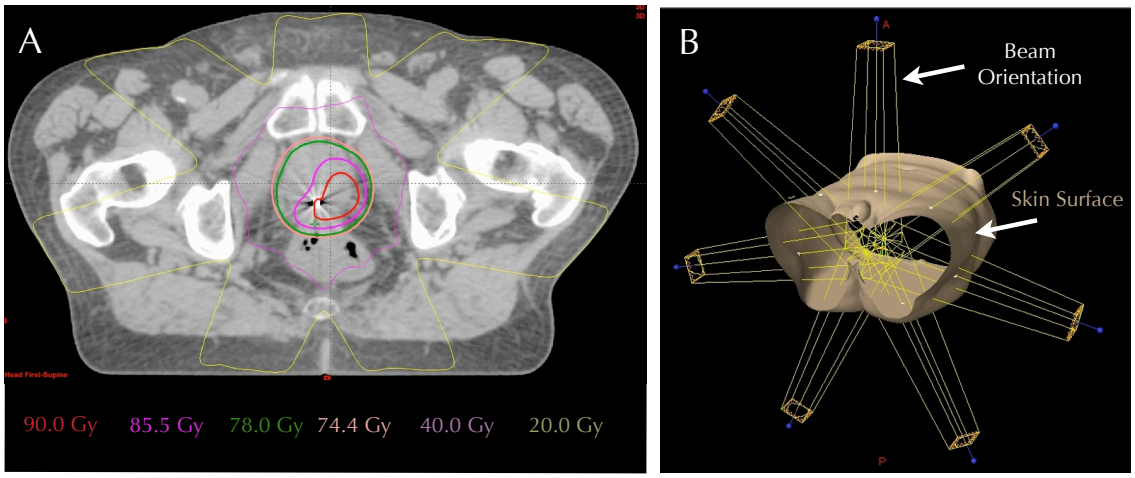

Figure 6.2 Isodose lines for 7 field IMRT-DIL retrospective treatment
Isodose lines for 7 field IMRT-DIL treatment (A-axial, B-sagittal, and C-coronal).

6.3.1. TCP calculations and predicted doses

We present results of the three different treatment scenarios in Table 6.2. In the first scenario assuming the standard plan and conventional uniform radiobiological parameters as described in section 6.2.7.5 (above), we observe that the average TCP is 96.5%±1.4%, ranging in value from 94.4% to 98.3% over all subjects. In the second scenario described in section 6.2.7.5 (above), we include the impact of the spectroscopic data on the radiobiological parameters, while applying the standard plan to keep the target dose uniform. Each voxel was assigned unique radiobiological parameters based on the metabolite ratio determined by LCModel (i.e. α, α/β, T_d and number of clonogens) (see Figure 6.3). Over all patients, the TCP was reduced on average by 8.6%±4.9% (range 2.8%-15.3%). The average TCP was calculated as 87.9%±5.9% (range 79.1%-95.5%). In the third scenario, described in section 6.2.7.5 (above), we present results using the modified specTCP calculation and adjusting the delivered

dose to achieve the same TCP values as calculated in scenario one. The required dose to achieve similar TCP estimates, as compared to the standard uniform parameter assumptions, was calculated to be between 81-83 Gy to the prostate CTV, and between 85-87 Gy for the DIL, over all subjects. These doses represent an estimate of how much the therapeutic dose should be increased in order to maintain the current estimate of tumour control probabilities. They were used as starting points for the retrospective IMRT treatment plans using ^{1}H-MRSI data as described in the next section.

Table 6.2 Dose Predictions based on TCP calculations

Scenario One: Uniform dose to prostate, 78 Gy, uniform radiobiological parameters	
Standard IMRT plan using PROFIT protocol with no DIL (78Gy to CTV, and uniform number of clonogens throughout the CTV-105 cells/cm3, $\alpha = 0.15 \pm 0.04$ Gy^{-1}, $\alpha/\beta = 3.1 \pm 0.5$ Gy)	
Subject	Predicted TCP (%)
1	97.4
2	96.7
3	94.4
4	96.0
5	97.7
6	95.1
7	98.3
Scenario two: Uniform dose to prostate and DIL, 78 Gy, non-uniform radiobiological parameters	
Standard IMRT plan using PROFIT protocol with DIL identified by combined MRI/MRSI data (Linearly varying radiosensitivity parameters, using *specTCP* formalism)	
Subject	Predicted TCP (%)
1	90.3
2	81.4
3	79.1
4	87.3
5	92.4
6	89.4
7	95.5

Table 6.2 continued

Scenario three: Dose to prostate and DIL optimized to restore original estimate of TCP in scenario one.			
Modified IMRT plan using PROFIT protocol with DIL identified by combined MRI/MRSI data. The dose to the CTV and DIL were incrementally modified to match the TCP in scenario one, while keeping the dose to the DIL less than or equal to 90Gy. (Linearly varying radiosensitivity parameters, using specTCP)			
Subject	Prostate (Gy)	DIL (Gy)	TCP to match (%) (from scenario #1)
1	82	87	97.4
2	82	88	96.7
3	82	86	94.4
4	81	86	96.0
5	81	85	97.7
6	83	87	95.1
7	80	86	98.3

6.3.2. Initial IMRT treatment plan without ^{1}H-MRSI data (IMRT-PROFIT)

The results from the standard treatment plans are presented in Table 6.3. Using the treatment plan metrics put forward by the PROFIT trial, the TCP was calculated using the parameters from scenario one (i.e. uniform spread of disease through the prostate) and the actual voxel-by-voxel doses to the prostate as estimated in the treatment plan. The mean dose to the prostate CTV ranged from 78.6 to 79.7 Gy. Similar to the predicted TCP values calculated in scenario one, the measured TCP for the initial IMRT-PROFIT plan resulted in a mean TCP of 97.1% ±1.1% with values ranging from 95.6-98.6%. This result was comparable to the theoretically predicted value.

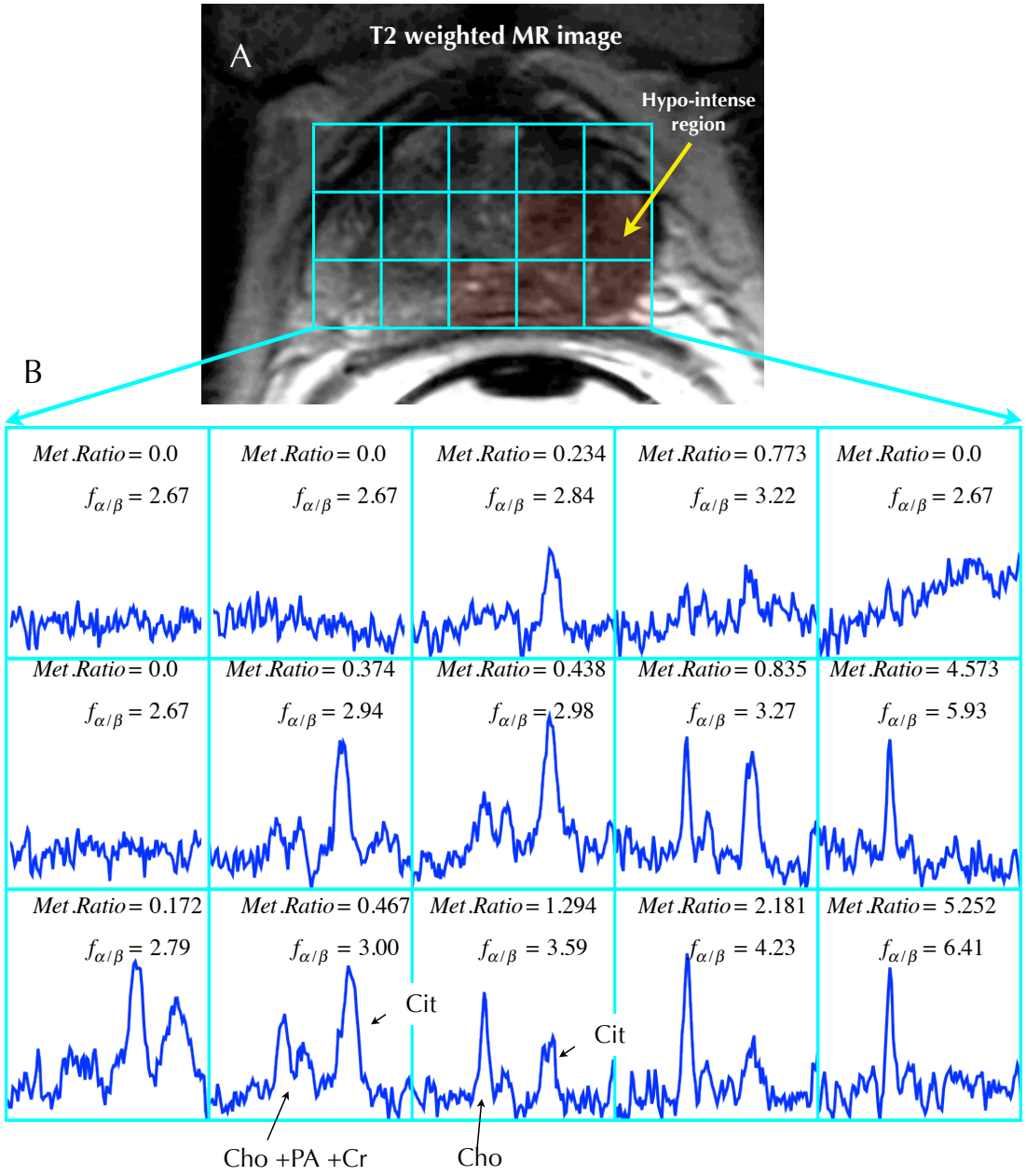

Figure 6.3 Metabolite ratio map with scaled α/β ratios

*(A) A T2 weighted image taken from a 65 year old male diagnosed with prostate cancer (subject 4, PSA=9.7 ng/ml, Gleason score =6), demonstrating a hyper-intense region along the right peripheral zone. (B) Metabolite ratio map with scaled α/β ratios for each voxel. 1H-MRSI confirmed the presence of prostatic cancer including a DIL. The metabolite ratio calculated by LCModel was used to determine the appropriate α/β ratios for each voxel, using the formula $f_{\alpha/\beta}$=0.71*Met_ratio +2.7 (Met_ratio is the (Cho+Cr)/Cit ratio determined by LCModel) as discussed in section 6.2.7.4.*

Table 6.3 IMRT-PROFIT and IMRT-DIL treatment planning results (Part 1)

	IMRT-PROFIT		IMRT-DIL			
	Prostate-CTV		Prostate-CTV	Prostate-CTV (without DIL)	DIL	
Subject	Mean Dose (Gy)	TCP (%)	Mean Dose (Gy)	Mean Dose (Gy)	Mean Dose (Gy)	TCP (%)
1	78.7	97.5	86.0	83.7	88.6	98.4
2	78.8	96.9	87.3	84.6	89.1	97.9
3	78.8	96.2	84.9	83.6	86.9	96.1
4	78.7	96.7	84.2	83.1	87.6	97.2
5	79.7	98.1	83.6	82.4	85.8	98.4
6	79.0	95.6	86.5	84.3	86.8	98.9
7	79.5	98.6	84.8	82.4	87.4	99

6.3.3. Retrospective IMRT treatment plan with ^{1}H-MRSI data (IMRT-DIL)

The results from the retrospective treatment IMRT plans including the DIL information (IMRT-DIL) are also shown in Table 6.3. The mean dose to the prostate CTV was 85.3±1.3 Gy over all subjects, ranging from 83.6 Gy to 87.3 Gy. Removing the DIL from the prostate CTV volume results in a slightly lower mean dose of 83.4±0.9 Gy (range 82.4 Gy to 84.6 Gy). Additionally, the mean dose to the DIL over all subjects was 87.5±1.1 Gy (range 85.8 Gy to 89.1 Gy). This resulted in mean TCP values of 98.0±1.0% over all subjects (range 96.1% to 99.0%). The TCP values calculated using the treatment plans including the DIL and the spectroscopic data are comparable to, but slightly higher than, the predicted TCP values achieved by delivering uniform dose and assuming uniform radiobiological parameters. The slight increase in calculated TCP is due to the fact that the increased dose to the DIL is not delivered as an ideal step function, but rather spills

over a small amount into the remainder of the prostate CTV, thus providing slightly improved TCP estimates.

The radiation treatment plans developed for the IMRT-DIL scenario all met the minimum dose criteria for organ's at risk specified by the PROFIT trial. The target dose volume histograms (DVH) (see Figure 6.4) demonstrate a tight conformity of the prescribed dose. In Figure 6.5 the DVHs for the organs-at-risk are displayed. Comparing both plans, the mean dose to the bladder, rectum, and femoral heads was comparable and did not significantly change, although maximum point dose values increased 5-7 Gy due to the higher prescription doses in the IMRT-DIL plans. Lastly, the resulting NTCP values for the bladder, rectum, right and left femoral heads are presented in Table 6.4. For the IMRT-PROFIT plan, the NTCP values for the bladder ranged from 1.1% to 3.6%, while for the IMRT-DIL plan the NTCP had a slightly larger range from 0.8% to 3.2%, but did not statistically differ. A similar outcome was also observed for the rectum, right femoral and left femoral head structures.

Table 6.4 IMRT-PROFIT and IMRT-DIL treatment planning results (Part 2)

	IMRT-PROFIT							
	Bladder		Rectum		Right Femoral Head		Left Femoral Head	
Subject	Mean Dose (Gy)	NTCP (%)	Mean Dose (Gy)	NTCP (%)	Mean Dose (Gy)	NTCP (%)	Mean Dose (Gy)	NTCP (%)
1	43.7	1.1	46.8	2.0	15.6	1.3	15.9	1.7
2	39.3	3.6	48.7	1.8	14.1	0.4	21.8	1.2
3	47.1	2.5	50.0	4.1	19.2	2.5	34.3	0.1
4	41.2	1.9	54.1	2.0	20.4	1.9	25.1	3.0
5	47.3	2.4	50.0	3.8	15.3	0.2	19.5	2.0
6	38.2	1.2	48.5	3.4	14.9	0.3	18.8	2.0
7	52.8	2.7	51.9	5.3	6.7	0.0	6.9	0.0

	IMRT-DIL							
	Bladder		Rectum		Right Femoral Head		Left Femoral Head	
Subject	Mean Dose (Gy)	NTCP (%)	Mean Dose (Gy)	NTCP (%)	Mean Dose (Gy)	NTCP (%)	Mean Dose (Gy)	NTCP (%)
1	43.5	1.0	47.5	2.3	15.0	0.8	15.2	0.9
2	36.6	1.1	48.7	1.8	13.3	0.2	21.4	0.9
3	44.2	0.8	50.7	4.7	22.0	0.1	19.3	0.0
4	39.7	1.0	52.4	1.4	19.9	1.3	24.8	2.6
5	48.1	3.2	51.3	5.0	15.6	0.3	19.5	2.1
6	39.8	2.4	50.1	4.8	15.3	0.5	19.4	3.2
7	50.9	1.5	51.9	5.3	6.0	0.0	6.2	0.0

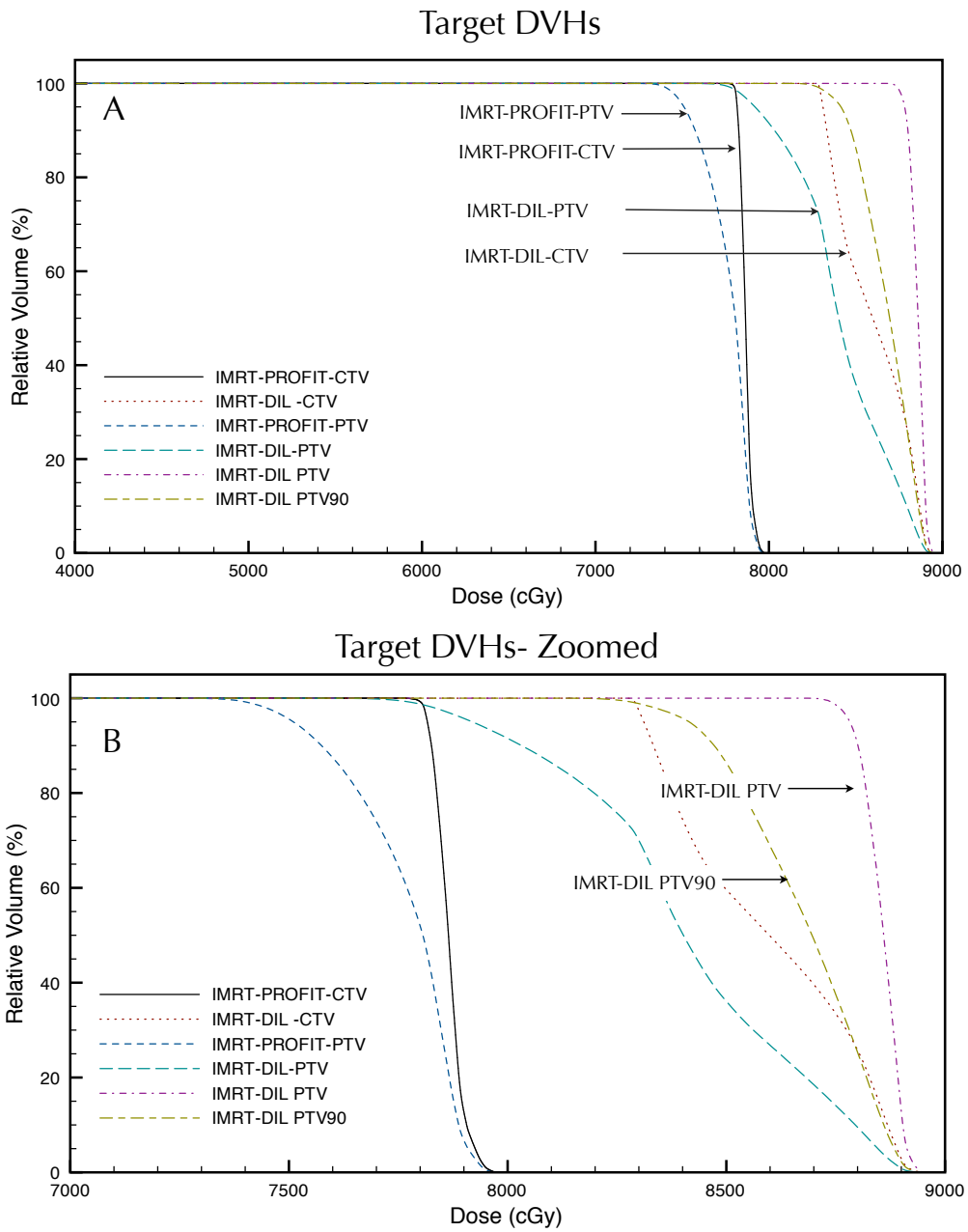

Figure 6.4 Target DVHs

In (A), the dose volume histograms for the CTV and PTV are shown for both treatment plans. In the case of IMRT-DIL treatment plan, the increased dose to the targets, including the DIL, is demonstrated. In (B), the dose volume histogram is magnified to examine the high dose region containing the DIL and DILPTV90 curves. The DIL has a sharp drop-off at 116 percent of the 78 Gy prescribed dose, with a mean dose of 88.6 Gy, and a D_{99} of 87.4 Gy.

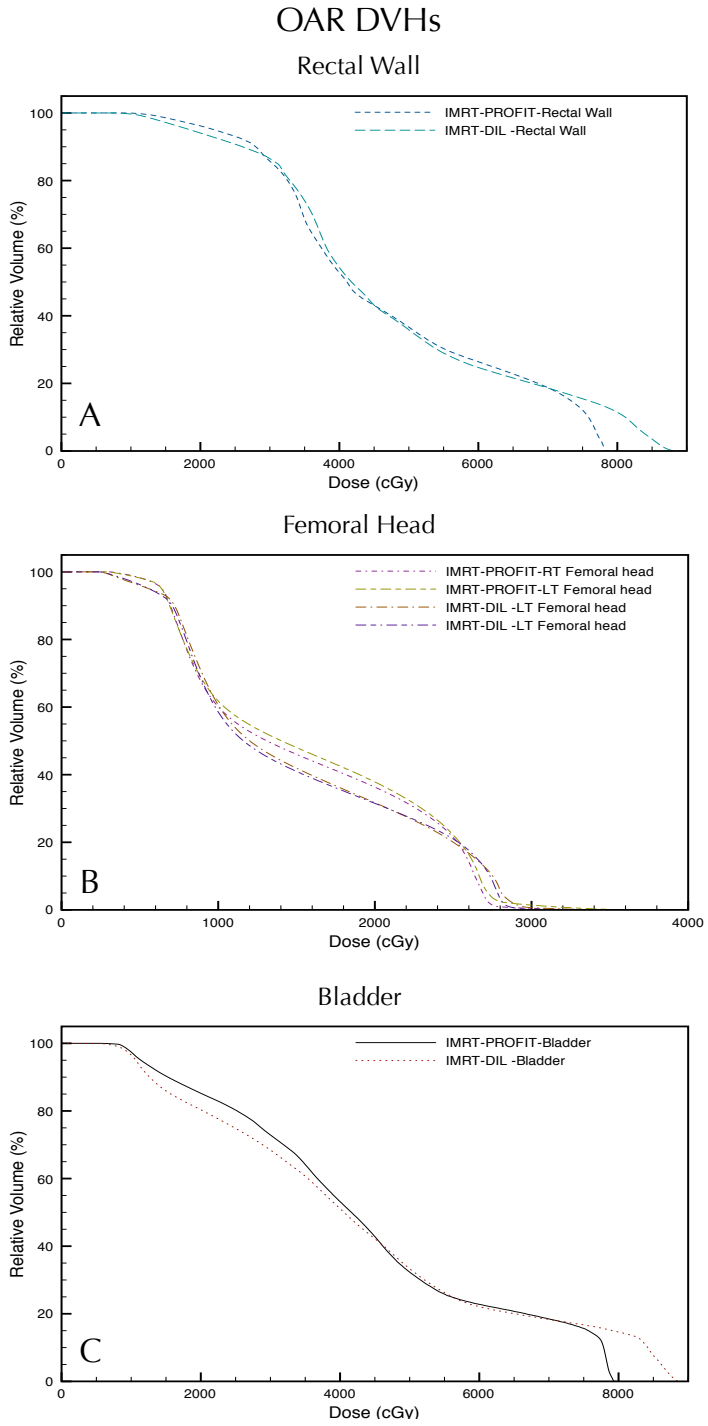

Figure 6.5 Organs at risk DVHs

Following the treatment protocol set out by the PROFIT protocol, both plans were able to meet the dose constraints of the bladder, rectum, right and left femoral heads. These constraints are: (A) Rectal wall – 50% to receive less than 53 Gy, and 70% to receive less than 71 Gy, (B) Femoral head – less than 5% to receive more than 53Gy, and (C) Bladder wall- 50% to receive less than 53 Gy, and 70% to receive less than 71 Gy.

6.4. Discussion

In this study we have demonstrated a novel way to incorporate the ^{1}H-MRSI data into the radiation treatment planning of prostate cancer. Using standard methods in deformable registration, we were able to register the MRI/MRSI data to the CT planning data on the treatment planning system. Using the combined MRI/MRSI, a DIL was delineated and contoured on the treatment planning system. Following the image registration, we then used the ^{1}H-MRSI data to better estimate the radiobiological model parameters on a voxel-by-voxel basis. Assuming the radiobiological parameter mapping was linear, the modified specTCP formula was then used to determine the appropriate additional dose required by the prostate CTV and DIL that was needed to obtain similar TCP values to those that would be obtained using a standard PROFIT protocol IMRT plan (without overdosing the DIL and surrounding OARs).

Recently, Van lin *et al*. demonstrated the use of ^{1}H-MRSI data for the delineation of the DIL, and reported boosting the DIL to 90 Gy while lowering the dose to the remainder of the prostate to ~70 Gy (72). In their study, which compared two IMRT plans (plan one: 70Gy to the prostate and 90Gy to the DIL; plan two: 78 Gy to the prostate) there was marginal improvement in the TCP going from a lower dose to a higher dose. This is mainly attributed by the reduction of dose to the entire prostate. In comparison to IMRT, brachytherapy is also able to deliver a localized boost to the intraprostatic lesions defined by combined MRI/MRSI (72, 230). In summary, there have been several studies that have looked at

methods of incorporating ^{1}H-MRSI data into the radiation treatment planning of prostate cancer (72, 139, 226, 227, 230). While in these studies the combined MRI/MRSI data was used to delineate the DIL and the dose administered was derived using TCP calculations, they did not directly use the metabolic information from spectroscopic imaging. While accurately targeting the disease is clinically important, there may be added benefit in incorporating biological information regarding the tumour aggressiveness to determine the necessary dose to maximize the TCP.

In comparison to previous studies, this work utilizes the ^{1}H-MRSI information in a novel manner: to directly estimate the tumour proliferation and tumour aggressiveness by incorporating it directly into the TCP calculation. Optimizing the required prescription dose based on the modified TCP equation (equation 6.2) may allow for better tumour control for aggressive cancer. Over all subjects studied here, we observed that an increased dose can be delivered to intraprostatic lesions along with a slightly higher dose to the entire prostate to ensure a high TCP, while keeping the NTCP for rectum, bladder, right and left femoral heads comparable to the standard, lower dose plans.

To reach this point, we assumed that the radiobiological parameters such as α, α/β, and the number of clonogens vary linearly with metabolite ratio. There are few studies that have examined the functional relationship between metabolite ratio derived from ^{1}H-MRSI and radiobiological estimations of TCP and NTCP. Using a simple linear relationship appears to be a reasonable approximation. In a similar way, Wang *et al.* (72) also proposed a linear relationship between tumour

aggressiveness (as estimated using the proliferating cell nuclear antigen) and prostate cancer metabolite ratio (Cho+Cr)/Cit (as estimated with ^{1}H-MRSI).

The work done by Zelefsky *et al*. laid the groundwork for utilizing prostate dose escalation methodologies to reach better long-term treatment outcomes, using doses that ranged from 66-86.4 Gy (240). In this study we demonstrate that when including the spectroscopic imaging data we observed an average decrease of 8.6%±4.9% (range 2.8%-15.3%) in TCP when compared to the standard IMRT-PROFIT plan (i.e. going from scenario 1 to scenario 2). To compensate for the decrease in TCP we calculate the optimal dose required to reproduce the TCP in the standard plan. The mean dose for the entire prostate was 87.5±1.1 Gy and ranged between 83.6 Gy to 87.3 Gy. These estimations fall within the clinically acceptable prescription doses that have been shown to have good clinical outcomes for intermediate-risk prostate patients. It is important to note that the dose escalation strategy proposed here represents an increase in TCP from scenario 2 to scenario 3 (use of ^{1}H-MRSI for radiobiological modeling combined with dose escalation), of approximately 9%. This would represent a significant improvement in patient outcomes.

Our results also indicate that it may not be necessary to go to very high doses to achieve adequate tumour control (i.e. in excess of 90 Gy) as described by other work (72, 73, 215, 216, 230). The modified prescription doses proposed here have been derived based on radiobiological calculation from spectroscopic imaging data, as opposed to simply escalating to an arbitrarily high value. Our approach provides for a better optimization of target dose versus critical structure

dose. Escalating the dose brings about certain challenges in the practical delivery of radiation, such as not exceeding the radiation tolerance of surrounding critical structures such as the rectum, bladder, and femoral heads. In our study, we show that it is feasible to escalate the dose to the prostate, while minimizing the dose to the OARs. Over all subjects we were able to meet the PROFIT tolerance criteria for irradiation of critical tissues. As seen in Figures 6.5(A-C), the DVHs for both the IMRT-PROFIT and IMRT-DIL plans demonstrate good dose conformity to the targets while minimizing dose to the critical structures.

One of the challenges to implementing a biologically guided radiation treatment is the day-to-day practical targeting of dose to the target volume and minimization of the dose to critical structures. We assume at the time the radiation treatment plan is prepared the prostate is in a stationary position. As such, all of planning is based on a static snapshot of the treatment position. In reality, we know from clinical experience that the daily position of the prostate may change, and that during treatment, motion induced by breathing, and rectal filling may significantly change the position of the prostate. The motion of the prostate poses a particularly difficult problem for radiation dose escalations, since it may cause unwanted delivery of high doses to critical structures. While this problem is outside the scope of this work, many centres are examining the use of daily imaging techniques to better assess prostate motion during radiation treatment. Including inter- and intra-fraction imaging has been shown to improve the delivery accuracy of biologically guided radiation treatment plans (241-244).

In this study, we have shown the feasibility of using spectroscopic imaging data to calculate the appropriate dose needed to achieve equivalent TCP of the prostate as calculated with the standard radiation plan and uniform radiobiological parameters.This approach is estimated to improve tumour control by approximately 9% on average for this group of patients. While this study has shown the feasibility of incorporating this type of biological information, a full clinical trial with a much larger patient pool would be needed to determine the long-term clinical efficacy of utilizing biologically guided radiation treatment.

6.5. Conclusion

In conclusion, we have derived a method that better characterizes the TCP for the purpose of estimating accurate dose-escalation strategies for the IMRT treatment planning of the prostate. A retrospective radiation treatment planning study was done for 7 subjects who were enrolled in the PROFIT trial in our clinic. Each subject underwent routine CT simulation, followed by a combined MRI/MRSI scan. Modifications to the TCP model were made to incorporate the ^{1}H-MRSI data, such that the relative radiobiological parameters varied linearly with the ^{1}H-MRSI data on a voxel-by-voxel basis. Two IMRT plans were created and compared with and without the modified TCP model. The first plan was a standard 7 field IMRT plan with a uniform dose of 78 Gy applied to the prostate. The estimated TCP, not including any information from ^{1}H-MRSI demonstrated a mean value of 97.1% ±1.1%. We next incorporated the ^{1}H-MRSI data to the first plan, and recalculated the TCP with a more realistic estimate of the relative radiobiological parameters

over each spectroscopy voxel throughout the prostate. The TCP was reduced by approximately ~9%, indicating that the variation of the cancer over the tumour volume may not be accurately assessed using current methods. Utilizing the spectroscopy-determined radiobiological parameters, the dose was methodically increased in the dominant intraprostatic lesion and the remainder of the prostate until the original estimate of TCP was recovered. Based on the higher revised prescription doses, the standard 7 field IMRT plans for the PROFIT patients were retrospectively modified to include the dominant intraprostatic lesions (DILs) identified by combined MRI/MRSI. For the second set of IMRT plans the prostate CTV received a mean dose of 85.3±1.3 Gy (range 83.6 Gy to 87.3 Gy) and the DIL received a mean dose of 87.5±1.1 Gy. The average TCP for the IMRT-DIL plans was 98.0%±1.0% (range 96.1%-99.0%), a small improvement in the TCP when compared to the initial IMRT plan. Despite boosting the dose to the prostate CTV and DIL, these plans had similar NTCP outcomes compared to the standard plan, and there was no increase in the dose to the bladder, rectum, right and left femoral heads. The result of this study indicates that optimizing the dose to the prostate according to ^{1}H-MRSI information is possible, and that it can be used to logically derive new prescription doses leading to improved TCP.

Chapter 7

Discussion

In this last chapter we summarize the major results that were achieved in this thesis, and discuss future work. We conclude that this thesis has been beneficial in improving the methods for diagnosing prostate cancer by implementing a robust spectroscopic imaging technique and retrospectively assessing an optimal radiation treatment strategy for potentially better treatment outcomes.

7. Discussion

Over the last two decades a significant amount of work has been done to examine the use of combined MRI/MRSI methods to aid in the diagnosis of prostate cancer (18, 72, 130, 183, 192, 209, 245-248). The result of this effort, including the work done in this thesis, has demonstrated that combined MRI/MRSI can identify and delineate small regions of well-defined cancers within the prostate. As combined MRI/MRSI techniques have now become clinically feasible, several centers are starting to explore the clinical applications of this data for diagnosis and treatment of prostate cancer (72, 230, 247, 249, 250).

The acquisition of ^{1}H-MRSI data is a multi-step process (i.e. shimming of the B0 field, modifications to the pulse sequence for optimal water and lipid suppression, etc.). Each step is important for the acquisition of ^{1}H-MRSI data that are artifact-free and have optimal SNR. In this thesis the CV-MRS technique was examined as method to reduce lipid contamination at both long and short echo times prior to PRESS excitation. The optimized CV-MRS technique was experimentally tested with phantom experiments and then was verified through *in vivo* human experiments, which determine the efficacy of the technique. Furthermore, the technique was validated with histopathological data, and ^{1}H-MRSI data collected using the improved technique was incorporated in a novel way to help improved the assessment of radiation treatment planning of the prostate.

The next sections revisit some of the main results from each major work discussed in this thesis and also provide some additional comments regarding future directions.

7.1. Summary of Work

In chapter 2 the technical development of a modified OVS sequence that includes a variable number of spatial saturation planes that are optimized for spatial position, T_1-regrowth, and temporal ordering was described. Specifically, optimizations to the flip angles of all VSS pulses to account for the lipid regrowth due to T_1 processes were made. To counter balance the effects of modified flip angles and overlapping saturation pulses, an optimal ordering routine was introduced to minimize residual lipid magnetization. To help further reduce lipids at short echo time acquisitions, the pulse sequence was modified to incorporate a spectral-spatial RF excitation pulse, which nulls specific spectral components (i.e. water and lipids). Additionally, a modified version of the CV-MRS algorithm was implemented that uses advanced surface simplification methods and provided a significant speedup in the calculation of saturation plane locations (currently executing in less than one second). The modified software tool provides a much better user experience, and allows for improved viewing and manipulation of individual VSS planes.

From the experimental phantom work, it was shown that in both single voxel and multi-voxel acquisitions the CV-MRS technique significantly reduced lipid-

contaminating effects from peripheral lipids. On average we were able to reduce contaminating lipids by approximately 80% over all voxels within the ROI. To confirm that the CV-MRS technique has no deteriorating effect on the spectra, spectra with- and without the CV-MRS technique were acquired and demonstrated that there were no changes in the spectral shape or SNR. All metabolite peaks were fit with a modified version of LCModel using a simulated basis set. For both single and multi-voxel experiments, spectra acquired at short echo times demonstrated the expected phase of the inner and outer peaks of citrate and was accompanied by good quality LCModel fits. To reduce the analysis time, a UNIX shell scripts was written to take advantage of the multi-processor computer architecture. Doing this dramatically reduced the analysis time from ~45 minutes to ~5 minutes per data set. Lastly, the SNR map along the axial direction was calculated and demonstrated the expected SNR improvement near the peripheral zone when compared to the central/anterior zones of the prostate. In summary, in chapter 2 several phantom experiments were performed to test the modifications to the pulse sequence. These tests demonstrated effective nulling of contaminating signals from peripheral lipids while not interfering with the spectral shape. This yielded an effective technique that was ready for *in vivo* testing.

Following the phantom testing described in the Chapter 2, *in vivo* testing of the CV-MRS technique at both long (Chapter 3) and short (Chapter 4) echo times was performed. As previously discussed, an important step in the implementation of three-dimensional *in vivo* proton magnetic resonance spectroscopic imaging (^{1}H-MRSI) of the prostate is the placement of spatial saturation pulses around the region

of interest (ROI) for the removal of unwanted contaminating signals from peripheral tissue. In Chapter 3, the first use of the CV-MRS technique was demonstrated for the acquisition of *in vivo* ^{1}H-MRSI data. This method automates the placement, orientation, timing, and flip angle of very selective saturation (VSS) pulses around an irregularly shaped, user-defined ROI. The method employs a user adjustable number of automatically positioned VSS pulses (20 used in this study), which null the signal from periprostatic lipids while closely conforming to the shape of the excitation voxel to the shape of the prostate. A standard endorectal coil in combination with a torso phased array coil was used for all *in vivo* prostate studies. Three-dimensional *in vivo* prostate ^{1}H-MRSI data were obtained using the proposed semi-automated CV-MRS technique and compared with a standard PRESS technique at TE=130 ms using manual placement of saturation pulses. The *in vivo* prostate ^{1}H-MRSI data collected from 12 healthy subjects using the CV-MRS method showed significantly reduced lipid contamination throughout the prostate, and reduced baseline distortions. On average there was a 50±17% (range 12% – 68%) reduction in lipids throughout the prostate. A voxel-by-voxel benchmark test of over 850 voxels showed that there were 63% more peaks fitted using LCModel when using a Cramer-Rao Lower Bound cut-off of 40% when using the optimized conformal voxel technique in comparison to the manual placement approach. The evaluation of this CV-MRS technique demonstrated the potential for easy automation of the graphical prescription of saturation bands for use in ^{1}H-MRSI.

Following the successful execution of the technique at long echo times (TE =130ms), we continued with collection of data at short echo times (TE=40ms).

Visualization of short echo time metabolites in prostate magnetic resonance spectroscopic imaging is difficult due to lipid contamination and pulse timing constraints. In Chapter 4, the CV-MRS technique was used in combination with spectral-spatial excitation to permit short echo time (TE=40ms) acquisitions with reduced lipid contamination for the detection of short TE metabolites. Metabolites were measured and assessed using a modified version of LCModel for analysis of *in vivo* prostate spectra. In this chapter the feasibility of acquiring high quality spectra at short echo times was demonstrated, which showed the measurement of short TE metabolites myo-inositol, scyllo-inositol, taurine, and glutamine/glutamate for both single and multi-voxel acquisitions. In single voxel experiments, the reduction in echo time resulted in a 57% improvement in the signal-to-noise ratio (SNR). Additional 3D MRSI experiments comparing short (TE=40ms), and long (TE=130ms) echo time acquisitions revealed a 35% improvement in the number of adequately fitted metabolite peaks (775 voxels over all subjects). This resulted in a 42±24% relative improvement in the number of voxels with detectable citrate that were well-fitted using LCmodel. In summary, we demonstrated that high quality prostate spectra can be obtained by reducing the echo time to 40ms to detect short T_2 metabolites, while maintaining positive signal intensity of the spin-coupled citrate multiplet and managing lipid suppression.

In Chapter 5, ^{1}H-MRSI data was obtained using a newly improved technique for MRSI of the prostate with post-histopathological data. Eight subjects with prostate cancer were scanned on a GE 1.5T MR scanner using a standard endorectal coil in combination with a torso phased-array coil. MR spectroscopic

imaging data were obtained using the newly optimized CV-MRS technique at both short and long echo times. Pre-operative biopsy was done using transrectal ultrasound, with multiple cores taken. Following radical prostatectomy, the prostate was prepared for histopathological analysis using the local standard protocol. An experienced anatomical pathologist identified normal prostate tissue and areas of carcinoma. Spectra from voxels that correspond to malignant and normal tissue were analyzed using LCModel. Multifocal prostatic adenocarcinoma was identified on pre-operative biopsy. Post-operative pathology similarly revealed multicentric prostatic adenocarcinoma in all subjects. The spectroscopic data showed an increase in the (choline+creatine)/citrate ratio in voxels containing tumour compared to voxels that were free of tumour. For long and short echo times the mean normal metabolite ratios were 0.31±0.20 and 0.29±0.12 respectively. In contrast, for long and short echo times the mean cancer metabolite ratios were 0.74±0.23 and 0.78±0.16. The reduction of citrate in voxels corresponding to regions of malignant tissue matches well with expected spectral patterns of cancerous tissue. In conclusion, spectra using the optimized CV-MRSI technique correlated well with initial histopathological findings.

Lastly, combining the elements that were developed from the previous chapters (2-5), in Chapter 6 a method to incorporate ^{1}H-MRSI data into the radiation treatment planning of prostate cancer was examined. Spectroscopic imaging gives us a snapshot of the tumour's metabolic activity at the time of acquisition. This metabolic information was used to assess the appropriate radiation dose that would enable good control over the prostate cancer. A retrospective

comparison of IMRT treatment plans of the prostate with and without the inclusion of the metabolite ratio as identified by ^{1}H-MRSI data was performed. The retrospective radiation treatment planning study was done for 7 subjects who were enrolled in the PROFIT trial in our clinic. Each subject underwent routine CT simulation, and also received a combined MRI/MRSI scan using the newly developed CV-MRS technique. For each subject, a 7-field IMRT plan using 6 MV photons was created following the local radiation treatment plan protocol. Using radiobiological models (TCP and NTCP) we estimated the required increase in dose based on the ^{1}H-MRSI data, since the data tells us where and how active the tumour is. We first calculate the TCP with standard assumptions of uniform radiobiological parameters across the entire target structure. Over all subjects, the TCP ranged from 94.4 to 98.3%, with a mean value of 96.5±1.4%. Next the TCP was calculated with the radiobiological parameters determined by the spectroscopic data on a voxel-by-voxel basis. The mean TCP over all subjects was found to decrease to 87.9±5.9%. We then recalculated what the prescription dose would be to achieve the same TCP response when using the ^{1}H-MRSI data. Based on this result, the standard 7-field IMRT plans for the PROFIT patients were modified were modified using the new prescription doses The modified prescription doses ranged from 85-87 Gy for the DIL and 81-83 Gy for the remainder of the prostate. The results of the standard planning demonstrated a mean dose prostate CTV dose of 79.0±0.4 Gy (TCP of 96.5±1.4%) as compared to the modified plan which received a mean dose to the prostate CTV of 85.3±1.3 Gy and DIL of 87.5±1.1 Gy (TCP of 98.0±1.0%). In performing a radiation boost to the prostate

CTV and DIL, we observed that both IMRT plans (IMRT-PROFIT and IMRT-DIL) had similar NTCP outcomes and there was no significant increase in the dose to the bladder, rectum, right and left femoral heads. In this study we demonstrated the utility of spectroscopic imaging for the radiation treatment planning of prostate.

7.2. Future Directions

The current implementation of the CV-MRS technique has taken into account many aspects to help it become more robust, but there are still some aspects of the overall technique that could be improved. From a pulse sequence development point of view, the current pulse sequence is fairly robust. The current pulse sequence can vary the number of VSS pulses and change the flip-angles of each pulse on-the-fly. The CHESS and OVS sequence is well integrated, and the execution of the PRESS sequence is concise (i.e. without interleaving water and lipid suppression pulses). At present, some literature has been recently published on the use of cosine-modulated VSS pulses (i.e. dual-band pulses)(44). The CV-MRS technique may benefit from using this type of RF pulse, since it will reduce the number of pulses in an already long chain of VSS pulses and reduce the overall pulse sequence time. Introducing cosine-modulated pulses would present an interesting challenge in modifying the current flip-angle and ordering optimizations, since a single cosine modulated VSS pulse saturates two locations in space. While this may introduce a more complicated optimization scheme, it would also bring about some interesting research. This might include modifying the algorithm to calculate the optimal number of saturation planes needed for specific

anatomical sites or optimizing the saturation band spatial width to compensate for multiple overlapping planes.

Examining the current software implementation of the CV-MRS technique, we see that there are still some areas that could use improvement. The current platform was developed in IDL, and as such was limited by the tools available by the vendor specific GUI development environment. IDL's current implementation for windowing and leveling of displayed images is very slow, making it difficult to quickly adjust the viewing of the images. Quick adjustments to the grayscale of the image are a necessity for routine clinical use. Future versions of the software could include using a faster image display routine that could be incorporated into the IDL framework. Concurrently we are also investigating techniques to automatically contour the prostate (15, 251, 252). By including this technique into future versions of the code, we remove any user variability and the time-consuming process of manually contouring the prostate. In this work, we have shown the usefulness of utilizing the CV-MRS technique for both long and short echo time ^{1}H-MRSI acquisitions. The next step in the evolution of this project would be to extend the study to a much larger cohort of subjects (including prostates with and without histopathologically proven cancer). Over the last two decades, the majority of studies have examined data collected at long echo times (TE ~130ms) (15, 49, 133, 192, 253, 254). In this work we have shown that it is possible to collect high quality data at short echo times (TE ~ 40ms). Building on the foundations of the current research, future *in vivo* studies could focus solely on short echo time acquisitions. Current methods have allowed us to get to the point where we can

now readily detect short TE metabolites (i.e. myo-inositol, scyllo-inositol, taurine, glutamine/glutamate). Future studies could examine the role of these metabolites and their distribution over the entire prostate for both populations of normal and cancerous prostates.

As well, it is clear from a number of recent publications that future work should be performed at a field strength greater than 1.5T (i.e. 3T or higher) (35, 49, 50, 133, 255-258). While our short echo time data is of high quality and in some cases comparable to spectra collected at higher field strengths (259), results will improve further by utilizing higher fields. At higher field strengths we will benefit from the increased available signal. The improved signal from both the higher field strength and short echo time may allow for acquisitions with smaller voxel sizes. This will be beneficial when imaging small lesions within the prostate volume. The CV-MRS technique, by design, is independent of field strength. However, there are still a number of steps that need to be examined before using our short echo time strategy at higher fields. This includes modifying the PRESS pulse timing (taking into account quantum mechanical simulations of the strongly coupled citrate AB system at higher fields), evaluation of RF pulse responses, and adjusting for the changes in T_1 and T_2 parameters for lipids and metabolites at higher fields.

One of the crucial pieces of equipment used in the acquisition of ^{1}H-MRSI is the endorectal coil. Recently there have been dual-channel rigid coil designs presented that have greatly improved the SNR along the peripheral zone (189). Using the short echo time technique in combination with an improved endorectal

coil design would further improve our approach and is another future area of research related to the development of this technique.

Comparing our work to recent studies that also examined the correlation of histopathology to spectroscopic imaging of the prostate, it is clear that future work must include whole-mount step-section histopathology (157, 162, 176, 187, 209). This capability was not available in our clinic, but whole-mount step-section histopathology has become the standard for comparing histopathology with spectroscopic imaging. Future local efforts in this comparison will need to utilize this technique. Recently some very interesting image segmentation algorithms have been developed by Madabushi *et al.*, which automatically identify cancerous regions within the histopathology slice with a high degree of accuracy (260-262). Before correcting for the deformation introduced by the endorectal coil, this algorithm could be used to identify cancerous regions within the histopathological slice. Using the approximate thickness of the histopathology slice and correcting for deformations, a three-dimensional volume of the cancerous region could be rendered and compared to the combined MR/MRSI data set. This approach is similar to some recent work done by Xu *et al.* that compared diffusion imaging characteristics of prostate cancer with whole-mount step-section histology (263). Since histopathology is the gold standard for identifying cancers, any future spectroscopic imaging studies attempting to validate the three-dimensional location of prostate cancers will have to be compared to histopathologically confirmed data.

The thesis was concluded by investigating the use of spectroscopic imaging data as applied to the radiation treatment planning of prostate cancer. To our

knowledge, there have been a limited number of studies that have started to examine using ^{1}H-MRSI data for the radiation treatment of the prostate (72, 139, 140, 226, 230, 264). Often this information is used solely for tumour localization and delineation. In our work we sought to use the spectroscopic data not only for tumour localization, but for direct assessment of the tumour control probability. Clearly, this part of the thesis is in its infancy and much more work needs to be done to test and validate these initial findings. For example, in the determination of the DIL we used spectroscopic imaging data that was obtained at long echo times. The main reason for this was because the majority of the existing literature that has studied the relationship between spectroscopy, histopathology, and tumour proliferation was done at long echo times. In our work we showed the feasibility of collecting high quality data at short echo times, and presented a limited comparison to histopathology. If we can establish a strong correlation between short echo time ^{1}H-MRSI data and tumour proliferation, this data could be used to modify our TCP calculations. Looking forward, the next stage in development of this work would be to continue a similar study for a larger number and range of prostate cancer patients, and statistically determine if it is feasible to start using the technique in routine radiation treatment.

7.3. General Summary

In summary, it was the goal of this thesis to first improve the method of obtaining high quality, artifact free, ^{1}H-MRSI data at short and long echo times. To that end we obtained very good results indicating that this technique could advance current acquisitions methods. Our technique was validated with histopathology, and it was shown that there may be added benefit to acquiring short echo time data to help clearly differentiate between cancerous and normal tissue. Using the CV-MRS technique, ^{1}H-MRSI data was acquired for subjects with confirmed prostate cancer who were scheduled for routine radiation treatment or radical prostatectomy. The spectroscopic data was utilized to identify molecular markers of malignant prostate tissue, which were then used to delineate the cancerous regions within the prostate. Furthermore, this information enabled a voxel by voxel assessment of radiobiological parameters that facilitated the calculation of optimal doses needed to achieve control over the cancer through targeted radiation dose-escalation. In conclusion, this thesis has accomplished its goals of improving the methods for diagnosing prostate cancer by implementing a robust spectroscopic imaging technique (confirmed by histopathology) and retrospectively assessing an optimal radiation treatment strategy for potentially better treatment outcomes.

Appendices

8.Appendix A

8.1. Radio-frequency excitations

A NMR experiment can be divided into two distinct steps: (1) excitation and (2) signal detection. In this most basic experiment, an observer measures the precessing magnetizations from the electromotive force created in the nearby receiving coil. After excitation, the signal is acquired and digitized with linear gradient fields applied for spatial encoding.

The RF excitation field $\vec{B}_1(t)$ *or* oscillating magnetic field is a radio-frequency (RF) pulse that is applied to a sample volume of spins, such that the RF pulse establishes a coherent phase among the randomly precessing spins in the volume. To create a coherent transition of spins from one state to another, the energy of the RF pulse is set to equal to the energy difference between the spin states. More precisely, the frequency of the oscillating magnetic field is defined by a specific Larmor frequency, ω_{RF}. The direction of $\vec{B}_1(t)$ is set perpendicular to the $\vec{B}_0$ field. For the purposes of this discussion in the following sections, the B_0 axis will be denoted as the *z-axis* or the longitudinal axis and the transverse direction will be called the *xy-axis*. According to Faraday's law of induction, the application of the $\vec{B}_1(t)$ along the perpendicular direction induces a torque on the magnetization causing the magnetization to rotate away from the main static magnetic field, $\vec{B}_0$. This results in

a transverse magnetization that can be detected by external coils by detecting a voltage caused by an electromotive force. The rotation frequency of the induced magnetization directed away from $\vec{B}_0$ and in the presence of $\vec{B}_1$ can be calculated by $\omega_1 = \gamma B_1$, γ is the gyromagnetic ratio. The angle between the main static field $\vec{B}_0$, and the tipped magnetization is called the flip angle, α and is defined as,

$$\alpha = \int_0^{\tau} \omega_1(t)dt \qquad \text{(A8.1)}$$

where τ is the RF pulse duration. The value of the flip angle varies by design of the experiment (i.e. 90°, 180°, etc.).

In the most basic RF experiment, the coil used to produce the oscillating $\vec{B}_1$ field, can also be used to detect the signal. The integration of the precessing transverse magnetization over the volume of interest is recorded as the MR signal. Following the application on a RF pulse on a sample volume, the detected signal is called the free induction decay, (FID). The FID signal can be transferred from the time domain into the frequency domain by a simple Fourier transformation, which will be discussed in detail in the following sections and illustrated in Figure A8.1.

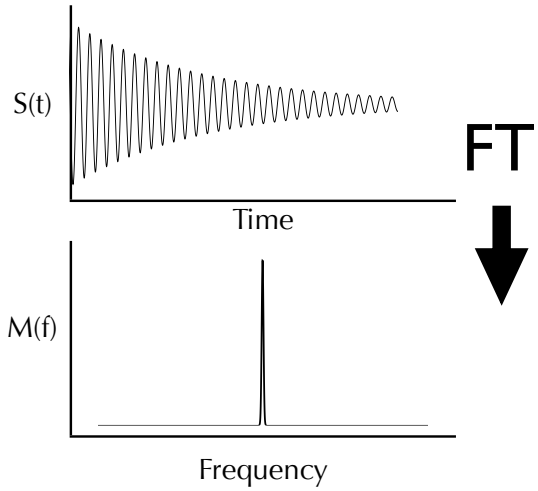

Figure A8.1 The free induction decay signal.
The FID signal can be transferred into frequency domain by applying the Fourier transform.

8.2. Bloch Equations

In our previous quantum mechanical discussions in section 1, it was shown that a magnetic moment $\vec{\mu}$, when placed in a magnetic field $\vec{B}$, will experience a torque that is proportional to the time derivative of the angular momentum. By integrating over all magnetic moments, the equation of motion for a single magnetic moment can be generalized for the total magnetization as:

$$\frac{d\vec{M}(t)}{dt} = \vec{M}(t) \times \gamma \vec{B}(t) \tag{A8.2}$$

In the laboratory frame of reference, consider a time varying RF field that is linearly polarized along the x-axis. This RF field can be written as:

$$\vec{B}_1(t) = 2\vec{B}_{1\max} \cos\left(\omega t \hat{x}\right) \tag{A8.3}$$

where the maximum amplitude of the applied field is $\vec{B}_{1max}$, $\hat{x}$ is the unit vector, and ω is the Larmor frequency. The linearly polarized field may also be broken up into two circularly polarized fields that are rotating in opposite directions about the z-axis, and re-written as (see Figure A8.2):

$$\vec{B}_1(t) = B_{1max}\left[\cos\left(\omega t\hat{x}\right) + \sin\left(\omega t\hat{y}\right)\right] + B_{1max}\left[\cos\left(\omega t\hat{x}\right) - \sin\left(\omega t\hat{y}\right)\right] \qquad \text{(A8.4)}$$

Ignoring any influences from any counter rotating fields, equation (A8.4) can be equivalently written to a rotating magnetic field as:

$$\vec{B}_{1x}(t) = B_{1x}\cos\left(\omega t\right) - B_{1y}\sin\left(\omega t\right) \qquad \text{(A8.5)}$$

and

$$\vec{B}_{1y}(t) = B_{1y}\sin\left(\omega t\right) + B_{1y}\cos\left(\omega t\right) \qquad \text{(A8.6)}$$

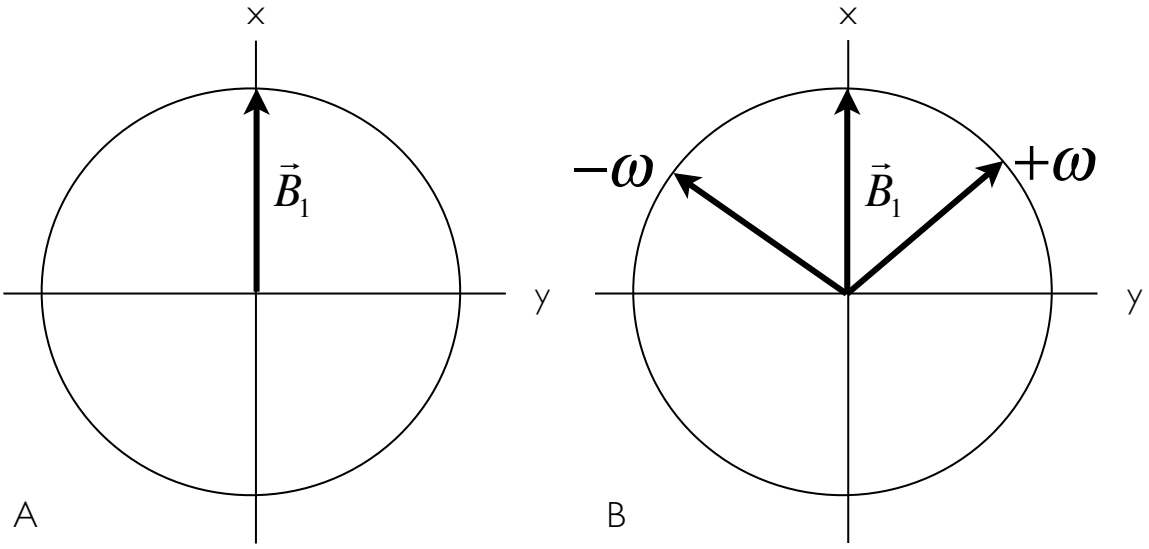

Figure A8.2 Decomposition of linearly oscillating magnetic field.
(A) In single oscillating magnetic field, and (B) its decomposition into two components.

From equation A8.2, in the laboratory frame and in the absence of relaxation, the Bloch equations in the presence of $\vec{B}_1$ and $\vec{B}_0$ can be written as:

$$\frac{dM_x(t)}{dt} = \gamma\left[M_y(t)B_0 - M_z(t)B_{1y}\right] \tag{A8.7}$$

$$\frac{dM_y(t)}{dt} = \gamma\left[M_z(t)B_{1x} - M_x(t)B_0\right] \tag{A8.8}$$

$$\frac{dM_z(t)}{dt} = \gamma\left[M_x(t)B_{1y} - M_y(t)B_{1x}\right] \tag{A8.9}$$

Following the excitation of the spins using an RF pulse, the spins gradually lose their phase coherence and relax back to thermal equilibrium in an exponential manner. This results in a decay of the detectable magnetization amplitude along the xy-axis and a simultaneous regrowth of the magnetization along the z-axis. The equations which describe this relaxation process can be written as:

$$\frac{dM_x(t)}{dt} = -\frac{M_x(t)}{T_2} \tag{A8.10}$$

$$\frac{dM_y(t)}{dt} = -\frac{M_y(t)}{T_2} \tag{A8.11}$$

$$\frac{dM_z(t)}{dt} = -\frac{M_z(t) - M_0}{T_1} \tag{A8.12}$$

In the above descriptions we have introduced the relaxation constants, T_1 and T_2. T_1 is the main process in which, after the excitation of an RF pulse, energy from the spins is transferred to the surrounding tissue or lattice (also called spin-lattice

relaxation or longitudinal relaxation). T_1 is characterized specifically as the time that the magnetization has grown back to 63% of its original value along the z-axis as illustrated in Figure A8.3. The above differential equations A8.10-12 can be integrated into the longitudinal magnetization as:

$$M_z = M_0(1-(1-\cos(\alpha))\cdot e^{\frac{-t}{T_1}}) \qquad \text{(A8.13)}$$

where, M_z is the longitudinal magnetization, α is the flip angle of the RF pulse, and t is the time over which the recovery occurs. As well, since the longitudinal relaxation is caused by interactions between the nuclei and their environment, the value of T_1 will vary with the molecule to which the nucleus is bound, and the type of tissue in which it is situated.

At the first instant when the RF pulse is applied, the spins in the system are brought down into the transverse plane and are completely in-phase. Directly following the RF pulse, the transverse component of the net magnetization begins to decay. This decay, or overall loss of the transverse magnetization, is the result of temporary and random interactions between two excited spins that cause a cumulative loss in phase. This loss of the phase coherence is called spin-spin relaxation or transverse relaxation. Similar to the longitudinal relaxation, the decay of signal due to transverse relaxation, is described mathematically by an exponential:

$$M_{xy} = M_0 e^{\frac{-t}{T_2}} \qquad \text{(A8.14)}$$

where, T_2 is the time constant for this process and is characterized when the magnetization returns to 37% of its initial value.

As mentioned in this section, the T_1 and T_2 time constants are unique to each specific tissue. Due to their unique nature, they become a valuable resource in determining the appropriate contrast needed under various imaging experiments (48, 265-267).

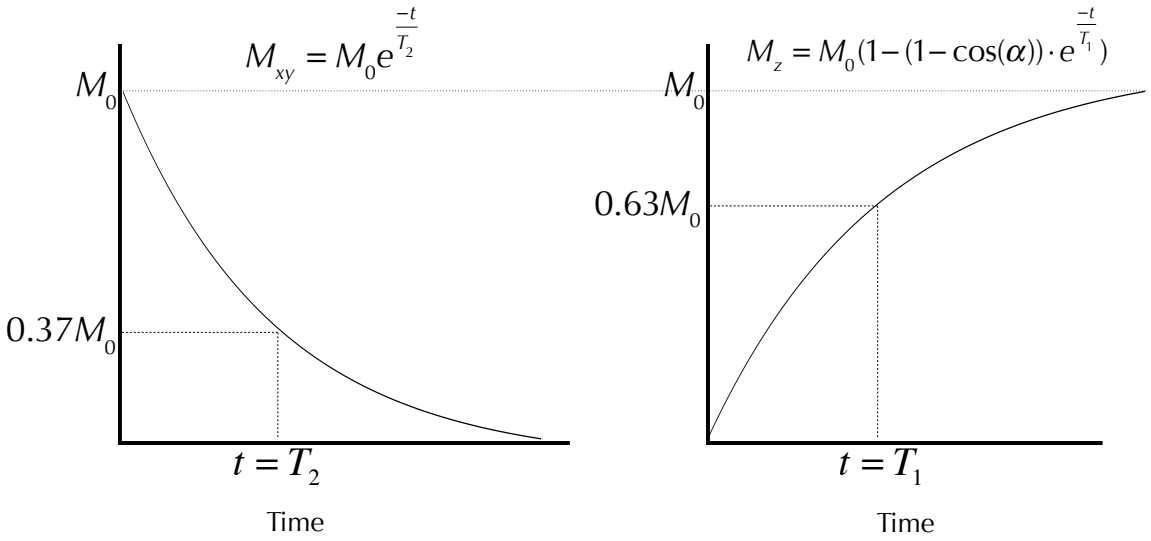

Figure A8.3 Relaxation curves for T_1 an T_2

8.3. Signal Detection and the Fourier Transform in NMR

In the previous section it was briefly mentioned that the FID signal can be detected using the principles of Faraday's Law and subsequently, using the Fourier Transform (FT) to take the signal from the time domain to the frequency domain. In this section, the signal detection and utility of the FT will be discussed in detail.In the process of a standard excitation an RF pulse rotates the net magnetization $\vec{M}_0$, by 90^0, the net magnetization is in the transverse plane of the rotating frame of reference.The magnetization is precessing about the $\vec{B}_0$ field, at the Larmor frequency. Due to T_2 effects, the signal begins to decay with time. In the simplest experimental setup, the same RF coil used for generating the RF signal can also be used to detect the signal. The sensitivity of detection of the receiver coil is determined by the principle of reciprocity[21](265). Now consider the magnetic flux through a coil by $\vec{M}(\hat{r},t)$ given by:

$$\Phi(t) = \int_{sample} \vec{B}_r(\hat{r}) \cdot \vec{M}(\hat{r},t) d\hat{r} \qquad \text{(A8.15)}$$

[21] The principle of reciprocity states that when you apply a unit direct current to a receiving coil and then measure the field $\vec{B}_r$created at the NMR sample, the signal induced in the coil by the precessing nuclear magnetic moment $\vec{M}$ would be proportional to the strength of this hypothetical field, and given by the scalar product, as described by equation A8.15.

Here we assume that $\vec{B}_r(\hat{r})$ is the magnetic field in the laboratory frame of reference, at a position, $\hat{r}$, produced by a hypothetical unit current flowing through the coil. Thus by Faraday's law of induction the voltage induced in the coil is:

$$V(t) = -\frac{\partial}{\partial t}\int_{sample} \vec{B}_r(\hat{r}) \cdot \vec{M}(\hat{r},t)d\hat{r} \qquad \text{(A8.16)}$$

The voltage, *V(t),* induced by the receive coil is the raw NMR signal, and represents the basic formula of detecting a MR signal that encompasses both the principle of reciprocity and Faraday's law of induction.

In this description we have shown that if a coil is placed in the transverse plane, a resulting signal can be detected due to Faraday's law. However, inhomogeneities in the B_0 field leads to small B_0 field variations across a sample, which results in a distribution of Larmor frequencies that are detected (267). To account for variations in the $\vec{B}_0$ field, the transverse signal in the presence of inhomogeneities can be rewritten from the form in equation (A8.14) to:

$$M_{xy}(t) = M_{xy}(0)e^{\frac{-t}{T_2^*}} \qquad \text{(A8.17)}$$

where, T_2^* includes the multi-exponential dependence on the local B_0 field, and is defined as:

$$\frac{1}{T_2^*} = \frac{1}{T_2} + \frac{1}{T_{2,\text{inhomogenities}}} \qquad \text{(A8.18)}$$

which is a combination of pure T_2 effects as described in the previous section, plus a component due to variations in the local B_0 caused by inhomogeneities.

The voltage V(t) that is generated in the coil and the time-dependent signal read by the NMR spectrometer is the FID. The FID is complex, containing both real and imaginary parts. It is commonly read in two components, along the $\vec{x}$ and $\vec{y}$ directions with time. Thus the transverse component, $M_{xy}(t)$, is then broken up in to two constituent time dependent parts,

$$M_x(t) = M_0 \cos(\Delta\omega t + \phi)e^{\frac{-t}{T_2^*}}, \text{ Real} \tag{A8.19}$$

and

$$M_y(t) = M_0 \sin(\Delta\omega t + \phi)e^{\frac{-t}{T_2^*}}, \text{ Imaginary} \tag{A8.20}$$

where ϕ is the phase (t=0), $\Delta\omega = \omega_0 - \omega$, $M_x(t)$ is the real component, and $M_y(t)$ is the imaginary component. The FID itself contains valuable information about the nuclear spins of the system, relative concentrations, and resonant frequencies, but the FID itself is not commonly used in a clinical setting. The time-domain data is transformed into the frequency domain by method of FT. The FT of the time-domain signal f(t) is given by,

$$FT(f(t)) = F(\omega) = \int_{-\infty}^{+\infty} f(t)e^{-i\omega t}dt \tag{A8.21}$$

where *FT(f(t))* is a completely reversible operation by performing the inverse FT by:

$$f(t) = \frac{1}{2\pi}\int_{-\infty}^{+\infty} F(\omega)e^{-i\omega t}d\omega \tag{A8.22}$$

Using the FT, the FID signal can be reconstructed into its major frequency components, and displayed as a spectrum, as seen Figure A8.4. The FT results in both real and imaginary parts,

$$\text{Real}(\omega) = \frac{M_0 T_2^* \cos(\phi)}{1 + \Delta\omega^2 T_2^{*2}} - \frac{M_0 \Delta\omega T_2^{*2} \sin(\phi)}{1 + \Delta\omega^2 T_2^{*2}} \tag{A8.23}$$

and

$$\text{Imaginary}(\omega) = \frac{M_0 T_2^* \sin(\phi)}{1 + \Delta\omega^2 T_2^{*2}} + \frac{M_0 \Delta\omega T_2^{*2} \cos(\phi)}{1 + \Delta\omega^2 T_2^{*2}} \tag{A8.24}$$

where the absorption and dispersive components can be factored out as:

$$\text{A}(\omega) = \frac{M_0 T_2^*}{1 + \Delta\omega^2 T_2^{*2}} \text{ and } \text{D}(\omega) = \frac{M_0 \Delta\omega T_2^{*2}}{1 + \Delta\omega^2 T_2^{*2}} \tag{A8.25}$$

Thus equations A8.23 and A8.24 can be re-written as,

$$\text{Real}(\omega) = A(\omega)\cos(\phi) - D(w)\sin(\phi) \tag{A8.26}$$

and

$$\text{Imaginary}(\omega) = A(\omega)\sin(\phi) + D(\omega)\cos(\phi) \tag{A8.27}$$

in which the real and imaginary components are written as a function of the absorption-A(ω) component, dispersion-D(ω) component, and the phase angle, ϕ . The absorption-A(ω) and dispersion-D(ω) components describe the line-shape of the spectrum, and are shown in Figure A8.4. Spectra that are a result of pure absorption can be obtained by mixing the real and imaginary components by interactively modifying the phase angle, ϕ, or "zero-order" phase characterized

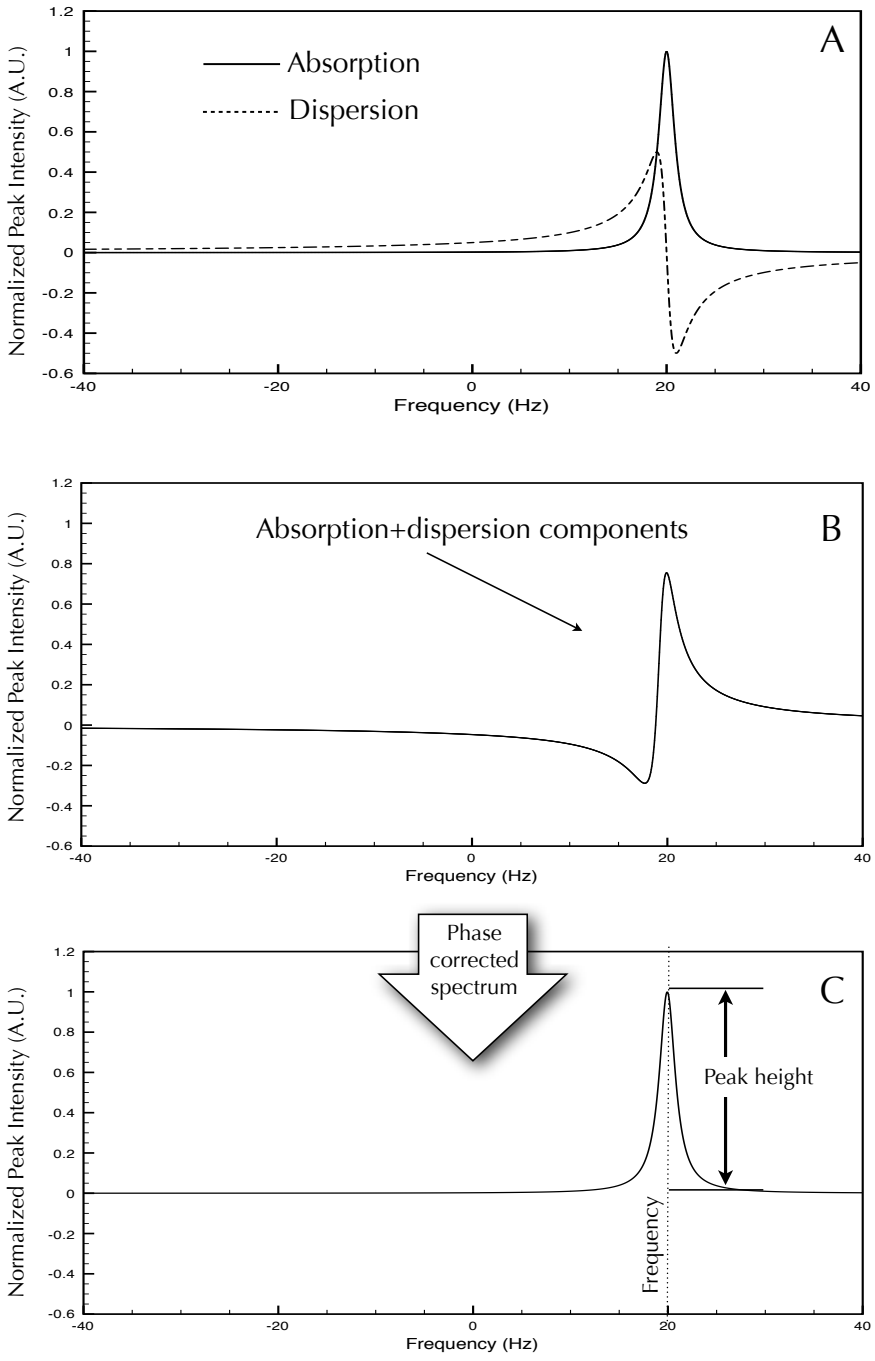

Figure A8.4 Absorption and dispersion components of an NMR spectrum
In (A), the FT of the FID produces two spectral components. At the beginning of the FID the phase is non-zero, such that is a mixture of the absorption and dispersion components (B). By performing a "phase" correction, we can eliminate the dispersive component, such that the absorption component remains.

sometimes as $\phi = \phi_1$. This manipulation or incremental changing of the phase, is also known as "phasing" of the spectrum, and is highly useful in correcting the line-shape of the spectrum as seen in Figure A8.4. When there are more frequency-dependent phase corrections needed (i.e. timing errors, hardware imperfections, etc.), it may be useful to extend the phase correction to include a linearly dependent frequency term. Thus the phase can be modified to include both zero-order, and first-order phase corrections such that,

$$\phi = \phi_1 + \Delta w \phi_2 \tag{A8.28}$$

where both ϕ_1 and ϕ_2 are user adjustable.

8.4. Signal Localization in NMR

8.4.1. What are RF echoes in NMR?

Up until now our discussions have focussed on one type of MR signal, namely the FID. In this section, let us introduce another type MR signal that is extensively used in modern imaging techniques, called an *echo*. The spin *echo* or *Hahn echo* was first report by Erwin Hahn, in 1950 (268). In his experiment, Hahn discovered that one could realign the magnetization of incoherent spins by refocussing them by an RF pulse. The main distinguishing feature of between an FID and an echo is the form of the signal. The formation of an echo is two-sided, containing a rising part from the refocussing phase of the transverse magnetization,

and a decaying part from the dephasing of the transverse magnetization. Echoes however, can also be created by the manipulation of gradient magnetic fields within the MR system. These type of echoes are called, *gradient echoes*. This section examines the nature of the *spin* and *gradient* echoes and their utility in signal localization.

8.4.2. Spin Echoes

The spin echo, also referred to as the Hahn echo, can be created by acquiring a signal from two consecutive RF pulses. The basic spin-echo pulse sequence has the form, $(90^0)_x - (TE/2) - (180^0)_x - (TE/2) - (acquistion)$ where a 90 degree RF pulse is followed by a 180 degree RF pulse and then the final acquisition, separated by a time interval of TE/2. The action of the 90 degree RF pulse initially brings the net magnetization into the transverse plane along the x-direction in the rotating laboratory frame. The action of the 180 RF pulse refocuses the magnetization that was de-phased by variations in the Larmor frequencies due to field inhomogeneities or susceptibility variations in the sample and chemical shifts. The refocused signal is called an "echo", and its maximum occurs at time TE. This is illustrated in Figure A8.5. A useful feature of this very simple spin-echo sequence is that it refocuses any dephasing that occurred due to random causes (i.e true T_2 decay). This sequence also provides a simple RF experiment to recover the true T_2 of a sample.

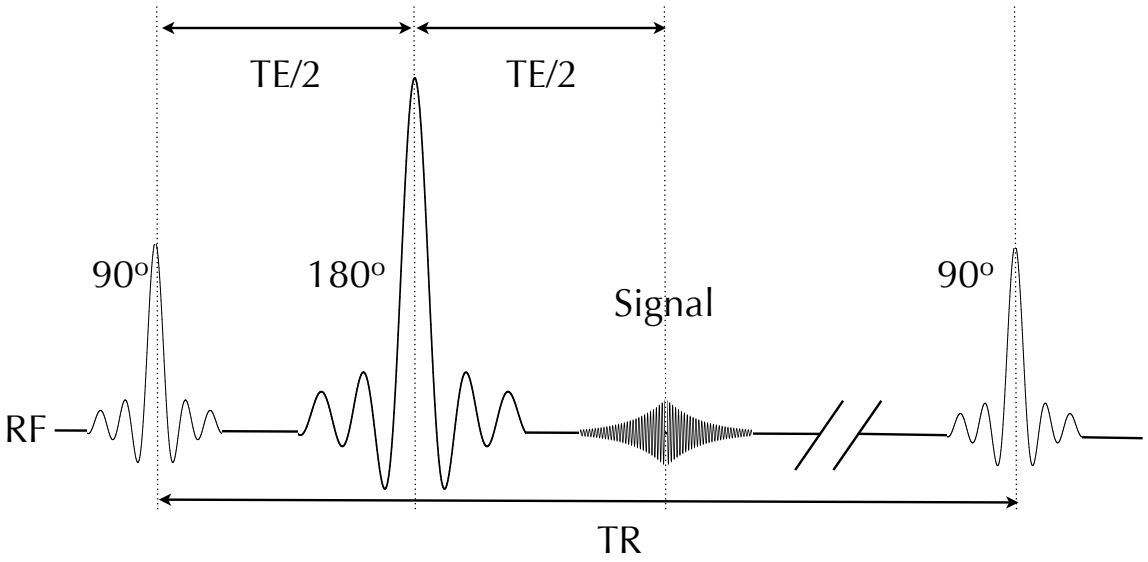

Figure A8.5 Spin echo formation(not to scale)

Figure A8.5 illustrates the process of refocussing the magnetization. In this illustration, a vector is shown to represent a population of spins that precess at the same Larmor frequency (also referred to as isochromats), labelled ω_f and ω_s for "fast" and "slow" components. A spin echo can be generated from any two RF pulses, and its signal which takes into account T_2-weighting is given by,

$$S(t) = \sin(\alpha_1)\sin^2(\alpha_2)\frac{\alpha_2}{2}\int_{-\infty}^{+\infty}\rho(\omega)\,e^{-t/T2(\omega)}\,e^{-i\omega(t-TE)}d\omega \qquad \text{(A8.29)}$$

where α_1 is the flip angle of the first pulse, α_2 is the flip angle of the second pulse, $\rho(w)$ is the spin density function, TE is the echo time, and for $|t-TE| \leq T_{acq}/2.\,T_{acq}$ is the acquisition time interval (269). The exponential terms describe both the refocussing and dephasing of the FID. The term, $e^{-t/T2(\omega)}$ describes the non-recoverable T_2 dephasing. The spin echo is a valuable resource in NMR, as it allows

the investigator a method to discover more information about T_2, T_2^*, B_0, and chemical shifts.

8.4.3. Gradient Echoes

Another method to generate an echo in an NMR experiment is to utilize the gradient coils that exist in the MR scanner. Gradient coils are integrated into the MR scanner to provide a method of producing a time-varying magnetic field that is used to localize a region of interest. Typically in a whole body MR system, there are three gradient coils, one for each spatial direction (i.e. x, y, z). The set of x-, y-, and z- gradient coils are used to produce a magnetic field which alter the main magnetic field, B_0, such that there is a linear change in the B_0 field, slightly increasing from one end to the other. This variation enables one to determine position as a function of the external field. The total magnetic field, in the presence of a gradient field is given by:

$$\vec{B}(r) = \vec{B}_0(r) + \vec{B}_G(r) \tag{A8.29}$$

where $\vec{B}_G$ is the gradient field which is defined as $\vec{B}_G(r) = G_x x \cdot \vec{i} + G_y y \cdot \vec{j} + G_z y \cdot \vec{k}$. The gradient field is written as a function of all three directions, but since the B_0 is much stronger along the z-direction and the x- and y-directional terms are close to zero, the x- and y- terms are often disregarded. The individual gradient components may be written as a differential function of x, y, and z coordinates such that,

$$\vec{B}_G(r) = \frac{\partial \vec{B}_G}{\partial x} + \frac{\partial \vec{B}_G}{\partial y} + \frac{\partial \vec{B}_G}{\partial z} \tag{A8.30}$$

where $\vec{G} = (G_x, G_y, G_z)$ is referred to as the gradient direction of $\vec{B}_G$. Therefore the gradient fields enable the main magnetic field to vary as a function of position, and also uniquely varies the Larmor frequency of spins at different positions. If the magnetic field intensity is known, the spatial position of the NMR signal can be determined by its frequency.

As mentioned previously, gradients can be used to generate an echo. Consider a simple experiment after interrogation with a 90 degree RF pulse to a sample. Immediately following the excitation of the sample, a gradient along the y-direction is switched on with negative amplitude, as see in Figure A8.6. This causes all the spins along the y-direction to acquire a slightly different phase, as expressed in the following equation,

$$\phi(y,t) = -\int_o^t \gamma G_y y dt = -\gamma G_y y t \qquad \text{(A8.31)}$$

where the loss of signal becomes greater with time. The gradient may be switched to refocus the spins, and subsequently create an echo. The switching of the gradients maybe done may times, and the characteristic T_2* can be ascertained.

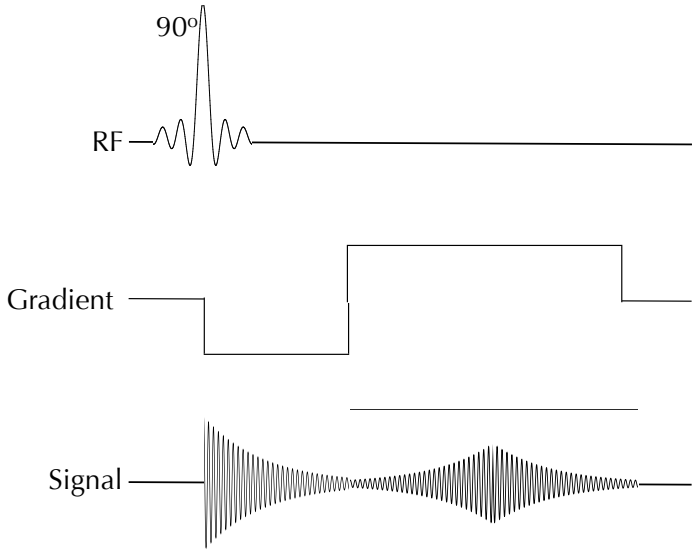

Figure A8.6 Gradient echo formation (not to scale).

8.4.4. Slice selection

The most common method of acquiring signal from a single "slab" of a sample is by performing slice-selective selection. The concept of slice selection incorporates ideas from the previous section. The simplest form of slice-selection occurs with the application of a RF pulse while a gradient is simultaneously turned on along the direction of interest. Consider the following example as illustrated in Figure A8.7. For a sample containing a nucleus with a resonant frequency ω_0 (with units rad/s) the variation in frequency in the presence of the a gradient along the z-direction is given by,

$$\omega(z) = \omega_0 + \gamma G_z z \tag{A8.32}$$

Suppose now the sample is irradiated with a sinc RF pulse, that has a range of frequency components with a nominal bandwidth (BW), with units rad/s. Along the

z-direction gradient, G_z (units T/m), the RF pulse will only excite a range of frequencies that extend from $\omega_0 + BW/2$ to $\omega_0 - BW/2$. Since the RF pulse is centered on the resonant frequency, ω_0, the resultant excitation will localize a slab such that only frequencies that lie within the above range will be excited. Nuclei outside the slab will remain unaffected. The thickness of the slice that is excited is given by a sinc RF pulse given by solving equation A8.32 to give:

$$BW = \gamma G_z \Delta z \Rightarrow \Delta z = \frac{BW}{\gamma G_z} \tag{A8.33}$$

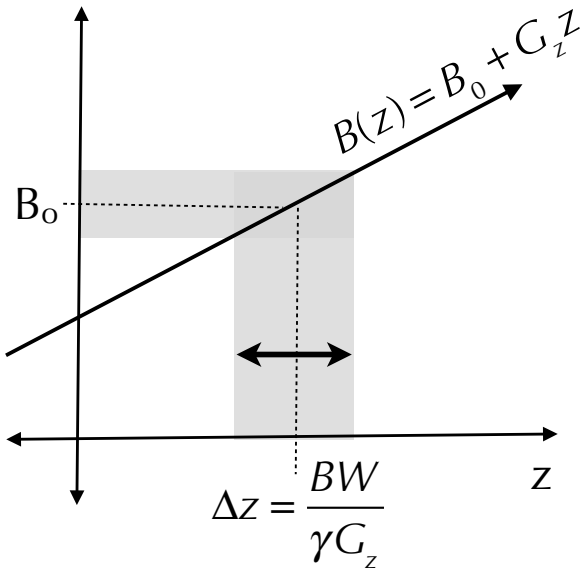

Figure A8.7 Slice Selection

8.4.5. Spatial encoding

This discussion has shown that a slab of a sample can be selectively excited at a specific location. But the question now arises, how can one spatially encode the signal within the "slab" such that an image can be formed in two dimensions? In the next section, the discussion will examine three guiding principles in spatial encoding: 1) Phase encoding, 2) Frequency encoding, and 3) K-space encoding (or spatial frequency space).

Up until now the discussions have looked at individual components of NMR experiments (i.e. RF pulses, RF echoes, gradients, etc.). In NMR experiments, a pulse sequence diagram provides a complete picture of an experiment. A pulse sequence diagram is a compact graphical representation of the timing of RF pulses and gradients along all three spatial directions. Each axis can contain many simultaneous events. For the purposes of the following discussion, please refer to the pulse sequence diagram of a conventional two-dimensional gradient echo experiment as shown in Figure A8.8. In this example, an RF pulse is executed for a duration, t_{total}, at time $t = 0$. Simultaneously, a slice-selection gradient is applied along the z-gradient for the same time interval as the RF pulse. During the time the RF pulse rises to its maximum amplitude over the time, t_{total}, some of the spins in the slab have already started to dephase. To account for this, a rephase gradient is added such that the area of the rephase gradient is exactly half the area of the slice-selection gradient.

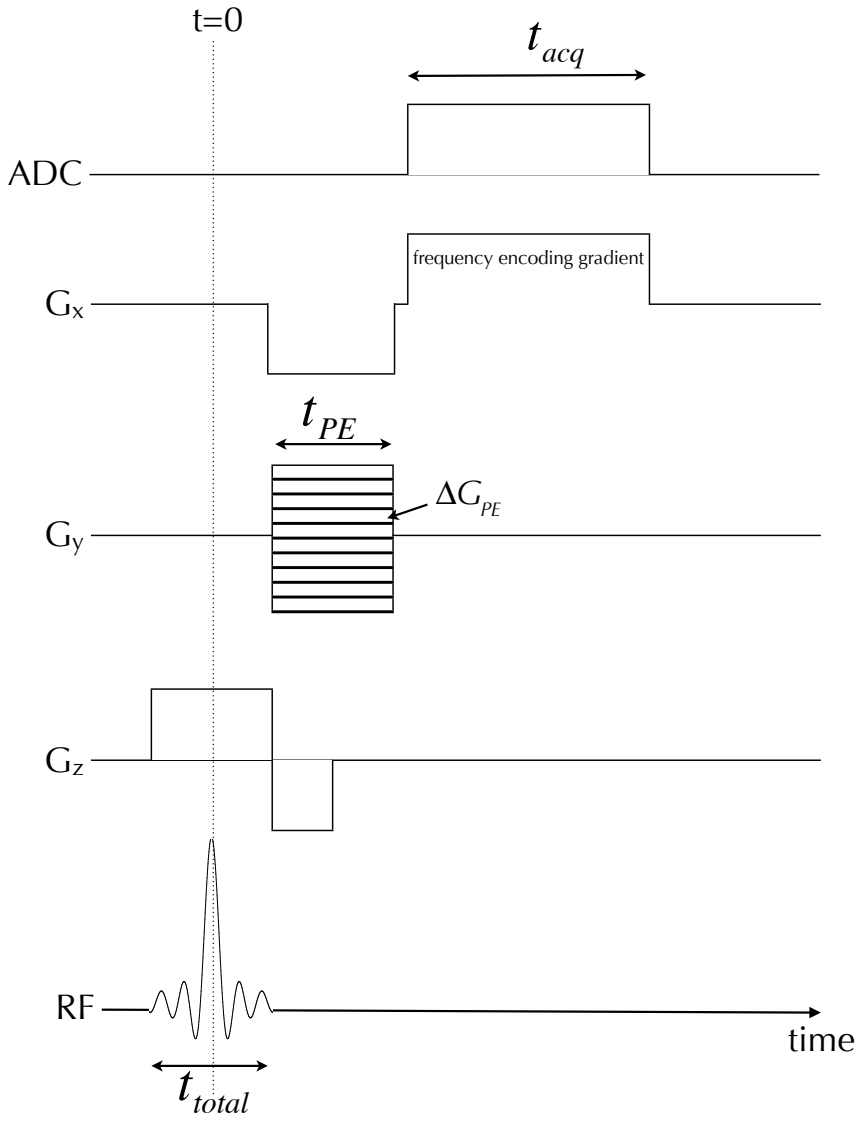

Figure A8.8 2D gradient imaging sequence

At the end of the rephasing gradient, all of the spins in the transverse plane are back in phase, with an accumulated phase value of zero. The signal within the slice is then given by,

$$S(t_{total}) \propto \int_{z_0-\Delta z}^{z_0+\Delta z} \int\int \rho(x,y,z)dxdydz \qquad \text{(A8.34)}$$

where $\rho(x,y,z)$ is the spin density function, and the center of the slice, z_0. Following slice selection, a second type of gradient is turned on along the y-gradient axis. This gradient is called a "phase encoding" gradient, G_{PE}. Similar to other gradients, the phase encoding gradient has a rectangular profile and is turned on for a duration of t_{PE}. During the time the phase encode gradient is turned on, the magnetization accumulates a y-dependent phase along the y-direction. This gradient refocusing of the signal results in a measurable signal given by,

$$S(t_{total}) \propto \int_{z_0-\Delta z}^{z_0+\Delta z} \int\int \rho(x,y,z) e^{-i\gamma G_{PE} t_{PE} y} dxdydz \qquad \text{(A8.35)}$$

where G_{PE} is only turned on for the duration of t_{PE}. A fundamental relationship in MR imaging is the unique relationship between the spin density and signal. Simply put, the Fourier Transform of the spin density as a function of spatial position is the signal as function of spatial frequency,

$$FT[Spin\,Density(x,y,z)] \quad \Rightarrow \quad Signal(k_x,k_y,k_z) \qquad \text{(A8.36)}$$

where, k_x, k_y , and k_z are the variables used to denote spatial frequency with units of $[m^{-1}]$. The encoding of the signal along the y-direction may be written by its k-space spatial frequency component where, $k_y(G_{PE}) = \gamma G_{PE} t_{PE}$. By varying the y-gradient in increments of ΔG_{PE} , one can then gather information about the y-dependence of the spin density. The experiment is repeated as many times as

needed to cover a specific field of view (FOV) in the y direction, while keeping t_{PE} constant during each run.

In the last step, the x-gradient or "frequency encoding" gradient is turned on. This gradient is sometimes also referred to as the "read" gradient. The read gradient, like the previous gradients presented, has a rectangular profile. It is first preceded by a rephase gradient, and then applied with a constant amplitude over time interval, t_{acq}. The combination of a phase-encoding gradient (with incremental amplitude, $G_{PE}+\Delta G_{PE}$), and frequency-encoding gradient uniquely describes a point in spatial frequency space. At this point the signal is now encoded by in all three spatial directions by the signal equation,

$$S(t') \propto \int_{z_0-\Delta z}^{z_0+\Delta z} \int\int \rho(x,y,z) e^{-i\gamma G_x t' x} e^{-i\gamma G_{PE} t_{PE} y} dxdydz \qquad \text{(A8.37)}$$

where t' is equal the echo time, TE or the time between center of the initial RF pulse and the center of the gradient echo shown in Figure A8.8. Since the phase can be represented by its individual phase components, $k_y(G_{PE}) = \gamma G_{PE} t_{PE}$ and $k_x(G_x) = \gamma G_x t'$, the total signal can be rewritten as a function of spatial frequency components,

$$S(k_x, k_y) \propto \int_{z_0-\Delta z}^{z_0+\Delta z} \int\int \rho(x,y,z) e^{-ik_x x} e^{-ik_y y} dxdydz \qquad \text{(A8.37)}$$

From this result it can be seen that the echo acquired over time, t_{acq}, in the presence of the read-out gradient after it has been phase encoded by a fixed value of G_{PE}, generates a line in spatial frequency space (or k-space) of the effective spin density for that slice. The phase encoding line in k-space is sampled at discrete points as a result of the sampling that occurs over t_{acq}. Therefore, the incremental steps in the phase-encode gradient, caused by ΔG_{PE}, produces a set of sampled lines in k-space. Once the acquisition is complete, a 2D FT can be applied to the k-space data to produce an image of the spin density.

Since the signal itself is discretely acquired through an analog-to-digital converter (ADC), the use of the discrete FT method is used. Discrete sampling of any signal is governed by the Nyquist theorem (48) . For a three-dimensional image reconstruction, the FOV and sampling are related by,

$$FOV_y = \frac{1}{\gamma \Delta G_{PE} \Delta t}, FOV_y = \frac{1}{\Delta k_y}, \text{ and } FOV_k = \frac{1}{\Delta y} \qquad \text{(A8.38)}$$

where Δk_y is the sampling interval in the k_y direction, Δy is the spatial resolution along the y-direction, and Δt is the dwell time used in the ADC. From these equations, it can been seen that the physical space of the FOV must be properly sampled in spatial-frequency space.

This section has described how the signal generated by an RF pulse can be spatially encoded using the set of the gradient coils and an ADC. The spatial encoding of an image is inherently linked to the specific timing of gradients and RF

pulses that are purposely imposed by the designer of the sequence. A myriad of sequences are used in modern medical imaging.

9. Appendix B

9.1. Prostate Cancer Staging

The staging of prostate cancer is the method in which a physician categorizes the risk of cancer being spread outside the prostate capsule. The most common system that is used is called the TNM system (T-describes the tumour size, N- describes the involvement of the lymph nodes, and M-describes distant spreading of the cancer or metastasis). Below is a chart that describes the standard clinical TNM staging used by physicians as described by the American Joint Committee on Cancer Society (http://www.cancerstaging.org/).

Anatomic staging					
Group	T	N	M	PSA	Gleason
I	T1a-c	N0	M0	PSA<10	Gleason≤6
	T2a	N0	M0	PSA<10	Gleason≤6
	T1-2a	N0	M0	No PSA	No Gleason
IIA	T1a-c	N0	M0	PSA <20	Gleason = 7
	T1a-c	N0	M0	PSA≥10<20	Gleason≤6
	T2a	N0	M0	PSA≥10<20	Gleason≤6
	T2a	N0	M0	PSA<20	Gleason<7
	T2b	N0	M0	PSA<20	Gleason≤7
	T2b	N0	M0	No PSA	No Gleason
IIB	T2c	N0	M0	Any PSA	Any Gleason
	T1-2	N0	M0	PSA≥20	Any Gleason
	T1-2	N0	M0	Any PSA	Any Gleason
III	T3a-b	N0	M0	Any PSA	Any Gleason
IV	T4	N0	M0	Any PSA	Any Gleason
	Any T	N1	M0	Any PSA	Any Gleason
	Any T	Any N	M1	Any PSA	Any Gleason

Primary Tumour (T)

TX	Primary tumour cannot be assessed
T0	No evidence of primary tumour
T1	Clinically not seen, the tumour neither palpable nor visible by imaging
T1a	Incidental histologic tumour finding in 5% or less of resected tissue
T1b	Incidental histologic tumour finding in more than 5% of resected tissue
T1c	Tumour identified by needle biopsy
T2	Tumour confined within prostate
T2a	Tumour involves one-half of one lobe or less
T2b	Tumour involves more than one-half of one lobe (but not both lobes)
T2c	Tumour involves both lobes
T3	Tumour extends through the prostate capsule
T3a	There is unilateral or bilateral extracapsular extension of the tumour
T3b	Tumour invades seminal vesicle(s)
T4	Tumour invades structures that are adjacent (besides the seminal vesicles)

Lymph Nodes (N)

NX	Regional lymph nodes were not assessed
N0	No regional lymph node metastasis
N1	Metastasis in regional lymph node

Metastasis (M)

M0	There is no metastatic spread
M1	There are distant metastasis
M1a	The tumour has spread to non-regional lymph nodes
M1b	The tumour has spread to the bone
M1c	The tumour has spread to other anatomical sites

10.Appendix C

10.1.Copyright forms

National Research Council Canada | Conseil national de recherches Canada | **Copyright Licence**

AUTHORITY TO REPRODUCE COPYRIGHT MATERIAL

To: Niranjan Venugopal

22-1048 Grant Avenue

Winnipeg, MB

R3M 2A3

This refers to the article or publication entitled: Automatic conformal prescription of very selective saturation bands for in vivo 1H-MRSI of the prostate

written by the author(s): N.Venugopal [a),b),c)], B. McCurdy[a),b),d)], J. Hovdebo[c)], S. Al Mehairi [e)], A. Alamri [e)], G. S. Sandhu [e)], S.Sivalingam [e)], D. Drachenberg [e)], and L. Ryner [a),c),d)]

[a)] Department of Physics and Astronomy, University of Manitoba, Winnipeg, Manitoba, Canada.
[b)] Department of Medical Physics, CancerCare Manitoba, Winnipeg, Manitoba, Canada.
[c)] National Research Council Institute for Biodiagnostics, Winnipeg, Manitoba, Canada.
[d)] Department of Radiology, University of Manitoba, Winnipeg, Manitoba, Canada.
[e)] Faculty of Medicine, Department of Surgery, Section of Urology, University of Manitoba, Winnipeg, Manitoba, Canada.

published in: NMR in Biomedicine

1. This material is subject to Crown Copyright, administered by the National Research Council of Canada.
2. Your request to reproduce and distribute this material is granted, free of charge, in accordance with the terms stated in your request, a copy of which is attached to this page.

Signed at Winnipeg, Manitoba (City and Province) on August 31, 2011 (Date)

NATIONAL RESEARCH COUNCIL OF CANADA

Per: R. Deslauriers

~~(Director General)~~ DIRECTOR, STRATEGIC PROGRAMS

(NRC-IBD)

AUTHORITY TO REPRODUCE COPYRIGHT MATERIAL

To: Niranjan Venugopal
22-1048 Grant Avenue
Winnipeg, MB
R3M 2A3

This refers to the article or publication entitled: SHORT ECHO TIME IN VIVO PROSTATE 1H-MRSI

written by the author(s): N.Venugopal [a),b),c)], B. McCurdy[a),b),d)], S. Al Mehairi [e)], A. Alamri [e)], G. S. Sandhu [e)], S.Sivalingam [e)], D. Drachenberg [e)], and L. Ryner [a),c),d)]
[a)] Department of Physics and Astronomy, University of Manitoba, Winnipeg, Manitoba, Canada.
[b)] Department of Medical Physics, CancerCare Manitoba, Winnipeg, Manitoba, Canada.
[c)] National Research Council Institute for Biodiagnostics, Winnipeg, Manitoba, Canada.
[d)] Department of Radiology, University of Manitoba, Winnipeg, Manitoba, Canada.
[e)] Faculty of Medicine, Department of Surgery, Section of Urology, University of Manitoba, Winnipeg, Manitoba, Canada.
published in: Magnetic Resonance Imaging

1. This material is subject to Crown Copyright, administered by the National Research Council of Canada.
2. Your request to reproduce and distribute this material is granted, free of charge, in accordance with the terms stated in your request, a copy of which is attached to this page.

Signed at Winnipeg, Manitoba (City and Province) on August 31, 2011 (Date)

NATIONAL RESEARCH COUNCIL OF CANADA

Per: R Desloges
~~(Director General)~~ Director, Strategic Programs
(NRC-IBD)

From: rialto@amc.seoul.kr <kim.jeongkon@gmail.com>
Subject: **Re: Permission Request**
Date: October 4, 2011 1:48:17 PM EDT
To: Niranjan Venugopal Niranjan.Venugopal@nrc-cnrc.gc.ca

Hi Niranjan,

No problem.

You can use it.

But if you are thinking of publication in journal, you need to get permission from publisher because I transferred the copyright to publisher.

Otherwise, nothing matters.

Jeong Kon Kim

On 2011. 10. 4., at 오전 11:18, Niranjan Venugopal wrote:

Dear Dr. Kim,

My name is Niranjan Venugopal. I'm a Ph.D. student at the University of Manitoba. I recently read your paper entitled, "Functional MR Imaging of Prostate Cancer" (Choi YJ et al., Functional MR imaging of prostate cancer. Radiographics. 2007 Jan-Feb;27(1):63-75; discussion -7.). I appreciate the paper and the level of detail in your figures.

Could I please use Figure 1 from this paper, for the purpose of my Ph.D. thesis?

I look forward to hearing from you.

Best wishes,

Niranjan

Niranjan Venugopal | Niranjan.Venugopal@nrc-cnrc.gc.ca
National Research Council Canada | Institute for Biodiagnostics
Tel: (204) 984-7070 | Fax: (204) 984-7036
435 Ellice Avenue, Winnipeg, MB R3B 1Y6

From: NKUDIC <nkudic@info.niddk.nih.gov>
Subject: **RE: Permission Request for image**
Date: October 4, 2011 2:21:37 PM EDT
To: "Venugopal, Niranjan" <Niranjan.Venugopal@nrc-cnrc.gc.ca>

Thank you for contacting the National Kidney and Urologic Diseases Information Clearinghouse (NKUDIC).

The National Institute of Diabetes and Digestive and Kidney Diseases (NIDDK) Image Library is a database of original full-color and black-and-white illustrations produced by the NIDDK Information Clearinghouses that are copyright free and are available to the public at no cost. The Library includes anatomical and medical, lifestyle and activity, and instructional illustrations presented in low, medium, and high resolutions.

We ask that you credit each illustration downloaded as follows: National Institute of Diabetes and Digestive and Kidney Diseases, National Institutes of Health.

We hope you find this information helpful.

If you need further information, please contact us by mail, phone, or email at

National Kidney and Urologic Diseases Information Clearinghouse
3 Information Way
Bethesda, MD 20892–3580
Phone: 1–800–891–5390
TTY: 1–866–569–1162
Fax: 703–738–4929
Email: nkudic@info.niddk.nih.gov
Internet: www.kidney.niddk.nih.gov

From: niranjan.venugopal@gmail.com [mailto:niranjan.venugopal@gmail.com] **On Behalf Of** Niranjan Venugopal
Sent: Tuesday, October 04, 2011 11:17 AM
To: NKUDIC
Subject: Permission Request for image

Dear Administrator at National Kidney and Urologic Diseases Information,

My name is Niranjan Venugopal. I'm a Ph.D. student at the University of Manitoba. I recently saw this image (Transrectal ultrasound and prostate biopsy) on your website located this url:

http://kidney.niddk.nih.gov/kudiseases/pubs/medtestprostate/

With your permission, could I please use this image for reference in my thesis?

I look forward to hearing from you.

Best wishes,

Niranjan

Niranjan Venugopal | Niranjan.Venugopal@nrc-cnrc.gc.ca
National Research Council Canada | Institute for Biodiagnostics

Bibliography

11.Bibliography

1. McNeal JE. The zonal anatomy of the prostate. Prostate. 1981;2(1):35-49.
2. Choi YJ, Kim JK, Kim N, Kim KW, Choi EK, Cho KS. Functional MR imaging of prostate cancer. Radiographics. 2007 Jan-Feb;27(1):63-75; discussion -7.
3. Society CC, Canada S, Registries PTC, Canada PHAo. Canadian Cancer Society's Steering Committee: Canadian Cancer Statistics 2011. 2011 April 2011.
4. Yuen JS, Thng CH, Tan PH, Khin LW, Phee SJ, Xiao D, Lau WK, Ng WS, Cheng CW. Endorectal magnetic resonance imaging and spectroscopy for the detection of tumor foci in men with prior negative transrectal ultrasound prostate biopsy. J Urol. 2004;171(4):1482-6.
5. Fuchsjager M, Shukla-Dave A, Akin O, Barentsz J, Hricak H. Prostate cancer imaging. Acta Radiol. 2008 Feb;49(1):107-20.
6. Kurhanewicz J, Vigneron DB. Advances in MR Spectroscopy of the Prostate. Magn Reson Imaging Clin N Am. 2008 Nov;16(4):697-710.
7. Mountford C. Magnetic resonance imaging and spectroscopy of the prostate. Magma. 2008 Nov;21(6):369-70.
8. Kurhanewicz J, Swanson MG, Wood PJ, Vigneron DB. Magnetic resonance imaging and spectroscopic imaging: Improved patient selection and potential for metabolic intermediate endpoints in prostate cancer chemoprevention trials. Urology. 2001;57(4 Suppl 1):124-8.
9. Costello LC, Franklin RB, Narayan P. Citrate in the diagnosis of prostate cancer. Prostate. 1999 Feb 15;38(3):237-45.
10. Cornel EB, Smits GA, de Ruijter JE, Oosterhof GO, Heerschap A, Debruyne FM, Schalken JA. In vitro proton magnetic resonance spectroscopy of four human prostate cancer cell lines. Prostate. 1995 May;26(5):275-80.
11. Kurhanewicz J, Vigneron DB, Hricak H, Narayan P, Carroll P, Nelson SJ. Three-dimensional H-1 MR spectroscopic imaging of the in situ human prostate with high (0.24-0.7-cm3) spatial resolution. Radiology. 1996;198(3): 795-805.
12. Kurhanewicz J, Vigneron DB, Nelson SJ, Hricak H, MacDonald JM, Konety B, Narayan P. Citrate as an in vivo marker to discriminate prostate cancer from benign prostatic hyperplasia and normal prostate peripheral zone: detection via localized proton spectroscopy. Urology. 1995;45(3):459-66.
13. Kurhanewicz J, Dahiya R, Macdonald JM, Chang LH, James TL, Narayan P. Citrate alterations in primary and metastatic human prostatic adenocarcinomas: 1H magnetic resonance spectroscopy and biochemical study. Magn Reson Med. 1993;29(2):149-57.
14. Yakar D, Heijmink SW, Hulsbergen-van de Kaa CA, Huisman H, Barentsz JO, Futterer JJ, Scheenen TW. Initial Results of 3-Dimensional 1H-Magnetic Resonance Spectroscopic Imaging in the Localization of Prostate Cancer at 3 Tesla: Should We Use an Endorectal Coil? Invest Radiol. 2011 Jan 7:In Press.
15. Crehange G, Parfait S, Liegard M, Maingon P, Ben Salem D, Cochet A, Funes de la Vega M, Cormier L, Bonnetain F, Mirjolet C, Brunotte F, Walker PM.

Tumor Volume and Metabolism of Prostate Cancer Determined by Proton Magnetic Resonance Spectroscopic Imaging at 3T Without Endorectal Coil Reveal Potential Clinical Implications in the Context of Radiation Oncology. Int J Radiat Oncol Biol Phys. 2010 Jul 7.
16. De Visschere P, Oosterlinck W, De Meerleer G, Villeirs G. Clinical and imaging tools in the early diagnosis of prostate cancer, a review. JBR-BTR. 2010 Mar-Apr;93(2):62-70.
17. Panebianco V, Sciarra A, Ciccariello M, Lisi D, Bernardo S, Cattarino S, Gentile V, Passariello R. Role of magnetic resonance spectroscopic imaging ([(1)H]MRSI) and dynamic contrast-enhanced MRI (DCE-MRI) in identifying prostate cancer foci in patients with negative biopsy and high levels of prostate-specific antigen (PSA). Radiol Med. 2010 Sep 17.
18. Sciarra A, Panebianco V, Ciccariello M, Salciccia S, Cattarino S, Lisi D, Gentilucci A, Alfarone A, Bernardo S, Passariello R, Gentile V. Value of magnetic resonance spectroscopy imaging and dynamic contrast-enhanced imaging for detecting prostate cancer foci in men with prior negative biopsy. Clin Cancer Res. 2010 Mar 15;16(6):1875-83.
19. Jagannathan NR, Kumar V, Kumar R, Thulkar S. Role of magnetic resonance methods in the evaluation of prostate cancer: an Indian perspective. Magma. 2008 Jul 17.
20. Casciani E, Gualdi GF. Prostate cancer: value of magnetic resonance spectroscopy 3D chemical shift imaging. Abdom Imaging. 2006 Sep 6;31(4): 490-9.
21. Wilman AH, Allen PS. The response of the strongly coupled AB system of citrate to typical 1H MRS localization sequences. J Magn Reson B. 1995 Apr;107(1):25-33.
22. Klomp DW, Scheenen TW, Arteaga CS, van Asten J, Boer VO, Luijten PR. Detection of fully refocused polyamine spins in prostate cancer at 7 T. NMR Biomed. 2010 Oct 6:In Press.
23. Klomp DW, Bitz AK, Heerschap A, Scheenen TW. Proton spectroscopic imaging of the human prostate at 7 T. NMR Biomed. 2009 Jun;22(5): 495-501.
24. Near J, Romagnoli C, Bartha R. Reduced power magnetic resonance spectroscopic imaging of the prostate at 4.0 Tesla. Magn Reson Med. 2009 Feb;61(2):273-81.
25. Kay LE, McClung RED. A product operator description of AB and ABX spin systems. Journal of Magnetic Resonance (1969). 1988;77(2):258-73.
26. Gambarota G, van der Graaf M, Klomp D, Mulkern RV, Heerschap A. Echo-time independent signal modulations using PRESS sequences: a new approach to spectral editing of strongly coupled AB spin systems. J Magn Reson. 2005 Dec;177(2):299-306.
27. Star-Lac J, Nelson SJ, Kurhanewicz J, Huang LR, Vigneron DB. Improved water and lipid suppression for 3D PRESS CSI using rf band selective inversion with gradient dephasing (basing). Magnetic Resonance in Medicine. 1997;38(2):311-21.

28. Star-Lack J, Nelson SJ, Kurhanewicz J, Huang LR, Vigneron DB. Improved water and lipid suppression for 3D PRESS CSI using RF band selective inversion with gradient dephasing (BASING). Magn Reson Med. 1997;38(2): 311-21.
29. Scheenen TW, Gambarota G, Weiland E, Klomp DW, Futterer JJ, Barentsz JO, Heerschap A. Optimal timing for in vivo 1H-MR spectroscopic imaging of the human prostate at 3T. Magn Reson Med. 2005 Jun;53(6):1268-74.
30. Schick F, Bongers H, Kurz S, Jung WI, Pfeffer M, Lutz O. Localized proton MR spectroscopy of citrate in vitro and of the human prostate in vivo at 1.5 T. Magn Reson Med. 1993 Jan;29(1):38-43.
31. van der Graaf M, Jager GJ, Heerschap A. Removal of the outer lines of the citrate multiplet in proton magnetic resonance spectra of the prostatic gland by accurate timing of a point-resolved spectroscopy pulse sequence. Magma. 1997 Mar;5(1):65-9.
32. Fuchsjager M, Akin O, Shukla-Dave A, Pucar D, Hricak H. The role of MRI and MRSI in diagnosis, treatment selection, and post-treatment follow-up for prostate cancer. Clin Adv Hematol Oncol. 2009 Mar;7(3):193-202.
33. Chang J, Thakur SB, Huang W, Narayana A. Magnetic resonance spectroscopy imaging (MRSI) and brain functional magnetic resonance imaging (fMRI) for radiotherapy treatment planning of glioma. Technol Cancer Res Treat. 2008 Oct;7(5):349-62.
34. McKenna DA, Coakley FV, Westphalen AC, Zhao S, Lu Y, Webb EM, Pickett B, Roach M, 3rd, Kurhanewicz J. Prostate cancer: role of pretreatment MR in predicting outcome after external-beam radiation therapy--initial experience. Radiology. 2008 Apr;247(1):141-6.
35. Thomas MA, Lange T, Velan SS, Nagarajan R, Raman S, Gomez A, Margolis D, Swart S, Raylman RR, Schulte RF, Boesiger P. Two-dimensional MR spectroscopy of healthy and cancerous prostates in vivo. Magma. 2008 Nov; 21(6):443-58.
36. Kwock L, Smith JK, Castillo M, Ewend MG, Collichio F, Morris DE, Bouldin TW, Cush S. Clinical role of proton magnetic resonance spectroscopy in oncology: brain, breast, and prostate cancer. Lancet Oncol. 2006 Oct;7(10): 859-68.
37. Shah N, Sattar A, Benanti M, Hollander S, Cheuck L. Magnetic resonance spectroscopy as an imaging tool for cancer: a review of the literature. J Am Osteopath Assoc. 2006 Jan;106(1):23-7.
38. Zhu XP, Young K, Ebel A, Soher BJ, Kaiser L, Matson G, Weiner WM, Schuff N. Robust analysis of short echo time (1)H MRSI of human brain. Magn Reson Med. 2006 Mar;55(3):706-11.
39. Casciani E, Bertini L, Gualdi G. Re: Alessandro Sciarra, Valeria Panebianco, Stefano Salciccia, et al. Role of dynamic contrast-enhanced magnetic resonance (MR) imaging and proton MR spectroscopic imaging in the detection of local recurrence after radical prostatectomy for prostate cancer. Eur Urol 2008;54:589-600. Eur Urol. 2009 Jan;55(1):e2-3; author reply e4-5.

40. Casciani E, Polettini E, Carmenini E, Floriani I, Masselli G, Bertini L, Gualdi GF. Endorectal and dynamic contrast-enhanced MRI for detection of local recurrence after radical prostatectomy. AJR Am J Roentgenol. 2008 May;190 (5):1187-92.
41. Casciani E, Polettini E, Bertini L, Masselli G, Emiliozzi P, Amini M, Pansadoro V, Gualdi GF. Contribution of the MR spectroscopic imaging in the diagnosis of prostate cancer in the peripheral zone. Abdom Imaging. 2007 Feb 10;32(6):796-802.
42. Tran TK, Vigneron DB, Sailasuta N, Tropp J, Le Roux P, Kurhanewicz J, Nelson S, Hurd R. Very selective suppression pulses for clinical MRSI studies of brain and prostate cancer. Magn Reson Med. 2000;43(1):23-33.
43. Park I, Chen AP, Zierhut ML, Ozturk-Isik E, Vigneron DB, Nelson SJ. Implementation of 3 T lactate-edited 3D 1H MR spectroscopic imaging with flyback echo-planar readout for gliomas patients. Ann Biomed Eng. 2010 Jan;39(1):193-204.
44. Osorio JA, Xu D, Cunningham CH, Chen A, Kerr AB, Pauly JM, Vigneron DB, Nelson SJ. Design of cosine modulated very selective suppression pulses for MR spectroscopic imaging at 3T. Magnetic Resonance in Medicine. 2009;61 (3):533-40.
45. Chen AP, Cunningham CH, Kurhanewicz J, Xu D, Hurd RE, Pauly JM, Carvajal L, Karpodinis K, Vigneron DB. High-resolution 3D MR spectroscopic imaging of the prostate at 3 T with the MLEV-PRESS sequence. Magn Reson Imaging. 2006 Sep;24(7):825-32.
46. Li Y, Osorio JA, Ozturk-Isik E, Chen AP, Xu D, Crane JC, Cha S, Chang S, Berger MS, Vigneron DB, Nelson SJ. Considerations in applying 3D PRESS H-1 brain MRSI with an eight-channel phased-array coil at 3 T. Magn Reson Imaging. 2006 Dec;24(10):1295-302.
47. Scheenen TW, Futterer J, Weiland E, van Hecke P, Lemort M, Zechmann C, Schlemmer HP, Broome D, Villeirs G, Lu J, Barentsz J, Roell S, Heerschap A. Discriminating cancer from noncancer tissue in the prostate by 3-dimensional proton magnetic resonance spectroscopic imaging: a prospective multicenter validation study. Invest Radiol. 2010 Jan;46(1): 25-33.
48. Haake EM, Brown RW, Thompson MR, Venkatesan R. Magnetic Resonance Imaging. New York: John Wiley & Sons, Inc., Publication; 1999.
49. Chen AP, Cunningham CH, Ozturk-Isik E, Xu D, Hurd RE, Kelley DA, Pauly JM, Kurhanewicz J, Nelson SJ, Vigneron DB. High-speed 3T MR spectroscopic imaging of prostate with flyback echo-planar encoding. J Magn Reson Imaging. 2007 Jun;25(6):1288-92.
50. Yu JS, Chung JJ, Hong SW, Chung BH, Kim JH, Kim KW. Prostate cancer: added value of subtraction dynamic imaging in 3T magnetic resonance imaging with a phased-array body coil. Yonsei Med J. 2008 Oct 31;49(5): 765-74.
51. Odrazka K, Zouhar M, Petera J, Vaculikova M, Dolezel M, Vosmik M, Tucek P. Comparison of rectal dose-volume constraints for IMRT prostate treatment planning. Phys Med. 2005 October - December;21(4):129-35.

52. Hall EJ, Giaccia AJ. Radiobiology for the radiologist. Philadelphia, Pa. [u.a.: Lippincott Williams & Wilkins; 2006.
53. Wilder RB, Barme GA, Gilbert RF, Holevas RE, Kobashi LI, Reed RR, Solomon RS, Walter NL, Chittenden L, Mesa AV, Agustin JK, Lizarde J, Macedo JC, Ravera J, Tokita KM. Preliminary results in prostate cancer patients treated with high-dose-rate brachytherapy and intensity modulated radiation therapy (IMRT) vs. IMRT alone. Brachytherapy. 2009 Oct 21.
54. Bortfeld T. Image guided IMRT Berlin; Heidelberg; New York: Springer; 2006.
55. Dearnaley DP, Khoo VS, Norman AR, Meyer L, Nahum A, Tait D, Yarnold J, Horwich A. Comparison of radiation side-effects of conformal and conventional radiotherapy in prostate cancer: a randomised trial. Lancet. 1999 Jan 23;353(9149):267-72.
56. Staff I, Salner A, Bohannon R, Panatieri P, Maljanian R. Disease-specific symptoms and general quality of life of patients with prostate carcinoma before and after primary three-dimensional conformal radiotherapy. Cancer. 2003 Dec 1;98(11):2335-43.
57. Leibel SA, Fuks Z, Zelefsky MJ, Hunt M, Burman CM, Mageras GS, Chui CS, Jackson A, Amols HI, Ling CC. Technological advances in external-beam radiation therapy for the treatment of localized prostate cancer. Semin Oncol. 2003;30(5):596-615.
58. Barney BM, Lee RJ, Handrahan D, Welsh KT, Cook JT, Sause WT. Image-guided radiotherapy (IGRT) for prostate cancer comparing kV imaging of fiducial markers with cone beam computed tomography (CBCT). Int J Radiat Oncol Biol Phys. 2010 May 1;80(1):301-5.
59. Middleton M, Frantzis J, Healy B, Jones M, Murry R, Kron T, Plank A, Catton C, Martin J. Successful Implementation of Image-Guided Radiation Therapy Quality Assurance in the Trans Tasman Radiation Oncology Group 08.01 PROFIT Study. Int J Radiat Oncol Biol Phys. 2010 Nov 11.
60. Cormack RA, Sridhar S, Suh WW, D'Amico AV, Makrigiorgos GM. Biological in situ dose painting for image-guided radiation therapy using drug-loaded implantable devices. Int J Radiat Oncol Biol Phys. 2009 Feb 1;76(2):615-23.
61. Mao W, Hsu A, Riaz N, Lee L, Wiersma R, Luxton G, King C, Xing L, Solberg T. Image-guided radiotherapy in near real time with intensity-modulated radiotherapy megavoltage treatment beam imaging. Int J Radiat Oncol Biol Phys. 2009 Oct 1;75(2):603-10.
62. Zhu X, Bourland JD, Yuan Y, Zhuang T, O'Daniel J, Thongphiew D, Wu QJ, Das SK, Yoo S, Yin FF. Tradeoffs of integrating real-time tracking into IGRT for prostate cancer treatment. Phys Med Biol. 2009 Sep 7;54(17):N393-401.
63. Nairz O, Merz F, Deutschmann H, Kopp P, Scholler H, Zehentmayr F, Wurstbauer K, Kametriser G, Sedlmayer F. A strategy for the use of image-guided radiotherapy (IGRT) on linear accelerators and its impact on treatment margins for prostate cancer patients. Strahlenther Onkol. 2008 Dec;184(12):663-7.
64. Zelefsky MJ, Fuks Z, Happersett L, Lee HJ, Ling CC, Burman CM, Hunt M, Wolfe T, Venkatraman ES, Jackson A, Skwarchuk M, Leibel SA. Clinical

experience with intensity modulated radiation therapy (IMRT) in prostate cancer. Radiother Oncol. 2000 Jun;55(3):241-9.
65. Vora SA, Wong WW, Schild SE, Ezzell GA, Halyard MY. Analysis of biochemical control and prognostic factors in patients treated with either low-dose three-dimensional conformal radiation therapy or high-dose intensity-modulated radiotherapy for localized prostate cancer. Int J Radiat Oncol Biol Phys. 2007 Jul 15;68(4):1053-8.
66. Zelefsky MJ, Yamada Y, Kollmeier MA, Shippy AM, Nedelka MA. Long-term outcome following three-dimensional conformal/intensity-modulated external-beam radiotherapy for clinical stage T3 prostate cancer. Eur Urol. 2008 Jun;53(6):1172-9.
67. Zelefsky MJ, Chan H, Hunt M, Yamada Y, Shippy AM, Amols H. Long-term outcome of high dose intensity modulated radiation therapy for patients with clinically localized prostate cancer. J Urol. 2006 Oct;176(4 Pt 1):1415-9.
68. Soete G, Verellen D, Storme G. Image guided radiotherapy for prostate cancer. Bull Cancer. 2008 Mar;95(3):374-80.
69. Enmark M, Korreman S, Nystrom H. IGRT of prostate cancer; is the margin reduction gained from daily IG time-dependent? Acta Oncol. 2006;45(7): 907-14.
70. Martin JM, Bayley A, Bristow R, Chung P, Gospodarowicz M, Menard C, Milosevic M, Rosewall T, Warde PR, Catton CN. Image guided dose escalated prostate radiotherapy: still room to improve. Radiat Oncol. 2009;4:50.
71. Basu KS, Bahl A, Subramani V, Sharma DN, Rath GK, Julka PK. Normal tissue complication probability: does simultaneous integrated boost intensity-modulated radiotherapy score over other techniques in treatment of prostate adenocarcinoma. J Cancer Res Ther. 2009 Apr-Jun;5(2):78-84.
72. van Lin EN, Futterer JJ, Heijmink SW, van der Vight LP, Hoffmann AL, van Kollenburg P, Huisman HJ, Scheenen TW, Witjes JA, Leer JW, Barentsz JO, Visser AG. IMRT boost dose planning on dominant intraprostatic lesions: gold marker-based three-dimensional fusion of CT with dynamic contrast-enhanced and 1H-spectroscopic MRI. Int J Radiat Oncol Biol Phys. 2006 May 1;65(1):291-303.
73. Li XA, Wang JZ, Jursinic PA, Lawton CA, Wang D. Dosimetric advantages of IMRT simultaneous integrated boost for high-risk prostate cancer. Int J Radiat Oncol Biol Phys. 2005 Mar 15;61(4):1251-7.
74. Ciernik IF, Brown DW, Schmid D, Hany T, Egli P, Davis JB. 3D-segmentation of the 18F-choline PET signal for target volume definition in radiation therapy of the prostate. Technol Cancer Res Treat. 2007 Feb;6(1):23-30.
75. Stewart RD, Li XA. BGRT: biologically guided radiation therapy-the future is fast approaching! Med Phys. 2007 Oct;34(10):3739-51.
76. Warkentin B, Stavrev P, Stavreva NA, Fallone BG. Limitations of a TCP model incorporating population heterogeneity. Phys Med Biol. 2005 Aug 7;50(15): 3571-88.

77. Warkentin B, Stavrev P, Stavreva N, Field C, Fallone BG. A TCP-NTCP estimation module using DVHs and known radiobiological models and parameter sets. J Appl Clin Med Phys. 2004 Winter;5(1):50-63.
78. Fowler JF. The linear-quadratic formula and progress in fractionated radiotherapy. Br J Radiol. 1989 Aug;62(740):679-94.
79. Reddy NM, Sood BM, Sampath S, Mazur A, Osian A, Ravi A, Poli J, Nori D. Single course IMRT plan to deliver 45 Gy to seminal vesicles and 81 Gy to prostate in 45 fractions. Technol Cancer Res Treat. 2006 Oct;5(5):503-11.
80. Wang JZ, Li XA, Yu CX, DiBiase SJ. The low alpha/beta ratio for prostate cancer: what does the clinical outcome of HDR brachytherapy tell us? Int J Radiat Oncol Biol Phys. 2003 Nov 15;57(4):1101-8.
81. King CR, DiPetrillo TA, Wazer DE. Optimal radiotherapy for prostate cancer: predictions for conventional external beam, IMRT, and brachytherapy from radiobiologic models. Int J Radiat Oncol Biol Phys. 2000 Jan 1;46(1):165-72.
82. Tobias CA. The repair-misrepair model in radiobiology: comparison to other models. Radiat Res Suppl. 1985;8:S77-95.
83. Tome WA, Fowler JF. On the inclusion of proliferation in tumour control probability calculations for inhomogeneously irradiated tumours. Phys Med Biol. 2003 Sep 21;48(18):N261-8.
84. Thames HD, Bentzen SM, Turesson I, Overgaard M, Van den Bogaert W. Time-dose factors in radiotherapy: a review of the human data. Radiother Oncol. 1990 Nov;19(3):219-35.
85. Carlson DJ, Stewart RD, Li XA, Jennings K, Wang JZ, Guerrero M. Comparison of in vitro and in vivo alpha/beta ratios for prostate cancer. Phys Med Biol. 2004 Oct 7;49(19):4477-91.
86. Ahmad S, Vogds BJ, McKenna F, Vlachaki MT. Tumor control probability (TCP) in prostate cancer: role of radiobiological parameters and radiation dose escalation. J Xray Sci Technol. 2009 Jan 1;17(4):347-54.
87. Deb P, Fielding A. Radiobiological model comparison of 3D conformal radiotherapy and IMRT plans for the treatment of prostate cancer. Australas Phys Eng Sci Med. 2009 Jun;32(2):51-61.
88. Guckenberger M, Baier K, Richter A, Vordermark D, Flentje M. Does intensity modulated radiation therapy (IMRT) prevent additional toxicity of treating the pelvic lymph nodes compared to treatment of the prostate only? Radiat Oncol. 2008;3:3.
89. Carlone MC, Warkentin B, Stavrev P, Fallone BG. Fundamental form of a population TCP model in the limit of large heterogeneity. Med Phys. 2006 Jun;33(6):1634-42.
90. Grigorov GN, Chow JC, Grigorov L, Jiang R, Barnett RB. IMRT: improvement in treatment planning efficiency using NTCP calculation independent of the dose-volume-histogram. Med Phys. 2006 May;33(5):1250-8.
91. Song WY, Schaly B, Bauman G, Battista JJ, Van Dyk J. Evaluation of image-guided radiation therapy (IGRT) technologies and their impact on the outcomes of hypofractionated prostate cancer treatments: a radiobiologic analysis. Int J Radiat Oncol Biol Phys. 2006 Jan 1;64(1):289-300.

92. Wang JZ, Li XA, Mayr NA. Dose escalation to combat hypoxia in prostate cancer: a radiobiological study on clinical data. Br J Radiol. 2006 Nov;79 (947):905-11.
93. Wang XZ, Wang B, Gao ZQ, Liu JG, Liu ZQ, Niu QL, Sun ZK, Yuan YX. 1H-MRSI of prostate cancer: the relationship between metabolite ratio and tumor proliferation. Eur J Radiol. 2010 Feb;73(2):345-51.
94. Ryner LN, Westmacott G, Latta P, Davison N, inventors; National Research Council of Canada, Ottawa (CA), assignee. Magnetic Resonance Spectroscopy using a conformal voxel. U.S.2008 Jan. 15, 2008.
95. Ryner L, Westmacott G, Davison N, Latta P. Automated Positioning of Multiple Spatial Saturation Planes for Non-Cuboidal Voxel Prescription in MR Spectroscopy. Proceedings of the 13th Annual Meeting ISMRM. 2005 May 7-13:350.
96. Hovdebo J, Ryner L. An Improved Method for Automatic Placement of Spatial Saturation Planes in MR Spectroscopy. Proceedings of the 17th Annual Meeting ISMRM. 2009 April 18-24:2376.
97. Sharma C, Bolinger L, Ryner L, editors. A hybrid data analysis and mesh refinement paradigm for conformal voxel spectroscopy. 3rd IEEE International Symposium on Biomedical Imaging: Nano to Macro, 2006; 2006: IEEE.
98. Garland M, Heckbert PS. Surface simplification using quadric error metrics. Proceedings of the 24th annual conference on Computer graphics and interactive techniques: ACM Press/Addison-Wesley Publishing Co.; 1997.
99. Males RG, Vigneron DB, Star-Lack J, Falbo SC, Nelson SJ, Hricak H, Kurhanewicz J. Clinical application of BASING and spectral/spatial water and lipid suppression pulses for prostate cancer staging and localization by in vivo 3D 1H magnetic resonance spectroscopic imaging. Magn Reson Med. 2000;43(1):17-22.
100. Star-Lack J, Spielman D, Adalsteinsson E, Kurhanewicz J, Terris DJ, Vigneron DB. In vivo lactate editing with simultaneous detection of choline, creatine, NAA, and lipid singlets at 1.5 T using PRESS excitation with applications to the study of brain and head and neck tumors. J Magn Reson. 1998;133(2): 243-54.
101. Star-Lack J, Vigneron DB, Pauly J, Kurhanewicz J, Nelson SJ. Improved solvent suppression and increased spatial excitation bandwidths for three-dimensional PRESS CSI using phase-compensating spectral/spatial spin-echo pulses. J Magn Reson Imaging. 1997;7(4):745-57.
102. Ryner L, Lauzon L. Simultaneous Water and Fat Suppression in Breast MRS Using Spectral/Spatial PRESS. Proceedings of the 9th Annual Meeting ISMRM. 2001 April 21-27:21.
103. Hajek M, Burian M, Dezortova M. Application of LCModel for quality control and quantitative in vivo 1H MR spectroscopy by short echo time STEAM sequence. Magma. 2000 Feb;10(1):6-17.
104. Jensen JE, Licata SC, Ongur D, Friedman SD, Prescot AP, Henry ME, Renshaw PF. Quantification of J-resolved proton spectra in two-dimensions

with LCModel using GAMMA-simulated basis sets at 4 Tesla. NMR Biomed. 2009 Aug;22(7):762-9.
105. Kanowski M, Kaufmann J, Braun J, Bernarding J, Tempelmann C. Quantitation of simulated short echo time 1H human brain spectra by LCModel and AMARES. Magn Reson Med. 2004 May;51(5):904-12.
106. Oakden WK, Noseworthy MD. Propylene glycol is essential in the LCModel basis set for pediatric 1H-MRS. J Comput Assist Tomogr. 2005 Jan-Feb;29(1): 136-9.
107. Opstad KS, Provencher SW, Bell BA, Griffiths JR, Howe FA. Detection of elevated glutathione in meningiomas by quantitative in vivo 1H MRS. Magn Reson Med. 2003 Apr;49(4):632-7.
108. Weis J, Johansson L, Ortiz-Nieto F, Ahlstrom H. Assessment of lipids in skeletal muscle by LCModel and AMARES. J Magn Reson Imaging. 2009 Nov;30(5):1124-9.
109. Baker EH, Basso G, Barker PB, Smith MA, Bonekamp D, Horska A. Regional apparent metabolite concentrations in young adult brain measured by (1)H MR spectroscopy at 3 Tesla. J Magn Reson Imaging. 2008 Mar;27(3):489-99.
110. Oz G, Terpstra M, Tkac I, Aia P, Lowary J, Tuite PJ, Gruetter R. Proton MRS of the unilateral substantia nigra in the human brain at 4 tesla: detection of high GABA concentrations. Magn Reson Med. 2006 Feb;55(2):296-301.
111. Hammen T, Stadlbauer A, Tomandl B, Ganslandt O, Pauli E, Huk W, Neundorfer B, Stefan H. Short TE single-voxel 1H-MR spectroscopy of hippocampal structures in healthy adults at 1.5 Tesla--how reproducible are the results? NMR Biomed. 2005 May;18(3):195-201.
112. Srinivasan R, Sailasuta N, Hurd R, Nelson S, Pelletier D. Evidence of elevated glutamate in multiple sclerosis using magnetic resonance spectroscopy at 3 T. Brain. 2005 May;128(Pt 5):1016-25.
113. Macri MA, Garreffa G, Giove F, Guardati M, Ambrosini A, Colonnese C, Maraviglia B. In vivo quantitative 1H MRS of cerebellum and evaluation of quantitation reproducibility by simulation of different levels of noise and spectral resolution. Magn Reson Imaging. 2004 Dec;22(10):1385-93.
114. Brief EE, Moll R, Li DK, Mackay AL. Absolute metabolite concentrations calibrated using the total water signal in brain (1)H MRS. NMR Biomed. 2009 Apr;22(3):349-54.
115. Provencher SW. Estimation of metabolite concentrations from localized in vivo proton NMR spectra. Magn Reson Med. 1993 Dec;30(6):672-9.
116. Provencher S. LCModel Manual (LCModel Version 6.2-4)2011: Available from: http://s-provencher.com/pages/lcm-manual.shtml.
117. Hovdebo J, Ryner L. An integrated Analysis Platform for Magnetic Resonance Spectroscopy. Proceedings of the 16th Annual Meeting ISMRM. 2008 May 3-9:1571.
118. Venugopal N, McCurdy BMC, Ryner L. Improved prostate MRSI employing a conformal voxel technique. Proceedings of the 16th Annual Meeting ISMRM. 2008 May 3-9:2767.

119. Venugopal N, McCurdy B, Ryner L. Cutting the Fat: Reducing periprostatic lipid contamination in Prostate MRSI. Joint CARO-COMP Conference: Image Guided and Adaptive Radiation Therapy; October 9-13; Toronto2007.
120. Venugopal N, McCurdy B, Ryner L. A 3D Model-Based Outer Volume Suppression Technique for MR Spectroscopic Imaging of The Prostate. CMS-MITACS Joint Conference 2007: Mathematical Algorithms for Medical Imaging; May; Winnipeg2007.
121. Venugopal N, McCurdy B, Hnatov A, Dubey A. Po-Thur Eve General-26: Tracking intraprostatic volumes for determining non-linear warping algorithm variability. Medical Physics. 2006;33(7):2665.
122. Kurhanewicz J, Thomas A, Jajodia P, Weiner MW, James TL, Vigneron DB, Narayan P. 31P spectroscopy of the human prostate gland in vivo using a transrectal probe. Magn Reson Med. 1991;22(2):404-13.
123. Cornel EB, Smits GA, Oosterhof GO, Karthaus HF, Deburyne FM, Schalken JA, Heerschap A. Characterization of human prostate cancer, benign prostatic hyperplasia and normal prostate by in vitro 1H and 31P magnetic resonance spectroscopy. J Urol. 1993;150(6):2019-24.
124. Rajesh A, Coakley FV, Kurhanewicz J. 3D MR spectroscopic imaging in the evaluation of prostate cancer. Clin Radiol. 2007 Oct;62(10):921-9.
125. Westphalen AC, McKenna DA, Kurhanewicz J, Coakley FV. Role of magnetic resonance imaging and magnetic resonance spectroscopic imaging before and after radiotherapy for prostate cancer. J Endourol. 2008 Apr;22(4): 789-94.
126. Scheenen TW, Klomp DW, Roll SA, Futterer JJ, Barentsz JO, Heerschap A. Fast acquisition-weighted three-dimensional proton MR spectroscopic imaging of the human prostate. Magn Reson Med. 2004 Jul;52(1):80-8.
127. Sciarra A, Panebianco V, Ciccariello M, Salciccia S, Gentilucci A, Lisi D, Passariello R, Gentile V, Di Silverio F. Complete response to the combination therapy with androgen blockade and somatostatin analogue in a patient with advanced prostate cancer: magnetic resonance imaging with 1H-spectroscopy. Eur Urol. 2008 Mar;53(3):652-5.
128. Coakley FV, Chen I, Qayyum A, Westphalen AC, Carroll PR, Hricak H, Chen MH, Kurhanewicz J. Validity of prostate-specific antigen as a tumour marker in men with prostate cancer managed by watchful-waiting: correlation with findings at serial endorectal magnetic resonance imaging and spectroscopic imaging. BJU Int. 2007 Jan;99(1):41-5.
129. Noworolski SM, Henry RG, Vigneron DB, Kurhanewicz J. Dynamic contrast-enhanced MRI in normal and abnormal prostate tissues as defined by biopsy, MRI, and 3D MRSI. Magn Reson Med. 2005 Feb;53(2):249-55.
130. Kurhanewicz J, Swanson MG, Nelson SJ, Vigneron DB. Combined magnetic resonance imaging and spectroscopic imaging approach to molecular imaging of prostate cancer. J Magn Reson Imaging. 2002;16(4):451-63.
131. Swanson MG, Vigneron DB, Tabatabai ZL, Males RG, Schmitt L, Carroll PR, James JK, Hurd RE, Kurhanewicz J. Proton HR-MAS spectroscopy and quantitative pathologic analysis of MRI/3D-MRSI-targeted postsurgical prostate tissues. Magn Reson Med. 2003;50(5):944-54.

132. Wang XZ, Wang B, Gao ZQ, Liu JG, Liu ZQ, Niu QL, Sun ZK, Yuan YX. 1H-MRSI of prostate cancer: The relationship between metabolite ratio and tumor proliferation. European Journal of Radiology. 2008;73(2):345-51.
133. Kurhanewicz J, Vigneron D, Carroll P, Coakley F. Multiparametric magnetic resonance imaging in prostate cancer: present and future. Curr Opin Urol. 2008 Jan;18(1):71-7.
134. Umbehr M, Bachmann LM, Held U, Kessler TM, Sulser T, Weishaupt D, Kurhanewicz J, Steurer J. Combined magnetic resonance imaging and magnetic resonance spectroscopy imaging in the diagnosis of prostate cancer: a systematic review and meta-analysis. Eur Urol. 2009 Mar;55(3): 575-90.
135. Westphalen AC, Coakley FV, Qayyum A, Swanson M, Simko JP, Lu Y, Zhao S, Carroll PR, Yeh BM, Kurhanewicz J. Peripheral zone prostate cancer: accuracy of different interpretative approaches with MR and MR spectroscopic imaging. Radiology. 2008 Jan;246(1):177-84.
136. Golder W. Magnetic resonance spectroscopy in clinical oncology. Onkologie. 2004 Jun;27(3):304-9.
137. Scheidler J, Hricak H, Vigneron DB, Yu KK, Sokolov DL, Huang LR, Zaloudek CJ, Nelson SJ, Carroll PR, Kurhanewicz J. Prostate cancer: localization with three-dimensional proton MR spectroscopic imaging--clinicopathologic study. Radiology. 1999 Nov;213(2):473-80.
138. Pickett B, Kurhanewicz J, Pouliot J, Weinberg V, Shinohara K, Coakley F, Roach M, 3rd. Three-dimensional conformal external beam radiotherapy compared with permanent prostate implantation in low-risk prostate cancer based on endorectal magnetic resonance spectroscopy imaging and prostate-specific antigen level. Int J Radiat Oncol Biol Phys. 2006 May 1;65 (1):65-72.
139. Kim Y, Hsu IC, Lessard E, Kurhanewicz J, Noworolski SM, Pouliot J. Class solution in inverse planned HDR prostate brachytherapy for dose escalation of DIL defined by combined MRI/MRSI. Radiother Oncol. 2008 Jul;88(1): 148-55.
140. Payne GS, Leach MO. Applications of magnetic resonance spectroscopy in radiotherapy treatment planning. Br J Radiol. 2006 Sep;79 Spec No 1:S16-26.
141. Sciarra A, Panebianco V, Salciccia S, Osimani M, Lisi D, Ciccariello M, Passariello R, Di Silverio F, Gentile V. Role of dynamic contrast-enhanced magnetic resonance (MR) imaging and proton MR spectroscopic imaging in the detection of local recurrence after radical prostatectomy for prostate cancer. Eur Urol. 2008 Sep;54(3):589-600.
142. Qayyum A, Coakley FV, Lu Y, Olpin JD, Wu L, Yeh BM, Carroll PR, Kurhanewicz J. Organ-confined prostate cancer: effect of prior transrectal biopsy on endorectal MRI and MR spectroscopic imaging. AJR Am J Roentgenol. 2004 Oct;183(4):1079-83.
143. Schricker AA, Pauly JM, Kurhanewicz J, Swanson MG, Vigneron DB. Dualband spectral-spatial RF pulses for prostate MR spectroscopic imaging. Magn Reson Med. 2001;46(6):1079-87.

144. Mescher M, Merkle H, Kirsch J, Garwood M, Gruetter R. Simultaneous in vivo spectral editing and water suppression. NMR Biomed. 1998 Oct;11(6): 266-72.
145. Singh S, Rutt BK, Mark Henkelman R. Projection presaturation: A fast and accurate technique for multidimensional spatial localization. Journal of Magnetic Resonance (1969). 1990;87(3):567-83.
146. Chen YJ, Rachamadugu S, Fernandez EJ. Three dimensional outer volume suppression for short echo time in vivo 1H spectroscopic imaging in rat brain. Magn Reson Imaging. 1997;15(7):839-45.
147. Chu A, Alger JR, Moore GJ, Posse S. Proton echo-planar spectroscopic imaging with highly effective outer volume suppression using combined presaturation and spatially selective echo dephasing. Magn Reson Med. 2003 May;49(5):817-21.
148. Choi H, Ma J. Use of perfluorocarbon compound in the endorectal coil to improve MR spectroscopy of the prostate. AJR Am J Roentgenol. 2008 Apr; 190(4):1055-9.
149. Bottomley PA, Foster TH, Argersinger RE, Pfeifer LM. A review of normal tissue hydrogen NMR relaxation times and relaxation mechanisms from 1-100 MHz: dependence on tissue type, NMR frequency, temperature, species, excision, and age. Med Phys. 1984 Jul-Aug;11(4):425-48.
150. Jung JA, Coakley FV, Vigneron DB, Swanson MG, Qayyum A, Weinberg V, Jones KD, Carroll PR, Kurhanewicz J. Prostate depiction at endorectal MR spectroscopic imaging: investigation of a standardized evaluation system. Radiology. 2004 Dec;233(3):701-8.
151. Reinsberg SA, Payne GS, Riches SF, Ashley S, Brewster JM, Morgan VA, deSouza NM. Combined use of diffusion-weighted MRI and 1H MR spectroscopy to increase accuracy in prostate cancer detection. AJR Am J Roentgenol. 2007 Jan;188(1):91-8.
152. Crehange G, Parfait S, Liegard M, Maingon P, Ben Salem D, Cochet A, Funes de la Vega M, Cormier L, Bonnetain F, Mirjolet C, Brunotte F, Walker PM. Tumor Volume and Metabolism of Prostate Cancer Determined by Proton Magnetic Resonance Spectroscopic Imaging at 3T Without Endorectal Coil Reveal Potential Clinical Implications in the Context of Radiation Oncology. International Journal of Radiation Oncology*Biology*Physics.In Press, Corrected Proof.
153. Weinreb JC, Blume JD, Coakley FV, Wheeler TM, Cormack JB, Sotto CK, Cho H, Kawashima A, Tempany-Afdhal CM, Macura KJ, Rosen M, Gerst SR, Kurhanewicz J. Prostate cancer: sextant localization at MR imaging and MR spectroscopic imaging before prostatectomy--results of ACRIN prospective multi-institutional clinicopathologic study. Radiology. 2009 Apr;251(1): 122-33.
154. Martinez-Ramon M, Gallardo-Antolin A, Cid-Sueiro J, Heileman GL, Yung KT, Zheng W, Zhao C, Posse S. Automatic placement of outer volume suppression slices in MR spectroscopic imaging of the human brain. Magn Reson Med. Mar;63(3):592-600.

155. Ozhinsky E, Vigneron DB, Nelson SJ. Improved spatial coverage for brain 3D PRESS MRSI by automatic placement of outer-volume suppression saturation bands. J Magn Reson Imaging. 2011 Apr;33(4):792-802.
156. Sciarra A, Panebianco V, Ciccariello M, Salciccia S, Lisi D, Osimani M, Alfarone A, Gentilucci A, Parente U, Passariello R, Gentile V. Magnetic resonance spectroscopic imaging (1H-MRSI) and dynamic contrast-enhanced magnetic resonance (DCE-MRI): pattern changes from inflammation to prostate cancer. Cancer Invest. 2010 May;28(4):424-32.
157. McLean MA, Barrett T, Gnanapragasam VJ, Priest AN, Joubert I, Lomas DJ, Neal DE, Griffiths JR, Sala E. Prostate cancer metabolite quantification relative to water in (1)H-MRSI in vivo at 3 Tesla. Magn Reson Med. 2010 Nov 16:In Press.
158. Venugopal N, McCurdy B, Mehairi SA, Alamri A, Sandhu GS, Drachenberg D, Ryner L. Short echo time in vivo prostate MRSI. Proceedings of the 18th Annual Meeting ISMRM. 2010 May 1-7:2807.
159. Henning A, Schar M, Schulte RF, Wilm B, Pruessmann KP, Boesiger P. SELOVS: brain MRSI localization based on highly selective T1- and B1-insensitive outer-volume suppression at 3T. Magn Reson Med. 2008 Jan;59 (1):40-51.
160. Henning A, Fuchs A, Murdoch JB, Boesiger P. Slice-selective FID acquisition, localized by outer volume suppression (FIDLOVS) for (1)H-MRSI of the human brain at 7 T with minimal signal loss. NMR Biomed. 2009 Aug;22(7): 683-96.
161. Wallner K. MR imaging for prostate cancer staging: beauty or beast? Int J Radiat Oncol Biol Phys. 2002;52(4):886-7.
162. Villeirs GM, De Meerleer GO, De Visschere PJ, Fonteyne VH, Verbaeys AC, Oosterlinck W. Combined magnetic resonance imaging and spectroscopy in the assessment of high grade prostate carcinoma in patients with elevated PSA: a single-institution experience of 356 patients. Eur J Radiol. 2009 Feb; 77(2):340-5.
163. Seitz M, Shukla-Dave A, Bjartell A, Touijer K, Sciarra A, Bastian PJ, Stief C, Hricak H, Graser A. Functional magnetic resonance imaging in prostate cancer. Eur Urol. 2009 Apr;55(4):801-14.
164. Scheidler J, Vogel M, Gross P, Heuck A. Combined MRI and MRS in prostate cancer: improvement of spectral quality by susceptibility matching. Rofo. 2009 Jun;181(6):531-5.
165. Rajesh A, Coakley FV. MR imaging and MR spectroscopic imaging of prostate cancer. Magn Reson Imaging Clin N Am. 2004 Aug;12(3):557-79, vii.
166. Cirillo S, Petracchini M, Della Monica P, Gallo T, Tartaglia V, Vestita E, Ferrando U, Regge D. Value of endorectal MRI and MRS in patients with elevated prostate-specific antigen levels and previous negative biopsies to localize peripheral zone tumours. Clin Radiol. 2008 Aug;63(8):871-9.
167. Kim HW, Buckley DL, Peterson DM, Duensing GR, Caserta J, Fitzsimmons J, Blackband SJ. In vivo prostate magnetic resonance imaging and magnetic

resonance spectroscopy at 3 Tesla using a transceive pelvic phased array coil: preliminary results. Invest Radiol. 2003;38(7):443-51.
168. Sciarra A, Panebianco V, Salciccia S, Cattarino S, Lisi D, Gentilucci A, Alfarone A, Mariotti G, Passariello R, Gentile V. Modern role of magnetic resonance and spectroscopy in the imaging of prostate cancer. Urol Oncol. 2009 Sep 5.
169. Nayyar R, Kumar R, Kumar V, Jagannathan NR, Gupta NP, Hemal AK. Magnetic resonance spectroscopic imaging: current status in the management of prostate cancer. BJU Int. 2009 Jun;103(12):1614-20.
170. Kumar V, Jagannathan NR, Kumar R, Nayyar R, Thulkar S, Gupta SD, Hemal AK, Gupta NP. Potential of (1)H MR spectroscopic imaging to segregate patients who are likely to show malignancy of the peripheral zone of the prostate on biopsy. J Magn Reson Imaging. 2009 Oct;30(4):842-8.
171. Zakian KL, Shukla-Dave A, Ackerstaff E, Hricak H, Koutcher JA. 1H magnetic resonance spectroscopy of prostate cancer: biomarkers for tumor characterization. Cancer Biomark. 2008;4(4-5):263-76.
172. Venugopal N, McCurdy B, Mehairi SA, Alamri A, Sandhu GS, Drachenberg D, Ryner L. A voxel-by-voxel benchmark comparison between two in vivo prostate MRSI techniques ISMRM 17th Scientific Meeting & Exhibition; April 18-24, 2009; Hawaii, USA: International Society for Magnetic Resonance in Medicine; 2009. p. 2145.
173. Provencher SW. Automatic quantitation of localized in vivo 1H spectra with LCModel. NMR Biomed. 2001 Jun;14(4):260-4.
174. Zapotoczna A, Sasso G, Simpson J, Roach M, 3rd. Current role and future perspectives of magnetic resonance spectroscopy in radiation oncology for prostate cancer. Neoplasia. 2007 Jun;9(6):455-63.
175. Jagannathan NR, Kumar V, Kumar R, Thulkar S. Role of magnetic resonance methods in the evaluation of prostate cancer: an Indian perspective. Magma. 2008 Nov;21(6):393-407.
176. Weis J, Ahlstrom H, Hlavcak P, Haggman M, Ortiz-Nieto F, Bergman A. Two-dimensional spectroscopic imaging for pretreatment evaluation of prostate cancer: comparison with the step-section histology after radical prostatectomy. Magn Reson Imaging. 2009 Jan;27(1):87-93.
177. Lange T, Schulte RF, Boesiger P. Quantitative J-resolved prostate spectroscopy using two-dimensional prior-knowledge fitting. Magn Reson Med. 2008 May;59(5):966-72.
178. van Asten JJ, Cuijpers V, Hulsbergen-van de Kaa C, Soede-Huijbregts C, Witjes JA, Verhofstad A, Heerschap A. High resolution magic angle spinning NMR spectroscopy for metabolic assessment of cancer presence and Gleason score in human prostate needle biopsies. Magma. 2008 Nov;21(6): 435-42.
179. Wu CL, Taylor JL, He W, Zepeda AG, Halpern EF, Bielecki A, Gonzalez RG, Cheng LL. Proton high-resolution magic angle spinning NMR analysis of fresh and previously frozen tissue of human prostate. Magn Reson Med. 2003;50(6):1307-11.

180. Swanson MG, Zektzer AS, Tabatabai ZL, Simko J, Jarso S, Keshari KR, Schmitt L, Carroll PR, Shinohara K, Vigneron DB, Kurhanewicz J. Quantitative analysis of prostate metabolites using 1H HR-MAS spectroscopy. Magn Reson Med. 2006 Jun;55(6):1257-64.
181. Swanson MG, Keshari KR, Tabatabai ZL, Simko JP, Shinohara K, Carroll PR, Zektzer AS, Kurhanewicz J. Quantification of choline- and ethanolamine-containing metabolites in human prostate tissues using 1H HR-MAS total correlation spectroscopy. Magn Reson Med. 2008 Jul;60(1):33-40.
182. Pauly J, Le Roux P, Nishimura D, Macovski A. Parameter relations for the Shinnar-Le Roux selective excitation pulse design algorithm [NMR imaging]. Medical Imaging, IEEE Transactions on. 1991;10(1):53-65.
183. van Dorsten FA, van der Graaf M, Engelbrecht MR, van Leenders GJ, Verhofstad A, Rijpkema M, de la Rosette JJ, Barentsz JO, Heerschap A. Combined quantitative dynamic contrast-enhanced MR imaging and (1)H MR spectroscopic imaging of human prostate cancer. J Magn Reson Imaging. 2004 Aug;20(2):279-87.
184. Carlani M, Mancino S, Bonanno E, Finazzi Agro E, Simonetti G. Combined morphological, [1H]-MR spectroscopic and contrast-enhanced imaging of human prostate cancer with a 3-Tesla scanner: preliminary experience. Radiol Med. 2008 Aug;113(5):670-88.
185. Mueller-Lisse UG, Swanson MG, Vigneron DB, Kurhanewicz J. Magnetic resonance spectroscopy in patients with locally confined prostate cancer: association of prostatic citrate and metabolic atrophy with time on hormone deprivation therapy, PSA level, and biopsy Gleason score. Eur Radiol. 2007 Feb;17(2):371-8.
186. Mueller-Lisse U, Scheidler J, Klein G, Reiser M. Reproducibility of image interpretation in MRI of the prostate: application of the sextant framework by two different radiologists. Eur Radiol. 2005 Sep;15(9):1826-33.
187. Mountford C, Lean C, Malycha P, Russell P. Proton spectroscopy provides accurate pathology on biopsy and in vivo. J Magn Reson Imaging. 2006 Sep; 24(3):459-77.
188. Garnick MB. Prostate cancer: screening, diagnosis, and management. Annals of Internal Medicine. 1993;118:804-18.
189. Venugopal N, McCurdy B, Mehairi SA, Alamri A, Sandhu GS, Drachenberg D, Ryner L, editors. Short echo time in vivo prostate MRSI. ISMRM 18th Scientific Meeting & Exhibition; 2010; Stockholm, Sweden: International Society for Magnetic Resonance in Medicine.
190. Beyersdorff D, Winkel A, Hamm B, Lenk S, Loening SA, Taupitz M. MR imaging-guided prostate biopsy with a closed MR unit at 1.5 T: initial results. Radiology. 2005 Feb;234(2):576-81.
191. Taylor JL, Wu CL, Cory D, Gonzalez RG, Bielecki A, Cheng LL. High-resolution magic angle spinning proton NMR analysis of human prostate tissue with slow spinning rates. Magn Reson Med. 2003;50(3):627-32.
192. Villers A, Lemaitre L, Haffner J, Puech P. Current status of MRI for the diagnosis, staging and prognosis of prostate cancer: implications for focal therapy and active surveillance. Curr Opin Urol. 2009 May;19(3):274-82.

193. Venugopal N, McCurdy B, Hnatov A, Dubey A. A feasibility study to investigate the use of thin-plate splines to account for prostate deformation. Phys Med Biol. 2005 Jun 21;50(12):2871-85.
194. Chen ME, Troncoso P, Johnston DA, Tang K, Babaian RJ. Optimization of prostate biopsy strategy using computer based analysis. J Urol. 1997 Dec; 158(6):2168-75.
195. Kumar V, Jagannathan NR, Kumar R, Thulkar S, Gupta SD, Hemal AK, Gupta NP. Transrectal ultrasound-guided biopsy of prostate voxels identified as suspicious of malignancy on three-dimensional (1)H MR spectroscopic imaging in patients with abnormal digital rectal examination or raised prostate specific antigen level of 4-10 ng/ml. NMR Biomed. 2007 Feb;20(1): 11-20.
196. Levine MA, Ittman M, Melamed J, Lepor H. Two consecutive sets of transrectal ultrasound guided sextant biopsies of the prostate for the detection of prostate cancer. J Urol. 1998 Feb;159(2):471-5; discussion 5-6.
197. Rabbani F, Stroumbakis N, Kava BR, Cookson MS, Fair WR. Incidence and clinical significance of false-negative sextant prostate biopsies. J Urol. 1998 Apr;159(4):1247-50.
198. Bhatia C, Phongkitkarun S, Booranapitaksonti D, Kochakarn W, Chaleumsanyakorn P. Diagnostic accuracy of MRI/MRSI for patients with persistently high PSA levels and negative TRUS-guided biopsy results. J Med Assoc Thai. 2007 Jul;90(7):1391-9.
199. Coleman JA. Editorial comment on: MR-guided biopsy of the prostate: an overview of techniques and a systematic review. Eur Urol. 2008 Sep;54(3): 525-6.
200. Elhawary H, Zivanovic A, Rea M, Davies B, Besant C, McRobbie D, de Souza N, Young I, Lamperth M. The feasibility of MR-image guided prostate biopsy using piezoceramic motors inside or near to the magnet isocentre. Med Image Comput Comput Assist Interv. 2006;9(Pt 1):519-26.
201. Pondman KM, Futterer JJ, ten Haken B, Schultze Kool LJ, Witjes JA, Hambrock T, Macura KJ, Barentsz JO. MR-guided biopsy of the prostate: an overview of techniques and a systematic review. Eur Urol. 2008 Sep;54(3): 517-27.
202. Sciarra A. Editorial comment on: MR-guided biopsy of the prostate: an overview of techniques and a systematic review. Eur Urol. 2008 Sep;54(3): 526-7.
203. Mueller-Lisse UG, Vigneron DB, Hricak H, Swanson MG, Carroll PR, Bessette A, Scheidler J, Srivastava A, Males RG, Cha I, Kurhanewicz J. Localized prostate cancer: effect of hormone deprivation therapy measured by using combined three-dimensional 1H MR spectroscopy and MR imaging: clinicopathologic case-controlled study. Radiology. 2001;221(2): 380-90.
204. Scheenen TW, Heijmink SW, Roell SA, Hulsbergen-Van de Kaa CA, Knipscheer BC, Witjes JA, Barentsz JO, Heerschap A. Three-dimensional proton MR spectroscopy of human prostate at 3 T without endorectal coil: feasibility. Radiology. 2007 Nov;245(2):507-16.

205. Shukla-Dave A, Hricak H, Moskowitz C, Ishill N, Akin O, Kuroiwa K, Spector J, Kumar M, Reuter VE, Koutcher JA, Zakian KL. Detection of prostate cancer with MR spectroscopic imaging: an expanded paradigm incorporating polyamines. Radiology. 2007 Nov;245(2):499-506.
206. Fayed N, Modrego PJ, Medrano J. Comparative test-retest reliability of metabolite values assessed with magnetic resonance spectroscopy of the brain. The LCModel versus the manufacturer software. Neurol Res. 2009 Jun; 31(5):472-7.
207. Lin Y, Zhang YP, Xiao ZW, Li H, Shen ZW, Chen XK, Huang K, Wu RH. Quantification of brain creatine concentration using PRESS sequence and LCModel: comparison with HPLC method. Conf Proc IEEE Eng Med Biol Soc. 2006;1:1928-31.
208. Srinivasan R, Vigneron D, Sailasuta N, Hurd R, Nelson S. A comparative study of myo-inositol quantification using LCmodel at 1.5 T and 3.0 T with 3 D 1H proton spectroscopic imaging of the human brain. Magn Reson Imaging. 2004 May;22(4):523-8.
209. Garcia-Martin ML, Adrados M, Ortega MP, Fernandez Gonzalez I, Lopez-Larrubia P, Viano J, Garcia-Segura JM. Quantitative (1)H MR spectroscopic imaging of the prostate gland using LCModel and a dedicated basis-set: Correlation with histologic findings. Magn Reson Med. 2010 Oct 11.
210. Heerschap A, Jager GJ, van der Graaf M, Barentsz JO, Ruijs SH. Proton MR spectroscopy of the normal human prostate with an endorectal coil and a double spin-echo pulse sequence. Magn Reson Med. 1997 Feb;37(2): 204-13.
211. Yacoe ME, Sommer G, Peehl D. In vitro proton spectroscopy of normal and abnormal prostate. Magn Reson Med. 1991;19(2):429-38.
212. Kobayashi T, Mitsumori K, Nishizawa K, Kawahara T, Ogura K, Ide Y. Use of effective core volume obtained from transrectal biopsies for predicting target tumor volume. Urology. 2005 Oct;66(4):794-8.
213. Lowry M, Zelhof B, Liney GP, Gibbs P, Pickles MD, Turnbull LW. Analysis of prostate DCE-MRI: comparison of fast exchange limit and fast exchange regimen pharmacokinetic models in the discrimination of malignant from normal tissue. Invest Radiol. 2009 Sep;44(9):577-84.
214. Zaidi H, Vees H, Wissmeyer M. Molecular PET/CT imaging-guided radiation therapy treatment planning. Acad Radiol. 2009 Sep;16(9):1108-33.
215. Maggio A, Fiorino C, Mangili P, Cozzarini C, de Cobelli F, Cattaneo GM, Rancati T, Maschio AD, Muzio ND, Calandrino R. Feasibility of safe ultra-high (EQD(2)>100 Gy) dose escalation on dominant intra-prostatic lesions (DILs) by Helical Tomotheraphy. Acta Oncol. 2010 Jan;50(1):25-34.
216. Housri N, Ning H, Ondos J, Choyke P, Camphausen K, Citrin D, Arora B, Shankavaram U, Kaushal A. Parameters Favorable to Intraprostatic Radiation Dose Escalation in Men With Localized Prostate Cancer. International Journal of Radiation Oncology*Biology*Physics. 2010;80(2):614-20.
217. Singh AK, Guion P, Sears-Crouse N, Ullman K, Smith S, Albert PS, Fichtinger G, Choyke PL, Xu S, Kruecker J, Wood BJ, Krieger A, Ning H. Simultaneous integrated boost of biopsy proven, MRI defined dominant intra-prostatic

lesions to 95 Gray with IMRT: early results of a phase I NCI study. Radiat Oncol. 2007;2:36.
218. Grosu AL, Wiedenmann N, Molls M. Biological imaging in radiation oncology. Z Med Phys. 2005;15(3):141-5.
219. Grosu AL, Piert M, Weber WA, Jeremic B, Picchio M, Schratzenstaller U, Zimmermann FB, Schwaiger M, Molls M. Positron emission tomography for radiation treatment planning. Strahlenther Onkol. 2005 Aug;181(8):483-99.
220. De Meerleer G, Villeirs G, Bral S, Paelinck L, De Gersem W, Dekuyper P, De Neve W. The magnetic resonance detected intraprostatic lesion in prostate cancer: planning and delivery of intensity-modulated radiotherapy. Radiother Oncol. 2005 Jun;75(3):325-33.
221. Chen L, Price RA, Jr., Wang L, Li J, Qin L, McNeeley S, Ma CM, Freedman GM, Pollack A. MRI-based treatment planning for radiotherapy: dosimetric verification for prostate IMRT. Int J Radiat Oncol Biol Phys. 2004 Oct 1;60 (2):636-47.
222. Wurschmidt F, Petersen C, Wahl A, Dahle J, Kretschmer M. [18F] fluoroethylcholine-PET/CT imaging for radiation treatment planning of recurrent and primary prostate cancer with dose escalation to PET/CT-positive lymph nodes. Radiat Oncol.6:44.
223. Ling CC, Humm J, Larson S, Amols H, Fuks Z, Leibel S, Koutcher JA. Towards multidimensional radiotherapy (MD-CRT): biological imaging and biological conformality. Int J Radiat Oncol Biol Phys. 2000 Jun 1;47(3):551-60.
224. Zelefsky MJ, Fuks Z, Hunt M, Yamada Y, Marion C, Ling CC, Amols H, Venkatraman ES, Leibel SA. High-dose intensity modulated radiation therapy for prostate cancer: early toxicity and biochemical outcome in 772 patients. Int J Radiat Oncol Biol Phys. 2002 Aug 1;53(5):1111-6.
225. Kirilova A, Damyanovich A, Crook J, Jezioranski J, Wallace K, Pintilie M. 3D MR-Spectroscopic Imaging Assessment of Metabolic Activity in the Prostate During the PSA "Bounce" Following (125)Iodine Brachytherapy. Int J Radiat Oncol Biol Phys. 2010 Feb 1;79(2):371-8.
226. Pickett B, Kurhanewicz J, Coakley F, Shinohara K, Fein B, Roach M, 3rd. Use of MRI and spectroscopy in evaluation of external beam radiotherapy for prostate cancer. Int J Radiat Oncol Biol Phys. 2004 Nov 15;60(4):1047-55.
227. Turesson I, Carlsson J, Brahme A, Glimelius B, Zackrisson B, Stenerlow B. Biological response to radiation therapy. Acta Oncol. 2003;42(2):92-106.
228. Wolbarst AB, Chin LM, Svensson GK. Optimization of radiation therapy: integral-response of a model biological system. Int J Radiat Oncol Biol Phys. 1982 Oct;8(10):1761-9.
229. Alber M, Paulsen F, Eschmann SM, Machulla HJ. On biologically conformal boost dose optimization. Phys Med Biol. 2003 Jan 21;48(2):N31-5.
230. Pouliot J, Kim Y, Lessard E, Hsu IC, Vigneron DB, Kurhanewicz J. Inverse planning for HDR prostate brachytherapy used to boost dominant intraprostatic lesions defined by magnetic resonance spectroscopy imaging. Int J Radiat Oncol Biol Phys. 2004;59(4):1196-207.
231. Noworolski SM, Crane JC, Vigneron DB, Kurhanewicz J. A clinical comparison of rigid and inflatable endorectal-coil probes for MRI and 3D

MR spectroscopic imaging (MRSI) of the prostate. J Magn Reson Imaging. 2008 May;27(5):1077-82.
232. Rosen Y, Bloch BN, Lenkinski RE, Greenman RL, Marquis RP, Rofsky NM. 3T MR of the prostate: reducing susceptibility gradients by inflating the endorectal coil with a barium sulfate suspension. Magn Reson Med. 2007 May;57(5):898-904.
233. Gering DT, Nabavi A, Kikinis R, Hata N, O'Donnell LJ, Grimson WE, Jolesz FA, Black PM, Wells WM, 3rd. An integrated visualization system for surgical planning and guidance using image fusion and an open MR. J Magn Reson Imaging. 2001 Jun;13(6):967-75.
234. Burman C, Kutcher GJ, Emami B, Goitein M. Fitting of normal tissue tolerance data to an analytic function. Int J Radiat Oncol Biol Phys. 1991 May 15;21(1):123-35.
235. Nahum AE, Movsas B, Horwitz EM, Stobbe CC, Chapman JD. Incorporating clinical measurements of hypoxia into tumor local control modeling of prostate cancer: implications for the alpha/beta ratio. Int J Radiat Oncol Biol Phys. 2003 Oct 1;57(2):391-401.
236. Steel GG. The growth kinetics of tumors in relation to their therapeutic response. Laryngoscope. 1975 Feb;85(2):359-70.
237. Steel GG. Chemotherapeutic response of experimental solid tumors. Can J Otolaryngol. 1975;4(1):18-20.
238. Steel GG, Lamerton LF. Cell population kinetics and chemotherapy. I. The kinetics of tumor cell populations. Natl Cancer Inst Monogr. 1969 May; 30:29-42.
239. Shukla-Dave A, Hricak H, Eberhardt SC, Olgac S, Muruganandham M, Scardino PT, Reuter VE, Koutcher JA, Zakian KL. Chronic prostatitis: MR imaging and 1H MR spectroscopic imaging findings--initial observations. Radiology. 2004;231(3):717-24.
240. Zelefsky MJ, Yamada Y, Fuks Z, Zhang Z, Hunt M, Cahlon O, Park J, Shippy A. Long-term results of conformal radiotherapy for prostate cancer: impact of dose escalation on biochemical tumor control and distant metastases-free survival outcomes. Int J Radiat Oncol Biol Phys. 2008 Jul 15;71(4):1028-33.
241. Chen T, Kim S, Zhou J, Metaxas D, Rajagopal G, Yue N. 3D meshless prostate segmentation and registration in image guided radiotherapy. Med Image Comput Comput Assist Interv. 2009;12(Pt 1):43-50.
242. Chow JC, Jiang R, Markel D. The effect of interfraction prostate motion on IMRT plans: a dose-volume histogram analysis using a Gaussian error function model. J Appl Clin Med Phys. 2009;10(4):3055.
243. Rothe Arnesen M, Eilertsen K, Malinen E. Optimal treatment margins for radiotherapy of prostate cancer based on interfraction imaging. Acta Oncol. 2008;47(7):1373-81.
244. Showalter TN, Nawaz AO, Xiao Y, Galvin JM, Valicenti RK. A cone beam CT-Based Study for Clinical Target Definition Using Pelvic Anatomy During Postprostatectomy Radiotherapy. Int J Radiat Oncol Biol Phys. 2008 Feb 1;70 (2):431-6.

245. Heerschap A, Jager GJ, van der Graaf M, Barentsz JO, de la Rosette JJ, Oosterhof GO, Ruijter ET, Ruijs SH. In vivo proton MR spectroscopy reveals altered metabolite content in malignant prostate tissue. Anticancer Res. 1997 May-Jun;17(3A):1455-60.
246. DiBiase SJ, Hosseinzadeh K, Gullapalli RP, Jacobs SC, Naslund MJ, Sklar GN, Alexander RB, Yu C. Magnetic resonance spectroscopic imaging-guided brachytherapy for localized prostate cancer. Int J Radiat Oncol Biol Phys. 2002 Feb 1;52(2):429-38.
247. Huisman HJ, Futterer JJ, van Lin EN, Welmers A, Scheenen TW, van Dalen JA, Visser AG, Witjes JA, Barentsz JO. Prostate cancer: precision of integrating functional MR imaging with radiation therapy treatment by using fiducial gold markers. Radiology. 2005 Jul;236(1):311-7.
248. van der Graaf M, Schipper RG, Oosterhof GO, Schalken JA, Verhofstad AA, Heerschap A. Proton MR spectroscopy of prostatic tissue focused on the detection of spermine, a possible biomarker of malignant behavior in prostate cancer. Magma. 2000;10(3):153-9.
249. Citrin D, Ning H, Guion P, Li G, Susil RC, Miller RW, Lessard E, Pouliot J, Huchen X, Capala J, Coleman CN, Camphausen K, Menard C. Inverse treatment planning based on MRI for HDR prostate brachytherapy. Int J Radiat Oncol Biol Phys. 2005 Mar 15;61(4):1267-75.
250. Heijmink SW, Scheenen TW, Futterer JJ, Klomp DW, Heesakkers RA, Hulsbergen-van de Kaa CA, van Lin EN, Heerschap A, Barentsz JO. Prostate and lymph node proton magnetic resonance (MR) spectroscopic imaging with external array coils at 3 T to detect recurrent prostate cancer after radiation therapy. Invest Radiol. 2007 Jun;42(6):420-7.
251. Flores-Tapia D, Thomas G, Venugopal N, McCurdy B, Pistorius S. Semi automatic MRI prostate segmentation based on wavelet multiscale products. Conf Proc IEEE Eng Med Biol Soc. 2008;2008:3020-3.
252. Flores-Tapia D, Venugopal N, Thomas G, McCurdy B, Ryner L, Pistorius S. Real time MRI prostate segmentation based on wavelet multiscale products flow tracking. Conf Proc IEEE Eng Med Biol Soc. 2010;1:5034-7.
253. Futterer JJ, Scheenen TW, Huisman HJ, Klomp DW, van Dorsten FA, Hulsbergen-van de Kaa CA, Witjes JA, Heerschap A, Barentsz JO. Initial experience of 3 tesla endorectal coil magnetic resonance imaging and 1H-spectroscopic imaging of the prostate. Invest Radiol. 2004 Nov;39(11): 671-80.
254. Kim CK, Park BK, Lee HM. Prediction of locally recurrent prostate cancer after radiation therapy: incremental value of 3T diffusion-weighted MRI. J Magn Reson Imaging. 2009 Feb;29(2):391-7.
255. Kim CK, Park BK, Kim B. Localization of prostate cancer using 3T MRI: comparison of T2-weighted and dynamic contrast-enhanced imaging. J Comput Assist Tomogr. 2006 Jan-Feb;30(1):7-11.
256. Kim CK, Park BK, Lee HM, Kwon GY. Value of diffusion-weighted imaging for the prediction of prostate cancer location at 3T using a phased-array coil: preliminary results. Invest Radiol. 2007 Dec;42(12):842-7.

257. Noworolski SM, Reed GD, Kurhanewicz J, Vigneron DB. Post-processing correction of the endorectal coil reception effects in MR spectroscopic imaging of the prostate. J Magn Reson Imaging. 2010 Sep;32(3):654-62.
258. Sakoda J, Uchida M, Nagata S, Matsuoka K, Abe T, Hayabuchi N. MR imaging of prostate cancer at 3T with an external phased-array coil: evaluation of T2-weighted images. Kurume Med J. 2009;56(3-4):71-7.
259. Near J, Romagnoli C, Curtis AT, Klassen LM, Izawa J, Chin J, Bartha R. High-field MRSI of the prostate using a transmit/receive endorectal coil and gradient modulated adiabatic localization. J Magn Reson Imaging. 2009 Aug;30(2):335-43.
260. Tiwari P, Rosen M, Madabhushi A. Consensus-locally linear embedding (C-LLE): application to prostate cancer detection on magnetic resonance spectroscopy. Med Image Comput Comput Assist Interv. 2008;11(Pt 2): 330-8.
261. Madabhushi A, Feldman MD, Metaxas DN, Tomaszeweski J, Chute D. Automated detection of prostatic adenocarcinoma from high-resolution ex vivo MRI. IEEE Trans Med Imaging. 2005 Dec;24(12):1611-25.
262. Madabhushi A, Shi J, Rosen M, Tomaszeweski JE, Feldman MD. Graph embedding to improve supervised classification and novel class detection: application to prostate cancer. Med Image Comput Comput Assist Interv. 2005;8(Pt 1):729-37.
263. Xu J, Humphrey PA, Kibel AS, Snyder AZ, Narra VR, Ackerman JJ, Song SK. Magnetic resonance diffusion characteristics of histologically defined prostate cancer in humans. Magn Reson Med. 2009 Apr;61(4):842-50.
264. Claus FG, Hricak H, Hattery RR. Pretreatment evaluation of prostate cancer: role of MR imaging and 1H MR spectroscopy. Radiographics. 2004 Oct;24 Suppl 1:S167-80.
265. Chen CN, Hoult DI. Biomedical Magnetic Resonance Technology. New York: Adam Hilger; 1989.
266. Bernstein MA, King KF, Zhou XJ. Handbook of MRI pulse sequences. Burlington, MA: Elsevier Academic Press; 2004.
267. De Graaf RA. In vivo NMR spectroscopy : principles and techniques. 2nd ed. Chichester, West Sussex, England ; Hoboken, NJ: John Wiley & Sons; 2007.
268. Hahn EL. Spin Echoes. Physical Review. 1950;80(4):580.
269. Liang Z-P, Lauterbur PC. Principles of magnetic resonance imaging : a signal processing perspective. New York: SPIE Optical Engineering Press, IEEE Press; 2000.

"No road is long with good company."~Turkish Proverb